The University of Crete

SADDLE–NODE BIFURCATIONS IN THE VIBRATIONAL SPECTRA OF SMALL POLYATOMIC MOLECULES

By

Stamatis Stamatiadis

Submitted in partial fulfillment of the requirements
for the degree of Doctor of Philosophy
to the Department of Physics
of the University of Crete

April 2003

Typeset in LaTeX by the author.

Contents

Chapter 1

Introduction

A major goal of molecular spectroscopy is to understand the forces which couple the degrees of freedom of a polyatomic molecule and thereby control the internal energy flow. These forces manifest indirectly in the vibrational–rotational energy levels of the molecule. In the context of internal vibrational energy redistribution, interesting issues to spectroscopists, both experimentalists and theorists, are the dissociation and the isomerization processes in highly excited molecules and, specifically, the way these processes are reflected in the vibrational–rotational energy spectra. The recognition of patterns in a spectrum attributed to such unimolecular reactions is greatly facilitated by the appropriate assignment of the quantum states, especially the highly excited ones. The departure from the simple picture of the independent normal modes as energy increases can be quite dramatic and puzzling. New classification schemes ought to be devised and diagnostic features should be identified. If we can interpret a spectrum and understand the mechanisms which influence it, we may be able to identify the chemical character of a molecule in a reaction, predict its spectral characteristics and account for or even control the evolution of a chemical process.

Our understanding of atoms and molecules is rapidly enhanced by the advances in laser spectroscopy. Experimental techniques and instruments have allowed the spectroscopists to analyze spectra in detail with very high resolution. The development of modern spectroscopic techniques such as the *Dispersed Fluorescence (DF)* and the *Stimulated Emission Pumping (SEP)* [1], enables researchers to trace out the vibrational motions of highly excited small polyatomic molecules, in particular those taking place in the course of chemical reactions. Moreover, the sustained availability of ever powerful computers and the progress made in numerical algorithms and ab initio electronic structure methods in recent years, make feasible a very satisfactory, complete, ab initio study of realistic systems of few particles. Nowadays, the construction of a global ab initio potential energy surface for light polyatomic molecules, in excellent agreement with experiment, is common place, as well as the complete solution of the Schrödinger equation using such a potential. A very thorough review on the present status of molecular spectroscopy is given in [2].

One of the research interests of our group is the study of highly excited vibrational levels of small polyatomic molecules. Specifically, the recognition of the spectroscopic signatures of a qualitative change in the character of the vibrational

states—such as a transition from a normal- to local- mode picture or the onset of bond rearrangement in an isomerization process, is one of the central issues of our work. Special consideration is given on the implications on the spectrum of resonances that may be exhibited between the normal modes in the molecule. We follow a novel approach through periodic orbit analysis of the classical phase space in order to study the behavior of a molecule.

The experimental observation, theoretical calculation, and identification of isomerization states are quite intricate tasks due to the high energy required to overcome the barrier separating the isomers, the subsequently large density of states and the special character these states have as they explore large parts of the phase space. Similar remarks apply to resonance states in unbound systems. At high energies, the chaotic nature of the nonlinear potential of the molecules is most prominent; saddle–node bifurcations occur in the classical phase space, and, as it will be shown, influence considerably the energy spectrum. The large density of states in high energy regime together with the chaotic effects complicate the analysis and understanding of the spectrum, making imperative the close collaboration between experiment, classical, semiclassical and quantum treatment in order to achieve a complete and detailed interpretation of the rotational–vibrational spectrum.

The "traditional" approach of spectroscopists to the reconstruction of the observed spectrum and the interpretation of the dynamics of a molecule, starts by determining various molecular constants such as vibrational frequencies, rotational constants and so on. Then, a simple parametric Hamiltonian of uncoupled harmonic oscillators, valid around the equilibrium configuration, is fitted to these experimental data (or ab initio calculated force constants for low energies). This way, each state in the spectrum can be assigned a set of quantum numbers based either on regular patterns of the energy levels or the nodal patterns in the eigenfunctions. The simple Hamiltonian is gradually extended with anharmonic terms and couplings of the normal modes as the energy increases. The eigenvalues of the resulting *effective* Hamiltonian are typically expressed in a series of powers of the quantum numbers, the *Dunham expansion* form. This model gradually breaks down in higher energies as the normal modes deviate from the actual oscillators, exhibiting a substantial change in their character. Nonlinear effects set in and the coupling of the electronic, vibrational and rotational degrees of freedom becomes non-negligible. Normal modes may be destroyed and others appear; spectra become too dense and complex to be described by a simple model. Processes such as dissociation or isomerization, exploring regions well above the energy minima, cannot be treated successfully in this approach. The construction of accurate *global* Potential Energy Surfaces from ab initio data, covering not only the equilibrium configuration but all the accessible space, and the solution of the corresponding multidimensional Schrödinger equation, calculating highly excited bound states, are necessary. These tasks were achieved for small molecules with three of four atoms only in the last decade [3]; it is still a computational challenge to treat more atoms with ab initio methods [4].

Still, the calculation of thousands of wave functions has little merit without the proper assignment of quantum numbers which itself is a quite formidable and at the same time, questionable task as the energy increases. The assignment should consist of not only a set of numbers but, also, the exact type of vibration associated

with each normal mode. The qualitative dependence on energy of the character, and even of the existence, of the normal modes, renders the classification in terms of independent vibrations meaningless. More important than compiling a parametrized list of all energy levels, are the identification of specific patterns in the spectrum, their interpretation in terms of particular features of the system, and the extraction of dynamical information encoded in the spectrum. These are the actual challenges for the theorists and this is where classical mechanics steps in.

During the last few decades, various techniques were developed to interpret qualitatively highly congested and complex spectra. Methods of statistical nature based on random matrix theory [5], adjust statistical distributions with few parameters to describe energy levels [6], eigenfunctions [7], and intensities. These methods assume either regularity or ergodicity in the systems they apply on.

Techniques which employ particular sortings of the spectral lines, facilitating the recognition of patterns and the hierarchical coupling in spectra have been developed. Such a method is the one by Davis [8], in which hierarchical "trees" are generated from molecular spectra by following the branching of peaks as resolution is changed continuously. The trees can then be analyzed using several techniques developed in the classification and multivariate analysis literature. This way, information is obtained on the time scales of the dynamics and the hierarchical structure of spectra. Other methods for pattern recognition and extraction in experimental molecular spectra are the extended cross-correlation [9] and extended auto-correlation methods [10] of Coy, Jacobson, and Field. The first allows the rapid identification and extraction of patterns that are repeated in multiple experimental records. The second technique permits the identification of complex patterns that are parameterized in a multidimensional way, even when the patterns are obscured by the presence of interfering data.

Other approaches, of dynamical nature, are the semiclassical methods, in the broad sense, which attempt to establish a correspondence between quantum states and classical entities. These methods can describe specific spectral characteristics and contribute an understanding of the intramolecular vibrational redistribution process. Numerical experiments show that, in general, the quantum eigenfunctions and the distributions of eigenvalues reflect the structure of the classical phase space: in regular regions, the eigenfunctions are localized with well-ordered nodal patterns while in chaotic regimes the opposite is in general true. In hard chaos the complete delocalization of wave functions can be proven. The distributions of the differences of adjacent energy levels also differ in regular and chaotic areas. There are notable exceptions in this picture, though; in classically chaotic regions, wave functions can be localized to some extent. This localization is associated with periodic orbits, as we will see below.

Direct application of Classical Mechanics can certainly not justify the stability of atoms and molecules and, in general, account for their behavior in low energy levels. However, the dynamics of highly excited atoms and molecules are often characterized by actions much larger than the Planck constant; chaotic effects prevail over regular motion and the density of states rises exponentially, approaching the classical limit. A large number of low intensity lines, practically continuous, interspersed with more intense ones comprise the energy spectra in this regime; the assignment of energy

levels in terms of quantum numbers is incomplete and dubious there. It is, therefore, important to understand the nonlinear features of the classical systems and relate them to quantum characteristics in high energy regimes where other approaches may break down.

In regular systems, the correspondence of classical and quantum mechanics is fully established in the form of the Einstein–Brillouin–Keller (EBK) theory which will be outlined in a subsequent chapter. Classical mechanics turns out to be very useful in understanding certain aspects of molecular processes—such as ionization, dissociation, molecular collisions, isomerization, interaction of electromagnetic radiation with molecules—taking place at higher energies where chaos sets in. Apart from the qualitative interpretation that can be achieved through the classical treatment, many long-time quantum properties can be quantitatively understood using short-time classical dynamics information; these include wave function intensity distributions, intensity correlations in phase space and correlations between wave functions, and distributions of decay rates and conductance peaks in weakly open systems. The correspondence of classical and quantum systems in high-energy chaotic regions is a far from closed research issue.

Pioneering studies on model potentials and, more recently, on realistic systems, have demonstrated the crucial assistance of classical theory in the recognition and interpretation of specific experimental or quantum features. Among other classical objects, periodic orbits and bifurcations in the corresponding classical systems have been shown to relate to the localization of wave functions [11, 12], the distribution of the prominent peaks in low resolution spectra, the density of states [13], and the sudden birth of important classes of quantum states [14]. The periodic orbits of a system, in conjunction with continuation techniques providing their quantitative dependence on energy in the form of continuation/bifurcation diagrams, and their structural changes (bifurcations) exhibited on specific energy values are very useful concepts and tools in interpreting the evolution of spectra from the low energy regime deep into the potential well up to highly excited regions [15]. Periodic orbits born around the potential minima and through the bifurcation mechanisms, proliferate with increasing energy, thus providing a framework on which assignment of the ever complex quantum states is meaningful and liberated from the constraint of the fixed number of normal modes. Other special characteristics of the classical phase space, such as the stable and unstable manifolds and the remnants of tori, relate with and influence specific states and patterns of the quantum spectra [16, 17]. Being exact objects, living in approximately the same nonlinear phase space which yields the experimental or quantum spectrum, classical entities express, within the limits of the uncertainty principle, all features governing the actual behavior.

Polyatomic molecules offer real systems for testing the theories of nonlinear classical mechanics; they are realistic cases where the interpretation of the spectrum and the dynamics in terms of periodic orbits can be applied and developed further. Our research group was interested in various triatomic molecules: hydrogen cyanide (HCN), phosphaethyne and deuterated phosphaethyne (HCP/DCP), formyl radical and deuterated formyl radical (HCO/DCO), hypochlorous acid (HOCl), hypobromous acid (HOBr), and $HeH_2^+/HeHD^+/HeDH^+$. Our contribution in the study of some of them will be presented in this thesis. The classical treatment for them complements the quantum mechanical, semiclassical, and, in cases, experimental

results obtained by the collaborating research groups, making these molecules prototypes for which a complete and extensive study is available and valuable tests of the theories can be conducted.

The presentation of this work is developed with the specific consideration of being accessible to non-experts. To this end it summarizes hopefully all necessary topics for a newcomer to the field providing an extensive reference to the relevant literature for those who wish to pursue these matters further. This thesis is organized as follows: In the next chapter, a detailed presentation of the classical view of dynamical systems, both regular and chaotic, and their phase space characteristics is given, along with an overview of the semiclassical methods relating them to the quantum picture. In the third chapter, the framework of theoretical molecular spectroscopy is presented, with an overview of the methods used for the derivation of potentials and the solution of the quantum Hamiltonian. The fourth chapter is technical in nature: it presents the methods and algorithms employed in constructing the continuation/bifurcation diagrams; among them, the, relatively new in computational physics, genetic algorithms are adapted to our type of problems. The subsequent chapter presents a program facilitating the automatic differentiation of mathematical functions encoded in the FORTRAN 90 programming language; it was developed during our research, tested in highly complex functions—the potentials we used, and published. The sixth, seventh and eighth chapters present our work on the HCP/DCP, HCO/DCO, and HOCl molecules, the results we obtained by the periodic orbit analysis and their relation to the outcome of the quantum and experimental treatment. The thesis concludes with a brief overview of our findings. Parts of our research work were published in the following articles:

1. Pankaj Bhatia, Biswajit Maiti, Narayanasami Sathyamurthy, Stamatis Stamatiadis, and Stavros C. Farantos. Exploring molecular motions in collinear HeH_2^+ and its isotopic variants using periodic orbits. *Physical Chemistry Chemical Physics*, 1(6):1105–1114, March 1999.

2. J. Weiß, J. Hauschildt, S. Yu. Grebenshchikov, R. Düren, R. Schinke, J. Koput, S. Stamatiadis, and S. C. Farantos. Saddle–node bifurcations in the spectrum of HOCl. *J. Chem. Phys.*, 112(1):77–93, January 2000.

3. B. Maiti, N. Sathyamurthy, S. Stamatiadis, and S. C. Farantos. Periodic Orbit Analysis for HeH_2^+ in three dimensions. *Indian Journal of Chemistry*, 39A(1–3):338–344, 2000.

4. J. Bredenbeck, C. Beck, R. Schinke, J. Koput, S. Stamatiadis, S. C. Farantos, and M. Joyeux. The vibrational spectrum of deuterated phosphaethyne: A quantum mechanical, classical, and semiclassical analysis. *J. Chem. Phys.*, 112(20):8855–8865, May 2000.

5. S. Stamatiadis, R. Prosmiti, and S. C. Farantos. AUTO_DERIV: Tool for automatic differentiation of a FORTRAN code. *Comput. Phys. Commun.*, 127(2&3):343–355, May 2000. URL address: `www.cpc.cs.qub.ac.uk/cpc/summaries/adls`.

6. S. Stamatiadis, S. C. Farantos, Hans-Martin Keller, and Reinhard Schinke. Saddle–node states in the spectra of HCO and DCO: a periodic orbit classification of vibrational levels. *Chem. Phys. Lett.*, 344(5–6):565–572, August 2001.

7. S. C. Farantos, E. Filippou, S. Stamatiadis, G. E. Froudakis, M. Mühlhäuser, M. Massaouti, A. Sfounis, and M. Velegrakis. Photofragmentation spectra of $Sr^{+}CO$ complex: experiment and ab initio calculations. *Chem. Phys. Lett.*, 366(3–4):231–237, December 2002.

Chapter 2

Classical Mechanics

2.1 Introduction

As mentioned in the introductory chapter, an important research issue in the field of chemical physics is the evolution of the vibrational motion of small polyatomic molecules with increasing energy. In realistic systems, non-linear effects set in when the molecule deviates far from the equilibrium configuration and explores an extended region of the phase space. The classical and quantum phase spaces encompass growing chaotic regions which influence considerably the behavior of the system. The rotational–vibrational spectrum can exhibit a considerable chaotic character for which the normal-mode analysis is inadequate. It is necessary to understand how and why certain chaotic entities relate to qualitative variations of the molecular spectra in high energies and devise new approaches to interpret such spectra.

In this chapter, we will provide a concise summary of certain notions of classical mechanics, essential to anyone wishing to analyze and interpret meaningfully the features of complex, chaotic spectra. We will also develop the framework and the definitions on which subsequent chapters are based. Equilibrium points, invariant tori, periodic orbits and bifurcations of them, stable and unstable manifolds can be shown to relate to the distribution of energy levels, influence the form of wave functions, provide the path for chemical reactions, and describe, qualitatively at least, many aspects of the quantum behavior. We will focus especially on periodic orbits and their bifurcations. In subsequent chapters, ample evidence will corroborate that periodic orbits form the "backbone" of quantum wave functions of actual physical systems regardless the energy region; something first noted on model systems. Moreover, we will show that saddle–node and pitchfork bifurcations profoundly affect the vibrational spectra in high energies and can relate to specific types of wave functions.

This chapter is laid out as follows: the first section presents the foundations of classical mechanics, deriving the equations of motion and their properties. Definitions and terminology is given in an attempt to make the chapter as self-sufficient as possible. The second deals with certain characteristic features and phase space structures of dynamical systems: the various kinds of equilibrium points, periodic orbits, and bifurcation types are analyzed in detail. The third section presents the definitions and an overview of integrable and non-integrable systems, leading to an introduction to chaos. Finally, semiclassical methods, which relate aspects of clas-

sical and quantum behavior, are briefly presented, and an introduction to quantum chaos is given.

2.2 Equations of Motion

Let us consider a set of n dimensionless (non-relativistic) particles, with masses $m_i \quad (i = 1, \ldots, n)$, in positions $\vec{r}_i \quad (i = 1, \ldots, n)$ with respect to an inertial reference frame, subject to p independent, *holonomic* constraints of the form:

$$h_j(\vec{r}_1, \vec{r}_2, \ldots, \vec{r}_n, t) = 0 \qquad j = 1, \ldots, p.$$

We say this system has $f = 3n - p$ *degrees of freedom*. The particles may be interacting and external forces may act on them.

We can associate to such a system a particular twice–differentiable function of f independent variables $q_1, q_2, \ldots, q_f$ (collectively denoted by $\mathbf{q}$), their time derivatives $\dot{q}_1, \dot{q}_2, \ldots, \dot{q}_f$ ($\dot{\mathbf{q}}$), and time t; this function $\mathcal{L}(\mathbf{q}, \dot{\mathbf{q}}, t)$ is called the *Lagrangian*. The $q_i = q_i(t)$ are the *generalized coordinates*, functions of $\vec{r}_1, \vec{r}_2, \ldots, \vec{r}_n$. According to the *Hamilton's Variational Principle*, the evolution of the positions of the particles from an initial time t_1 through a final time t_2, is such that the *action integral*, a functional of $\mathbf{q}$,

$$I[\mathbf{q}] = \int_{t_1}^{t_2} \mathcal{L}(\mathbf{q}, \dot{\mathbf{q}}, t)\, \mathrm{d}t, \tag{2.1}$$

assumes an extreme value. The Principle reads:

$$\delta\, I[\mathbf{q}] = 0. \tag{2.2}$$

Note that eq. (2.2) is invariant under gauge transformations of the form

$$\mathcal{L} \to \mathcal{L} + \frac{\mathrm{d}}{\mathrm{d}t} G(\mathbf{q}, t),$$

where G is an arbitrary triply–differentiable function of $\mathbf{q}, t$; that means $\mathcal{L}$ is not unique. If we can further assume that all forces $\vec{F}_i$ acting on the particles are *potential forces*, that is, a scalar function $\mathscr{V}(\vec{r}_1, \vec{r}_2, \ldots, \vec{r}_n, t)$ exists and the equations

$$\vec{F}_i = -\nabla_i \mathscr{V}, \qquad i = 1, \ldots, n$$

hold, then the *Euler–Lagrange* differential equations,

$$\frac{\partial \mathcal{L}}{\partial q_i} - \frac{\mathrm{d}}{\mathrm{d}t}\left(\frac{\partial \mathcal{L}}{\partial \dot{q}_i}\right) = 0 \qquad i = 1, \ldots, f, \tag{2.3}$$

can be derived from this principle.

The Lagrangian for mechanical systems can be defined as the difference of the kinetic energy from the potential,

$$\mathcal{L} = \mathscr{T} - \mathscr{V} = \sum_{i=1}^{n} \frac{1}{2} m_i \dot{\vec{r}}_i^{\,2} - \mathscr{V},$$

expressed in $\mathbf{q}, \dot{\mathbf{q}}$.

There are situations where we prefer to describe the system with another set of generalized coordinates,

$$Q_i = Q_i(q_j, t). \tag{2.4}$$

In such a case, we can express q_j as functions of Q_i, provided $Q_i(q_j, t)$ are independent and invertible, that is, $\det[\partial Q_i/\partial q_j] \neq 0$, and derive a new Lagrangian; $\mathcal{L}(q_i, \dot{q}_i, t)$ becomes $\widetilde{\mathcal{L}}(Q_j, \dot{Q}_j, t)$.

The Variational Principle, eq. (2.2), being independent of the particular choice of the generalized variables, reads

$$\delta I[\mathbf{Q}] = \delta \int_{t_1}^{t_2} \widetilde{\mathcal{L}} \left(\mathbf{Q}, \dot{\mathbf{Q}}, t \right) \, \mathrm{d}t = 0.$$

The form of the Euler–Lagrange equations, eq. (2.3), remains unchanged:

$$\frac{\partial \widetilde{\mathcal{L}}}{\partial Q_i} - \frac{\mathrm{d}}{\mathrm{d}t} \left(\frac{\partial \widetilde{\mathcal{L}}}{\partial \dot{Q}_i} \right) = 0 \qquad i = 1, \ldots, f.$$

Invertible transformations of the kind in eq. (2.4), which leave invariant the form of the Euler–Lagrange equations are called *point transformations*.

There is another way to derive equivalent equations of motion of a mechanical system. If we define the *generalized momenta* p_i *conjugate to the each coordinate* q_i as $p_i = \dfrac{\partial \mathcal{L}}{\partial \dot{q}_i}$, then, $\dot{\mathbf{q}} = \dot{\mathbf{q}}(\mathbf{q}, \mathbf{p}, t)$, provided $\left| \dfrac{\partial^2 \mathcal{L}}{\partial \dot{q}_i \, \partial \dot{q}_j} \right| \neq 0$ holds. We define the *Legendre transform of* $\mathcal{L}$ with respect to $\dot{\mathbf{q}}$ as the *Hamiltonian* function, $\mathcal{H}$:

$$\mathcal{H}(\mathbf{q}, \mathbf{p}, t) = \sum_{i=1}^{f} p_i \dot{q}_i(\mathbf{q}, \mathbf{p}, t) - \mathcal{L} \left(\mathbf{q}, \dot{\mathbf{q}}(\mathbf{q}, \mathbf{p}, t), t \right).$$

$\mathcal{H}$ is defined on the space spanned by $\{\mathbf{q}, \mathbf{p}\}$, called the *phase space*, and may have temporal dependence. If we apply the Hamilton's variational principle to the function

$$\mathscr{F}(\mathbf{q}, \mathbf{p}, \dot{\mathbf{q}}, \dot{\mathbf{p}}, t) = \sum_{i=1}^{f} p_i \dot{q}_i - \mathcal{H}(\mathbf{q}, \dot{\mathbf{q}}, t), \tag{2.5}$$

treating $\mathbf{q}, \mathbf{p}, \dot{\mathbf{q}}, \dot{\mathbf{p}}$ as independent, we derive the *canonical equations* which govern the evolution of the system:

$$\dot{p}_i = -\frac{\partial \mathcal{H}}{\partial q_i}, \qquad \dot{q}_i = \frac{\partial \mathcal{H}}{\partial p_i}. \tag{2.6}$$

In Hamiltonian mechanics, where the generalized momenta are independent of the generalized coordinates, we are allowed a broader choice of transformations compared to point ones, in the form

$$Q_i = Q_i(q_j, p_j, t), \qquad P_i = P_i(q_j, p_j, t).$$

We note that the function $\mathscr{F}$ in eq. (2.5) depends explicitly on the particular choice of $\mathbf{q}, \mathbf{p}$, and so, restrictions are imposed on the transformations in order to preserve

the form of the canonical equations, eq. (2.6). The allowed transformations are called *canonical*.

A canonical transformation can be generated by one or more, as they are not unique, functions of time and of $2f$ variables chosen among the $4f$ variables $\mathbf{q}$, $\mathbf{p}$, $\mathbf{Q}$, $\mathbf{P}$, regarded as independent. For example, let G be any function of $(\mathbf{q}, \mathbf{P}, t)$ with the proviso that $\left| \dfrac{\partial^2 G}{\partial q_i \, \partial P_j} \right| \neq 0$. If we choose

$$p_i = \frac{\partial G}{\partial q_i}, \qquad Q_i = \frac{\partial G}{\partial P_i},$$

and invert them, we get a canonical transformation and a new Hamiltonian,

$$\widetilde{\mathcal{H}}(Q_i, P_i, t) = \mathcal{H} + \frac{\partial G}{\partial t},$$

on which we can apply eq. (2.6). It can be shown [18] that *any two points on a given solution of the equations of motion are connected by a canonical transformation*. We will use this theorem below.

Any temporal dependence in a Hamiltonian function can be waived, without any loss of generality, by introducing an artificial degree of freedom, i.e.

$$\begin{aligned} \mathcal{H}(q_1, q_2, \ldots, q_n, p_1, p_2, \ldots, p_n, t) \quad &\rightarrow \quad \widetilde{\mathcal{H}}(q_1, q_2, \ldots, q_n, q_{n+1}, p_1, p_2, \ldots, p_n, p_{n+1}) \\ &= \quad \mathcal{H}(q_1, q_2, \ldots, q_n, p_1, p_2, \ldots, p_n, q_{n+1}) + p_{n+1}. \end{aligned}$$

This transformation from a *non-conservative* ($\dfrac{\partial \mathcal{H}}{\partial t} \neq 0$) system to a *conservative* one ($\dfrac{\partial \widetilde{\mathcal{H}}}{\partial t} = 0$), enables us to treat only *autonomous* systems with time–independent Hamiltonians on an extended phase space.

A much more compact notation for the canonical equations, eq. (2.6), can be achieved by denoting the $\{q_1, q_2, \ldots, q_f, p_1, p_2, \ldots, p_f\}$ phase space vector with $\mathbf{x}$, and with $\nabla\mathcal{H}$ the vector $\left\{ \dfrac{\partial \mathcal{H}}{\partial x_\alpha} \right\}, \alpha = 1, \ldots, 2f$. Then:

$$\dot{\mathbf{x}} = J \nabla \mathcal{H}, \tag{2.7}$$

where

$$J = \begin{bmatrix} O & I \\ -I & O \end{bmatrix}, \tag{2.8}$$

I the $f \times f$ unit matrix, and O the $f \times f$ zero matrix. In this notation, a transformation from $\mathbf{x} = \{q_1, q_2, \ldots, q_f, p_1, p_2, \ldots, p_f\}$ to $\mathbf{X} = \{Q_1, Q_2, \ldots, Q_f, P_1, P_2, \ldots, P_f\}$ is canonical when

$$M^T J M = J \tag{2.9}$$

holds, where

$$M_{\alpha\beta} = \frac{\partial x_\alpha}{\partial X_\beta}, \qquad \alpha, \beta = 1, \ldots, 2f.$$

As matrix J is orthogonal, $J^T = J^{-1}$, eq. (2.9) can be transformed into:

$$J^{-1} M^T J = M^{-1}.$$

This equation implies that M^{-1}, M^T, and M have the same eigenvalues; on the other hand, M and M^{-1} have inverse eigenvalues. Therefore, any symplectic matrix M has eigenvalues in pairs: $\{\lambda, 1/\lambda\}$.

We can easily prove a very important property of autonomous Hamiltonian systems: the volume in phase space of a domain U, $\int_U \prod_i^f \mathrm{d}q_i \mathrm{d}p_i$, is conserved during the evolution of a Hamiltonian system (*Liouville's theorem*); the Jacobian of the coordinate transformation between different times, being symplectic, has determinant equal to unity. If the system is not autonomous, the theorem holds for the volume in the extended phase space with dimension $2f + 2$.

2.3 Analysis of Dynamical Systems

The dynamics of a very great variety of systems can be cast into the form

$$\dot{\mathbf{x}}(t) = \mathbf{F}(\mu, \mathbf{x}(t), t), \qquad \mathbf{x}(t_0) = \mathbf{x}_0, \tag{2.10}$$

a system of n first order differential equations with a specific initial condition. t is the time variable, $\mathbf{x}(t)$ is a point in the configuration space of the system—a manifold $M \subseteq \mathscr{R}^n$—and $\mathbf{F}$ a *vector field* that may contain one or more parameters (collectively denoted by μ) such as the coupling to or the characteristics of external fields. The values of these parameters may play an decisive role on the structure of the solutions of the equations above.

An important theorem (see [19]) of ordinary differential equations gives precise information on the *local in space and time* existence and uniqueness of solutions for eq. (2.10), provided the function $\mathbf{F}(\mu, \mathbf{x}, t)$ fulfills certain broad conditions.

In what follows, we focus on the *critical elements* (stationary points, periodic orbits) of a dynamical system and their stability characterization. We will also mention briefly integral manifolds and define the attractor, a phase space structure which plays an important role in a non-conservative dynamical system. We conclude this section by studying the effect on the critical elements of the variation of the extra parameter(s) μ in eq. (2.10); we formulate the notion of *bifurcation*.

2.3.1 Equilibrium Points

Suppose, at first, that $\mathbf{F}$ has no explicit temporal dependence; it is autonomous.

The point $\mathbf{x} = \mathbf{x}_e$ is a *critical* or *equilibrium* point of eq. (2.10) for $\mu = \mu_0$ if $\mathbf{F}(\mu_0, \mathbf{x}_e) = 0$. Consequently, $\mathbf{x}(t) = \mathbf{x}_e$ is a solution for all times.

A fundamental property of an equilibrium point is its stability. The following definitions hold:

> The critical point $\mathbf{x} = \mathbf{x}_e$ for eq. (2.10) is said to be (*Liapunov*) *stable* if, for every neighborhood U of $\mathbf{x}_e$, there is another neighborhood V such that a solution passing through an arbitrary point of it never leaves U;

and

> The critical point $\mathbf{x} = \mathbf{x}_e$ for eq. (2.10) is said to be *asymptotically stable* if there is a neighborhood U of $\mathbf{x}_e$, such that a solution passing through an arbitrary point of it exists in the limit $t \to +\infty$ and tends to $\mathbf{x}_e$.

It follows that an asymptotically stable point is also Liapunov stable. Any point not stable or asymptotically stable is *unstable*.

In order to derive information on the stability of a critical point, *linearization* of the vector function $\mathbf{F}(\mu, \mathbf{x})$, that is, a Taylor expansion in $\mathbf{x}$ around this point up to the first derivative, is performed. The following remarks hold:

- It can be proven (see [20]) that, if an equilibrium point is asymptotically stable for the linear system, so is for the original non-linear.

- Hartman–Grobman theorem [21] and its generalization by Shoshitaishvili (see [22]), define a local topological conjugacy between a non-linear and the respective linear systems; the dynamics are qualitatively the same in an area around the critical point. The first theorem refers to unstable critical points with the center subspace $E^c = \emptyset$ (defined below), while the second deals with the case where E^c is not empty. They prove that an unstable point of a linear system is also unstable for the original non-linear.

- In the case where a critical point of a linear system is stable, there is a subtle difference: it is not guaranteed to retain the stability when non-linear terms appear. Its linear stability is necessary but not sufficient condition for its stability in the non-linear system. In this case, we employ the *direct method of Liapunov*: we try to find a scalar function $V(t, \mathbf{x})$ which vanishes at the critical point and is positive everywhere else in a neighborhood U of it. If the total time derivative of V along the orbits of the system is non-positive everywhere in U, the point is Liapunov stable;[1] if it is strictly negative, the point is asymptotically stable.

Let us elaborate on the linearization method. Without any loss of generality, we can translate the origin of the coordinate system to the critical point and set $\mu = \mu - \mu_0$; this way the critical point is at $\mu = 0$, $\mathbf{x} = 0$. Eq. (2.10) is then linearized into

$$\dot{\mathbf{x}} = \mathbf{F}(0,0) + \mathbf{x} \cdot \left(\nabla \mathbf{F}\right)\big|_{\mu=0,\mathbf{x}=0} \quad \Rightarrow \qquad \dot{\mathbf{x}} = A\,\mathbf{x}, \tag{2.11}$$

where A a real constant matrix with elements $A_{ij} = \left.\dfrac{\partial F_i}{\partial x_j}\right|_{\mu=0,\mathbf{x}=0}$, $i, j = 1, \ldots, n$. The general solution of eq. (2.11) depends on the eigenvalues λ_i and eigenvectors of A (see [19, 20, 23]). In brief, when all eigenvectors are linearly independent the solution assumes the form

$$\mathbf{x}(t) = U \ \mathrm{diag}[e^{\lambda_i t}]\ U^{-1}\ \mathbf{x}(0),$$

[1] A function V with these properties is called a *Liapunov function*.

where the $n \times n$ matrix U is constructed using the eigenvectors of A as columns. If there are no n independent eigenvectors, something that may occur when an eigenvalue is degenerate, the columns of U are the non-trivial solutions of

$$(A - \lambda_i I)^k u_i = 0, \qquad k = 1, \ldots, m_i,$$

where m_i is the multiplicity of λ_i. Then

$$\mathbf{x}(t) = U \ \mathrm{diag}[e^{\lambda_i t}] \ U^{-1} \sum_{k=0}^{n-1} \frac{N^k \, t^k}{k!} \ \mathbf{x}(0),$$

where $N = A - U \ \mathrm{diag}[\lambda_i] \ U^{-1}$.

The matrix A is real and therefore, if λ is one of its eigenvalues, so is the conjugate, λ^*. If $\Re(\lambda_k) < 0$, the corresponding component of the vector $U^{-1} \cdot x$ decays to zero; $\Re(\lambda_k) > 0$ implies exponential growth of this component. We can define a subspace E_λ of the configuration space M for each λ; it is spanned by the corresponding eigenvectors if λ is real,

$$E_\lambda \equiv \{u \in M \mid (A - \lambda I)u = 0\},$$

or the real, u_R, and imaginary, u_I, parts of the complex eigenvector(s) if λ is complex. As both parts satisfy $(A - \lambda I)(A - \lambda^* I)u_{\{R,I\}} = 0$ then

$$E_\lambda \equiv \{u \in M \mid (A - \lambda I)(A - \lambda^* I)u = 0\}.$$

The union of all spaces E_λ with $\Re(\lambda) > 0$ is the *unstable subspace* E^u, the union of all spaces E_λ with $\Re(\lambda) < 0$ is the *stable subspace* E^s, and the union of all E_λ with $\Re(\lambda) = 0$ is the *center subspace* E^c. These spaces are invariant; if a solution of eq. (2.11) belongs to one of them, it lies for all times in it. If it starts in E^s it converges to the critical point as $t \to +\infty$; if it lies on E^u it diverges away exponentially, and if it is on E^c it remains at a fixed distance away from it.

We can classify a fixed point of a linear system in one of the following categories:

- If all eigenvalues of A have negative real parts, the critical point is asymptotically stable.
- If all eigenvalues have non-positive real parts and the imaginary ones are distinct, the equilibrium point is Liapunov stable.
- If at least one eigenvalue has positive real part, it is unstable.

There is a number of criteria to determine, avoiding the explicit computation, whether the eigenvalues of A have negative real parts or not; for details see [24].

An asymptotically stable critical point of a non-linear system is called a *sink*. If all eigenvalues of matrix A for the corresponding linear system have positive real parts, the fixed point is called a *source*. If no eigenvalues of A are imaginary, the fixed point is *hyperbolic*.

A further classification, valid for both linear and non-linear systems, is the following:

- If all eigenvalues of A are real and, either, all positive or all negative, the critical point is called a *node*.
- If the eigenvalues are real and mixed (positive and negative) the critical point is a *saddle*.
- If all eigenvalues are imaginary, the critical point is a *center*.
- If all eigenvalues of A are complex with non-zero real part, the critical point is a *focus*.

For a non-linear system, we can define (local) stable S and unstable U manifolds, which are unique and tangent to E^s, E^u of the corresponding linear system at the critical point; this is a result of the *stable manifold theorem* [25]:

> All initial conditions in a neighborhood D of the equilibrium point for which the solutions for $t \geq 0$ of eq. (2.10) lie in D and tend to the critical point as $t \to +\infty$ comprise the stable manifold S.
>
> All initial conditions in a neighborhood D of the equilibrium point for which the solutions for $t \leq 0$ of eq. (2.10) lie in D and tend to the critical point as $t \to -\infty$ comprise the unstable manifold U.

The evolution of S for $t \leq 0$ produces the *global stable manifold*, W^s, while the evolution of U for $t \geq 0$ yields the *global unstable manifold*, W^u.

We can also define (but not uniquely) a *center manifold*, W^c, tangent to E^c.

Let us briefly mention what happens when eq. (2.10) is not autonomous (see [26] for details):

Linear terms of the form $A + B(t)$

Assume the matrix $\left.\dfrac{\partial F_i}{\partial x_j}\right|_{\{\mu=0,\mathbf{x}=0\}}$ is of the form $A+B(t)$, where A is constant. The eigenvalues of A control and reveal the stability of the critical point of the original non-linear system, in the same manner as in the autonomous, if $\sum_{i,j} B_{ij}(t)$ tends to 0 when $t \to +\infty$ and, additionally for Liapunov stability, if $\int_0^\infty \sum_{i,j} B_{ij}(t)\,\mathrm{d}t$ is bounded.

Linear terms with periodic coefficients

If the matrix $\left.\dfrac{\partial F_i}{\partial x_j}\right|_{\{\mu=0,\mathbf{x}=0\}}$ is periodic in t with period T, a theorem by Floquet ensures that the solution $\mathbf{x}(t)$ of the linear system with initial displacement $\mathbf{x}(t_0) = \mathbf{x}_0$, can be written as

$$\mathbf{x}(t) = P(t)e^{B(t-t_0)}P^{-1}(t_0)\,\mathbf{x}_0, \tag{2.12}$$

where $P(t)$ a matrix with period T and B a constant matrix. According to the theorem, the kind of stability of the critical point for eq. (2.10) is determined by

the eigenvalues of B in a similar way as in the autonomous system. Indeed, if we introduce the transformation

$$\mathbf{x} = P(t)\mathbf{z},$$

the linear equation eq. (2.11) becomes

$$\dot{\mathbf{z}} = B\mathbf{z}.$$

Therefore, we can apply the theory for a linear system with constant coefficients; the solutions in $\mathbf{z}$ contain terms of the form $e^{\lambda t}$ which are retained in the solution in $\mathbf{x}$, ultimately controlling the stability.

Application on Hamiltonian systems

A particular restriction arises on Hamiltonian systems, described by eq. (2.7), a special case of eq. (2.10). In this kind of systems, the matrix A is JB where B is a real symmetric matrix with elements $B_{ij} = \dfrac{\partial^2 \mathcal{H}}{\partial x_i \, \partial x_j}$, the Hessian of $\mathcal{H}$ evaluated at the equilibrium point. We can show that for each positive eigenvalue $+\lambda$ of A, the negative $-\lambda$ is also an eigenvalue. Matrices A, A^T, JA^TJ^{-1} have the same eigenvalues; but as $J^T = -J$:

$$A^T = (JB)^T = B^T J^T = -BJ, \qquad JA^T J^{-1} = J(-BJ)J^{-1} = -JB = -A.$$

Therefore, A and $-A$ have the same eigenvalues. This also holds for A and A^*.

We conclude that in a Hamiltonian system, eigenvalues of the linearized equations come in quartets: $\{\lambda, \lambda^*, -\lambda, -\lambda^*\}$. Some of them may coincide. As a consequence, no asymptotically stable points can exist for such systems. A stable point exists only if all eigenvalues are imaginary.

2.3.2 Periodic Solutions

Any solution $\mathbf{x}(t)$ of eq. (2.10) which satisfies

$$\mathbf{x}(t+T) = \mathbf{x}(t) \qquad T > 0, \quad \forall t,$$

is called *periodic with period* T or T*–periodic*. For such a solution, naturally, kT ($k \in \mathscr{Z}^*$) is also a period; conventionally, the minimum $T > 0$ satisfying the equation above is regarded as the period. An equilibrium point is a trivial periodic orbit.

Brouwer's fixed point theorem and its extensions (see [27]) prove that there exists at least one periodic solution of eq. (2.10), under various broad conditions.

An important theorem by Weinstein [28], based on earlier work by Liapunov, and generalized by Moser [29], predicts that at least f families, where f is the number of degrees of freedom, of periodic solutions of a Hamiltonian system exist at the vicinity of a stable equilibrium point. Their periods are close to those of the periodic solutions for the corresponding linear system. Montaldi *et al.* [30] extended the theorem to utilize the symmetries possessed by the system; in such a case it provides a higher estimate for the number of principal families. Further generalizations were made by Bartsch [31]. Liapunov demonstrated that the periodic solutions

corresponding to the normal modes of the linearized problem can be continued to periodic solutions of the non-linear system provided the frequencies of the normal modes are incommensurate or some of them are negative.

We can define stability for a periodic orbit, and, in general, any orbit, any solution of eq. (2.10). In the following definitions, A is the orbit in question, starting at $\mathbf{a}$ on $t = t_0$, and B a neighboring orbit starting at an arbitrary $\mathbf{b}$ with their initial distance smaller than a given $\delta > 0$, i.e. $|\mathbf{b} - \mathbf{a}| < \delta$. Orbit A is:

***(Orbitally or Poincaré) stable*,** if, for every orbit B there is an $\epsilon > 0$ such that, for $t \geq 0$, orbit B never leaves, as a whole, a tube with radius ϵ around A.

***Asymptotically stable*,** if, for every orbit B, the distance of $\mathbf{x}_B(t)$ from orbit A tends to zero in the limit $t \to +\infty$.

***Liapunov stable*,** if, for every orbit B, the distance of $\mathbf{x}_B(t)$ from $\mathbf{x}_A(t)$ tends to zero in the limit $t \to +\infty$.

Analogous criteria can be applied to the past, in the limit $t \to -\infty$.

Information on the stability of an orbit $\mathbf{X}(t)$ can be derived by the linearization of eq. (2.10) in the neighborhood of this orbit. If we keep terms linear in $\mathbf{x}$ in the Taylor expansion of $\mathbf{F}$ around $\mathbf{X}$ and set $\mathbf{y}(t) = \mathbf{x}(t) - \mathbf{X}(t)$, the equation is modified into

$$\dot{\mathbf{x}} = \mathbf{F}(\mu, \mathbf{X}(t), t) + (\mathbf{x} - \mathbf{X}) \cdot \nabla \mathbf{F}|_{\mathbf{x}=\mathbf{X}} \quad \Rightarrow \qquad \dot{\mathbf{y}} = A\mathbf{y}, \tag{2.13}$$

where A a matrix with elements $A_{ij} = \left.\dfrac{\partial F_i}{\partial x_j}\right|_{\mathbf{x}=\mathbf{X}}$. Note that the partial derivatives must be taken along the orbit $\mathbf{X}$. Matrix A is not time–independent, even if $\mathbf{F}$ has no explicit dependence on t.

Let us study a particular, important case for matrix A, the one where A has periodic elements; there are no systematic results for a general matrix A. If we linearize a system around a T–periodic orbit $\mathbf{X}(t)$ and the elements of $A(t)$ turn out to be periodic in t with the same period T, then the Floquet theorem we referenced in §2.3.1 applies. According to it, the general solution $\mathbf{y}(t) = \mathbf{x}(t) - \mathbf{X}(t)$ of the linear system in eq. (2.13) at $t = t_0 + T$ reads:

$$\mathbf{y}(t_0 + T) = P(t_0 + T)\, e^{BT} P^{-1}(t_0)\, \mathbf{y}_0 = Z(t_0, t_0 + T)\, \mathbf{y}_0. \tag{2.14}$$

As P is periodic with period T, the matrix $Z(t_0, t_0 + T) = P(t_0 + T)\ e^{BT} P^{-1}(t_0)$ and the matrix $C = e^{BT}$ have the same eigenvalues; therefore, the eigenvalues of $Z(t_0, t_0 + T)$ reveal the stability of the orbit $\mathbf{X}(t)$. Note that, as $\mathbf{y}(t) = Z(t_0, t)\mathbf{y}(t_0)$, the matrix Z satisfies the *variational equation*:

$$\frac{\mathrm{d}Z(t_0, t)}{\mathrm{d}t} = A(t_0, t) Z(t_0, t). \tag{2.15}$$

Matrix C introduced above is called the *monodromy* matrix of eq. (2.13). Its eigenvalues, ρ, are called the *characteristic* or *Floquet multipliers*. They (and the eigenvalues of $Z(t_0, t_0 + T)$) are related to the eigenvalues λ of B, the *characteristic exponents*, via

$$\rho = e^{\lambda T}.$$

The stability criteria for an orbit $\mathbf{X}(t)$ apply on the characteristic exponents in the same manner as in the previous section. Assuming that the monodromy matrix can be diagonalized, the criteria formulated in terms of the Floquet multipliers read:

- if all characteristic exponents have modulus less than unity, the orbit is asymptotically stable;
- if all characteristic exponents have modulus less or equal to unity, and those on the unit circle are distinct, the orbit is (orbitally) stable;
- if there exits at least one characteristic exponent with positive real part then the orbit is unstable.

Application on autonomous systems

Autonomous systems linearized around a periodic orbit, yield equations with periodic coefficients; it can be proven that

- Liapunov stable periodic orbits cannot exist (see [26] §5.3). By heuristic arguments, stability in the sense of Liapunov assumes that at $t \to +\infty$ all neighboring orbits intersect the "central" one. This, by the existence and uniqueness theorem mentioned in the introduction of this section, can occur only at a stationary point; such a point, cannot be part of a periodic orbit.
- there are no asymptotically stable periodic orbits. An outline of the proof is the following:

  If $\mathbf{X}(t)$ is a T–periodic solution of eq. (2.10), for autonomous $\mathbf{F}$, then

  $$\dot{\mathbf{X}} = \mathbf{F}(\mu, \mathbf{X}) \quad \Rightarrow \quad \ddot{\mathbf{X}} = \nabla \mathbf{F}(\mu, \mathbf{X}) \cdot \dot{\mathbf{X}}.$$

  Therefore, $\dot{\mathbf{X}}$, which is also T–periodic, satisfies eq. (2.13). Consequently, eq. (2.14) yields

  $$\dot{\mathbf{X}}(t_0 + T) = Z(t_0, t_0 + T)\dot{\mathbf{X}}(t_0).$$

  We conclude that $\dot{\mathbf{X}}$ is an eigenvector of $Z(t_0, t_0 + T)$ with eigenvalue equal to unity;[2] the criteria for asymptotic stability cannot be met.

Application on Hamiltonian systems

In T–periodic Hamiltonian systems, the transformation $\mathbf{y}(t_0) \to \mathbf{y}(t_0 + T)$ is canonical (cf. §2.2). Consequently, the Jacobian—the real matrix Z introduced above—has determinant equal to unity, and its eigenvalues come in quartets: $\{\rho, 1/\rho, \rho^*, 1/\rho^*\}$. Some or all of them may coincide. Therefore, in Hamiltonian systems we cannot have asymptotically stable orbits; orbitally stable exist only if all characteristic exponents are imaginary.

[2] The time reversal symmetry, $t_0 + t \to t_0 - t$, of the autonomous system, require Z and Z^{-1} to have the same eigenvalues; therefore, there is another eigenvalue equal to unity.

2.3.3 Integral Manifolds

Any differentiable function $C(\mathbf{q}, \mathbf{p}, t)$ which remains constant during the evolution of a Hamiltonian system, is an *integral of motion*. It obeys the following relations:

$$\begin{aligned} 0 = \frac{\mathrm{d}C}{\mathrm{d}t} &= \frac{\partial C}{\partial t} + \sum_{i=1}^{f} \frac{\partial C}{\partial q_i}\dot{q}_i + \frac{\partial C}{\partial p_i}\dot{p}_i \\ &= \frac{\partial C}{\partial t} + \sum_{i=1}^{f} \frac{\partial C}{\partial q_i}\frac{\partial \mathcal{H}}{\partial p_i} - \frac{\partial C}{\partial p_i}\frac{\partial \mathcal{H}}{\partial q_i} \\ &= \frac{\partial C}{\partial t} + \{C, \mathcal{H}\} \\ &= \frac{\partial C}{\partial t} + [\nabla_{\mathbf{x}} C]^T J\, [\nabla_{\mathbf{x}} \mathcal{H}]. \end{aligned}$$

The notation {A, B} introduced above is the *Poisson bracket* of two dynamic variables $A(\mathbf{q}, \mathbf{p}, t)$, $B(\mathbf{q}, \mathbf{p}, t)$:

$$\{A, B\} \equiv \sum_{i=1}^{f} \frac{\partial A}{\partial q_i}\frac{\partial B}{\partial p_i} - \frac{\partial A}{\partial p_i}\frac{\partial B}{\partial q_i}. \tag{2.16}$$

The surface $C(\mathbf{q}, \mathbf{p}, t) =$ const. consists of a family of orbits as we will see in §2.4.1, and is called an *integral manifold*.

2.3.4 Attractors

A subset A of the manifold M on which the dynamical system in eq. (2.10) is defined, is said to be an *attractor* if it is closed and invariant (all orbits starting from A remain in it for all times) and

- there is an open domain U in M, that contains A and does not disperse under the evolution of the system, and
- every orbit in a neighborhood $V \subseteq U$, asymptotically converges to the attractor.

The union of all neighborhoods of A that fulfill the above conditions is the *basin* of the attractor A. In a weaker condition, an attractor is stable if every orbit starting from V remains in U for all positive times.

An attractor can be a point, an orbit or any other hypersurface.

2.3.5 Bifurcations

Let us examine what happens to the equilibrium points and the periodic orbits of a dynamical system, regarding their existence and stability, when an external parameter μ is varied. Recall that a stationary point $\mathbf{x}_0$ satisfies $\mathbf{F}(\mu_0, \mathbf{x}_0) = 0$ for a certain value μ_0 of μ. With no loss of generality we can assume $\mu_0 = 0$, $\mathbf{x}_0 = 0$.

We mentioned that in the case of a hyperbolic point (either asymptotically stable or unstable), theorems predict the direct correspondence between the non-linear and

the linear system. The *implicit function theorem* states that if the matrix A with elements

$$A_{ij} = \left.\frac{\partial F_i}{\partial x_j}\right|_{\mu=0,\mathbf{x}=0}, \qquad i,j = 1,\ldots,n$$

is non-singular, then the equation $\mathbf{F}(\mu,\mathbf{x}) = 0$ can be solved uniquely for $\mathbf{x}$ as a function of μ, at least in a neighborhood of $(0,0)$. This means that if no eigenvalue of the linear stability matrix is zero, there exists locally a unique curve of equilibrium points in the $\{\mu,\mathbf{x}\}$ space passing through the origin. In other words, the equilibrium $(0,0)$ is unique and survives small variations of μ, though, in general, shifts its location.

The eigenvalues of A are functions of μ; therefore, they move on the complex plane when μ varies. They may cross the imaginary axis, leading to loss of hyperbolicity. This qualitative change has implications on the local structure of phase space, as we will see below, and is an example of *bifurcation*. The kinds of bifurcations presented here are referred to as *codimension-one* bifurcations; they appear in systems depending on one parameter and survive small perturbations.

In order to study the behavior of the non-linear system when hyperbolicity is lost, we can use the techniques of *center-manifold reduction* and *normal-form theory*. This approach is outlined in the following:

1. Identify the center manifold and restrict the dynamical system to it;
2. perform coordinate changes on the reduced system in order to simplify it; this yields the *normal form* of the bifurcation;
3. study the resulting equations, expanding them around the stationary point, keeping linear and, possibly, small non-linear terms of the parameter and coordinates.

One of two cases may occur when hyperbolicity is lost:

- If a simple eigenvalue becomes zero, the case is referred to as *steady-state bifurcation* and the non-linear behavior may take several forms. Most typical is a *saddle–node* bifurcation but we can also encounter *transcritical* and *pitchfork* bifurcations.
- If a pair of distinct conjugate eigenvalues becomes imaginary, we have a *Hopf* bifurcation.

Below, the normal forms and the corresponding diagrams in the reduced parameter–coordinate space are presented (their derivation can be found, for example, in [32]), for each kind of bifurcation. The "reverse," in a sense, conclusions apply when hyperbolicity is gained, that is, when eigenvalues leave the imaginary axis. It is important to realize that the stability of the branches presented here refer to the reduced space; the actual stability depends on all eigenvalues of the full system.

Saddle–node: The non-linear system reduces to the one-dimensional equation

$$\dot{x} = \epsilon_1\mu + \epsilon_2 x^2$$

where $\epsilon_{1,2} = \pm 1$.

The point $(\mu = 0, x = 0)$ is an equilibrium with zero eigenvalue. The exact behavior depends on the values of $\epsilon_{1,2}$. If they are both equal to unity, the equilibria of the reduced system are the points $(\mu, \pm\sqrt{-\mu})$. We note that they exist for $\mu < 0$, and as the stability matrix is $2x$, the upper branch (for positive x) is unstable while the lower (for negative x) is asymptotically stable. Similar is the analysis for the other values of $\epsilon_{1,2}$. Their diagrams are depicted in fig. (2.1)(I). As we can see, the (asymptotically) stable branch merges with the unstable one at the origin in a mutual annihilation or creation; recalling the definitions, stable *nodes* merge with *saddle* points, hence the name of the bifurcation. Notice that when the zero eigenvalue of the original linear system is degenerate, the normal form is not one-dimensional, and the branches might both consist of unstable points.

Transcritical: It may happen that an asymptotically stable equilibrium loses stability through a steady-state bifurcation, but persists for all $\mu \neq 0$. The normal form turns out to be:

$$\dot{x} = \epsilon_1 \mu x + \epsilon_2 x^2$$

where $\epsilon_{1,2} = \pm 1$.

The point $x = 0$ is an equilibrium for all μ; the eigenvalue, being equal to $\epsilon_1 \mu$, changes sign at $\mu = 0$, thus inverting the stability. A second branch of equilibria is the curve $x = -(\epsilon_1/\epsilon_2)\mu$. The eigenvalue for this branch is $-\epsilon_1 \mu$, opposite of the $x = 0$ equilibrium. At $\mu = 0$ the equilibria collide and "exchange" stabilities. The diagrams for the transcritical bifurcation are depicted in fig. (2.1)(II).

Pitchfork: This kind of steady-state bifurcation arises when the system, at least locally, has a reflection symmetry, i.e. $\mathbf{F}(\mu, \mathbf{x}) = -\mathbf{F}(\mu, -\mathbf{x})$. The normal form then is:

$$\dot{x} = \epsilon_1 \mu x + \epsilon_2 x^3$$

where $\epsilon_{1,2} = \pm 1$.

In this case too, $x = 0$ persists through $\mu = 0$ changing its stability. Another branch exists, $x = \pm\sqrt{-(\epsilon_1/\epsilon_2)\mu}$, only for $\mathrm{sgn}(\epsilon_1 \mu/\epsilon_2) = -1$. It is a parabola lying on one side of the x axis. The corresponding eigenvalue is $-2\epsilon_1 \mu$; it has opposite sign of the eigenvalue for $x = 0$. As we see in fig. (2.1)(III), the diagrams resemble pitchforks, hence the name.

Hopf: Assume that the distinct pair of eigenvalues crossing the imaginary axis is of the form $\gamma(\mu) \pm i\omega(\mu)$ with $\gamma(0) = 0, \omega(0) \neq 0$. The center manifold is two-dimensional and the normal form, written in polar coordinates, turns out to be:

$$\begin{aligned} \dot{r} &= \gamma(\mu) r + \alpha(\mu) r^3 + \mathscr{O}(r^5) \\ \dot{\theta} &= \omega(\mu) + \sum_{j=1}^{\infty} b_j(\mu) r^{2j}. \end{aligned}$$

These equations lead to

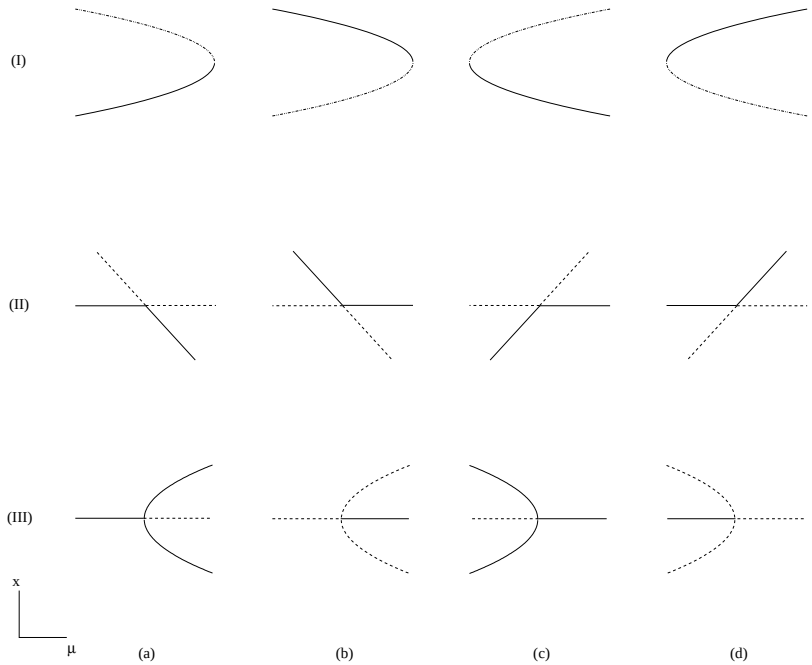

Figure 2.1: Diagrams for (I) saddle–node, (II) transcritical, (III) pitchfork bifurcations for (a) $\epsilon_1 = 1$, $\epsilon_2 = 1$, (b) $\epsilon_1 = -1$, $\epsilon_2 = -1$, (c) $\epsilon_1 = -1$, $\epsilon_2 = 1$, (d) $\epsilon_1 = 1$, $\epsilon_2 = -1$. The origin is at the point where stability changes. Solid lines represent asymptotically stable points. Dashed ones indicate instability.

- one branch of equilibria, at $r = 0$. Its stability is determined by the sign of $\gamma(\mu)$; it changes stability at $\mu = 0$.

- when $\dfrac{\gamma(\mu)}{\alpha(\mu)} < 0$, a periodic orbit with amplitude $r_H(\mu) \approx \sqrt{-\dfrac{\gamma(\mu)}{\alpha(\mu)}}$ and angular frequency $\omega_H(\mu) = \omega(\mu) + \displaystyle\sum_{j=1}^{\infty} b_j(\mu)\ {r_H}^{2j}$. Its stability is controlled by the sign of $-2\gamma(\mu)$, the eigenvalue: if $\gamma(\mu) > 0$ or, equivalently, $\mu > 0$, it is asymptotically stable; otherwise, it is unstable. Fig. (2.2) presents the diagrams for the Hopf bifurcation.

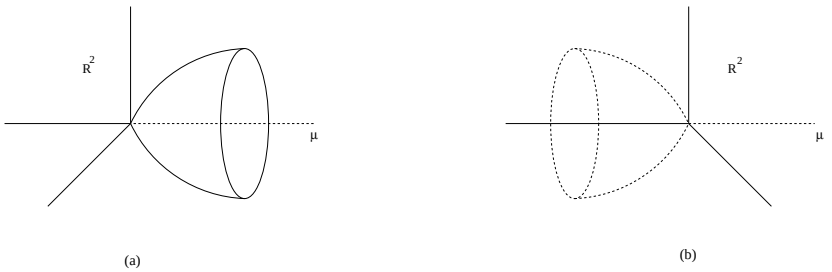

Figure 2.2: Diagrams for Hopf bifurcations: (a) $\alpha(\mu) < 0$, (b) $\alpha(\mu) > 0$. Solid lines represent asymptotically stable points or orbits. Dashed ones indicate instability.

The clear-cut figures for steady–state bifurcations are modified when we take into consideration higher order terms. The perturbation results in breaking certain assumptions and therefore, restoring the "generic" behavior, i.e. saddle node bifurcations. For example, in the transcritical bifurcation, the addition of a perturbation controlled by ε, leads one to expect the modifications in fig. (2.3)(I): the diagram contains either two saddle-node bifurcations or no bifurcation at all. For a pitchfork bifurcation the four modifications depicted in fig. (2.3)(II) are possible. The last two exhibit a hysteresis effect.

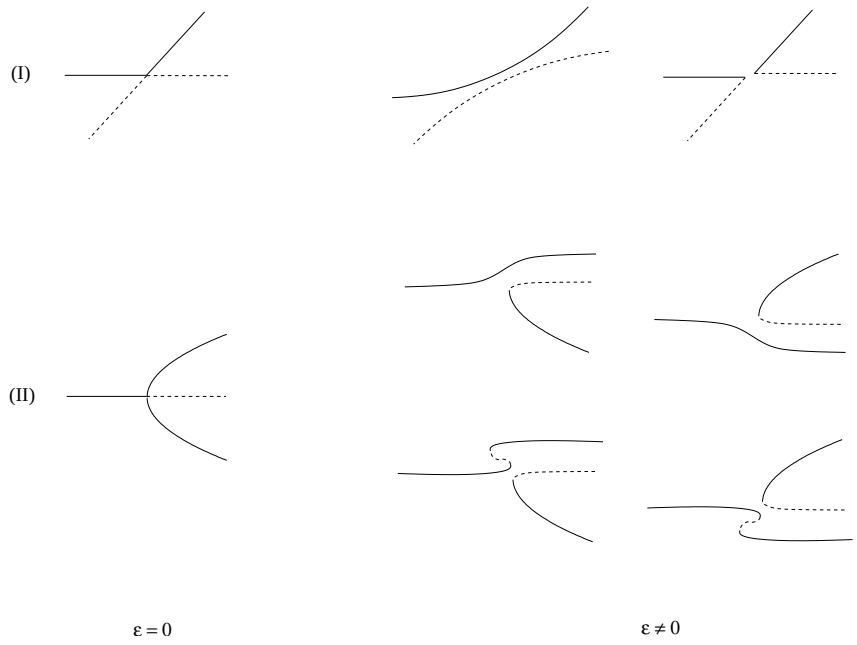

Figure 2.3: Perturbation of steady–state bifurcations: (I) transcritical (II) pitchfork.

As we saw earlier, the analysis of the stability of stationary points and periodic orbits can be very similar under certain conditions. All results presented above can also be extended to periodic orbits:

- a steady-state bifurcation occurs when a Floquet multiplier becomes equal to unity; then, two branches of periodic orbits with opposite stability are created or merge (saddle–node), collide and exchange stability (transcritical) or one branch changes stability, passing it over to other two branches which are created (pitchfork). In the pitchfork bifurcation, the two branches created give rise to the same family of periodic orbits.

- a Hopf bifurcation takes place when a pair of multipliers touch (or leave) the unit circle. In that case, the "central" periodic orbit persists and a two-dimensional invariant torus encapsulates it.

Let us examine another mechanism leading to a qualitative change in the local dynamics around a T–periodic orbit. Recall that if the linearization of the equations

in its neighborhood is periodic, Floquet theory enables us to cast the evolution into the form

$$\mathbf{x}(T) = Z(T)\mathbf{x}(0).$$

Eigenvalues of $Z(T)$ control the stability.

Let us assume that κ forward iterations of this mapping,

$$\mathbf{x}(\kappa T) = Z^{\kappa}(T)\mathbf{x}(0),$$

produce a monodromy matrix with an eigenvalue equal to unity. In terms of the eigenvalues of $Z(T)$ this happens when a Floquet multiplier equals

$$e^{2\pi i \frac{m}{\kappa}}, \qquad \kappa \in \mathscr{Z}^*, \quad m = 0, \ldots, \kappa - 1.$$

Its conjugate multiplier will also exist (as long as $m \neq 0, \kappa/2$). The system undergoes a steady-state bifurcation, which is a pitchfork because of the reflection symmetry of the mapping

$$Z^{\kappa}(T)\mathbf{x}(0) = -Z(T)^{\kappa}(-\mathbf{x}(0)).$$

Note that when two distinct multipliers exist, the reduced coordinate space is two-dimensional. It can be shown that a periodic orbit with period κT exists in the neighborhood of the original. For example, if -1 is an eigenvalue of $Z(T)$ then $\kappa = 2$, and the *period–doubling* bifurcation takes place.

We notice in fig. (2.1) and fig. (2.2) that stability is, in a sense, inherited during a bifurcation or, in general, conserved before and after the critical point $\mu = 0$. This can be formulated rigorously in terms of the *Poincaré index* and its conservation in autonomous systems [33]. This index is defined for a closed curve C that passes through no periodic orbits as the number of times the vector $\vec{x}(T) - \vec{x}(0)$ with $\vec{x}(0) \in C$ encircles 0 as $\vec{x}(0)$ traverses C. The index is a continuous function of C; as it is integer valued, it is constant. This quantity can also characterize a periodic orbit, referring to the index of a closed curve surrounding it and no other periodic orbits. The index is summable i.e. the index of a curve formed by traversing first one and then another curve is the sum of the separate indices. Thus, the index of any curve is the sum of the indices of the periodic orbits it encircles. It can be shown that the index of a center or a single hyperbolic orbit is $+1$ and -1 respectively. The index of a curve surrounding a periodic orbit is constant through a bifurcation; in plain terms, this means that the number of stable orbits minus the number of unstable ones is the same before and after the point of bifurcation.

Recall that when the monodromy matrix is symplectic, the multipliers come in quartets: $\{\rho, 1/\rho, \rho^*, 1/\rho^*\}$. Therefore, a simple multiplier cannot leave the unit circle unless it collides with its conjugate (at ± 1) or with another multiplier with modulus equal to unity. After this collision, the multipliers may continue on the unit circle or leave it, rendering the system complex unstable. Further results constitute the Krein theory and can be found in [34].

2.4 Classification of Dynamical Systems

A Hamiltonian of a system with f degrees of freedom is called *integrable* if there exist f single valued analytic functions $C_1, C_2, \ldots, C_f$ of $(\mathbf{x}, t)$, which are

- functionally independent, i.e. the vectors

$$\left\{ \frac{\partial C_i}{\partial t}, \frac{\partial C_i}{\partial x_1}, \frac{\partial C_i}{\partial x_2}, \ldots, \frac{\partial C_i}{\partial x_{2f}} \right\}, \qquad i = 1, \ldots, f,$$

  are linearly independent,

- integrals of motion, i.e. $\{C_i, \mathcal{H}\} + \dfrac{\partial C_i}{\partial t} = 0$,

- in *involution*, i.e. $\{C_i, C_j\} = 0, \qquad \forall\, i, j = 1, \ldots, f.$

As a remark without further comment, there exist systems which possess more than f independent integrals, though only f of them are in involution. There is no systematic method of finding the integrals in a given dynamical system; under certain conditions the existence or not of them can be predicted.

2.4.1 Integrable Systems

The following theorem by Liouville and Arnol'd, can be proven:

If a system is integrable, there exists a canonical transformation from $\{\mathbf{q}, \mathbf{p}\}$ to $\{\vec{\varphi}, \mathbf{I}\}$, yielding a function of only the generalized momenta $\mathbf{I}$ as the transformed Hamiltonian:

$$\mathcal{H} = \mathcal{H}(\mathbf{I}). \tag{2.17}$$

The canonical equations, eq. (2.6), for the transformed system then read:

$$\dot{I}_i = -\frac{\partial \mathcal{H}}{\partial \varphi_i} = \quad 0 \quad \Rightarrow I_i = c_i, \tag{2.18}$$

$$\dot{\varphi}_i = \quad \frac{\partial \mathcal{H}}{\partial I_i} = \quad \omega_i(I_i) \quad \Rightarrow \varphi_i = \varphi_i(0) + \omega_i t, \tag{2.19}$$

with $c_i, \varphi_i(0), \omega_i$ constants depending on the initial conditions. The $\{\varphi_i, I_i\}$ are the *angle–action* variables. As the transformation is canonical, it preserves the symplectic area for any closed loop in phase space:

$$\oint \mathbf{p}\, \mathrm{d}\mathbf{q} = \oint \mathbf{I}\, \mathrm{d}\vec{\varphi}.$$

In an integrable system of f degrees of freedom, no solution of its equations of motion can wander all over the $2f$-dimensional phase space, but, since the trajectory preserves the integrals of motion, it is restricted on a smooth $(2f - f)$-dimensional hypersurface, the *integral manifold*. If, in addition, this hypersurface is compact and connected, as it is in bounded motion, it can be shown to be diffeomorfic to a $T^f = S^1_{I_1} \times S^1_{I_2} \ldots \times S^1_{I_f}$ torus. This "invariant" torus is characterized by the actions eq. (2.18), which are the radii of the circles, and the angles eq. (2.19), which parameterize them. If the angular velocities $\omega_i(I_i)$ are commensurate, i.e. multiple of an angular velocity Ω, then any trajectory is closed and periodic with period $2\pi/\Omega$ and the torus is called *resonant*; otherwise, a trajectory fills densely the torus without crossing itself and is quasi-periodic. Notice that all trajectories on a torus are either periodic or quasi-periodic as ω_i characterize the torus via I_i. Each set of

values for the integrals of motion corresponds to a distinct torus; the tori cannot intersect each other. The phase space, therefore, is comprised of nested invariant tori; among them, densely interspersed, are the resonant tori.

All of the above can be extended on systems on which the motion is not bounded. In this case, the manifold on which motion takes place is diffeomorfic to $\mathscr{R}^k \times T^{f-k}$ $(k \leq f)$.

Poincaré in [35] states that if a Hamiltonian system possesses p integrals in involution with each other and their gradients are linearly independent on a periodic solution, then this orbit has $2p$ characteristic exponents equal to zero (or $2p$ Floquet multipliers equal to one). Therefore, an integrable Hamiltonian system has—in the linear approximation at least—only stable periodic orbits.

2.4.2 Non–Integrable Systems

Consider an integrable system with eq. (2.17) as its Hamiltonian. If it is perturbed, in general it will become non-integrable. There will be not enough integrals of motion to restrain the trajectories on tori; qualitative changes of the phase space structure will occur but, assuming $\mathcal{H}$ is non-degenerate, i.e. its Hessian has non-zero determinant, most of the invariant tori which exist for the unperturbed system, will continue to exist, albeit deformed. Moreover, the area of the chaotic region where tori were destroyed, diminishes to zero as the perturbation tends to zero. Whether a torus is destroyed or not depends on its characteristic frequencies: if they are sufficiently incommensurate, the torus survives a small perturbation. This is a result of the famous KAM theorem outlined by Kolmogorov [36] and subsequently proved by Moser [37] and Arnol'd [38].

One of the last theorems formulated by Poincaré [39] and proven by Birkhoff [40], provides information on the structure of the phase space areas previously occupied by the destroyed tori. Among those tori were the resonant ones; the theorem predicts that the periodic orbits on them are replaced by families of pairs of stable and unstable periodic orbits. These chains of successive stable and unstable orbits lie arbitrarily close to tori resistant to adequately small perturbations (*KAM tori*). The stability regions around the stable periodic orbits grow with the perturbation, eventually piercing and destroying the neighboring KAM torus. The torus transforms from a continuous barrier to a Cantor set of points; it is then called a *cantorus*.

The existence of tori in $2f$-dimensional non-integrable systems implies the existence of $2f$ integrals of motion on these tori; the integrals though are not Cauchy-analytic functions (the KAM tori are isolated), and therefore can not lead to integrability.

For a conservative non-integrable system with two degrees of freedom, the KAM tori enclose completely the chaotic regions; as these regions are not connected, a chaotic orbit in one of them cannot visit another. This is not the case for higher dimensions; there exist paths through which an orbit can "leak" from one region to another, albeit with very small probability. This is the *Arnol'd diffusion* (see [41]).

2.5 Integrability and Chaos

No procedure presently exists for predicting whether a generic system is integrable or not. There are several methods which enable us to characterize dynamical systems, at least locally in regions of phase space, as non-integrable or *chaotic*. There are also criteria—apart from separability—which, when satisfied, the system is integrable.

A very descriptive means of studying dynamical systems of two degrees of freedom is the Poincaré *surface of section* method: a three-dimensional hypersurface is embedded in the four-dimensional phase space, chosen in such a way that no orbits are tangent to it. The evolution of the points of this surface according to the dynamics of the system (i.e. the orbits with these points as initial conditions) may bring them back on it, generating a mapping (the Poincaré mapping) between points on the surface. In mechanical systems the momenta enter the Hamiltonian quadratically; when the system is also autonomous, the time reversal symmetry enables us to keep only the points on the surface where a momentum is positive.

When integrals of motion exist, the effective dimension of the phase space is reduced and so is the dimension of the surface of section. Thus, in a conservative system, each point on a surface $f(\mathbf{q}, \mathbf{p}) = 0$ defines completely the state of the system. Through Poincaré mapping, a periodic orbit in such a system appears as a finite number of points on the surface of section; the sequence of these points is repeated. Their number defines the *order* of the points: that many iterations of the Poincaré mapping generate the identity mapping. In this sense, these points are fixed. A quasi-periodic orbit fills densely the surface, subject to the integrals of motion that must remain constant. On an integrable system, the images of a quasi-periodic orbit lie on a closed curve surrounding a fixed point (the image of a periodic orbit).

Let us examine what happens in the neighborhood of a hyperbolic periodic orbit in a two degree-of-freedom system; similar but richer structure is observed in systems with higher dimensionality. Recall that on a surface of section, periodic orbits project as fixed points; each hyperbolic point is associated with a stable and an unstable manifold which correspond to curves on the surface. If the system is integrable, the unstable manifold of a hyperbolic fixed point joins smoothly the stable manifold of the same or other hyperbolic point, forming a *separatrix* curve, fig. (2.4). An orbit starting at $t = -\infty$ from the first hyperbolic point, projects on this curve and reaches at $t = +\infty$ the other point.

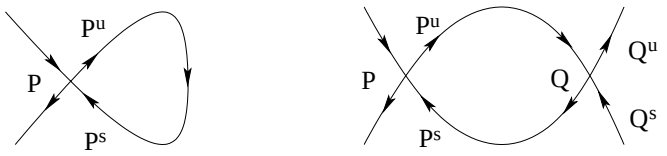

Figure 2.4: Neighborhood of hyperbolic points (P,Q) in an integrable system. The arrows indicate the stable and unstable manifolds.

When the system is perturbed and loses its integrability, the stable and unstable curves in general do not join smoothly but on a infinite set of discrete points; these are characterized as *homoclinic* or *heteroclinic* depending on whether the intersecting

manifolds emanate from fixed points of the same or different families (cf. Poincaré–Birkhoff theorem). According to a theorem established by Birkhoff, the presence of a homoclinic point associated with an unstable periodic orbit implies the existence of an uncountable set of non-periodic trajectories which contains a dense and countable set of periodic orbits of arbitrarily long periods. Without going into details, the curves are forced to approach the fixed point, looping through the intersection points, while avoiding both themselves and the fixed point: the intersection points form a kind of lattice with infinitely tight loops (*homoclinic tangle*), fig. (2.5). According to the Newhouse theorem [42], saddle-node bifurcations occur as a consequence of tangencies of the stable and unstable manifolds of unstable periodic orbits. In subsequent chapters we will encounter other mechanisms for their birth (systematic resonances of at least two coordinates).

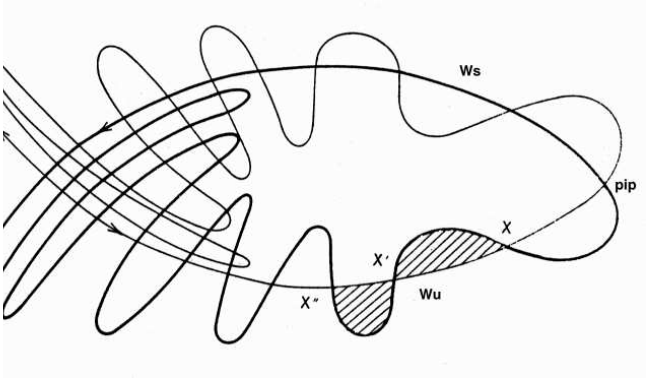

Figure 2.5: Schematic representation of the neighborhood of a hyperbolic point in a non-integrable system. W_s and W_u are the stable and unstable manifolds.

A surface of section for the $HeHD^+$ system we studied in [43] is depicted in fig. (2.6). We can distinguish in the center the islands of stability of *one* periodic orbit; between them an unstable orbit appears. Three islands at the edges surround an order-3 periodic orbit. A major portion of the surface is covered by chaotic orbits.

Another method to study the dynamics, applicable to systems of any dimensionality, involves the examination of the Fourier spectrum of individual trajectories:

$$I(\omega) = \frac{1}{2\pi} \lim_{\tau\to\infty} \frac{1}{\tau} \left| \int_{-\tau}^{\tau} f[\mathbf{q}(t)] e^{-i\omega t}\, \mathrm{d}t \right|^2 , \tag{2.20}$$

where $f[\mathbf{q}(t)]$ any function evaluated on a trajectory. In an integrable system, all orbits yield discrete and sharp (within computational limits) power spectra, consisting of the fundamental frequencies, their overtones and their combinations. A chaotic system has orbits with broad, banded spectra, possibly with a fractal dimension; the bands occur near the sharp lines of any neighboring quasi-periodic trajectory.

The comparison of the phase space and time averages of some function of the dynamical variables can also serve as an indication of chaos. In the quasi-periodic regime they will be substantially different; in the chaotic they are expected to be roughly the same (ergodicity in statistical mechanics).

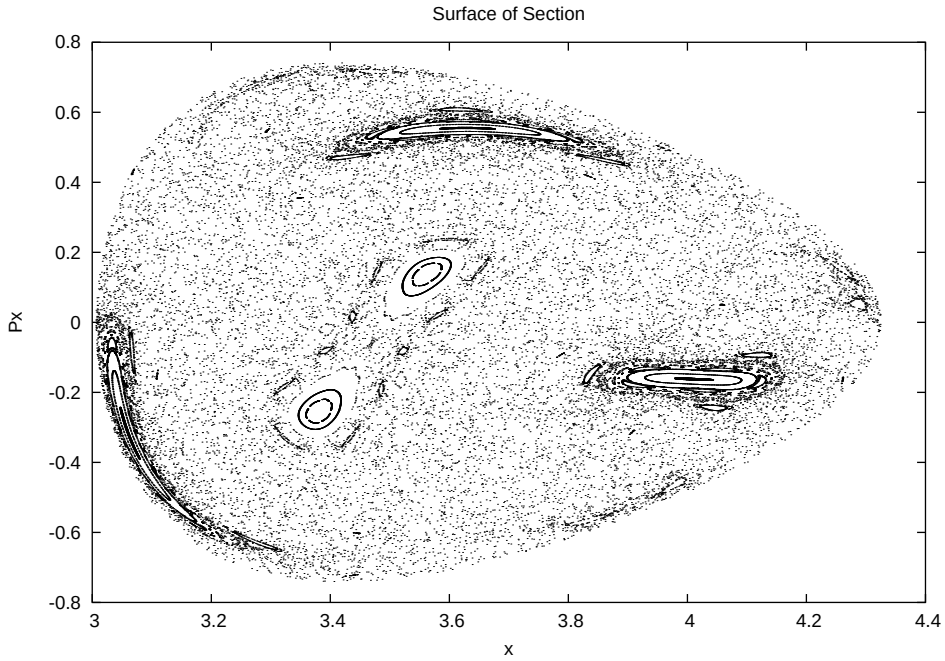

Figure 2.6: Poincaré surface of section for the $HeHD^+$ system, at y=1.3 α_0, E=−0.15 eV.

Liapunov exponents can also be used as a means to characterize a given region of phase space as regular or chaotic (see [44]). Consider two neighboring phase space points at an initial distance $d(0)$. At time t this distance is $d(t)$. The Liapunov characteristic exponent, λ, is defined as

$$\lambda = \lim_{t\to\infty} \ln \frac{d(t)}{d(0)}. \tag{2.21}$$

In a $2f$-dimensional system there are $2f$ directions, each characterized by a Liapunov exponent. It can be shown that in a volume-preserving dynamical system the exponents come in pairs, $\{\lambda, -\lambda\}$. For every integral of motion a pair is zero. In areas where the motion is regular, the exponents are zero; they are positive (and negative) in chaotic regions. Other quantities, such as the *Kolmogorov–Sinai (KS) metric entropy* [45], directly related to the sum of Liapunov exponents, can serve as a measure to the "irregularity" of a region. The local exponential divergence of trajectories of a bounded system implied by non-zero Liapunov exponents, or equivalently, the sensitive dependence on initial conditions, may serve as a definition of chaos. The divergence produces a local stretching in the phase space; due to confinement this stretching must fold. The continual stretching and folding produces the complicated behavior associated with chaos.

A dynamical system can be shown to be integrable if—according to the *Kovalevskaya–Painlevé* conjecture [46]—it satisfies the *Painlevé property*: all complex time singularities in the solutions of the differential equations depending only on the "external parameters" (i.e. initial conditions, coupling, etc.), the "movable" singularities, are poles. Integrability can also be expected if the system fulfills the

"extended" or "weak" Painlevé property which allows rational branch singularities in addition to poles.

Two other phenomena can indicate a chaotic region: the accumulation of period–doubling bifurcations of unstable periodic orbits and the scaling behavior associated with these bifurcations (see, for example, [47]). Also, there are a few techniques which, in certain cases, can give good qualitative, and even semi-quantitative, prediction of the minimum energy necessary to ensure "substantial" chaos. For a brief presentation see [48].

2.6 Classical–Quantum Correspondence

2.6.1 Semiclassical Quantization

Information on the classical behavior of a system can be used to compute quantum quantities. Semiclassical methods, being developed since the beginning of quantum mechanics, relate the quantum description of a highly excited system to the classical one: quantum mechanical eigenvalues and wave functions are determined from information on the classical orbits. Early methods assumed the separability of the system (Wentzel–Kramers–Brillouin) or the classical integrability (Born–Sommerfeld, Einstein–Brillouin–Keller [49]) or the adiabatic separation of degrees of freedom (Ehrenfest [50]).

An important quantization condition is the Einstein–Brillouin–Keller (EBK) rule. It provides an approximation to the energy spectrum by quantizing the actions:

$$I_i = \frac{1}{2\pi} \oint_{C_i} \mathbf{p}\, \mathrm{d}\mathbf{q} = \left(m_i + \frac{\alpha_i}{4} \right) \hbar, \tag{2.22}$$

where m_i are the (integer) quantum numbers and α_i the constant Keller–Maslov indices. These indices depend on the topology of the appropriate tori (those yielding integer quantum numbers) via the topologically independent paths C_i on which the integration takes place. Recall that in an integrable system, a transformation to action-angle variables is possible, yielding a Hamiltonian of the form of eq. (2.17). Substituting the quantized actions in it, the energy spectrum is derived, occasionally on excellent agreement with the quantum calculation. Classical frequencies of quantized tori are related to quantum energy differences via the correspondence principle. For systems with tori of mixed topologies, isolated by separatrices, this simple quantization rule has to be modified, because the Keller–Maslov indices change across a separatrix; moreover, one has to take into consideration the quantum mechanical tunneling between tori of different topology [51].

Common assumption of all techniques is the existence of tori or remnants of tori. Therefore, these methods for semiclassical quantization apply only on systems which are integrable or not far from integrability. In order to cover non-integrable systems, techniques that are not based on the existence of tori had to be developed. Approximate Hamiltonians or quantization schemes employing the individual orbits rather than the underlying phase space structure can be used. The uncertainty principle precludes the association of a single periodic orbit, with a precisely defined period, with a particular energy eigenvalue; a family, though, of energy levels relates to a

periodic orbit. The spectrum basically results from the interference between the semiclassical quantum amplitudes associated with the fundamental, low-period, orbits. This suggests that the spectrum may become irregular in classically chaotic systems; this irregularity can be regarded as a manifestation of quantum chaos and results from a dispersion in the periods of the periodic orbits and not their instability. Few methods are outlined below. Among the most notable are the trace formulas; they express a fundamental local–global duality: the spectrum of periodic orbits is dual to the spectrum of eigenvalues.

The Birkhoff–Gustavson technique [52] is applicable to chaotic systems. Basically, the method is a systematic procedure to canonically transform the Hamiltonian into a truncated power series in harmonic oscillator terms. The resulting Hamiltonian is a function of only the new generalized momenta. The EBK quantization on it, can yield a semiclassical spectrum with very good agreement, depending on the system, with the quantum one not only in regular regions of the phase space but also in the chaotic part. Another related method is the canonical Van Vleck perturbation theory [53]. This technique expands the Hamiltonian in a perturbative series and rewrites it employing the harmonic oscillator raising and lowering operators. Van Vleck unitary transformations are then applied in such a way that decoupling occurs and good quantum numbers emerge in the new coordinates. Both methods have been applied, with satisfactory results, to actual non-linear systems such as the molecules of phosphaethyne (HCP) [54] and hydrogen cyanide (HCN) [55].

Gutzwiller [13] using Feynman's path integral formulation [56], and Balian and Bloch [57], have derived a semiclassical expression for the trace of the resolvent (or Green operator) of the quantum Hamiltonian operator as a sum over all *isolated* periodic orbits, taking into account their linear stabilities. This formula can be used to obtain approximate values for the quantum energy eigenvalues of classically chaotic systems that are not separable. The trace formula has been augmented with terms in powers of the Planck constant by Alonso and Gaspard [58]. The terms in the $\hbar$-expansion depend on the nature and the non-linear stabilities of the periodic orbits. The Berry–Tabor trace formula [59], based on the EBK quantization rule, was derived in a different way than Gutzwiller's trace formula; it also provides the quantum density of states as a coherent summation over resonant tori and therefore is applicable only to integrable systems. A uniform result bridging the Berry–Tabor and Gutzwiller trace formulas for the case of a resonant island chain was derived by Ozorio de Almeida [60].

Other methods proposed on semiclassical quantization include a technique [61] which exploits generic classical trajectories; periodic orbits do not play any special role. This method, applicable to both integrable and non-integrable systems, is based on the semiclassical approximation of the equilibrium density matrix using trajectories on the upside down potential surface. It also offers a good approximation to the quantum wave functions, something that other semiclassical methods can not achieve. Another technique employed in the study of the intermediate regime between the quantum and classical ones, is the quasi-classical method. It is complementary to semiclassical methods. It uses the Wigner-Weyl representation [62] for the physical observables and expands it in a series of $\hbar$. It cannot reproduce quantization effects but it is very useful in the statistical description of a system.

It should be noted that semiclassical quantization often predicts a simpler, more degenerate energy spectrum than is computed quantum mechanically or observed experimentally. This estimate is attributed to coalescence of levels in the semiclassical limit ($\hbar \to 0$), coalescence which may manifest itself in real spectra as an excess of near-degeneracies. A more detailed treatment in the semiclassical framework can derive these "avoided crossings" (accidental Fermi resonant interactions).

Thorough reviews of semiclassical quantization can be found in [63, 64].

2.6.2 Quantum Chaos

It is well known that a correspondence of classical and quantum mechanics is obtained by promoting the dynamical variables (observables) to Hermitian operators and the classical Poisson brackets, eq. (2.16), to commutators. Therefore, a quantum system of f degrees of freedom is integrable if there exist f globally defined operators $\widehat{C}_i(\widehat{q}_j, \widehat{p}_j), \quad i, j = 1, \ldots, f$, whose mutual commutators vanish

$$[\widehat{C}_i, \widehat{C}_k] = \widehat{C}_i \widehat{C}_k - \widehat{C}_k \widehat{C}_i = 0, \qquad i, k = 1, \ldots, f.$$

When the above conditions hold, there exist common eigenstates of them characterized by f quantum numbers.

Many definitions were proposed to specify what *quantum chaos* is; what happens when the conditions above are not satisfied. Closely related is the question of the way and the circumstances under which a quantum system reflects the underlying classical dynamics. In order to study the classical–quantum correspondence, the form of wave functions and the distribution of energy levels were examined. The analysis which follows refers to bound systems; it can be extended to unbound ones as long as it is applied to orbits and wave functions which behave as confined for a considerable time. An important conclusion drawn from all of them is that classical chaos does not necessarily imply quantum chaos.

In order to formulate one definition of quantum chaos, let us briefly describe one way to solve the Schrödinger equation: the wave function is expanded in a (finite) set of basis functions and the resulting matrix is diagonalized to obtain (some) approximate eigenvalues and eigenvectors. It was proposed [65] that an eigenstate with contributions from a large number of basis functions is chaotic. Such a quantum state was termed "global;" those consisting of a few basis functions were named "local." Such a definition of quantum chaos was basis set dependent; it satisfied, though, the "expected" behavior for the systems on which it was applied: in low energies, where classical systems are regular, most wave functions were assigned as "local," while in higher energies more "global" wave functions were found. However, it was demonstrated in other systems that "global" wave functions may correspond semi-classically to quasi-periodic states, while "local" ones may map to classically chaotic regions.

It has been suggested [66] that "irregularity" of the energy spectrum and a large sensitivity of an energy level to a perturbation, reflected in the second derivative of the eigenvalue with respect to a perturbation parameter, can serve as criteria for the quantum analog of classical chaos. Again, these conditions were not necessarily met in classically chaotic regions.

Numerical experiments show that in a classically regular phase space, the probability amplitude of an eigenfunction of the corresponding quantum system may be localized on the coordinate space projection of an eigentorus (a torus satisfying eq. (2.22)). Such pattern of the wave function gave rise to the term *scars* [11, 67]. The nodal pattern permits a straight assignment of quantum numbers to the eigenfunction. On the other hand, in an classically chaotic region, a wave packet may interfere with random direction and phase with itself, resulting in a wave function spread more or less uniformly over the accessible configuration space with more or less random nodal pattern. This fundamental difference in the form of the wave functions could serve as a defining characteristic of quantum regular and chaotic regions. However, it was shown [68] that this difference may be attributed to an increase of the non-separability of the system, which is not related to chaos.

Among other criteria suggested on the onset of quantum chaos is the extensive appearance of avoided crossings: a quantum state participating simultaneously in many such resonances, exhibits a statistical character and can be described as chaotic, while avoided crossings produce irregularities in the quantum spectrum. Also, a considerably more rapid dispersion of an initially highly localized wave packet, measured by $|\langle\psi(0)|\psi(t)\rangle|^2$, can serve as an indication of quantum chaos.

An important characteristic of chaotic spectra was first observed by Wigner [69]. He realized that assignment of individual lines was not only infeasible, but also not useful. Instead, he studied the statistical distribution of adjacent energy levels. It was found that the level density $P(S)$ of spacings S of irregular spectra can be modeled by the Wigner distribution

$$P(S) = \frac{\pi}{2} S \, e^{-\frac{\pi}{4}S^2},$$

while in regular spectra the spacing density follows the Poisson distribution

$$P(S) = e^{-S}.$$

In both formulas, S is given in mean spacing units. It is assumed that the number of energy levels is very large, suitable for statistical treatment. This is indeed the case in the semiclassical limit, where the density of states, $(2\pi\hbar)^{-f}$, tends to infinity.

It was observed that irregular energy levels tend to "repel" each other, yielding zero probability of finding degeneracies, as reflected in the Wigner distribution. The opposite is true for regular spectra where the levels tend to cluster.

The mathematical model from which the Wigner distribution can be derived is the *Gaussian Orthogonal Ensemble (GOE)*; a set of real symmetric matrices with elements taken from a gaussian distribution. An average over the ensemble members was found to be equivalent to the spectral average. Matrices with uniformly distributed elements yield the Poisson distribution. The spectrum of a generic system with mixed chaotic and regular regions, is expected to be modeled by a weighted superposition of the two distributions. The weights can be the classical volumes of the corresponding phase space domains. It is important to note that the qualitative difference in the distributions exhibited by regular and irregular spectra has not been proven rigorously.

Another statistical measure of level correlations on larger than first-neighbor scale, is the Δ_3-statistic or *spectral rigidity*. It is defined by (see [70]),

$$\Delta_3(L) = \left\langle \frac{1}{L} \min_{A,B} \int_E^{E+L} [N(E') - AE' - B]^2 \, \mathrm{d}E' \right\rangle_E ,$$

where $N(E)$ the number of levels below energy E, and $< \ldots >_E$ denotes averaging over a suitable energy range. $\Delta_3(L)$ gives the average least squares deviation of $N(E)$ from the best straight line, fitting it over an interval of length L. Spectral rigidity and spacing distribution are independent statistics giving complementary information as they are measures of long and short spectral correlations.

It can be shown by analytical calculations on GOE that, for $L \gg 1$, the spectral rigidity is

- for irregular spectra: $\Delta_3(L) = \dfrac{1}{\pi^2} \ln L - 0.007,$
- for regular spectra: $\Delta_3(L) = L/15.$

On model systems with dense spectra, these remarks on the distributions of the level spacings can serve as definitions of quantum chaos. Moreover, the degree of chaos of a system can be estimated by the way its spectrum evolves from a Poisson to a Wigner distribution as energy increases. However, the applicability of such a criterion on small molecular systems is problematic. The number of states is too small to be statistically treated and their density varies considerably when a dissociation limit or isomerization barrier is approached. Most importantly, there are molecules whose spectra are neither Poisson at low energies nor Wigner at high energies, so no definite conclusions can be drawn by the level spacing distribution. The triatomic molecules with a hydrogen atom, such as those we studied, generally exhibit one fundamental frequency much larger and fairly decoupled from the other two; they fall into such a category.

Chapter 3

Quantum Chemistry

3.1 Introduction

An overview of the framework of molecular spectroscopy and the methods which comprise the "toolbox" of researchers in this field is necessary in order to understand the way classical mechanics contributes. The presentation which follows, deals mainly with the theoretical treatment and is oriented towards the methods employed in the molecular species we studied.

In general, the spectrum recorded by the experimentalists is reconstructed in detail, and in a greater extent, via quantum mechanical calculations based on ab initio or empirical potentials. The semiclassical analysis of the system, which involves a simpler Hamiltonian incorporating the basic features of it and adjusted to reproduce specific quantitative results, can often provide meaningful interpretation of various spectral characteristics. The classical analysis, via the full Hamiltonian, of the phase space and dynamics, paying attention to the way, and the conditions under which, periodic orbits come into existence, evolve and disappear, reveals a different facet of the underlying system and helps us clarify puzzling quantum or experimental findings. These approaches can also assist the quantum analysis by providing guidance on the assignment and grouping of wave functions.

In this chapter we will give a brief outline of the Stimulated Emission Pumping (SEP) and Dispersed Fluorescence (DF) experimental techniques which produced the spectra of the molecules we studied. We will also describe the methods employed to derive the potentials. Among them, the Self-Consistent Field method—the basis for all ab initio techniques—and the Configuration Interaction method and its variants are presented in adequate detail. We will elaborate on the approximations leading to the construction of the nuclear Hamiltonian, and an outline of the methods developed to solve the corresponding Schrödinger equation will be given. The way classical mechanics assists the interpretation of spectra, the main objective of this thesis, is left for subsequent chapters where specific molecules are analyzed. The semiclassical approach is also briefly outlined here for completeness.

This chapter is laid out as follows: the first section provides a review of the necessary theoretical background in an attempt to facilitate comprehension of the subsequent sections and to lay out the terminology and notation. The full Hamiltonian for a molecule is then constructed and the fundamental Born–Oppenheimer

approximation is explained along with an outline of the cases where it is not applicable. The next section deals mainly with the ab initio and, in a lesser extent, the empirical methods developed for the calculation of the Potential Energy Surfaces governing the nuclear motion. The most common theoretical approaches to the solution of the Schrödinger equation follow. The experimental techniques and the introduction on the semiclassical treatment conclude this chapter.

3.2 Theoretical Background

Before we proceed to the main subjects of this chapter, it is appropriate to clarify the notation and remind us of certain notions of quantum mechanics and point group theory which will be used below.

3.2.1 Elements of Quantum Mechanics

The theoretical treatment of a set of non-relativistic particles calls for the solution of the *time-dependent Schrödinger equation*:

$$\widehat{\mathscr{H}}\Psi(\mathbf{q},t) = i\hbar\frac{\partial\Psi(\mathbf{q},t)}{\partial t}. \tag{3.1}$$

In the equation above, $\mathbf{q}$ denotes the set of degrees of freedom for the system, Ψ is the *wave function*, and $\widehat{\mathscr{H}}$ is the *Hamiltonian operator*.

If $\mathbf{q}$ are Cartesian coordinates, the Hamiltonian operator can be derived by the classical Hamiltonian function $\mathcal{H}(\vec{q},\vec{p},t)$, through the simple promotion of q_i and p_i to quantum operators $\widehat{q}_i$ and $\widehat{p}_i$ with the properties (in position space representation):

$$\widehat{q}_i\Psi = q_i\Psi, \qquad \widehat{p}_i\Psi = -i\hbar\frac{\partial\Psi}{\partial q_i}.$$

If the classical Hamiltonian function is expressed in generalized coordinates and their conjugate momenta, the *Podolsky transformation* can be used to reformulate it prior to applying the above promotions. This method is outlined below for a Hamiltonian where p_i enter solely in the kinetic term. It can be similarly applied when any other quadratic term in p_i appears (see [71]).

The classical kinetic term can be cast into the form

$$T = \frac{1}{2}\sum_i\sum_j g_{ij}p_ip_j,$$

where g_{ij} can be functions of the generalized coordinates. Let us denote with J the determinant of the Jacobian of the transformation from a set of Cartesian coordinates $\{x_i\}$ to the particular set of generalized coordinates $\{q_j\}$, $J = |\partial q_j/\partial x_i|$, and with g the determinant of the g_{ij} matrix. Podolsky in [72] showed that the kinetic operator can be obtained by quantizing the equivalent term

$$T = \frac{1}{2}J^{-1/2}g^{1/4}\left[\sum_i\sum_j p_ig^{-1/2}g_{ij}p_j\right]g^{1/4}J^{1/2}.$$

If the Hamiltonian operator does not depend explicitly on time, a separation of variables $\{\mathbf{q}, t\}$ is possible, factoring out of Ψ the temporal dependence:

$$\Psi(\mathbf{q}, t) = \Phi(\mathbf{q})\, e^{-iEt/\hbar}.$$

The form of the temporal term is chosen such that eq. (3.1) assumes a simpler form:

$$\widehat{\mathscr{H}}(\mathbf{q}, \mathbf{p})\ \Phi(\mathbf{q}) = E\ \Phi(\mathbf{q}). \tag{3.2}$$

This is the *time-independent Schrödinger equation* and contains a parameter, E.

Solving eq. (3.1) or eq. (3.2) under specific boundary conditions for the wave functions Ψ or Φ or their spatial derivatives, provides non-trivial solutions (the wave functions) for certain values of E. This parameter corresponds to the total energy of the system in question. Bound systems exhibit *discrete* values of it while unbound systems possess a *continuous* energy spectrum. Both wave function and energy are parametrized by a set of one or more *quantum numbers* collectively denoted by n: Φ_n, E_n. When the energies are equal for different values of the quantum numbers, we speak of *degeneracy*.

As the time-independent Hamiltonian operator is hermitian it can be shown that its eigenfunctions comprise a complete basis in configuration space; moreover, they can be chosen to be orthonormal. These mean that

$$\int_V \Phi_m^* \Phi_n \,\mathrm{d}\mathbf{q} \equiv \langle m|n\rangle = \delta_{mn} \qquad \forall\ m, n \tag{3.3}$$

holds, and that any function $F(\mathbf{q})$ can be expanded on the eigenfunctions Φ_n,

$$F(\mathbf{q}) = \sum_n c_n \Phi_n(\mathbf{q}) \equiv \sum_n c_n \,|n\rangle\,,$$

where

$$c_n = \int_V \Phi_n^* F \,\mathrm{d}\mathbf{q} \equiv \langle n|F\rangle\ .$$

In all integrals, $\mathrm{d}\mathbf{q}$ denotes the volume element expressed in the generalized coordinates, that is

$$\mathrm{d}\mathbf{q} = |J^{-1}| \prod_i \mathrm{d}q_i,$$

where J is defined above.

It is appropriate to present here a special kind of unbound states which play an important role in, among others, the unimolecular dissociation process we will encounter in a subsequent chapter. *Resonances* are quasi-bound states embedded in the continuum above the dissociation threshold of a system. They act as analogues of the bound states in the sense that their wave functions are mainly localized over the potential well, having tails with significantly smaller amplitude over the dissociation channels. This topography is in contrast to other states in the continuum which extend with roughly the same amplitude over all energetically accessible space. The durability of resonances can be intuitively justified by a particular energy distribution; a system can live an appreciable time on a excited state above the fragmentation threshold if the energy is initially deposited on degrees of freedom weakly coupled

to the dissociation modes. This delay in fragmentation is reflected as a pronounced variation of the cross sections if the fragmentation energy lies in the neighborhood of the energy of a resonance. The amplitude distribution of resonances is not static as is in bound states; resonances eventually wither away, in a rate depending on the coupling between the well region and the product channels. Due to the time-energy uncertainty relation, their limited lifetime τ is inversely proportional to the energy width Γ they exhibit.

In systems with relatively weak coupling between the degrees of freedom associated to fragmentation and the rest, we can distinguish two classes of resonances: *Feshbach* and *shape* ones. The former refers to resonances which turn into bound states when the coupling goes to zero, while the latter refers to the opposite.

The profile of (Breit-Wigner) resonances can be described by a Lorentzian function

$$\sigma(E) \propto \frac{(\Gamma/2)}{(E - E_{\text{res}})^2 + (\Gamma/2)^2},$$

where $\sigma(E)$ is an energy dependent cross section and Γ is the full width at half maximum. One can regard resonances as eigenstates with a complex energy eigenvalue $E = E_{\text{res}} - i\Gamma/2$. Using this in the formula for the time evolution of a quantum mechanical wave function we get

$$|\Psi(t)|^2 \propto |e^{-iEt/\hbar}|^2 = |e^{-iE_{\text{res}}t/\hbar} e^{-\Gamma t/(2\hbar)}|^2 = e^{-\Gamma t/\hbar},$$

that is, the population of a resonance state decays exponentially in time. We can determine the dissociation rate to be $\Gamma_i/\hbar$, which is thus the inverse of the lifetime τ_i. In addition to E_{res} and Γ, a resonance is characterized by the final state distribution of the products of dissociation. E_{res} provides information mainly on the Hamiltonian in the well region, Γ is influenced by the coupling between the exit channels and the potential well, and the products can reveal much on the dynamics of the system in the dissociation channels.

Fundamental methods to solve the Schrödinger equation

Exact solution of the Schrödinger equation is generally not feasible; approximation methods are employed to solve it. Among those developed to that end, the *variational method* is the most central. Based on it are the ab initio methods for the calculation of potentials presented in §3.5.1; an outline will be given here, along with an overview of the perturbative treatment, another important tool in solving specific forms of the Schrödinger equation. A full presentation of both of them can be found in any advanced quantum mechanics textbook. Specialized techniques, applicable to the vibration-rotation nuclear Hamiltonian we will derive, are presented in §3.6. The calculation of states in the continuum is another case where variations of the methods presented here can be applied.

Variational method. We can construct a function $F(\mathbf{q}; \lambda)$ as a parametric sum of N linearly independent functions $\{\varphi_i(\mathbf{q})\}$ $(i = 1 \ldots, N)$, which, in turn, are

expanded on all the (unknown) eigenfunctions $\{|\mu\rangle\}$ of $\widehat{\mathscr{H}}$:

$$\left.\begin{aligned} F(\mathbf{q};\lambda) &= \sum_{i=1}^{N} c_i(\lambda)\,\varphi_i(\mathbf{q}) \\ |\varphi_i\rangle &= \sum_{\mu} a_{i\mu}\,|\mu\rangle \end{aligned}\right\} \Rightarrow F(\mathbf{q};\lambda) = \sum_{i=1}^{N}\sum_{\mu} c_i(\lambda)\,a_{i\mu}\,|\mu\rangle = \sum_{\mu} d_\mu(\lambda)\,|\mu\rangle\,.$$

The *expectation value*, $\widehat{\mathscr{H}_F}(\lambda)$, of the Hamiltonian operator for this function is defined as:

$$\widehat{\mathscr{H}_F}(\lambda) \equiv \frac{\langle F|\,\widehat{\mathscr{H}}\,|F\rangle}{\langle F|F\rangle} \equiv \frac{\displaystyle\int_V F(\mathbf{q};\lambda)^*\;\widehat{\mathscr{H}}\,F(\mathbf{q};\lambda)\,\mathrm{d}\mathbf{q}}{\displaystyle\int_V F(\mathbf{q};\lambda)^*\;F(\mathbf{q};\lambda)\,\mathrm{d}\mathbf{q}}.$$

But

$$\begin{aligned} \langle F|\,\widehat{\mathscr{H}}\,|F\rangle &= \sum_{\mu}\sum_{\nu} d_\mu^* d_\nu\,\langle\mu|\,\widehat{\mathscr{H}}\,|\nu\rangle = \sum_{\mu}\sum_{\nu} d_\mu^* d_\nu E_\nu\,\langle\mu|\nu\rangle \\ &\geq E_1 \sum_{\mu}\sum_{\nu} d_\mu^* d_\nu\,\langle\mu|\nu\rangle = E_1\,\langle F|F\rangle\,, \end{aligned}$$

where E_1 is the energy of the lowest (or *ground*) state. We conclude that

$$\widehat{\mathscr{H}_F}(\lambda) \geq E_1,$$

i.e. the expectation value provides an upper limit on the lowest energy.

Minimization of $\widehat{\mathscr{H}_F}(\lambda)$ with respect to the parameter(s) λ can give an estimate of the energy for the ground state; the function F for the set of the critical values of λ is an approximation to the ground wave function. This approximation can be very accurate if the set of $\{\varphi_i\}$ is chosen so that the expected physical characteristics of the ground eigenfunction are reproducible by the basis functions.

The same procedure can be applied to estimate successively higher states with the proviso that F is taken orthogonal to all lower eigenfunctions, i.e.

$$\langle F|\Phi_1\rangle = \langle F|\Phi_2\rangle = \ldots = 0.$$

The minimization of the expectation value of $\widehat{\mathscr{H}}$ is then constrained by the above relations.

A related method, also referred to as the (linear) variational method, assumes that the parameters collectively denoted by λ above, are the coefficients in the expansion on $\{\varphi_i\}$:

$$F(\mathbf{q};\lambda) = \sum_{i=1}^{N} \lambda_i\,\varphi_i(\mathbf{q}).$$

With this as a trial function, the resolution of Schrödinger equation, eq. (3.2), can be turned into a generalized matrix diagonalization problem:

$$\sum_{j=1}^{N} \lambda_j \int_V \varphi_i^*\,\widehat{\mathscr{H}}\varphi_j\,\mathrm{d}\mathbf{q} = E\sum_{j=1}^{N} \lambda_j \int_V \varphi_i^*\varphi_j\,\mathrm{d}\mathbf{q} \Rightarrow \quad H\lambda = ES\lambda, \tag{3.4}$$

where H is the Hamiltonian matrix with elements $H_{ij} = \langle\varphi_i|\,\widehat{\mathscr{H}}\,|\varphi_j\rangle$ and S the overlap matrix with $S_{ij} = \langle\varphi_i|\varphi_j\rangle$, $(1 \leq i, j \leq N)$. The diagonalization provides E, a diagonal matrix containing the eigenvalues which we can arrange in ascending order: $E_1 \leq E_2 \leq \cdots \leq E_N$. The variational treatment ensures that E_1 is an upper bound to the exact ground state energy; moreover, each energy E_i also bounds the exact energy of the corresponding ith excited state. This follows from the mutual orthogonality of the eigenvectors, the corresponding sets of λ_i, which express the eigenfunctions in the $\{\varphi\}$ basis. The larger and more "appropriate" for the specific problem the basis is, the better approximation we can achieve, especially for the low-lying states.

Time-independent perturbation method. Let us assume we can write the Hamiltonian operator as a sum of an operator $\widehat{\mathscr{H}^o}$ for which the eigenvalues ${E^o}_n$ and eigenfunctions ${\varphi^o}_n \equiv |n^o\rangle$ are analytically known, and another operator, $\epsilon\widehat{\mathscr{H}'}$, which represents a small correction to $\widehat{\mathscr{H}^o}$. Moreover, we assume the set $\{|n^o\rangle\}$ is orthonormal, and the set of energies $\{{E^o}_n\}$ is discrete and non-degenerate. If we expand the wave function Φ and the energy E in powers of ϵ, substitute them along with $\widehat{\mathscr{H}}$ in eq. (3.2), and equate the coefficients of same orders of ϵ we get:

$$E_k = {E^o}_k + \epsilon\,\langle k^o|\,\widehat{\mathscr{H}'}\,|k^o\rangle + \epsilon^2 \sum_{m\neq k} \frac{|\,\langle m^o|\,\widehat{\mathscr{H}'}\,|k^o\rangle\,|^2}{{E^o}_k - {E^o}_m} + \cdots$$

and

$$\Phi_k = |k^o\rangle + \epsilon \sum_{m\neq k} \frac{\langle m^o|\,\widehat{\mathscr{H}'}\,|k^o\rangle}{{E^o}_k - {E^o}_m}\,|m^o\rangle + \cdots.$$

3.2.2 Elements of Point Group Theory

There are certain geometrical entities (point, lines, planes) with respect to which a transformation of the nuclear frame of a molecule casts it into a configuration indistinguishable from the original. These entities are the *symmetry elements* and the transformations related to them are the *symmetry operations*. Such operations are, for example, an *inversion* through a point (denoted by i), a *rotation* about an axis by an angle $2\pi/n$ (denoted by C_n), a *reflection* through a plane (denoted by σ).

The set of all symmetry operations applicable on a particular nuclear configuration of a molecule possesses the properties of a mathematical group. In each group we can gather the elements into *classes* comprised of all symmetry operations related via a similarity transformation. We can construct a set of square matrices *isomorphic* to such a group; this means that there is a one to one correspondence between matrices and symmetry operations and that any relation between the elements of the symmetry group holds also for their images in the matrix group. There is an infinite number of such matrix groups; the are called the *reducible representations* of the point group. There are transformations which can cast the elements of such a representation into the same block diagonal form. It can easily be shown that the corresponding blocks from each of the elements of the matrix group, form themselves a group isomorphic to the parent one and to the point group. This reduction process will eventually produce distinct groups which can not be reduced further; they

constitute the *irreducible representations* of the point group and they are equal in number to the number of classes of the symmetry group. In each irreducible representation, the traces of the matrices are termed the *characters* of the corresponding symmetry operations. One of the irreducible representations is totally symmetric (the characters are all +1) and the others have distinct character sets.

An important physical requirement is that the electronic eigenfunctions, which we will define in a subsequent section, and the vibrational normal modes of any molecule, belong to (or form a basis for) one of the irreducible representations of the point group of the molecule. This means that the eigenfunctions and the normal modes are also eigenfunctions of the symmetry operations in the irreducible representation and their eigenvalues are its characters. Moreover, if an irreducible representation is not one dimensional, that is, the matrices forming it have rank greater than 1, the degeneracy of the relevant eigenfunctions is symmetry dictated.

The symmetry of the wave functions and of certain operators (dipole moment, polarizability, etc.) is very useful in determining whether an integral involving them vanishes. For example, the product of such entities, each belonging to specific irreducible representations, is a reducible representation. The *vanishing integral rule* requires an integral to be zero if the integrand belongs to a reducible representation which does not contain the totally symmetric irreducible one.

The irreducible representations of a point group are commonly denoted with the aid of Mulliken symbols: A and B are used for one dimensional, E for two dimensional and T (or F) for three dimensional representations. The character (+1 or −1) of the principal rotational operation, if it exists, determines the symbol A or B respectively. If the molecule has a center of inversion, the character of i in the irreducible representation is denoted by a subscript g (*gerade*) or u (*ungerade*) for the symmetric (+1) and antisymmetric (−1) cases. A single or a double prime by the name denotes the character (+1, −1) of the reflection through a horizontal symmetry plane (if it exists). If more than one irreducible representations have these eigenvalues equal, they are distinguished by a numerical subscript. For infinite point groups describing linear molecules, the symbols $\Sigma, \Pi, \Delta, \Phi, \Gamma \ldots$ are used. A + or − superscript in Σ denotes the character of the reflection through the (infinite number of) vertical planes of symmetry (if they exist). The ground electronic state is usually denoted by X; for the excited states the symbols $A, B, \ldots$ are used. A tilde on them denotes linear configuration.

Vast literature exists on this subject; see, for example, [73].

3.3 The Molecular Hamiltonian

For a mechanical system of N dimensionless particles with masses m_j, position vectors $\vec{q}_j$, on which forces generated by a potential $\mathscr{V}(\vec{q}_j, \vec{p}_j, t)$ are exerted, the Hamiltonian operator turns out to be

$$\widehat{\mathscr{H}} = \widehat{\mathscr{T}} + \widehat{\mathscr{V}} = \sum_{j=1}^{N} \frac{\vec{\hat{p}}_j^{\,2}}{2m_j} + \mathscr{V}(\vec{\hat{q}}_j, \vec{\hat{p}}_j, t) = -\sum_{j=1}^{N} \frac{\hbar^2}{2m_j} \nabla_j^2 + \mathscr{V}(\vec{q}_j, -i\hbar\nabla_j, t). \quad (3.5)$$

An isolated non-relativistic molecule consisting of one or more nuclei and one or more electrons, can be treated as a set of point-like particles. Let N_n be the number

of nuclei, M_i their masses, $\mathscr{Z}_i$ their atomic numbers, $\vec{R}_i \equiv (X_i, Y_i, Z_i)$ and $\vec{P}_i$ their position and momentum vectors ($i = 1 \ldots, N_n$); let N_e be the number of electrons, in positions $\vec{r}_j \equiv (x_j, y_j, z_j)$, with momenta $\vec{p}_j$, ($j = 1 \ldots, N_e$). $\mathbf{R}$ and $\mathbf{r}$ will be used to denote the nuclear and the electronic configurations (sets of position vectors), respectively; $\mathbf{P}$ and $\mathbf{p}$ will collectively be the momenta.

The kinetic part of the Hamiltonian operator is

$$\widehat{\mathscr{T}} = \widehat{\mathscr{T}^n} + \widehat{\mathscr{T}^e}$$

where

$$\widehat{\mathscr{T}^n} = \sum_{i=1}^{N_n} \frac{-\hbar^2}{2M_i} \left(\frac{\partial^2}{\partial X_i^2} + \frac{\partial^2}{\partial Y_i^2} + \frac{\partial^2}{\partial Z_i^2} \right)$$

and

$$\widehat{\mathscr{T}^e} = -\frac{\hbar^2}{2m_e} \sum_{i=1}^{N_e} \left(\frac{\partial^2}{\partial x_i^2} + \frac{\partial^2}{\partial y_i^2} + \frac{\partial^2}{\partial z_i^2} \right).$$

The interaction of these particles is represented by the potential

$$\mathscr{V}(\mathbf{R}, \mathbf{r}, \mathbf{P}, \mathbf{p}) = \mathscr{V}^{nn}(\mathbf{R}) + \mathscr{V}^{ee}(\mathbf{r}) + \mathscr{V}^{ne}(\mathbf{R}, \mathbf{r}) + v(\mathbf{R}, \mathbf{r}, \mathbf{P}, \mathbf{p}), \tag{3.6}$$

where (in S.I.)

$$\mathscr{V}^{nn}(\mathbf{R}) = \frac{e^2}{4\pi\varepsilon_0} \sum_{i=1}^{N_n} \sum_{j=i+1}^{N_n} \frac{\mathscr{Z}_i \mathscr{Z}_j}{\left| \vec{R}_i - \vec{R}_j \right|}, \tag{3.7}$$

$$\mathscr{V}^{ee}(\mathbf{r}) = \frac{e^2}{4\pi\varepsilon_0} \sum_{i=1}^{N_e} \sum_{j=i+1}^{N_e} \frac{1}{|\vec{r}_i - \vec{r}_j|}, \tag{3.8}$$

$$\mathscr{V}^{ne}(\mathbf{R}, \mathbf{r}) = -\frac{e^2}{4\pi\varepsilon_0} \sum_{i=1}^{N_n} \sum_{j=1}^{N_e} \frac{\mathscr{Z}_i}{\left| \vec{R}_i - \vec{r}_j \right|}. \tag{3.9}$$

v incorporates all non-electrostatic interactions of the particles (due to their spins, orbital angular momenta, etc.). It includes terms representing the interaction of each of the electron spin magnetic moments with (see [74, 75]):

- the magnetic moments generated by the orbital motions of the electrons

$$\frac{1}{4\pi\varepsilon_0} \frac{g\mu_B}{c^2} \sum_{i=1}^{N_e} \sum_{\substack{j=1 \\ j \neq i}}^{N_e} \frac{-e}{|\vec{r}_i - \vec{r}_j|^3} \left[(\vec{r}_i - \vec{r}_j) \times \left(\frac{\vec{p}_i}{2m_e} - \frac{\vec{p}_j}{m_e} \right) \right] \cdot \vec{s}_i,$$

- the magnetic moments generated by the orbital motions of the nuclei

$$\frac{1}{4\pi\varepsilon_0} \frac{g\mu_B}{c^2} \sum_{i=1}^{N_e} \sum_{j=1}^{N_n} \frac{\mathscr{Z}_j e}{|\vec{r}_i - \vec{R}_j|^3} \left[(\vec{r}_i - \vec{R}_j) \times \left(\frac{\vec{p}_i}{2m_e} - \frac{\vec{P}_j}{M_j} \right) \right] \cdot \vec{s}_i,$$

- the spin magnetic moments of the other electrons

$$\frac{1}{4\pi\varepsilon_0}\frac{g^2{\mu_B}^2}{c^2}\sum_{i=1}^{N_e}\sum_{j=i+1}^{N_e}\left\{\frac{1}{|\vec{r}_i-\vec{r}_j|^3}(\vec{s}_i\cdot\vec{s}_j)\right.$$
$$\left.-\frac{3}{|\vec{r}_i-\vec{r}_j|^5}[\vec{s}_i\cdot(\vec{r}_i-\vec{r}_j)][\vec{s}_j\cdot(\vec{r}_i-\vec{r}_j)]-\frac{8\pi}{3}\delta(\vec{r}_i-\vec{r}_j)(\vec{s}_i\cdot\vec{s}_j)\right\},$$

where μ_B is the Bohr magneton, and g, $\vec{s}_i$ the Landé g-factor and spin of the ith electron.

Similar terms, smaller in magnitude and responsible for the hyperfine structure in the energy spectrum, arise from the interaction of the electric and magnetic moments of the nuclei with the other moments in the molecule. Nuclei with non-zero spin, I, have non-vanishing magnetic dipole moment. The relevant terms in v are analogous to the above for electrons, namely

- $$\frac{1}{4\pi\varepsilon_0}\frac{m_p\mu_N}{c^2}\sum_{i=1}^{N_n}\sum_{\substack{j=1\\j\neq i}}^{N_n}\frac{G_i\mathscr{Z}_i e}{M_i}\frac{1}{|\vec{R}_i-\vec{R}_j|^3}\left[(\vec{R}_i-\vec{R}_j)\times\left(\frac{\vec{P}_i}{2M_i}-\frac{\vec{P}_j}{M_j}\right)\right]\cdot\vec{I}_i$$
- $$\frac{1}{4\pi\varepsilon_0}\frac{m_p\mu_N}{c^2}\sum_{i=1}^{N_n}\sum_{j=1}^{N_e}\frac{-G_i e}{M_i}\frac{1}{|\vec{R}_i-\vec{r}_j|^3}\left[(\vec{R}_i-\vec{r}_j)\times\left(\frac{\vec{P}_i}{2M_i}-\frac{\vec{p}_j}{m_e}\right)\right]\cdot\vec{I}_i$$
- $$\frac{1}{4\pi\varepsilon_0}\frac{(m_p\mu_N)^2}{c^2}\sum_{i=1}^{N_n}\sum_{j=i+1}^{N_n}\frac{G_i^2}{M_i^2}\left\{\frac{1}{|\vec{R}_i-\vec{R}_j|^3}(\vec{I}_i\cdot\vec{I}_j)\right.$$
$$\left.-\frac{3}{|\vec{R}_i-\vec{R}_j|^5}[\vec{I}_i\cdot(\vec{R}_i-\vec{R}_j)][\vec{I}_j\cdot(\vec{R}_i-\vec{R}_j)]-\frac{8\pi}{3}\delta(\vec{R}_i-\vec{R}_j)(\vec{I}_i\cdot\vec{I}_j)\right\},$$

where μ_N is the nuclear magneton, m_p the proton mass, and G_i, $\vec{I}_i$ the g-factor and spin of the ith nucleus.

Additionally, nuclei with spin equal to 1 or greater have non-vanishing electric quadrupole moments; higher order moments arise for greater spins. These moments interact with each other and result in additional terms in v; the one comparable in magnitude to the dipole–dipole nuclear terms is

$$-\frac{1}{6}\sum_{i=1}^{N_n}\sum_{\alpha=1}^{3}\sum_{\beta=1}^{3}Q_i^{(\alpha\beta)}F_i^{(\alpha\beta)},$$

where $Q_i^{(\alpha\beta)}$ is the component in a molecule-fixed coordinate system of the electric quadrupole moment of the ith nucleus and $F_i^{(\alpha\beta)}$ is the α-component of the gradient of the β-component of the electric field felt by the ith nucleus due to the other charges in the molecule.

Collecting all the above yields the Hamiltonian operator for the molecule as

$$\widehat{\mathscr{H}}=\widehat{\mathscr{T}}^n+\widehat{\mathscr{T}}^e+\widehat{\mathscr{V}}^{nn}+\widehat{\mathscr{V}}^{ee}+\widehat{\mathscr{V}}^{ne}+\widehat{v}. \tag{3.10}$$

Simplifying approximations are necessary in order to solve with adequate accuracy the Schrödinger equation with this Hamiltonian for any real molecule. We can

reduce by three the number of degrees of freedom by extracting the motion of the center of mass; this is useful for a two particle system but does not gain us much in realistic molecular systems. To derive equations more suitable for our present algorithmic and computational capabilities, we can apply the *Born–Oppenheimer approximation.*

3.4 The Born–Oppenheimer Approximation

The total forces exerted on each of the nuclei and the electrons are of the same order of magnitude, while the nuclei are thousands of times heavier than the electrons. Therefore, the electrons move much more rapidly than the nuclei and adjust their positions almost instantaneously on any change of the nuclear configuration, leading us to consider the separation of these motions. This is qualitatively the *adiabatic* or *Born–Oppenheimer* approximation. We can fix the nuclear configuration at various sets of $\{\vec{R}_i\}$ and solve for the electronic wave functions $\Phi^e(\mathbf{r};\mathbf{R})$ and energies E^e, both depending only parametrically on the nuclear configuration. If we do this for a range of configurations, we obtain the potential energy surface along which the nuclei move.

The time-independent equation for the electrons is the *clamped–nuclei Schrödinger equation.* It reads

$$\begin{aligned} E^e\Phi^e(\mathbf{r};\mathbf{R}) &= \widehat{\mathscr{H}}^e\Phi^e(\mathbf{r};\mathbf{R}) \\ &= \left[\widehat{\mathscr{T}}^e + \widehat{\mathscr{V}}^{nn}(\mathbf{R}) + \widehat{\mathscr{V}}^{ee}(\mathbf{r}) + \widehat{\mathscr{V}}^{ne}(\mathbf{r};\mathbf{R})\right]\Phi^e(\mathbf{r};\mathbf{R}). \end{aligned} \tag{3.11}$$

If spin–orbit effects are important (as are for molecules with highly charged nuclei) we can incorporate the $\widehat{v}$ operator in the electronic Hamiltonian. Note that $\widehat{\mathscr{V}}^{nn}$ is a constant for each nuclear configuration and just shifts the electronic energy levels. The different notation used here for the dependence of potentials and wave functions on $\mathbf{R}$ reflects its parametric nature.

Let us revisit the total Hamiltonian eq. (3.10). The solution of eq. (3.11), the set of $\{\Phi^e{}_k\}$, can serve as a basis (characterized as *adiabatic*) for the expansion of the total wave function

$$\Phi(\mathbf{R},\mathbf{r}) = \sum_k \left[\chi_k(\mathbf{R})\ \Phi^e{}_k(\mathbf{r};\mathbf{R})\right].$$

The Schrödinger equation for the Hamiltonian in eq. (3.10) is then

$$\widehat{\mathscr{H}}\sum_k \left[\chi_k(\mathbf{R})\ \Phi^e{}_k(\mathbf{r};\mathbf{R})\right] = E\ \sum_k \left[\chi_k(\mathbf{R})\ \Phi^e{}_k(\mathbf{r};\mathbf{R})\right],$$

or, making use of the orthonormality relation eq. (3.3),

$$\int_V \Phi^{e*}_s(\mathbf{r};\mathbf{R})\ \widehat{\mathscr{H}}\sum_k \left[\chi_k(\mathbf{R})\ \Phi^e{}_k(\mathbf{r};\mathbf{R})\right]\,\mathrm{d}\mathbf{r} = E\ \chi_s(\mathbf{R}).$$

Simplifying it further,

$$\begin{aligned} E\,\chi_s(\mathbf{R}) &= \sum_k \int_V \mathrm{d}\mathbf{r}\; \Phi^{e*}{}_s(\mathbf{r};\mathbf{R})\left(\widehat{\mathscr{T}^n} + \widehat{\mathscr{H}^e} + \widehat{v}\right)\chi_k(\mathbf{R})\,\Phi^e{}_k(\mathbf{r};\mathbf{R}) \\ &= \sum_k \int_V \mathrm{d}\mathbf{r}\; \Phi^{e*}{}_s(\mathbf{r};\mathbf{R})\;\widehat{\mathscr{T}^n}\chi_k(\mathbf{R})\;\Phi^e{}_k(\mathbf{r};\mathbf{R}) + \sum_k \left(\widehat{\mathscr{H}^e}_{sk} + \widehat{v}_{sk}\right)\chi_k(\mathbf{R}) \end{aligned}$$

holds, where the notation $\widehat{\mathscr{A}_{sk}}$ is used for the matrix elements of an operator $\widehat{\mathscr{A}}$ in the adiabatic basis,

$$\widehat{\mathscr{A}_{sk}} \equiv \langle s|\,\widehat{\mathscr{A}}\,|k\rangle \equiv \int_V \mathrm{d}\mathbf{r}\;\Phi^{e*}{}_s(\mathbf{r};\mathbf{R})\;\widehat{\mathscr{A}}\,\Phi^e{}_k(\mathbf{r};\mathbf{R}).$$

After some straightforward algebra the Schrödinger equation for the molecule reads:

$$\begin{aligned} &\left[\widehat{\mathscr{T}^n} + \widehat{\mathscr{T}'_{ss}} + \widehat{\mathscr{T}''_{ss}} + \widehat{\mathscr{H}^e}_{ss} + \widehat{v}_{ss} - E\right]\chi_s(\mathbf{R}) \\ &\quad = \; -\sum_{k\neq s}\left[\widehat{\mathscr{T}'_{sk}} + \widehat{\mathscr{T}''_{sk}} + \widehat{\mathscr{H}^e}_{sk} + \widehat{v}_{sk}\right]\chi_k(\mathbf{R}), \end{aligned} \tag{3.12}$$

with

$$\begin{aligned} \widehat{\mathscr{T}'_{sk}}(\mathbf{R}) &= -2\sum_i \frac{\hbar^2}{2M_i}\int_V \mathrm{d}\mathbf{r}\;\Phi^{e*}{}_s(\mathbf{r};\mathbf{R})\;\nabla_i[\Phi^e{}_k(\mathbf{r};\mathbf{R})]\cdot\nabla_i, \\ \widehat{\mathscr{T}''_{sk}}(\mathbf{R}) &= -\sum_i \frac{\hbar^2}{2M_i}\int_V \mathrm{d}\mathbf{r}\;\Phi^{e*}{}_s(\mathbf{r};\mathbf{R})\;\nabla_i^2[\Phi^e{}_k(\mathbf{r};\mathbf{R})], \end{aligned} \tag{3.13}$$

where $\nabla_i \equiv \left(\dfrac{\partial}{\partial X_i}, \dfrac{\partial}{\partial Y_i}, \dfrac{\partial}{\partial Z_i}\right)$ the differentiation operator with respect to the coordinates of the ith nucleus.

As we chose the eigenfunctions of $\widehat{\mathscr{H}^e}$ as the basis for the expansion of the molecular wave function, we can achieve further simplification given that

$$\widehat{\mathscr{H}^e}_{sk} = E^e{}_s\;\delta_{sk}.$$

Eq. (3.12) is nevertheless formally exact, regardless of the basis chosen. One could prefer to minimize other coupling terms, such as $\widehat{\mathscr{T}'_{sk}}$, resulting in a diabatic electronic basis. Additionally, by taking the derivative of $\langle\Phi^e{}_s(\mathbf{r};\mathbf{R})|\Phi^e{}_s(\mathbf{r};\mathbf{R})\rangle$, it is easy to show that if the electronic wave function $\Phi^e{}_s$ is real then

$$\widehat{\mathscr{T}'_{ss}} = 0.$$

The Born–Oppenheimer approximation consists in neglecting the couplings on the right-hand side of eq. (3.12). With the further assumption that the wave function is real, we obtain the following approximate equation for the motion of the nuclei:

$$\left[\widehat{\mathscr{T}^n} + \left(\widehat{\mathscr{T}''_{ss}} + E^e{}_s + \widehat{v}_{ss}\right)\right]\chi_s(\mathbf{R}) = E\chi_s(\mathbf{R}). \tag{3.14}$$

Eq. (3.14) is the time-independent Schrödinger equation describing in the Born–Oppenheimer approximation the nuclear motion on a Potential Energy Surface (PES) set up primarily by the electrons on a specific electronic state:

$$V_s(\mathbf{R}) = \widehat{\mathscr{T}}''_{ss} + {E^e}_s + \widehat{v}_{ss}.$$

$\chi_s(\mathbf{R})$ assumes the role of the nuclear eigenfunction and acquires a "nuclear" index in addition to the electronic quantum number s.

The principal contribution to the PES comes from the electronic energy; the others are much smaller. The magnitude of the diagonal term T''_{ss}, called the *Born–Oppenheimer diagonal correction*, can be estimated if we derive from eq. (3.13) the formula

$$\widehat{\mathscr{T}}''_{ss}(\mathbf{R}) = \sum_i \frac{1}{2M_i} \langle s| \vec{P}_i^2 |s\rangle ,$$

where $\vec{P}_i$ the momentum of the ith nucleus. The nuclear momenta are of the order of the electronic momenta, p, and so

$$\langle s| P^2 |s\rangle \approx \langle s| p^2 |s\rangle \approx 2m \langle s| H^e |s\rangle = 2m{E^e}_s.$$

Therefore, the term $\widehat{\mathscr{T}}''_{ss}$ in the PES is roughly $m/M \approx 10^{-4}$ times the larger term ${E^e}_s$ and can be ignored in an approximation.

The Born–Oppenheimer approximation yields differential equations with greatly reduced dimensionality, assuming that there is negligible interaction between the electronic levels and no coupling of the electronic with the nuclear degrees of freedom. These are, in many cases, valid assumptions; however, small or large deviations from the experiment are to to be expected. For example, transitions "forbidden" in the Born–Oppenheimer framework may be observed, occasionally strongly, in the actual experimental spectra (*Herzberg–Teller effect* [76]). Another interesting consequence is *predissociation*: a crossing between bound and repulsive potential surfaces causes the mixing of the corresponding rovibrational states and affects their properties; a system can dissociate from a bound state through this tunneling. The Born–Oppenheimer approximation certainly breaks down severely if the electronic states are close together (compared to the nuclear energies spacing) or the coupling terms do not allow a separation of electronic and nuclear motion. Such a situation arises in the vicinity of an avoided crossing of two energy surfaces; for example, near the crossing between the covalent and ionic potential energy curves of NaCl, fig. (3.1) [reprinted from [77]], the character of the electronic wave functions varies rapidly as the bond length changes, while at large separations it remains more or less constant. Other cases are presented below.

3.4.1 Breakdown of the Born–Oppenheimer Approximation

The most important cases where the Born–Oppenheimer approximation can not be applied are the *Renner–Teller effect*, the *Jahn–Teller effect*, and the calculation of energy levels of *Rydberg states*.

There are certain symmetrical nuclear configurations for which the point group possesses degenerate irreducible representations. This fact requires the degeneracy of

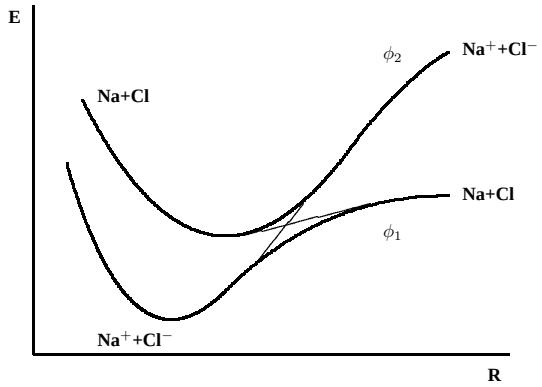

Figure 3.1: Avoided crossing between the covalent and ionic adiabatic potential curves of NaCl (thin lines: crossing of diabatic states).

specific electronic states at these configurations. In a nuclear distortion that reduces the symmetry, the degeneracy may be resolved and result in discrete potential energy surfaces, which only accidentally can coincide.

The Renner–Teller effect

In linearity, the point group to which the molecule belongs is $\mathbf{C}_{\infty v}$ or $\mathbf{D}_{\infty h}$; thus, there exist excited doubly degenerate electronic states with $\Pi, \Delta, \Phi, \ldots$ symmetry. When the molecule is bent, the point group becomes $\mathbf{C}_s$ or $\mathbf{C}_{2v}$ respectively; the irreducible representations for them are all one-dimensional. The degeneracy is lifted and the electronic states split. The amount of splitting has to be an even—as required by symmetry—function of the angle measuring the deviation from linearity. This splitting upon bending of the two, degenerate in linear configuration, electronic states and the subsequent interaction of their rotational-vibrational levels, is called the *Renner–Teller effect* [78]. It results in coupling the electronic to the rotational and vibrational degrees of freedom, breaking down the main assumption of the Born–Oppenheimer approximation.

The Renner–Teller effect is a particular case of the Jahn–Teller effect.

The Jahn–Teller effect

A molecule in a particular nonlinear nuclear configuration belonging to a point group with at least a C_n ($n > 2$) principal symmetry axis, exhibits degeneracy in excited electronic states. According to the *Jahn–Teller theorem* [79], a nuclear distortion must occur to lower the point group symmetry, raise the degeneracy and cause an energy split. This spontaneous symmetry breaking and the subsequent interaction between the vibrational levels of each electronic state is the *Jahn–Teller effect*.

At the symmetrical nuclear configuration, the two potential energy surfaces intersect at a special case of level crossing, a conical intersection. It can be shown, see [79], that the splitting is linear at first approximation in the nuclear coordinates. This means that two degenerate non totally symmetric vibrational modes (Jahn–Teller active modes) exist which makes the symmetrical configuration unstable in

the lower energy level. This is described as the *Jahn–Teller instability*. The lower PES has minima away from the high-symmetry geometry; in the absence of non-linear Jahn–Teller coupling, they are infinite and at a certain distance, forming a "trough" allowing the molecule to "pseudo-rotate" (acquiring in the wave function a Berry phase [80]). The quadratic terms in the coupling can be shown, see [81], to give rise to a finite number of symmetrically equivalent minima in the lower potential energy surface. If n in the principal axis C_n of the high symmetry geometry is odd, there are n minima while with even n there exist $n/2$ minima.

If the Jahn–Teller distortion is large enough it will result in a wave function localized around the minima of the lower PES. This case is referred to as the *static* Jahn–Teller effect. The *dynamic* Jahn–Teller effect occurs when the there is no permanent distortion of the molecule. The theoretical treatment of the two cases is substantially different.

In the case of molecules with a non-degenerate ground electronic state but with a very low lying excited state, distortions of proper symmetry arise which mix the, approximately degenerate, ground and excited states, and thereby lower the ground state energy (*pseudo Jahn–Teller effect*).

In contrast to the Renner–Teller effect, which is essentially a *rovibronic* interaction which can perturb significantly the rotational energy level patterns in the vibronic states affected by it, the perturbations resulting from the Jahn–Teller effect are predominantly *vibronic*; they couple the electronic to the vibrational degrees of freedom.

Rydberg states

Rydberg states are special electronic states for which there are systematic degeneracies and near degeneracies that, in general, prohibit the application of the Born–Oppenheimer approximation. A Rydberg state for a molecule can be regarded as being an electronic state in which one electron orbits in large distance, compared to the molecular dimensions, around the molecular ionic core.

For Rydberg states the treatment is analogous to the hydrogen-like atoms, as the interaction of electron with the core can be regarded as independent of the structure of the core. The *Quantum Defect Theory* [82] is based on this idea and can be applied to solve the Schrödinger equation. An example of the application of this technique can be found in [74].

3.5 Determining the Potential Energy Surface

The calculation of the potential which controls the nuclear motion is an important first step towards understanding the behavior of molecules. The analysis of the PES topography allows us to determine the equilibrium geometries or stationary points in general, their relative energies and the reaction paths connecting them, the dissociation channels, the fundamental vibrational frequencies; the dynamical picture of the molecules in terms of classical trajectory simulations, bifurcations in the phase space or evolution of wave packets among others, is obviously governed by the PES. The interpretation of the characteristics of the PES and their relation to experimental results is the next major step.

There are various techniques employed to derive the potential energy surface. They all fall into two major categories: *ab initio* and *empirical* methods. With the advents of computers, accurate ab initio methods are applicable to small molecules and empirical techniques are less used; we will briefly present them for completeness.

3.5.1 Introduction to Ab Initio Methods

The term "ab initio" is used to describe methods which calculate molecular properties by solving the Schrödinger equation without resorting to any empirical or experimental data. They are all based on the Born–Oppenheimer approximation. Under this approximation, the electronic wave functions and energies are determined by eq. (3.11), the Schrödinger equation for the Hamiltonian

$$\widehat{\mathscr{H}}^e = \widehat{\mathscr{T}}^e + \widehat{\mathscr{V}}^{ee} + \widehat{\mathscr{V}}^{ne}, \tag{3.15}$$

ignoring any relativistic effects of all kinds, which, if necessary, can be treated perturbatively. In this section we regard the nuclei fixed at a specific configuration and focus on the eigenproblem of the electronic Hamiltonian. For simplicity, we ignore the constant term V^{nn}, which must be added, though, to the electronic energies to provide the PES. Also, bear in mind that all calculations leading to the electronic energy must be repeated for a multitude of nuclear configurations and then a function should be fitted to these results to provide a continuous PES. The advances in computer speed and the improvements in molecular-orbital software made alternative approaches, which do not require the construction of a global potential energy surface, feasible. According to them, the potential and its derivatives can be computed by electronic structure calculations only on certain configurations dictated by the method used in solving the nuclear Hamiltonian or the classical equations of motion. For a recent review on these approaches see [83].

By dropping the term representing the interactions between the electrons, $\widehat{\mathscr{V}}^{ee}$, we can separate the electronic degrees of freedom and reduce $\widehat{\mathscr{H}}^e$ into a sum of N_e one-electron Hamiltonians, i.e.

$$\widehat{\mathscr{H}}^e \to \widehat{\mathscr{H}}^e_o = \sum_{i=1}^{N_e} \left[-\frac{\hbar^2}{2m_e}\nabla_i^2 - \frac{e^2}{4\pi\varepsilon_0} \sum_{j=1}^{N_n} \frac{\mathscr{Z}_j}{\left|\vec{R}_j - \vec{r}_i\right|} \right].$$

If we solve the Schrödinger equation $\widehat{h}\varphi = \epsilon\varphi$ for the one-electron Hamiltonian

$$\widehat{h}(\vec{r},\vec{p}) = \frac{\vec{p}^{\,2}}{2m_e} - \frac{e^2}{4\pi\varepsilon_0} \sum_{j=1}^{N_n} \frac{\mathscr{Z}_j}{\left|\vec{R}_j - \vec{r}\right|}, \tag{3.16}$$

we obtain the eigenfunctions $\varphi_k(\vec{r})$, called the *molecular orbitals (MO)*, and the eigenenergies ϵ_k, called the *molecular orbital energies*. Augmenting the molecular orbitals $\varphi(\vec{r})$ with the electron spin functions, $\sigma(s = \pm 1/2)$, we can derive the *spin–orbitals* $\phi(\vec{r}; s) \equiv \varphi(\vec{r})\sigma(s)$, the basis functions describing the full state of one electron. For a set of N_e electrons, the product

$$\prod_{i=1}^{N_e} \phi_{n_i}(\vec{r}_i; s_i),$$

where n_i is the quantum number of the spatial state occupied by the ith electron and s_i its spin projection, does not satisfy the *Pauli exclusion principle*. This principle, applied for electrons, requires the total wave function to be antisymmetric in the exchange of any two particles. This requirement is fulfilled by a particular combination of the (degenerate) basis functions, best formulated in the *Slater determinant*:

$$\Phi^e_{o\mathbf{n}}(\mathbf{r};\mathbf{s}) = \frac{1}{\sqrt{N_e!}} \begin{vmatrix} \phi_{n_1}(\vec{r}_1;s_1) & \phi_{n_2}(\vec{r}_1;s_1) & \cdots & \phi_{n_{N_e}}(\vec{r}_1;s_1) \\ \phi_{n_1}(\vec{r}_2;s_2) & \phi_{n_2}(\vec{r}_2;s_2) & \cdots & \phi_{n_{N_e}}(\vec{r}_2;s_2) \\ \vdots & \vdots & \vdots & \vdots \\ \phi_{n_1}(\vec{r}_{N_e};s_{N_e}) & \phi_{n_2}(\vec{r}_{N_e};s_{N_e}) & \cdots & \phi_{n_{N_e}}(\vec{r}_{N_e};s_{N_e}) \end{vmatrix}. \quad (3.17)$$

The corresponding eigenenergies are

$$E^e_{o\mathbf{n}} = \sum_{i=1}^{N_e} \epsilon_{n_i}.$$

The approach presented above, the *independent particle model*, does not provide an acceptable solution of eq. (3.11); nevertheless, it is useful as it serves as the starting point for the more sophisticated techniques described below.

In another step made in the ab initio methods, the molecular orbitals are expanded in a basis of N_b, suitably chosen, linearly independent, functions $\{\chi_1, \chi_2, \ldots, \chi_{N_b}\}$:

$$\varphi_i(\vec{r}) = \sum_{k=1}^{N_b} c_{ki}\chi_k(\vec{r}). \quad (3.18)$$

As the basis is necessarily finite, the above equation represents an approximation to the molecular orbitals; this is the *Linear Combination of Atomic Orbitals (LCAO)* approximation.

The basis set used to consist of functions localized on a nucleus and resembling the hydrogen atom wave functions

$$\chi(\vec{r}) \propto r^{n-1}Y_{lm}(\theta,\phi)e^{-\zeta r},$$

with suitably chosen ζ's, referred to as *Slater-type orbitals (STO)*. Modern basis sets use *Gaussian-type orbitals (GTO)*, functions of the form

$$\chi(\vec{r}) \propto x^{n_x}y^{n_y}z^{n_z}e^{-\zeta r^2}.$$

STO's are more accurate than GTO's but their exact computational treatment is cumbersome. To utilize, in some extent, the desired properties of both, a basis set may be constructed from a combination of n GTO's fitted to STO's; such are the STO-nG basis sets. Various other extensions and combinations of these basis sets are available to computational chemists. The double (DZ) or triple (TZ) zeta basis set uses two or three STO's per orbital to increase accuracy near the nucleus. Other sets were developed to include the valence shells so the accuracy at high energies is increased; for example, the basis $6-31G$ uses a single basis function for the core orbitals with six GTO's for each STO, and two sets for valence orbitals,

one with three GTO's per STO and the other, more diffuse, with one. Adding a set of d atomic orbitals for each non-hydrogen atom to account for polarization is indicated by a single asterisk in the basis name ($6-31G*$); a double asterisk implies that polarization functions are also used for hydrogen. Other orbitals with certain properties might be necessary when other quantities, apart from energy, are to be computed.

The modern quantum chemistry ab initio packages, such as GAUSSIAN98 [84], MOLPRO [85], GAMESS [86], offer a wide set of basis sets to the computational chemist to choose from.

3.5.2 Self-Consistent Field (SCF)

Substantial improvement on the previous treatment is the *Self-Consistent Field (SCF)* [87], or, in the limit where the number of basis functions is very large, the *Hartree–Fock (HF)* method. In these, the interaction between electrons is taken into account to some extent, as each particle is regarded as moving in a average field due to the other electrons in addition to the nuclear attraction. Apart from that, the electrons are oblivious to each other; the SCF method describes them with single-particle wave functions.

The (non-degenerate) ground electronic wave function is represented in SCF calculations by a single Slater determinant eq. (3.17), that is, the electrons are allowed to occupy a specific set of (parametric) spin orbitals, $\{\phi_1, \phi_2, \ldots, \phi_{N_e}\}$. The molecular orbitals in them are then expanded in the functions $\{\chi_1, \chi_2, \ldots, \chi_{N_b}\}$:

$$\varphi_i(\vec{r}) = \sum_{k=1}^{N_b} c_{ki}\chi_k(\vec{r}).$$

The Slater determinant, $\widetilde{\Phi}^e$, constructed with the orbitals $\{\phi_i\}$, depends on the coefficients $\{c_{ki}\}$. According to the variational principle, these coefficients can be determined by minimizing $E^e(\{c_{ki}\}) = \left\langle \widetilde{\Phi}^e \middle| \widehat{\mathscr{H}^e} \middle| \widetilde{\Phi}^e \right\rangle$ with respect to $\{c_{ki}\}$, subject to the conditions $\langle \phi_i | \phi_j \rangle = \delta_{ij}$ (which imply $\left\langle \widetilde{\Phi}^e \middle| \widetilde{\Phi}^e \right\rangle = 1$). At the critical set of the coefficients, $\widetilde{\Phi}^e$ approximates the correct ground state wave function, and $E^e(\{c_{ki}\})$ gives an estimate (actually, an upper limit) for the corresponding energy.

The exact mathematical treatment for the generic case laid out above, where a single set of spatial orbitals is used and no assumption is made on their occupancy, is quite complicated. It results into a system of integro-differential equations, the *Hartree–Fock equations*:

$$\begin{aligned} E_\nu \varphi_\nu(\vec{r}) \;=\; & \widehat{h}\varphi_\nu(\vec{r}) + \frac{e^2}{4\pi\varepsilon_0}\left[\sum_{\mu=1}^{N_e}\int_V \frac{\varphi_\mu^*(\vec{r}')\varphi_\mu(\vec{r}')}{|\vec{r}-\vec{r}'|}\,\mathrm{d}^3r'\right]\varphi_\nu(\vec{r}) \\ & - \frac{e^2}{4\pi\varepsilon_0}\sum_{\mu=1}^{N_e}(\sigma_\mu,\sigma_\nu)\left[\int_V \frac{\varphi_\mu^*(\vec{r}')\varphi_\nu(\vec{r}')}{|\vec{r}-\vec{r}'|}\,\mathrm{d}^3r'\right]\varphi_\mu(\vec{r}). \end{aligned} \tag{3.19}$$

$\widehat{h}$ is the one-electron Hamiltonian eq. (3.16), (σ_μ, σ_ν) the inner product of the spin parts of ϕ_μ, ϕ_ν, and ν runs from 1 to N_e.

In the equations above the first term in the right hand side represents the motion of individual electrons in the field due to the nuclei, the second is the electrostatic potential arising from the charge distribution of the N_e electrons and the third is the exchange energy and has no classical analogue; it accounts for the tendency of electrons with same spin to "avoid" each other. It also cancels an unphysical self-interaction for the electrons introduced by the second term. The quantity E_ν approximates, according to *Koopmans' theorem* [88], the ionization energy of the electron in ϕ_ν.

The Hartree–Fock equations eq. (3.19), can be cast into a simpler form if we utilize information on the spin orientation of the electrons and occupancy of the orbitals.

When closed-shell systems are studied, the ground state is singlet and all orbitals are doubly occupied with electrons of opposite spin. Therefore, $N_e/2$ distinct molecular orbitals are occupied and are used in the Slater determinant. The *restricted closed-shell Hartree–Fock (RHF)* theory which deals with this case, elaborates on eq. (3.19) deriving the *Roothaan–Hall* equations [89]:

$$\sum_{\nu=1}^{N_b}(F_{\mu\nu}-\epsilon_i S_{\mu\nu})c_{\nu i}=0, \qquad \mu=1\ldots,N_b. \tag{3.20}$$

In the equations above,

$$S_{\mu\nu}=\int_V \chi_\mu^*(\vec{r})\chi_\nu(\vec{r})\,\mathrm{d}V \equiv \langle\chi_\mu|\chi_\nu\rangle$$

is the overlap integral of the two atomic orbitals, ϵ_i the energy of the molecular orbital $\sum_{k=1}^{N_b} c_{ki}\chi_k$, and $F_{\mu\nu}$ are the elements of the $N_b \times N_b$ Fock matrix:

$$F_{\mu\nu}=\langle\chi_\mu|\,\widehat{h}\,|\chi_\nu\rangle + 2J_{\mu\nu}-K_{\mu\nu}, \tag{3.21}$$

with

$$J_{\mu\nu}=\sum_{\lambda=1}^{N_b}\sum_{\rho=1}^{N_b}(\mu\nu,\lambda\rho)P_{\lambda\rho}, \qquad K_{\mu\nu}=\sum_{\lambda=1}^{N_b}\sum_{\rho=1}^{N_b}(\mu\rho,\lambda\nu)P_{\lambda\rho} \tag{3.22}$$

the Coulomb and exchange matrices,

$$(\mu\nu,\lambda\rho)=\frac{e^2}{4\pi\varepsilon_0}\int_V\int_V \frac{\chi_\mu^*(\vec{r}_1)\chi_\lambda^*(\vec{r}_2)\chi_\nu(\vec{r}_1)\chi_\rho(\vec{r}_2)}{|\vec{r}_1-\vec{r}_2|}\,\mathrm{d}^3r_1\mathrm{d}^3r_2$$

the two-electron integrals, and

$$P_{\lambda\rho}=\sum_{k=1}^{N_e/2} c_{\lambda k}^* c_{\rho k}$$

the core density matrix element.

The ground state of many molecules can not be described by a closed-shell SCF wave function because, either the number of electrons is odd, or, certain orbitals are

singly occupied due to a spin coupling. This is the subject of the *restricted open-shell Hartree-Fock (ROHF)* theory. Following [90], we assume a molecular orbital set consisting of N_2 doubly occupied MO's and $N_1 = N_e - 2N_2$ singly occupied. Similar equations as in the previous case hold, with $(1 + N_1)$ Fock matrices, one for the core orbitals,

$$F^c_{\mu\nu} = f_c \langle\chi_\mu| \widehat{h} |\chi_\nu\rangle + \sum_{k=1}^{1+N_1} \left(a_{ck} J^k_{\mu\nu} + b_{ck} K^k \mu\nu \right),$$

and one for each of the N_1 open-shell orbitals,

$$F^i_{\mu\nu} = f_i \langle\chi_\mu| \widehat{h} |\chi_\nu\rangle + \sum_{k=1}^{1+N_1} \left(a_{ik} J^k_{\mu\nu} + b_{ik} K^k \mu\nu \right), \qquad (i = 1 \ldots, N_1).$$

In the equations above, f_i is the occupation for the ith orbital, having the values 1 or 1/2 if the orbital is doubly or singly occupied respectively; $a_{ij} = 2 f_i f_j$ and $b_{ij} = -f_i f_j$ with the added condition that $b_{ij} = -1/2$ if both i, j orbitals are singly occupied. The J, K matrices are given by eq. (3.22); the density matrices there, are also one for the core and N_1 for the singly occupied orbitals

$$P^c_{\lambda\rho} = \sum_{k=1}^{N_2} c^*_{\lambda k} c_{\rho k}, \qquad P^i_{\lambda\rho} = c^*_{\lambda i} c_{\rho i}.$$

Another approach to the generic problem is referred to as the *unrestricted Hartree–Fock (UHF)* theory. It is mathematically much simpler than ROHF and easier to use as a basis for correlated methods such as Møller–Plesset (§3.5.4). On the other hand, the wave function it produces is not an eigenfunction of the total spin $\widehat{\mathscr{S}^2}$ while the true electronic states are.

In UHF theory, two distinct sets of spatial orbitals are used, one for the electrons with $\sigma(+1/2) \equiv \alpha$ spin and the other for electrons having $\sigma(-1/2) \equiv \beta$ spin. They are represented with different coefficients on the same basis in the LCAO approximation:

$$\varphi^\alpha_i(\vec{r}) = \sum_{k=1}^{N_b} a_{ki} \chi_k(\vec{r}), \qquad \varphi^\beta_i(\vec{r}) = \sum_{k=1}^{N_b} b_{ki} \chi_k(\vec{r}).$$

The coefficients $\{a_{ki}, b_{ki}\}$ are varied independently yielding the *Pople–Nesbet* equations [91]:

$$\begin{aligned} \sum_{\nu=1}^{N_b} (F^\alpha_{\mu\nu} - \epsilon^\alpha_i S_{\mu\nu}) a_{\nu i} &= 0, \qquad \mu = 1 \ldots, N_b, \\ \sum_{\nu=1}^{N_b} (F^\beta_{\mu\nu} - \epsilon^\beta_i S_{\mu\nu}) b_{\nu i} &= 0, \qquad \mu = 1 \ldots, N_b. \end{aligned} \tag{3.23}$$

These equations obviously degenerate to the Roothaan–Hall equations, eq. (3.20), when the two sets of orbitals coincide, i.e. all electrons come in pairs.

The procedure to solve the equations produced by any of the above methods is iterative: An initial guess of the coefficients in the LCAO expansions of $\{\varphi_\nu\}$, is chosen; it should reproduce the physical characteristics and the general form of the desired wave function so the equations can converge to the correct electronic state. It should be noted that convergence is not mathematically guaranteed. With the initial wave functions, the integrals in eq. (3.19) or the Fock matrices in the other equations are computed and then the differential system or the generalized eigenfunction problem are solved for a new approximation to the coefficients; this process is repeated until the change in the coefficients in successive steps is negligible.

Closely related to HF methods is the *Generalized Valence Bond (GVB)* theory [90]. Without getting into details, in this theory each molecular orbital in closed-shell HF (RHF), which is occupied by two electrons, is replaced in the Slater determinant by two other orbitals which are non-orthogonal

$$\varphi_i(\vec{r}_1)\varphi_i(\vec{r}_2) \rightarrow \varphi_{i1}(\vec{r}_1)\varphi_{i2}(\vec{r}_2) + \varphi_{i2}(\vec{r}_1)\varphi_{i1}(\vec{r}_2).$$

The resulting determinant, the GVB-Perfect Pairing (GVB-PP) wave function, incorporates the mixing of ionic and covalent character for any bond. It overcomes this way the exclusion of electron correlation by the HF theory, producing more accurate results for many molecular properties.

While the SCF theory predicts adequate estimates for many properties of atoms and molecules, it is not comparable to experiment in reactions were bonds break and form (ionization, dissociation, isomerization), or, in general, away from equilibrium. The assumption of a single Slater determinant severely hampers the variational method to achieve a satisfactory approximation. Another shortcoming, inherent to the variational method, is that, in practice, it is very difficult to derive excited states. On the other hand, the SCF method is *size-extensive*; it means that the energy relative error in the calculations increase linearly with the number of particles in the molecule. A special case of this property is the *size-consistency*: if we perform separate SCF calculations with a certain basis for two non-interacting molecules and add the ground energies, the result will be, as expected, the same as if we made one SCF calculation with the same basis for the system of the two molecules. Another advantage of SCF, in comparison to the other methods we present below, is that it requires less computer resources (CPU time and memory).

Numerous variations have been developed to address the drawbacks and extend the standard SCF method. A mention should be made to semi-empirical methods which address the main time-consuming step of SCF computation, the one- and two-electron integrals. In these methods, most of the integrals are neglected and others are approximated by parametric functions; the parameters are such that experimental data are reproduced. Below, the most notable ab initio methods building on SCF are presented.

3.5.3 Configuration Interaction (CI)

Electron correlation effects left out of an SCF calculation can be taken into consideration by extending the trial wave function in the SCF method from a single Slater

determinant to a sum of determinants formed by different sets of orbitals. This way, the "contamination" by the actual excited electronic states inherent in the SCF wave function is canceled out yielding a better approximation to the ground level. Let us limit the discussion in the RHF method; similar remarks hold for the others.

We note that solving the Roothaan–Hall equations eq. (3.20), N_b eigenvalues and eigenvectors are produced, that is, equal in number to the LCAO basis. Therefore, N_b different molecular orbitals are determined while the Slater determinant is formed by only $N_e/2$ functions. The orbitals used in the determinant are the *occupied* ones, while the rest are called *virtual* orbitals. From the N_b MO's we can construct $\binom{N_b}{N_e/2}$ Slater determinants. The configurations in which one occupied orbital from the SCF determinant is replaced by a virtual, are characterized as *single excitations*; the substitution of two occupied orbitals by virtual ones yields doubly excited configurations. In practice, we choose $N_b \gg N_e$ so the number of constructible determinants is quite large. In a *Configuration Interaction (CI)* calculation, the SCF result is used to construct N_s suitably chosen Slater determinants $\{\Phi_i^{(SCF)}\}$; the wave function in the electronic Schrödinger equation, eq. (3.11), is represented by a superposition of these:

$$\Phi^{(CI)} = \sum_{i=1}^{N_s} c_i \Phi_i^{(SCF)}.$$

If we choose the maximum N_s then the CI calculation is characterized as *full*; normally, computational restrictions do not allow this magnitude of calculations.

Eq. (3.11) can be cast into an eigenvalue problem, yielding the energies and the coefficients in the expansion above. This way, we can determine an approximation to the first N_s electronic levels. *MacDonald's theorem* [92] guarantees that the eigenenergies in ascending order provide an upper limit for the respective energy levels.

The CI technique converges very slowly but it can yield results very close to the experimentally deduced for small molecules. The exact solution would require an infinite basis set for the LCAO expansion ($N_b \to \infty$), and an infinite number of Slater determinants ($N_s \to \infty$) in the CI wave function; both requirements cannot be met in actual computations.

It can be shown that single excitations do not improve by themselves the SCF wave function with respect to electron correlation; double (or higher) do. Accordingly, the variant mostly used in actual calculations is the *configuration interaction with single and double excitations (CISD).* Although computationally tractable, the CISD method is not size consistent (cf. SCF method). An approximate way to correct this deficiency is to introduce the Davidson correction [93],

$$\Delta E = (1 - c_0^2) E_{SD},$$

where c_0 is the coefficient of the SCF wave function in the normalized CISD wave function and E_{SD} the correlation energy computed by CISD. Another approach to make the CISD size consistent was suggested in [94]. The *Quadratic Configuration Interaction (QCISD)* method is formed by the addition of higher excitation terms, quadratic in the expansion coefficients, which enforce size consistency.

A detailed presentation of CI methods can be found in [87]. Below, we briefly describe three extensions and variants of the CI method, which were employed in the PES calculation of the molecules we studied: the *Complete Active-Space Self-Consistent Field (CASSCF)*, the *Multi-reference Configuration Interaction (MRCI)*, and the *Coupled Cluster (CC)* method.

In **CASSCF**, the trial wave function is a multi-configuration expansion constructed as in CI by a set of molecular orbitals, which, in turn, are expanded in the LCAO basis. Both sets of coefficients are optimized in a CASSCF calculation leading to a fully optimized wave function.

MRCI generalizes the CI method in the sense that a CASSCF result is used instead of plain SCF. The constructed MRCI wave function is a multi-configuration expansion on wave functions obtained by applying on a previous CASSCF result the excitation operators from occupied orbitals to unoccupied ones.

The **CC method** is another size-consistent technique to incorporate electron correlation. It approximates the electron wave function by a sum of ground and excited configurations in the following manner:

$$\Phi^{(CC)} = e^{(\widehat{T}_1+\widehat{T}_2+\cdots)}\Phi^{(SCF)}.$$

$\widehat{T}_i$ on the SCF wave function produces a linear combination of all ith-order excitations. The first terms in the expansion of the exponential, $1+\widehat{T}_1+\widehat{T}_2+\cdots$, applied on the SCF result give a wave function similar to CI. The exponential operator is used to ensure the size-consistency of the calculation; for example, the CCSD method, which includes single and double excitations, applied on two separate molecules A,B with SCF wave functions Φ^A, Φ^B, yields

$$e^{(\widehat{T}_1^A+\widehat{T}_2^A)}\Phi^A e^{(\widehat{T}_1^B+\widehat{T}_2^B)}\Phi^B = e^{(\widehat{T}_1^A+\widehat{T}_2^A+\widehat{T}_1^B+\widehat{T}_2^B)}\Phi^A\Phi^B.$$

The right hand side is the wave function which is constructed in the CCSD method if the two non-interacting molecules are treated as a system. Quasi-perturbative treatment of the connected triples (T) and quadruples (Q) leads to the CCSD(T) and CCSD(TQ) approaches.

A method closely related to CCSD is Brueckner Doubles [95], which uses the Brueckner orbitals rather than the HF orbitals for a CCSD treatment. The Brueckner orbitals are defined as the set of orbitals for which the single excitation coefficients are zero. The theory is slightly more computationally intensive but more accurate than CCSD.

The applicability of the MRCI and CCSD methods, scaling from N_e^5 to N_e^8, is limited by the molecule size.

3.5.4 Møller–Plesset Perturbation Theory (MP)

A common form of many-body perturbation theory, the *Møller–Plesset (MP)* theory [96], is a size-consistent method which treats the deviation of the electron repulsion from the average field of the SCF calculation as perturbation. The zeroth order Hamiltonian is the sum of the one-electron Fock operators: $\widehat{\mathscr{H}_0} = \sum_i F^i$; F^i is the Fock operator acting on the ith electron. The perturbation is then $\widehat{\mathscr{H}^e} - \widehat{\mathscr{H}_0}$. The

zeroth approximation in the wave function is the SCF Slater determinant (which is an eigenfunction of $\widehat{\mathscr{H}_0}$) and its energy is the sum of the energies of the occupied orbitals. The energy including the first correction is the SCF prediction and from the second order the electron correlation appears. The approximations mostly used are the MP2 and MP4 levels, keeping up to the second and fourth order in the expansion, respectively. MP3 and MP5 have additional computational cost, compared to MP2 and MP4 respectively, without substantial improvements on accuracy over them.

It was shown that the convergence of the MP series is slow when bonds are stretched or when a UHF wave function with high spin contamination is used.

A variant of MP2 is the *Complete Active-Space Perturbation Theory at second order (CASPT2)*. This method uses a multi-reference CASSCF zero-order wave function.

3.5.5 Density Functional Theory (DFT)

Density Functional Theory (DFT) [97] is a method developed initially by solid-state physicists. It is not strictly an ab initio method as it does not solve directly the Schrödinger equation. Instead, it is based on a theorem by Hohenberg and Kohn [98], which states that the knowledge of the electron density of a system in its ground state is enough to determine the energy. The exact electron density has cusps in the positions of the nuclei and its gradient yields the charges of the nuclei. This information is in principle sufficient to derive the Hamiltonian and the energy, thus justifying the Hohenberg–Kohn theorem. The energy is considered a functional of the electron density, which is proven to exist although the theory does not provide a specific form for it. Many functionals are proposed in the literature.

The method is computationally less demanding than CI-type theories as it does not calculate the molecular wave function, thus drastically reducing the dimensionality of the problem. DFT is presently restricted to the ground electronic state and is not guaranteed to converge as the variational techniques are. On the other hand, it scales with the number of electrons in a more favorable power law than CI methods, making it applicable to larger molecules.

Another form of DFT is based on Kohn–Sham theory [99] which derives similar equations to SCF theory, but with a local exchange potential as exchange contribution.

3.5.6 Empirical Methods

In empirical methods, the PES is derived by choosing a suitable function of a relatively simple form, to describe the interaction of atoms. This model potential depends on an adequate number of parameters which are fitted to experimental data or accurate ab initio calculations. The analytical forms commonly chosen are polynomial expansions or many-body functions.

Polynomial expansions are appropriate when a local representation of the PES is sought. If large amplitude motion away from a minimum is not relevant for the particular study of the system, then, around the stationary point, a Taylor series expansion of the potential energy in nuclear coordinates up to a certain order is a candidate function.

Many-body expansion, developed mainly by Murrell and co-workers [100], provides a global representation of the PES. The potential is represented as a sum of two-body, three-body,... terms. For example, the Sorbie–Murrell potential [101] for a triatomic molecule ABC expressed in bond coordinates $R_1 \equiv R_{AB}$, $R_2 \equiv R_{BC}$, $R_3 \equiv R_{AC}$ is formally

$$V(R_1, R_2, R_3) = V_{AB}(R_1) + V_{BC}(R_2) + V_{AC}(R_3) + V_{ABC}(R_1, R_2, R_3),$$

where V_{AB}, V_{BC}, V_{AC} the corresponding adiabatic diatomic potential curves. V_{ABC} is the three-body term having a relatively simple functional form such as

$$V_{ABC}(R_1, R_2, R_3) = \sum_{ijk} u_{ijk}\, s_1^i\, s_2^j\, s_3^k \prod_{m=1}^{3} \left[1 - \tanh\left(\frac{\gamma_m s_m}{2}\right)\right],$$

where s_i are the displacement coordinates. The coefficients u_{ijk}, γ_m are derived from experimental or ab initio data.

The most widely used diatomic terms are the Morse potential

$$V(R) = D\left(e^{-2a(R-R_e)} - 2e^{-a(R-R_e)}\right), \tag{3.24}$$

and the Lennard–Jones potential

$$V(R) = A\left[\frac{1}{2}\left(\frac{R_e}{R}\right)^{12} - \left(\frac{R_e}{R}\right)^{6}\right].$$

The former is appropriate for atoms which form a chemical bond, while the latter best fits the interaction of atoms for which a shallow van der Waals minimum exists in large internuclear separations. Variations of them are the Hulbert and Hirschfelder potential,

$$V_{HH} = D\left[\left(1 + g\rho^3 + h\rho^4\right) e^{-2a\rho} - 2e^{-a\rho}\right] \quad \rho \equiv R - R_e,$$

which improves the fit around the equilibrium R_e, and the Born–Meyer potential which amends the repulsive term in the Lennard–Jones potential, making it exponential because of its relationship to the overlap between the wave functions:

$$V(R) = Ae^{-BR} - CR^{-6}.$$

Another satisfactory candidate for a diatomic term is the Extended Rydberg function,

$$V(R) = -De^{-a_1\rho}\left(1 + a_1\rho + a_2\rho^2 + a_3\rho^3 + \cdots\right) \quad \rho \equiv R - R_e,$$

which can fit high derivatives of the potential. Morse and Rydberg functions do not reproduce the dispersion energy of the atoms in large distances so they are most usually augmented by including a R^{-6} term and possibly other powers of R^{-1}.

Semi-empirical potentials based on a simple quantum mechanical description of the electronic wave function and incorporating empirical parameters have been developed. Among them are the LEPS (London–Eyring–Polanyi–Sato) function and the one produced by the diatomics-in-molecules method. Also, many model potentials appropriate to specific molecular systems have been proposed.

3.6 The Nuclear Hamiltonian

The Born–Oppenheimer approximation allows us to describe the nuclear motion in a molecule via eq. (3.14). The assumption that the nuclei are not subject to external forces, or that these forces exist but their corresponding terms can be isolated in the potential, enables the complete extraction of the translational nuclear degrees of freedom from this equation. A further separation and reduction of the dimensionality for the remaining $3N_n - 3$ translation-free coordinates is desirable for all but the most trivial molecular systems; this can be achieved, in a greater or lesser degree, by separating the uniform rotation of the molecule as a whole from the vibration or internal motion (the relative, with respect to each other, motion of the nuclei). One should define

- an axis system, attached to the molecule and rotating with it, the *body-fixed* or *molecular axis* system,
- the coordinates which describe the rotation of this system with respect to the *laboratory axis* system, and
- the coordinates describing the vibrational motion of the nuclei in the body-fixed system.

All choices are equivalent in the sense that none alters the Schrödinger equation describing the molecule. However, particular choices can minimize (but never eliminate) the coupling of rotation and vibration coordinates, enabling the approximate separation of equations for each of the two sets.

The body-fixed system is usually a Cartesian axis frame originating at the molecular center of mass. Its orientation with respect to an inertial system originating at the same point is described by the three *Euler angles*, χ, ϕ, θ. The most common of the various definitions for them given in fig. (3.2). The relation of the coordi-

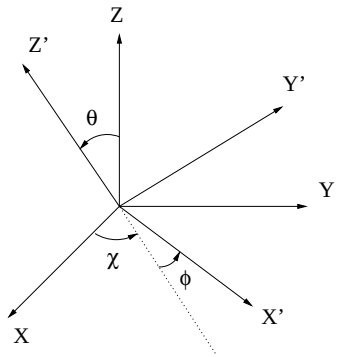

Figure 3.2: Definition of the Euler angles, χ, ϕ, θ. {X,Y,Z} are the axes of the laboratory system, {X',Y',Z'} are the axes of the body-fixed system. Both originate at the nuclear center of mass.

nates (X_i, Y_i, Z_i), (X_i', Y_i', Z_i'), of the ith nucleus in the laboratory system and the body-fixed system respectively, is

$$(X_i, Y_i, Z_i)^T = A(\phi, \theta, \chi)\ (X_i', Y_i', Z_i')^T$$

where

$$A(\phi,\theta,\chi) = \begin{bmatrix} \cos\phi & -\sin\phi & 0 \\ \sin\phi & \cos\phi & 0 \\ 0 & 0 & 1 \end{bmatrix} \cdot \begin{bmatrix} 1 & 0 & 0 \\ 0 & \cos\theta & -\sin\theta \\ 0 & \sin\theta & \cos\theta \end{bmatrix} \cdot \begin{bmatrix} \cos\chi & -\sin\chi & 0 \\ \sin\chi & \cos\chi & 0 \\ 0 & 0 & 1 \end{bmatrix}.$$

As we have already separated the translational motion by locating the origin of the laboratory system on the center of mass, the relation above extracts the three rotation coordinates and implies that from the $3N_n$ coordinates (X'_i, Y'_i, Z'_i), only $3N_n - 6$ are independent.[1] Therefore, we are allowed to define 6 (or 5) constraints on the (X'_i, Y'_i, Z'_i) in order to bring the kinetic term of the Hamiltonian in a more appropriate form. In the case of a nonlinear molecule in which the nuclei perform small vibrations around their equilibrium positions $\vec{R}'^{\,0}_i$, the *Eckart conditions* (see [71] or [102])

$$\sum_{i=1}^{N_n} M_i(\vec{R}'_i - \vec{R}'^{\,0}_i) = 0, \qquad \sum_{i=1}^{N_n} M_i(\vec{R}'_i \times \vec{R}'^{\,0}_i) = 0$$

achieve the maximum uncoupling of the nuclear degrees of freedom. Other choices or, even, other approaches are appropriate in the case of large amplitude motion; see, for example, [103, 104]. We will elaborate the vibrational coordinate systems in §4.2. Worth mentioning, without further analysis, is a novel aspect in the dynamics of multi-body systems: the realization that certain gauge fields play an important role in the elimination of degrees of freedom and in the description of the reduced dynamics [105].

After grouping in the nuclear Hamiltonian the rotation and the vibration coordinates, collectively denoted by Θ and q respectively, and the identification of the coupling terms, one should choose a basis set on which the eigenfunctions are to be expanded, according to the methods presented in §3.2.1. Usually, the set is constructed from the direct product of a pure rotation basis by a pure vibration set, which can be obtained from approximate solutions of the corresponding pure rotation and vibration problems. The *Wigner functions* $D^J_{KM}(\Theta)$ (see [106]), parametrized by the rotational angular momentum quantum number J, the magnetic quantum number M, and the vibrational angular momentum quantum number K, are used for the rotation basis, while the vibration set is comprised of products of harmonic oscillators for each of the normal modes. The rotation-vibration eigensolutions for weak coupling terms can be parametrized by the quantum numbers of the most dominant basis function in their expansion. However, the most interesting cases, exhibited in the molecules we studied, are those where this classification breaks down and new quantum numbers should be defined, such as the polyad number, or, even, new identification schemes ought to be devised.

The variational method is widely used in nuclear, atomic, molecular, and solid-state physics. The availability of powerful computers and efficient computational algorithms makes possible nowadays to diagonalize dense matrices with an order of at least 10^5, even with commodity hardware. Despite the advances in hardware and algorithms, as impressive as they may be, the variational method is incapable of treating fully anything but the very small molecules. The exponential growth of the size of the necessary basis set with the degrees of freedom has led to the development of techniques which do not call for the full diagonalization of a huge matrix. Such methods are the *Lanczos diagonalization scheme* [107] and other filtering algorithms [108], the *mean-field optimizations*, and the *diagonalization–truncation* methods [109]. The filtering methods compute selected eigenvalues and eigenvectors of a

[1] Note that in the special case of a linear molecule only two of the Euler angles act as independent rotation coordinates.

matrix, those inside a specific energy window. The algorithms of the second category optimize the basis sets in the framework of the mean-field approach we encountered in §3.5.1; this solves approximately a many-body problem by reducing it to a set of coupled one-body problems. The *vibrational self-consistent field (VSCF)* [110] and *vibrational multiconfigurational self-consistent field (VMCSCF)* [111] are such methods. We will outline the basic notion of the algorithms comprising the third class as it is the one used in the quantum treatment of the molecules we studied.

The diagonalization–truncation procedure progressively improves a basis set by spanning initially a portion of the configuration space. Separate Hamiltonian matrices are constructed for limited sets of degrees of freedom, they are diagonalized and the resulting set of eigenvectors is truncated based on a energy criterion. The coupling of different sets of degrees of freedom is progressively introduced. At each step, a new diagonalization is performed, followed by a truncation of the basis in ways that attempt to retain the information encoded in the coupling terms. The accuracy of the calculations on a certain contracted basis is tested by repeating the calculations with a different energy criterion.

A very powerful simplification of the variational calculation is also achieved by the *Discrete Variable Representation (DVR).* It was introduced by Light and coworkers (for a review see [109]) and it is widely used in the vibration-rotation literature. It was also employed in the molecules we studied. In this method, a trial wave function is expanded as a linear combination of N basis functions and the coefficients are determined to satisfy the Schrödinger equation at N particular points in the configuration space. This leads to a problem equivalent to the generalized diagonalization; its resolution produces eigenvalues, the energies, and eigenvectors, the coefficients. Alternatively, the trial function can be defined by its values at the N points of the grid. The two representations are related and by exploiting both one can usually derive sparse Hamiltonian matrices which can be efficiently diagonalized.

Another method worth mentioning is the *Morse Oscillator Rigid Bender Internal Dynamics (MORBID)* approach. It is a variational method developed by Jensen [103], specifically for "floppy" triatomic molecules, in order to describe highly excited vibrational states involving large amplitude bending motion.

The case of unimolecular dissociation and the calculation of resonances require special methods. Resonance energies and widths can be determined from an absorption spectrum which is calculated by solving the time–independent Schrödinger equation for a set of energy values and evaluating the overlaps of the corresponding continuum eigenstates with the initial wave function from which dissociation occurs [112]. This can be a time-consuming process as it requires a dense grid and the repeated solution of the Schrödinger equation for different energies. Additionally, the resonance position and widths are extracted through a fitted spectrum, a procedure that can be difficult and ambiguous.

Another method for the extraction of resonances, based on the variational principle of Kohn (see [113]), has been developed and applied to several molecules, including HCO [114] and DCO [115]. In brief, the coordinate space is divided in two regions, the inner and the outer, judging by the coupling between the product states. In the inner region, the Hamiltonian is expanded on a dense set of basis functions, developed through a general contraction–truncation scheme, and diagonalized. This

procedure is computationally demanding but is performed once for all wave functions as the basis set is energy–independent. As a by-product, the bound states and their energies are determined at this step. In the outer region where the coupling between the products is assumed to be small, the time–independent Schrödinger equation is solved quite fast by direct integration for each value of energy. Matching the wave functions at the boundary of the two regions results in algebraic equations which, when solved, determine uniquely the wave function.

More recently, two other methods for calculating resonance energies and widths have been implemented and applied to HCO. The *artificial boundary inhomogeneity method* of Jang and Light [116] relies on a simple modification of the time-independent Schrödinger equation. An inhomogeneity B_i is introduced rendering the equation in the form $(\widehat{\mathscr{H}} - E)^{-1} B_i = \Phi_i$. The correct eigenfunction Φ_i is the solution in the region where $B_i = 0$. Scattering information can be deduced by imposing appropriate boundary conditions on a linear combination of the Φ_i. For details on the procedure see [117]. Poirier and Carrington [118] devised a complex–symmetric version of the *preconditioned inexact spectral transform*, which uses an iterative linear solver to compute inexact Lanczos vectors for $(\widehat{\mathscr{H}} - E)^{-1}$ and then diagonalizes the augmented, complex Hamiltonian in the basis they form. This last method offers many advantages over the alternatives and it was shown to derive more accurate results for HCO than any other previously applied.

3.7 Experimental Techniques

In recent years, huge progress took place in experimental spectroscopy mainly due to instrumental and technical advances. It is today possible to record a number of overtone transitions in polyatomic species with the sensitivity, resolution and simplification required to perform high-resolution investigations, despite their very low intensities and high densities.

Let us briefly present the *Franck–Condon principle* which controls whether a transition is observed in the experimental spectrum and, consequently, which states are accessible. The intensities of the spectral lines in the electric dipole transition are proportional to the absolute square of the matrix element between the initial and final states of the electric dipole moment operator. Assuming that the electronic redistribution is orders of magnitude more rapid than the nuclear motion, the wave functions are separable into an electronic and a nuclear part. In the dipole moment matrix element for a transition between states belonging to different electronic levels, the overlap integral of the initial and final vibrational wave functions can be, in the first approximation, factored out. The $\left|\left\langle \psi_{vib}^{(f)} \middle| \psi_{vib}^{(i)} \right\rangle\right|^2$ term is the *Franck–Condon factor*; a symmetry dictated zero value renders a transition *forbidden*.

The most widely used methods to record experimental spectra of the molecules our group studied are the *Stimulated Emission Pumping (SEP)* and *Dispersed Fluorescence (DF)* spectroscopies. They are double-resonance techniques, very useful in the investigation of highly excited vibrational levels of polyatomic molecules in the electronic ground state [119]. Both are variants of *Laser–Induced Fluorescence (LIF)* which relies on the detection of radiation emitted by a molecule after the absorption of light photons with appropriate energies. High-resolution direct absorption spec-

troscopic methods are sensitive primarily to the stretch overtone states; unfavorable Franck–Condon factors inhibit probing highly excited bending states. The SEP and DF techniques are based on electronic transitions and, therefore, can give access to complementary classes of states involving high excitation in bending. This characteristic makes them ideal for the experimental study of the isomerization process. Moreover, in the case of molecules with an inversion center, the electronic emission samples gerade vibrational levels while direct overtone spectroscopy can access mostly ungerade levels.

In the SEP technique, a first laser promotes the molecule to a single rovibrational level of an electronically excited state, while a tunable dye laser stimulates the emission down to one or more particular vibrational levels of the ground electronic state. Because the initial and final electronic states often have quite different equilibrium structures, the initial rovibrational level may overlap substantially with many in the ground state, and probe them all. The spectral resolution which is achieved in this process is ~ 0.03 cm^{-1}. The SEP spectrum is measured as a decrease of the side fluorescence when the dump beam causing the stimulated emission is scanned. However, only a very narrow energy range (~ 20 cm^{-1}) can be sampled in a single scan and, in addition, the accurate measurement of relative intensities is very difficult; they are usually corrupted by experimental artifacts. DF is a suitable alternative to SEP when high resolution is not necessary. It involves a spontaneous emission from the excited state allowing a much easier and quicker coverage of large spectral regions but with much lower resolution. This fact is not necessarily a disadvantage because low resolution spectra contain information exclusively relevant to the early time dynamics of the perfectly specified and initially localized state that is prepared by short-pulse excitation. DF spectra give us an overview of the vibrational spectrum in the ground state and reveal the most important anharmonic effects, complementing the more detailed SEP spectra.

One should mention another spectroscopic technique employed in addition to DF and SEP. In the *Resonance-Enhanced Multiphoton Ionization (REMPI)*, a molecule is excited by a laser to some intermediate state and, even before it predissociates, it is ionized by another photon. The ion (or, equivalently, the electron) intensity reflects the energy levels of the intermediate state.

In order to reproduce the spectrum, the spectroscopists construct an *effective* (or *resonance*) Hamiltonian matrix. The diagonal terms of it are given as an expansion in the quantum numbers (*Dunham expansion*). For example, for a system with 3 normal modes and zero angular momentum this reads

$$\langle v_1, v_2, v_3 | \, H \, | v_1, v_2, v_3 \rangle = \sum_{i=1}^{3} \omega_i v_i + \sum_{i=1}^{3} \sum_{j=i}^{3} x_{ij} v_i v_j + \sum_{i=1}^{3} \sum_{j=i}^{3} \sum_{k=j}^{3} y_{ijk} v_i v_j v_k + \cdots \ .$$

The spectroscopic constants $\omega_i, x_{ij}, y_{ijk}, k, k_i, \ldots$ are determined by the spectrum through the fitting procedure.

In case where a systematic degeneracy exists, such as a 1:2 Fermi resonance between the first and second mode, the quantum numbers v_1, v_2 are not separately conserved while the *polyad* number, $P = v_1 + 2v_2$ is. The Fermi resonance couples levels in the basis of harmonic oscillator products with the same values of P and v_3;

off-diagonal terms should be considered in the effective Hamiltonian. These can be given as

$$\langle v_1, v_2, v_3 | \, H \, | v_1 + 2, v_2 - 1, v_3 \rangle = \\ - (v_1 + 2)\sqrt{v_2} \left(k + \sum_{i=1}^{3} k_i v_i + \sum_{i=1}^{3} \sum_{j=i}^{3} k_{ij} v_i v_j + \cdots \right).$$

Assuming no interpolyad coupling, the block-diagonal effective Hamiltonian matrix is diagonalized to give an estimate on the energy levels.

3.8 Semiclassical Treatment

The semiclassical approach is quite similar to the experimental one. Because it is quite difficult to formulate a general procedure for arbitrary PES, this method resorts to the construction of an effective Hamiltonian function in action-angle variables. It is assumed that all couplings of the normal modes are negligible except for specific terms such as a Fermi resonance inherent to the system. The resonance Hamiltonian for a system of f degrees of freedom, exhibiting a 1:2 Fermi resonance among the first two modes, is written as a sum of the Dunham expansion, H_D, and the Fermi coupling, H_F, which, for zero vibrational angular momentum, are

$$\begin{aligned} H_D &= \sum_{i=1}^{f} \omega_i I_i + \sum_{i=1}^{f} \sum_{j=i}^{f} x_{ij} I_i I_j + \sum_{i=1}^{f} \sum_{j=i}^{f} \sum_{k=j}^{f} y_{ijk} I_i I_j I_k + \cdots \\ H_F &= 2 I_1 \sqrt{I_2} \cos(2\phi_1 - \phi_2) \left(k + \sum_{i=1}^{f} k_i I_i + \sum_{i=1}^{f} \sum_{j=i}^{f} k_{ij} I_i I_j + \cdots \right). \end{aligned}$$

The parameters are fitted to experimentally measured or calculated quantities.

The quantities $(\mathbf{I}, \phi)$ are action-angle-like set of conjugate coordinates built on dimensionless normal coordinates $(\mathbf{q}, \mathbf{p})$ according to

$$I_i = \frac{q_i^2 + p_i^2}{2}, \qquad q_i = \sqrt{2I_i}\cos(\phi_i), \qquad p_i = -\sqrt{2I_i}\sin(\phi_i).$$

The inclusion of a built-in Fermi resonance, which is only approximate in the actual system, offers to the quantum version of the effective Hamiltonian a built-in conserved quantity, the polyad number $P = v_1 + 2v_2$, in addition to v_3. For a system of 3 degrees of freedom with an inherent resonance, an appropriate choice of action-angle variables leads to two classical constants of motion and an effective one-dimensional problem parametrically dependent on them. The system is suitable for quantization through the EBK rule, eq. (2.22), thus reconstructing the spectrum. A drawback in this approach is the fact that the resonance Hamiltonian cannot be decomposed in kinetic and potential operators, making ambiguous the relation of the generalized coordinates q_i to the real coordinates of the molecule.

The fixed points of this Hamiltonian in terms of the action-angle variables define periodic orbits in the space of dimensionless coordinates which are coupled by the

Fermi resonance. These orbits, characterized by the conserved quantum numbers, are sufficient for understanding the properties of the quantum wave functions as long as the third mode remains decoupled. Both qualitative and quantitative results can be derived by analyzing the system through these periodic orbits. The fact that the classical equations of motion can be solved analytically and the trajectories can be calculated and analyzed for each set of quantum numbers, makes the semiclassical approach, though artificial in a sense, advantageous in certain aspects compared to the classical treatment.

Chapter 4

Algorithms and Techniques

4.1 Introduction

The analysis of certain features of the molecular vibrational spectra in the context of classical mechanics, calls for the location of periodic orbits and their continuation with respect to variations in energy. Their bifurcations should also be located, identified, and continued. In this chapter we will present the algorithmic procedures followed to achieve these tasks. Schematically, the Hamilton equations of motion are integrated for a specific time T. The set of initial conditions should be chosen such that the distance of the final point in the phase space from the initial one approaches zero. The trajectory traced out is then a periodic orbit with period T. The choice for the tentative period T is of the order of the time scale of the vibrational motions in the system. This procedure can be treated as a root-finding or a minimization problem. The integration of the differential equations defines a system of implicit nonlinear equations with the initial conditions acting as the unknowns. Alternatively, the differences of the corresponding components in the initial and final points can be zeroed by employing minimization techniques to calculate the appropriate initial point. It turns out that an optimization method is more robust compared to a root-finding one in the search of an unstable orbit.

In both classes of root-finding and minimization problems, the appropriate guess of the initial point is crucial to the success of the algorithms. We mentioned in §2.3.2 the Weinstein–Moser theorem which provides tentative conditions for periodic orbits in the vicinity of an equilibrium or a stationary point. Apart from these orbits, many others exist, especially in high energies, emanating from a saddle–node bifurcation; no theorem provides a definite and—more importantly—practical prediction of their location or periods. A painstaking trial-and-error search in the region of "kinks" in the potential or at the vicinity of a qualitative change in a family of periodic orbits is one way to find periodic orbits. In this chapter we will also present another technique which pinpoints initial guesses based on *Genetic* Algorithms. They belong to the novel class of the *Evolutionary* Algorithms, and are emerging as valuable tools to computational scientists, applicable wherever a random-like selection based on a property is necessary. The conventional methods (gradient descent, simplex, variational methods) are inherently inefficient in cases when multiple extrema need to be determined; apart from the periodic orbit location problem, protein folding

in Biology, the determination of structure of atomic clusters in Chemical Physics or crystals in Solid State Physics are such cases. Simulated Annealing and Genetic Algorithms are being applied with, sometimes, spectacular results on such problems.

The application of the implicit function theorem of §2.3.5 to the Poincaré mapping, ensures that, away from bifurcations, an isolated periodic orbit survives a slight change in the energy of the system and remains unique. By this, continuation/bifurcation diagrams can be constructed in order to organize the periodic orbits into families and expose the dependence of their periods on energy. The application of this procedure will be discussed below.

In the following sections we will lay out the coordinate systems used, present the corresponding Hamiltonian functions, and explain the integration algorithm. We will elaborate on the method we used to construct and solve the nonlinear systems of equations. We will also formulate the minimization problem and describe the optimization algorithms employed. The introduction to genetic algorithms will be given at the end of this chapter. All computations were performed by our code in C or FORTRAN 77 and FORTRAN 95 programming languages and the following libraries or packages: various codes from Numerical Recipes [120] and LAPACK [121], CVODE [122] for the integration of ordinary differential equations, FFTW [123] for Fourier analysis, an updated version of POMULT [124] for the continuation and stability analysis of periodic orbits, and PGAPACK [125] for the search of initial conditions and optimization based on Genetic Algorithms.

4.2 Coordinate Systems

In principle, any set of coordinates can be used to describe a molecular configuration. In practice, the choice of the algorithm employed to treat the classical or quantum problem, its outcome and the precision of the results, are determined by the particular set of coordinates used. These sets fall in general into two classes: the *curvilinear* and *rectilinear* coordinates. The former is comprised of internal coordinates, defined in terms of the bond stretchings and the bond angles. These, in conjunction with coordinates pertaining to the overall molecular motion, can be meaningfully applied to small systems, offering a high chemical flavor in describing the molecular vibrational problem. The latter class consists of the projections onto a fixed Cartesian frame of the internal coordinates. The Cartesian position vectors or the normal mode coordinates, specific linear combinations of Cartesian displacements which diagonalize the quadratic part of the potential and kinetic energy, fall into this category.

Cartesian coordinates with respect to the molecular center-of-mass are suitable for large polyatomic species as they render the Hamiltonian in a particularly simple form. On the other hand, by using internal coordinates we can get a lot of insight into how the different motions of the atoms in the molecule contribute to the internal energy flow. The choice of a particular set of internal coordinates is based on the configuration space to be sampled, the relative atomic masses, the excitation energies, and the coupling strength between the nuclear degrees of freedom.

Various internal coordinate systems with specific properties have been proposed, tailored to particular types of molecules or Potential Energy Surfaces (PES). For

example, *bond–angle* coordinates, the set of bond distances and bending angles, is an obvious choice for describing moderate amplitude vibrational motion in the vicinity of a PES minimum. *Local-mode* coordinates, simple internal coordinates which describe specific vibrations and ensure that the diagonal anharmonicity parameter exceeds the non-diagonal coupling strength, are appropriate for problems related to overtone spectroscopy. *Jacobi* vectors, describing the position of a given nucleus with respect to the center of mass of a set of nuclei or *Radau* coordinates which define the positions of a set of light nuclei with respect to a heavier one, are suitable for molecules exhibiting large amplitude vibrations or in the study of dissociation. Special sets of coordinates can be also employed in systems with symmetries or with special features in order to exploit them. Other systems can be defined as specific functions of the bond stretchings and bending angles, adapted to particular problems or algorithms, or optimized to improve the separability of nuclear degrees of freedom. For a detailed investigation on coordinate systems offering separability see [126]; for an overview of coordinate sets applied to molecules see [2].

Let us present the coordinate sets we applied to the systems we studied. The triatomic molecules we dealt with were considered as non-rotating. This, along with the extraction of the center-of-mass motion, reduces by 6 the degrees of freedom. The remaining three independent coordinates describing the plane configuration of a general, nonlinear ABC molecule can be, among others, the Jacobi set, the valence coordinates or the bond distances as defined in fig. (4.1). The formulas relating the various sets of coordinates can be easily derived from it.

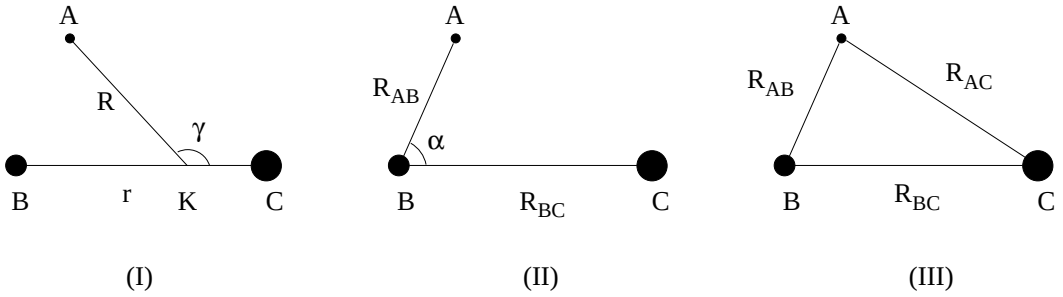

Figure 4.1: Coordinates for an ABC triatomic molecule: (I) Jacobi, (II) valence, (III) bond distances. K indicates the B–C center-of-mass.

The Jacobi set are the (R,r,γ) coordinates, where R is the distance of atom A from K, the mass center of B and C atoms, r is the distance of B and C, and γ is the $\widehat{AKC}$ angle, ranging from 0 to π rad. This set is the most natural in describing a unimolecular dissociation process, a non-reactive scattering of an atom by a diatomic molecule, a Van der Waals complex where one atom is weakly bound to a diatom, or, in general, in cases where the motion of atom A is largely decoupled from the motion of the other two. The Hamiltonian function expressed in Jacobi coordinates reads

$$\mathcal{H}(R,r,\gamma,P_R,P_r,P_\gamma)=\frac{P_R^2}{2\,m_R}+\frac{P_r^2}{2\,m_r}+\left(\frac{1}{m_R R^2}+\frac{1}{m_r r^2}\right)\frac{P_\gamma^2}{2}+V(R,r,\gamma),$$

where P_R, P_r, P_γ are the conjugate momenta of R, r, γ and

$$m_R = \frac{m_A(m_B + m_C)}{m_A + m_B + m_C}, \qquad m_r = \frac{m_B\, m_C}{m_B + m_C}$$

the reduced masses for the (A,BC) and (B,C) systems.

The valence coordinates are comprised of the AB and BC bond distances R_{AB} and R_{BC}, and the angle α between them. They are most appropriate for analyzing the low vibrational states of a molecule as the potential expressed in them is quadratic in small displacements from the equilibrium (ΔR_{AB}, ΔR_{BC}, $\Delta\alpha$). The Hamiltonian function in terms of R_{AB}, R_{BC}, α and their conjugate momenta P_{AB}, P_{BC}, P_α is

$$\begin{aligned}\mathcal{H}(R_{AB}, R_{BC}, \alpha, P_{AB}, P_{BC}, P_\alpha) &= \frac{P_{AB}^2}{2m_{AB}} + \frac{P_{BC}^2}{2m_{BC}} + \frac{P_{AB}P_{BC}\cos\alpha}{m_B} \\ &- \frac{P_\alpha \sin\alpha}{m_B}\left(\frac{P_{AB}}{R_{BC}} + \frac{P_{BC}}{R_{AB}}\right) + \left(\frac{1}{2m_{BC}R_{BC}^2} + \frac{1}{2m_{AB}R_{AB}^2} - \frac{\cos\alpha}{m_B R_{AB} R_{BC}}\right) P_\alpha^2 \\ &+ V(R_{AB}, R_{BC}, \alpha),\end{aligned}$$

where

$$m_{AB} = \frac{m_A\, m_B}{m_A + m_B}, \qquad m_{BC} = \frac{m_B\, m_C}{m_B + m_C}$$

the reduced masses for (A,B) and (B,C) systems.

The bond coordinates, R_{AB}, R_{AC} and R_{BC}, treat all atoms on equal footing and express the PES and other properties in a physically meaningful manner. A drawback which makes their use cumbersome is that they are not independent, in the sense that they must satisfy the triangle inequalities, $R_{AB} \leq R_{BC} + RAC$ and permutations in it. To overcome this, other sets of coordinates have been proposed, offering the equivalent treatment of the atoms; hyper-spherical systems are among them. These coordinate sets are mass-weighted and, therefore, not easily related to the geometric shape of the molecules they describe. Perimetric coordinates [127] remedy this.

Let us also give here the Hamiltonian operator for a triatomic molecule in Jacobi coordinates:

$$\widehat{\mathscr{H}} = \left[-\frac{\hbar^2}{2m_R}\frac{\partial^2}{\partial R^2} - \frac{\hbar^2}{2m_r}\frac{\partial^2}{\partial r^2} + \frac{\hbar^2}{2m_R R^2}\,\widehat{\ell}^{\,2} + \frac{\hbar^2}{2m_r r^2}\,\widehat{j}^{\,2} + V(R, r, \gamma)\right] Rr, \quad (4.1)$$

where m_r, m_R are the reduced masses of B–C and A–BC respectively. $\widehat{\ell}$ is the orbital angular momentum operator associated with the motion of the A atom with respect to the center of mass of BC and $\widehat{j}$ is the rotational angular momentum operator pertaining to the BC diatom. The total angular momentum of the molecule is conserved; to account for this, we can employ the relevant operator $\widehat{\mathscr{J}}$ and replace $\widehat{j}$ by $\widehat{\mathscr{J}} - \widehat{\ell}$. Some straightforward algebra yields eq. (4.1) in the form

$$\begin{aligned}\widehat{\mathscr{H}} \;=\; &\left[-\frac{\hbar^2}{2m_R}\frac{\partial^2}{\partial R^2} - \frac{\hbar^2}{2m_r}\frac{\partial^2}{\partial r^2} + \frac{\hbar^2}{2m_R R^2}\,\widehat{\ell}^{\,2}\right. \\ &\left. + \frac{\hbar^2}{2m_r r^2}\left(\widehat{\mathscr{J}}^{\,2} + \widehat{\ell}^{\,2} - \widehat{\mathscr{J}}_+\widehat{\ell}_- - \widehat{\mathscr{J}}_-\widehat{\ell}_+ - 2\,\widehat{\mathscr{J}}_z\widehat{\ell}_z\right) + V(R, r, \gamma)\right] Rr,\end{aligned}$$

where $\widehat{\mathscr{J}_\pm}$ and $\widehat{\ell_\pm}$ the appropriate raising and lowering operators and $\widehat{\mathscr{J}_z}$ and $\widehat{\ell_z}$ are the projections on the molecule-fixed z-axis. The eigenfunctions for this Hamiltonian are normalized with respect to the volume element $\mathrm{d}V = R^2 r^2 \sin\gamma \mathrm{d}R\mathrm{d}r\mathrm{d}\gamma$. This Hamiltonian was employed by our collaborators in the quantum calculations of the molecules we studied.

4.2.1 Integration of the Equations of Motion

The equations governing the evolution of the triatomic system, easily derived by eq. (2.6) and the appropriate Hamiltonian, are Ordinary Differential Equations (ODE) with initial conditions in a 6-dimensional space. Their general form is

$$\dot{\mathbf{x}} = \mathbf{f}(\mathbf{x}, t), \qquad \mathbf{x}(0) = \mathbf{x}_0. \tag{4.2}$$

Given the solution $\mathbf{x}(t_n)$ at a point t_n, the algorithms available for the integration of this type of systems compute an approximation to the solution at a point $t_n + h$, $\mathbf{x}(t_n + h)$. In our work we applied the Runge–Kutta family of algorithms to integrate eq. (4.2), an outline of which is given below. Other general methods are the *predictor–corrector* and *Bulirsch–Stoer* techniques [120] and their variants. The equations of motion of the molecular systems we studied are, at most, mildly stiff, so these methods suffice.

If the first $M-1$ derivatives with respect to t of the smooth vector field $\mathbf{f}$ in eq. (4.2) are known, we can approximate the solution at $t_n + h$, given the values $\mathbf{x}(t_n)$, by a truncated Taylor series:

$$\mathbf{x}(t_n + h) = \mathbf{x}(t_n) + \sum_{m=1}^{M} \frac{h^m}{m!} \mathbf{f}^{(m-1)}(\mathbf{x}(t_n), t_n) + \mathscr{O}(h^{M+1}).$$

Normally, it is very hard to compute the derivatives; they can be approximated instead by values of $\mathbf{f}(z_i)$ at various points along the step h: $z_{ni} = t_n + a_i h$, $i = 1, \ldots M+1$. The Taylor series becomes

$$\mathbf{x}(t_n + h) \simeq \mathbf{x}(t_n) + h \sum_{i=1}^{M+1} c_i \mathbf{f}(\mathbf{x}(z_{ni}), z_{ni}).$$

The appropriate selection of the coefficients a_i, c_i, the approximation of $\mathbf{x}(z_{ni})$, and the order M can yield an error term of the order of h^{M+1}. The Runge–Kutta algorithms define $a_1 = 0$ and expand $\mathbf{x}(z_{ni})$ as follows:

$$\mathbf{x}(z_{ni}) = \mathbf{x}(t_n) + h \sum_{j=1}^{i-1} b_{ij}\, \mathbf{f}(\mathbf{x}(z_{nj}), z_{nj}) \qquad i > 1.$$

Various sets of the a_i, c_i, b_{ij} coefficients and the order M have been proposed. We have used the fifth order Runge–Kutta–Fehlberg algorithm with the set of coefficients derived by Cash and Karp [128], reproduced in [120] §16.2. It offers the additional advantage of the adaptive stepsize control. An error estimate $\boldsymbol{\Delta}_n$, given by

$$\boldsymbol{\Delta}_n = h \sum_{i=1}^{6} (c_i - \tilde{c}_i) \mathbf{f}(\mathbf{x}(z_{ni}), z_{ni}),$$

can be used to modify the step h to attain the accuracy one seeks. The coefficients $\tilde{c}_i$ and more on Runge–Kutta methods can be found in [120].

An important class of algorithms comprises the *symplectic integrators* (see, for example, [129]) which rigorously preserve specific properties of the system during the integration such as the constraints, the reversibility, the integrals of motion (energy, orbital momentum, angular momentum, etc.). Symplectic integrators have been proved more stable than "general" methods for Hamiltonian systems [130].

4.3 Continuation/Bifurcation Diagrams

A very helpful tool to visualize the dependency of periodic orbits on energy and the way bifurcations are organized is the *Continuation/Bifurcation Diagram* (or *Diagram of Characteristics*). It depicts the variation of the period with respect to energy, or, in general, the evolution of a characteristic quantity related to a periodic orbit, such as a turning point (the maximum value of a coordinate), as energy changes. In such a diagram, the orbits are organized into continuous families stemming from stable equilibrium points or from bifurcations. The diagram is a direct fingerprint of the classical dynamics of a system; it facilitates the recognition of energy regimes in which interesting qualitative changes appear in the classical picture and consequently affect the quantum behavior. In subsequent chapters we will attempt to extrapolate classical quantitative and qualitative results to the quantum picture. We should always bear in mind that, due to the uncertainty relation between time and energy, only the structures in the Period–Energy continuation/bifurcation diagram having an area larger than $\hbar = 0.6582\ \text{eV} \cdot \text{fs}$ are meaningful.

The issue of locating periodic orbits is formally a two-point boundary value problem: the initial and final, after time T, points of a solution of eq. (4.2) should coincide:

$$\mathbf{x}(0) = \mathbf{x}(T).$$

Note that the unknowns are both the initial point and the period.

Several techniques have been proposed to solve this type of problem. In the *shooting method* [120], the boundary value problem above is converted to an *initial value* one. An initial point in the phase space is chosen, the differential equations are integrated for an appropriate time T and the final point is obtained. By varying the initial conditions, the difference of the two points can diminish yielding a periodic trajectory. In *relaxation methods* [120], the differential equations are replaced by difference equations on an appropriate mesh of points for the independent variable. An approximate solution is then iteratively varied to satisfy both finite difference equations and boundary conditions. *Collocation methods* with cubic spline interpolation of the periodic solutions of autonomous ordinary differential equations [131] are also an option. Another method can be based on the expansion of a tentative solution in a Fourier series; this could be considered as a a way to inherently satisfy the boundary conditions during the search as the orbit is by construction closed. Among the multitude of algorithms developed for location of periodic orbits in realistic dynamical systems worth noting are the characteristic bisection method [132], and the Newton–Picard scheme [133].

The technique we employed is the *multiple shooting method*. It attempts to incorporate the benefits of the relaxation algorithms in the shooting technique, thus improving the stability of integration in chaotic systems. In this method, the one-point initial value problem is converted to $(m-1)$ initial value problems by choosing m nodes in time along the period, the first and the last matching the initial and final times. The equations of motion are integrated to produce $(m-1)$ shorter trajectories. The initial conditions at each node (except the last) are the unknowns and a set of nonlinear implicit equations is formed if we require at each intermediate node the final point of the trajectory that ends there to match the initial point of the trajectory that starts from this node. This set is augmented by the boundary conditions to yield in total $N(m-1)$ equations of $N(m-1)$ unknowns, where N is the dimension of the phase space.

The continuation to higher or lower energies of a family of periodic orbits is relatively easy as long as an orbit in it has been located; any point of this orbit can serve as initial condition for a search with a slightly altered period which normally converges.

In order to determine the stability of a computed periodic orbit, the eigenvalues of the monodromy matrix (cf. §2.3.2) have to be evaluated. Recall that the linearized system around a periodic orbit $\mathbf{X}(t)$ is

$$\dot{\mathbf{y}}(t) = A(t)\mathbf{y}(t),$$

where $\mathbf{y}(t) = \mathbf{x}(t) - \mathbf{X}(t)$, $A_{ij} = \sum_k J_{ik} \left.\frac{\partial^2 \mathcal{H}}{\partial x_k \, \partial x_j}\right|_{\mathbf{x}=\mathbf{X}}$ and J is the matrix of the symplectic form, eq. (2.8). The monodromy matrix has the same eigenvalues with matrix $Z(t_0, t_0+T)$ in eq. (2.14). The latter can be calculated via its definition, $\mathbf{y}(t) = Z(t_0,t)\mathbf{y}(t_0)$, or as the solution for $t = t_0 + T$ of the variational equation eq. (2.15),

$$\dot{Z}(t_0,t) = A(t_0,t)Z(t_0,t)$$

with the initial condition $Z(t_0,t_0) = I$.

When the eigenvalues of Z indicate a bifurcation (cf. §2.3.5), a search along the corresponding eigenvectors for a periodic orbit with the predicted period is usually successful and a new branch of a family can be followed.

In the procedure described above, a set of nonlinear equations is constructed. It has the general form

$$f_i(x_1, x_2, \ldots, x_n) = 0, \qquad i = 1, \ldots n. \tag{4.3}$$

Various algorithms have been developed to solve it [120]. It could also be treated as an optimization problem if we take the sum of squares or absolute values of all f_i as a function to be minimized. Below, we outline the algorithms we used to solve this type of problems in both approaches.

4.3.1 Roots of Nonlinear Equations

The codes we employed in finding roots of a nonlinear system implemented the most common methods in the vast majority of problems: the *Newton–Raphson method* with backtracking and the *Broyden's method*. Both methods are iterative,

i.e. an initial guess is gradually improved towards the actual solution by repeated application of a procedure.

Newton–Raphson method

In the Newton–Raphson method, a set of n nonlinear functions $f_i(x_j)$ is expanded in a Taylor series up to the second order around the unknown solution $\{x_i^0\} \equiv \mathbf{x}^0$,

$$\begin{aligned} f_i(x_j) &= f_i\left(x_j^0\right) + \sum_{k=1}^{n} \frac{\partial f_i\left(x_j^0\right)}{\partial x_k}\left(x_k - x_k^0\right) + \cdots \Rightarrow \\ \mathbf{f}(\mathbf{x}) &\simeq \mathbf{J}(\mathbf{x}^0)\cdot(\mathbf{x}-\mathbf{x}^0) \qquad \Rightarrow \qquad \mathbf{x}^0 \simeq \mathbf{x} - \mathbf{J}^{-1}(\mathbf{x})\cdot\mathbf{f}(\mathbf{x}) \end{aligned}$$

where $\mathbf{J}$ the Jacobian of the functions with elements $J_{ik}(x_j^0) \equiv \frac{\partial f_i(x_j^0)}{\partial x_k}$. The last relation is derived as $\mathbf{J}^{-1}(\mathbf{x}^0) = \mathbf{J}^{-1}(\mathbf{x})$ in first order.

The Taylor expansion yields the iterative procedure which provides an, in general, better approximation $\mathbf{x}^f$ to the actual solution, given an approximate solution $\mathbf{x}^i$,

$$\mathbf{x}^f = \mathbf{x}^i - \mathbf{J}^{-1}(\mathbf{x}^i)\cdot\mathbf{f}(\mathbf{x}^i).$$

The direction $\mathbf{p}^i = -\mathbf{J}^{-1}(\mathbf{x}^i)\cdot\mathbf{f}(\mathbf{x}^i)$ towards which the procedure shifts the initial guess is not necessarily closer to the actual solution; we may be far from it for the quadratic approximation to be valid. Therefore, a modification in the procedure above is necessary to ensure that the new approximation is better than the old one. The shift is taken as a fraction λ of the full step:

$$\mathbf{x}^f = \mathbf{x}^i + \lambda\mathbf{p}^i, \qquad 0 < \lambda \leq 1.$$

When a direction $\mathbf{p}$ is computed, we try at first the full step; when the approximate solution is close to the actual one the convergence is quadratic i.e. the accuracy is squared in successive steps. If, on the other hand, the function $h = \mathbf{f}(\mathbf{x})\cdot\mathbf{f}(\mathbf{x})$ does not diminish in the full step, we backtrack on the direction $\mathbf{p}$ until it does. We are guaranteed that this direction is a descent direction for $h(\mathbf{x})$; its derivative on $\mathbf{p}$ is negative:

$$\nabla h\cdot\mathbf{p} = (2\,\mathbf{f}\cdot\mathbf{J})(-\mathbf{J}^{-1}\cdot\mathbf{f}) = -2\,\mathbf{f}\cdot\mathbf{f} < 0.$$

There are various models proposed on the choice of λ in eq. (4.3.1); successive halving of the full step can work. For a more complex and more efficient algorithm see [120].

Broyden's method

Broyden's method falls in the category of *quasi–Newton* or *secant* methods (see [120]). It provides an approximation to the Jacobian of the nonlinear functions when it is very difficult or computationally expensive to produce their analytic derivatives. It converges superlinearly once we are close enough to the root and it may do so in fewer function evaluations than the Newton–Raphson method. The idea is as follows:

Let us denote the approximate Jacobian by $\mathbf{B}$. The ith quasi–Newton step $(\mathbf{x} - \mathbf{x}^0)$ is then the solution of

$$\mathbf{B}^i \cdot (\mathbf{x}^{i+1} - \mathbf{x}^i) = -\mathbf{f}(\mathbf{x}^i).$$

The quasi–Newton or secant condition is that $\mathbf{B}^{i+1}$ satisfies

$$\mathbf{B}^{i+1} \cdot (\mathbf{x}^{i+1} - \mathbf{x}^i) = \mathbf{f}(\mathbf{x}^{i+1}) - \mathbf{f}(\mathbf{x}^i).$$

This equation does not define $\mathbf{B}^{i+1}$ uniquely if the dimension is larger than one. Broyden's method formulates $\mathbf{B}^{i+1}$ by making the least change to $\mathbf{B}^i$ consistent with the secant condition:

$$\mathbf{B}^{i+1} = \mathbf{B}^i + \frac{\left[\mathbf{f}(\mathbf{x}^{i+1}) - \mathbf{f}(\mathbf{x}^i) - \mathbf{B}^i \cdot (\mathbf{x}^{i+1} - \mathbf{x}^i)\right] \otimes (\mathbf{x}^{i+1} - \mathbf{x}^i)}{(\mathbf{x}^{i+1} - \mathbf{x}^i) \cdot (\mathbf{x}^{i+1} - \mathbf{x}^i)};$$

the $\otimes$ indicates a tensor product. The initial guess $\mathbf{B}^0$ for $\mathbf{B}$ can be the identity matrix or the finite differences approximation to the Jacobian.

4.3.2 Optimization Methods

The solution of a system of equations as in eq. (4.3) can be found if we "collapse" the absolute values or the squares of f_i's into one function, e.g.

$$g(\mathbf{x}) \equiv g(x_1, x_2, \ldots x_n) = \sum_{i=1}^{n} |f_i(x_1, x_2, \ldots x_n)|.$$

The methods usually suggested for such a problem are the *Powell's method*, if the gradient of g is not known analytically, and the *conjugate gradient* and the related *variable metric* algorithms otherwise [120]. We employed both classes to locate specific unstable orbits. They were not our primary tools and, therefore, we will only describe their general idea.

Both types of methods reduce the multidimensional problem to a series of one-dimensional minimization problems along specific vectors, chosen differently for each technique. The minimization of a smooth function of one variable, $g(x)$, is greatly facilitated if we locate the range where the minimum we are after lies. That is, we should find three points a, b, c in increasing order, for which $g(a) > g(b)$ and $g(b) < g(c)$ hold; in that case, the minimum is in (a, c). A parabolic fit through these points provides an estimate for the minimum which can be used to narrow the interval. An appropriate number of iterations of this procedure will locate the exact minimum.

The main use of the sum of absolute values for the nonlinear functions we derive, was in the search of appropriate initial conditions through Genetic Algorithms, which we describe in the following section.

4.4 Genetic Algorithms

The principles of Genetic Algorithms (GA) were laid down by Holland [134] in 1975. He described how to apply the ideas of natural evolution as defined by Darwin to

optimization problems. For millions of years, biological organisms evolve into higher life forms according to natural selection rules such as "the survival of the fittest." In absence of intelligence, the, seemingly random, natural evolution process leads to better adapted species, with higher chance to survive the competition for food and shelter or attract mates. During reproduction, a recombination of the "good" characteristics of each ancestor are passed to the offsprings, potentially making them more "fit" than either parent. Spontaneous mutation, in which special features are gained or lost from a generation to the next, is another mechanism to produce species more adapted to their environment. Natural evolution is being tested successfully for millions of years; it was natural to simulate it and apply its rules to problems where better or "fitter" individuals in a population should emerge without loss of randomness.

Genetic Algorithms borrow their terminology from Biology. The *genes* code the characteristics of an individual in the form of *alleles*, different values expressing them. For example, the gene controlling the eye color can encode it in one of the black, brown, blue, and green alleles. The *gene pool* is the set of all possible alleles in a particular population and determines the diversity of the individuals in it. A *genome* is the set of all the genes of a specific species. In GA all genes are stored for simplicity in the same *chromosome*, something not true for most living organisms. Chromosome and genome are synonymous for GA. In actual biological systems, two genes exist in a chromosome for each characteristic, one being the dominant over the other; both have equal possibility to be inherited by the offspring. On the other hand, in typical Genetic Algorithms all genomes are *haploid* for simplicity, meaning that they store one gene for each feature, thus resolving the issue of dominance. *Recombination* is the process through which a new genome is created for an offspring by mixing the genes of the parents. The most common form of recombination of biology is the *crossover*: one chromosome from each parent is cut at one point and the halves from each are used to construct a new chromosome. Typical Genetic Algorithms do not differentiate between male and female; all individuals in a population can recombine. *Mutation* is another process to get new genomes. During this process, a random gene changes its value randomly among the available alleles, producing a new genome, probably fitter than the original. In GA, mutation is used as a means to introduce new individuals in a population which prematurely exhibits small diversity.

Genetic Algorithms adapt the ideas behind natural selection and the notions laid out above to algorithmic mechanisms. Suppose we can deem an individual "better" or "fitter" than another, through one well-defined quantitative property, the value of the *fitness function*. GA handles a population of individuals for which such a function is defined. For example, in an optimization problem the fitness function is the mathematical function to be maximized and each individual is one of the possible sets of unknowns. Each individual is represented by a chromosome which can encode any point in the search space. In optimization, the search space might be discretized so a possible set of values can be represented by its integer coordinates, or can be regarded as continuous and require real numbers to represent the unknowns. Integers or finite reals can in turn be encoded, if necessary, in binary, as dictated by the original definition of Genetic Algorithms. A set of reproduction operators should also be defined; these apply on the chromosomes and perform the mutations

and recombinations.

The algorithm goes as follows: An initial population of solutions is randomly constructed. The gene pool should be as diverse as possible in order to cover all accessible space. Then, individuals are selected from the population for reproduction, based on their relative fitness value. The best ones should have higher probability to be chosen. In the reproduction phase, new individuals are derived via recombination and mutation. The fitness value for each member of both the old and new populations is calculated and, based on it, a selection of a new set of individuals is made, equal in number to the initial one. The process {Selection, Reproduction, Evaluation, Replacement} is repeated until the population converges toward the optimal points or diversity is lost. Note that due to the large number of individuals, the population might not only gather around the "best" point (the solution to the problem) but also locate suboptimal points (for example, local maxima), a property which, in cases, is desirable. Sufficiently large number of iterations and adequately diverse initial population, though, will accumulate all individuals around the best solution.

We can point out certain features of the Genetic Algorithms from the presentation above. GA deal with a population of solutions, in contrast to the traditional optimization algorithms which manipulate a single point. This offers the advantage of versatility; a properly configured Genetic Algorithm cannot be trapped around a local maximum or be hampered by discontinuities or other unusual features of the function under optimization. Moreover, the large population and the independency of the fitness function evaluations—the time-consuming part of the algorithm—make GA particularly appropriate for parallelization, in contrast to other algorithms. This is an important advantage since serial computation is nowadays obsolescent due to the advents of machines and standards for parallel programming. We should also note that GA do not impose any requirement as other algorithms would, on the search space or the fitness function, of which they need only its value. This means that GA are robust since they can perform consistently well on a broad range of problem types. Additionally, they are particularly suited for cases where the solution space is too vast to be searched systematically; the problem of locating tentative initial conditions for periodic orbits in a multi-dimensional phase space is such a case.

It is also important to mention certain limitations of the Genetic Algorithms. As they are stochastic in nature, there is no guarantee that they will pinpoint the optimal solution. Instead, they can provide a good starting point for the traditional algorithms which will compute with the desired accuracy the solution. A hybrid method of GA with one of the traditional algorithms is probably the best approach to the optimization problem. Moreover, the behavior of Genetic Algorithms crucially depends on the population size, the choice of the representation in chromosomes and the action of the recombination and mutation operators. Experimenting with these will lead to a successful algorithm. It is worth noting that Genetic Algorithms is a relatively recent field of research being actively developed. No rigorous theory has been yet developed to justify the, nevertheless indisputable, success of GA at least in certain types of problems.

For more information on Genetic Algorithms one can consult [135, 136] and references therein.

Chapter 5

Automatic Differentiation via AUTO_DERIV

5.1 Introduction

Complicated analytical functions of many independent variables often appear in many scientific disciplines. Numerous problems can be reduced to the solution of systems of non-linear equations or the optimization of a function. The most efficient algorithms for these tasks depend on the first and, occasionally, the second partial derivatives of the functions. The feasibility of the computation of partial derivatives is imperative in the study of motion in a potential field or the stability analysis in classical mechanics and related scientific areas. Especially in chaotic systems, where errors accumulate exponentially, derivatives as accurate as possible are essential. For many of the tasks above, numerical differentiation is often inadequate and its implementation might be even inapplicable.[1] The need of accurate to machine precision derivatives, instead of approximate ones, frequently arises in many fields of physics, engineering, computational chemistry and applied mathematics. As we will explain below, the need for an easy and accurate way of evaluating the first and second partial derivatives of multidimensional functions was not well addressed within the FORTRAN programming community, which, until recently, included the vast majority of computational scientists. To remedy this we developed AUTO_DERIV.

AUTO_DERIV is a software module facilitating the analytical computation of the first and second partial derivatives of, in principle, an arbitrarily complex,[2] continuous mathematical function of any number of independent variables. The mathematical function should be expressed as one or more FORTRAN 90 or FORTRAN 77 procedures. It should be clarified that the module assists in computing the numerical values of the derivatives to machine precision at any given set of the independent variables; it does not deliver their analytical expressions. The mathematical rules for differentiation of sums, products, quotients, elementary functions in conjunction with the chain rule for compound functions are applied. A new *type* of variables is defined and the *overloading* mechanism of functions and operators provided by the

[1] The usual "black-box" codes for numerical differentiation cannot evaluate the derivatives of both $(x-1)^{3/2}$ and $(1-x)^{3/2}$ at $x=1$, for example.

[2] Depending on the available memory and the capabilities of the compiler.

FORTRAN 90 language is extensively used to implement the differentiation rules.

There are no restrictions on the complexity of the problem imposed by the program. There are certain limitations that may appear mostly due to the specific implementation chosen in the user code. They can always be overcome by recoding parts of the routines developed by the user or by modifying AUTO_DERIV according to specific instructions given below. The common restrictions of available memory and the capabilities of the compiler hold.

The description presented here was in part published in [137].

5.2 Motivation

Our motivation for developing AUTO_DERIV was the need to integrate and analyze classical trajectories in Molecular Dynamics simulations by using realistic potential functions. These require the solution of Hamilton equations, and thus, the computation of the gradient of the Hamiltonian function, $\mathscr{H}(q_i, p_i)$, of the problem. q_i are the generalized coordinates and p_i their conjugate momenta for a system of n degrees of freedom. In mechanical systems, $\mathscr{H}$ is comprised of the kinetic energy, $\mathscr{T}$—having a straightforward dependence on p_i, and possibly, q_i—and the potential energy $\mathscr{V}$, which, as usual in our field, is a function of q_i fitted to *ab initio* electronic structure calculations and/or empirical data, thus, lacking analytic expressions for the derivatives.

There exist commercial symbolic algebra packages, [138–140], which can evaluate derivatives of any order of relatively straightforward functions, or, rather, complex expressions of elementary functions and, even, encode them in a variety of programming languages. They can not, however—to the best of our knowledge—input a complex FORTRAN 90, or, even a FORTRAN 77, piece of code implementing a mathematical function and compute the derivatives. Publicly available alternatives and commercial versions of them[3] have been developed to achieve this, at least partially: as a rule, the first derivatives of a FORTRAN function are computed. They are cumbersome in their use as they require to formulate a stand-alone function which is then submitted or processed locally to compute the derivatives. The resulting code is in a separate file. Some of them were developed only for a particular type of computers. We are not aware of any other publicly available software that does not require translation from FORTRAN to another programming language and a significant amount of modifications to the user code in order to accomplish the differentiation. Prior to the development of our program, none of the alternatives were quite appropriate for the kind of functions, almost "black-box," we wanted to differentiate.

The potential functions we use are coded in FORTRAN and, thus, the language we chose to implement this tool was the one described in [141], commonly known as FORTRAN 90 (F90). By this standard, certain features and language constructs were introduced in FORTRAN, providing, among others, primitive support for *value–oriented programming*. Using *derived types*, function and operator *overloading*, and the encapsulation mechanism of *modules*, we constructed a *concrete class* which "instructs" the compiler on how to apply the chain rule of forward differentiation to

[3] see `http://www.autodiff.org` for an up-to-date review.

any mathematical function comprised of elementary, intrinsic FORTRAN 90 functions and to interpret appropriately all operators in order to compute the derivatives.

5.3 Elements of FORTRAN 90

A brief presentation of the concepts introduced in FORTRAN by the major revision of [141] and used by AUTO_DERIV, will be given in this section. For a detailed explanation of them the reader can consult any book on FORTRAN 90 (for example [142]).

By the new standard, the programmer can use not only the original data types (REAL, INTEGER, etc.) but also, can define and use aggregates of them. These structures can in turn serve as the building blocks of more complex entities. Such a *derived type* is defined through the keyword TYPE. For example:

TYPE vector
REAL :: x, y, z
END TYPE vector

defines a structure holding three real numbers (which can be the coordinates of a vector in 3D space, hence the name chosen). The user can declare the type of a variable to be a derived type (for example, `TYPE (vector) :: a, b, c`), address its components via % (for example, `a%x = 1.0`), and collectively pass them as arguments to a subroutine, effectively packing related information in one variable.

The programmer can also define operations involving derived types. For example, the cross product of two *vectors* can be computed via the `*` operator, as easily as in `c = a * b`, provided that a suitable definition for the intended action of this operator is made known to the compiler. This is done by first defining a function, in the same module as `TYPE (vector)`, being something like:

FUNCTION cross(a, b)
TYPE (vector), **INTENT** (**in**) :: a, b
TYPE (vector) :: cross

cross%x = a%y ∗ b%z − a%z ∗ b%y
cross%y = a%z ∗ b%x − a%x ∗ b%z
cross%z = a%x ∗ b%y − a%y ∗ b%x
END FUNCTION cross

An interface should exist to *overload* the operator `*`

INTERFACE OPERATOR (∗)
MODULE PROCEDURE cross
END INTERFACE

In addition to operator overloading, FORTRAN 90 supports function overloading; one could use the notation ABS(a), to compute the absolute value (norm) of a *vector* a. This requires a function

FUNCTION absvec(a)
TYPE (vector), **INTENT** (**in**) :: a

```
REAL :: absvec

absvec = sqrt(a%x**2 + a%y**2 + a%z**2)
END FUNCTION absvec
```

and an interface declaration to overload the generic name ABS with a new function

```
INTERFACE ABS
MODULE PROCEDURE absvec
END INTERFACE
```

Given these declarations, the same function (ABS) applied to a REAL returns the absolute value while when applied to a *vector* returns its norm.

The programmer can define functions accepting and returning derived types; for example, rotation of a *vector* in 3D space can be performed through such a function.

The access attribute (PRIVATE or PUBLIC) can be specified for an entity in a module. The former indicates that the entity can be used only inside the module, while the latter attribute "exports" it to any program unit which uses the module.

5.4 Usage

AUTO_DERIV is written in strict ISO FORTRAN 90 and should be accepted by any F90 conforming compiler. It is encoded in the form of a Fortran *module*, which, when USEd, provides the definition of a derived type, TYPE (func). TYPE (func) lays out the memory for the value, the first and the second partial derivatives of any variable declared as such. Functions for the manipulation and extraction of the numerical values are also available. The user should define the kind, the number and the values of the independent variables and the order (first or/and second) of the derivatives required.

5.4.1 Example

An example of how to use AUTO_DERIV is the following:

Let us suppose that we want to evaluate the first and (possibly) the second derivatives of the mathematical function f with respect to three variables x, y and z encoded in the subroutine in lst. (5.1). Note that it is not necessary to use a function or, even, only one procedure, as we will see. The modifications which are needed in this subroutine in order to evaluate the derivatives are the following:

We should augment the argument list with additional variables to hold the first and (if required) the second derivatives and, also, we should specify, either in the procedure or through an argument, the order of the derivatives we want. In order to use the same subroutine for both first and second order differentiation let us pass as argument an integer (*deriv*); different values of it will choose different order. Another way to do this is to use the facilities of the optional and keyword arguments of F90: over–simplifying, we can pass only those variables we need to be filled. The former approach enables us to call the subroutine from a F77 code or other programming languages lacking the concept of optional arguments; in the example we will follow this method.

There is no requirement imposed by AUTO_DERIV for the type, the number or, even, the existence of these additional variables. For simplicity we will pass a rank–1 array (Df) with n real elements to hold the first derivatives, and another rank–1 array (DDf) with $n\,(n+1)/2$ elements which will hold the upper triangle of the Hessian matrix (H), where n is the number of independent variables. In our example $n = 3$ so, the array DDf in F90 notation is:

$$DDf = (/H_{11}, H_{12}, H_{13}, H_{22}, H_{23}, H_{33}/).$$

Additionally, we will indicate with $deriv = 1$ that we need only the first derivatives and with $deriv = 2$ that we require *both* first and second derivatives.

The definition of the subroutine incorporating these changes and the necessary calls from *deriv_class* are presented in lst. (5.2). In order to preserve the same form of the statements in the main part of the subroutine, we reserve the names x, y, z, f for the new variables of TYPE (func), and we use other names, $(x\_, y\_, z\_, f\_)$, for their values.

The programmer should make the following modifications prior to incorporating AUTO_DERIV:

In module *deriv_class*:

1. Assign the number of independent variables to the variable n.

2. Change, if necessary, the *kind* variable *dpk* to the appropriate value for the input variables. The default is to have double precision. If required, the other *kind* variables provided to cope with mixed mode arithmetic, *spk* and *ik*, can be changed. Currently AUTO_DERIV supports all expressions among variables of the types REAL (*dpk*), REAL (*spk*) and INTEGER (*ik*).

In the user's subroutine or function:

1. Change the names of the input and output variables in the argument list and declare them as REAL having the same kind as in *deriv_class*. Their previous names should be used for the variables declared as TYPE (func).

2. Make *deriv_class* accessible through USE. If necessary, rename the few public variables provided by *deriv_class* to avoid name clashes with local entities. For example, `USE mod, newname => oldname` imports the variable `oldname` from module `mod`, but with the name `newname`. The public entities of *deriv_class* are: the subroutines *derivative*, *independent*, *extract*, the type *(func)*, and, of course, all operators and many intrinsic F90 functions. A newer version of AUTO_DERIV than the published one, available from the author, includes also the *ad_error* variable.

3. Declare as TYPE (func) all variables corresponding to mathematical functions; that is, both dependent and independent, and also, all intermediate (dependent) variables. Note that the use of IMPLICIT typing is permissible; this practice, however, has the side–effect of declaring constants and other variables not related to the differentiation as variables in the mathematical sense. This is not wrong as their derivatives are zeroed, it is only a waste of memory and triggers unnecessary computations. It is generally regarded as "good programming style" to avoid implicit declarations.

```
SUBROUTINE a(x, y, z, f)
IMPLICIT NONE

INTEGER, PARAMETER :: dpk = KIND(1.d0) ! double precision kind

REAL (dpk), INTENT (in) :: x, y, z
REAL (dpk), INTENT (out) :: f

REAL (dpk) :: g

g = y**2 * EXP(z)
f = SIN(x) * g

END SUBROUTINE a
```

Listing 5.1: Routine implementing a test function to be differentiated.

```
SUBROUTINE a(x_, y_, z_, f_, Df, DDf, deriv)
USE deriv_class       ! make the module accessible
IMPLICIT NONE

INTEGER, PARAMETER :: dpk = KIND(1.d0) ! double precision kind

REAL (dpk), INTENT (in) :: x_, y_, z_
REAL (dpk), INTENT (out) :: f_
REAL (dpk), INTENT (out) :: Df(3), DDf(3 * (3 + 1) / 2)
INTEGER, INTENT (in) :: deriv

TYPE (func) :: x, y, z, f
TYPE (func) :: g

CALL derivative(deriv)              ! declare the order of the derivative.
! declare as independent the variables (x, y, z) and assign them
! their values (x_, y_, z_)
CALL independent(1, x, x_)
CALL independent(2, y, y_)
CALL independent(3, z, z_)

g = y**2 * EXP(z)
f = SIN(x) * g

CALL extract(f, f_, Df, DDf)   ! extract from f the value and derivatives.
END SUBROUTINE a
```

Listing 5.2: Modification of the routine presented in lst. (5.1) for computing the first and second derivatives of function f by incorporating *deriv_class*.

4. Define the order of derivatives by calling the subroutine *derivative*. The integer argument passed (*deriv*) should have the value of 0, 1, or 2 indicating that we require the computation of the value of the function (included for symmetry and testing), the value and the first derivatives or the value, the first and the second derivatives respectively.

5. Declare the independent variables, their order and value, by calling the subroutine *independent* separately for each variable.

6. After the final assignment to the dependent variables, extract the derivatives and the value of the function. The subroutine *extract*, will return the derivatives in rank–1 arrays holding the gradient and the upper triangle of the Hessian.

Note that the statements in the main body of the subroutine need not be altered. In fact, AUTO_DERIV was designed in such a way that almost no modification of the existing code is required.

5.4.2 Special Cases

There are certain cases which the user should bear in mind:

- If the subroutine or function calls other subroutines or functions, their definition should be changed as follows:

  i) They must USE the module *deriv_class*.

  ii) All dependent and independent variables, either local or in the argument list, have to be declared as TYPE (func).

  No change is required in the argument list.

- Use of COMMON blocks and EQUIVALENCE statements, although discouraged by the introduction of modules and pointers in FORTRAN 90, is widespread. Transfered constants pose no problem. On the other hand, the awkward programming style of passing input and returning results from a subroutine or function through COMMON blocks or using EQUIVALENCEd variables, requires the user to treat them as if they were declared in the argument list; that is, their names must be changed, and other variables should be declared, as described above. The subroutine *independent* should be called for the input variables and their values should be extracted and update the COMMON blocks at the end. For example

```
REAL :: constant
REAL :: x              ! input variable

COMMON/block/constant, x
  ..........
!  use x
  ..........
```

should become

REAL :: constant
REAL :: x_ ! input variable
TYPE (func) :: x

COMMON/**block**/constant, x_

CALL independent(i, x, x_) ! i : unique index
.....
! use x
.....

! at the end of the routine
CALL extract(x, x_) ! assign to x_ the expected value

- The user must ensure, and modify the subroutine or function if necessary, that the generic names of trigonometric and other mathematical functions are used; that is, for example, SIN(x) is used instead of DSIN(x) irrespectively of the type of x, as encouraged by FORTRAN 77. Also, the user should eliminate all transformations from one kind to another between variables of TYPE (func). That is, statements such as `y = DBLE(x)` works for `x, y` if they are real (with the appropriate kinds), but as *deriv_class* provides a TYPE (func) with only one kind, such transformations have no meaning. Likewise, assignments of a TYPE (func) to a real are not supported.

5.5 Implementation

deriv_class is a collection of functions overloading all operators and all appropriate FORTRAN 90 functions and subroutines to accept not only real values but also variables of a derived type (TYPE (func)) comprised of the value, the first and the second derivatives of the corresponding mathematical quantity.

The compiler is "taught" how to handle expressions involving variables of this type —addition, subtraction, multiplication, etc. between them— and also, how to apply all meaningful FORTRAN 90 functions and subroutines on them in order to compute not only the value of the expression but, in addition, the numerical value of the first and second derivatives. *deriv_class* also provides functions to interpret mixed mode expressions between variables of TYPE (func), reals, and integers. Using this module, the compiler is able to apply the usual rules of differentiation, in conjunction with the chain rule, on any statement. That is, the compiler parsing a statement involving the TYPE (func) variables *a,b,c,d* like

```
d = a * b + c
```

will generate code to evaluate the following mathematical expressions:

$$\begin{aligned} d &= a\,b + c \\ \frac{\partial d}{\partial q_i} &= \frac{\partial a}{\partial q_i}\,b + a\,\frac{\partial b}{\partial q_i} + \frac{\partial c}{\partial q_i} \end{aligned}$$

$$\frac{\partial^2 d}{\partial q_i\,\partial q_j} = \frac{\partial^2 a}{\partial q_i\,\partial q_j}\,b + \frac{\partial a}{\partial q_i}\,\frac{\partial b}{\partial q_j} + \frac{\partial a}{\partial q_j}\,\frac{\partial b}{\partial q_i} + a\,\frac{\partial^2 b}{\partial q_i\,\partial q_j} + \frac{\partial^2 c}{\partial q_i\,\partial q_j}.$$

Allocatable components of a derived type are not yet part of FORTRAN. It is necessary, therefore, to define in the module prior to compiling, the number of independent variables (in the mathematical sense); n is the integer which holds it.

The components of a TYPE (func) variable are a REAL variable for the value (*value*) of the function, and two rank–1 arrays of n and $n\,(n+1)/2$ REAL elements (x, xx), for the first and second derivatives, respectively. The arrays hold the gradient and the upper triangle of the Hessian; it is stored in the format:

$$xx(i + n\,(j-1) - j\,(j-1)/2) = H_{ji} \;\; (i \geq j). \tag{5.1}$$

A few parameters are defined in the module: they are the kind of the components of TYPE (func), (*dpk*), and the kind for the reals (*spk*) and the integers (*ik*) that can appear in the same expression. Currently, FORTRAN provides no mechanism to utilize implicit promotions in expressions involving derived types or define conversions of one derived type to another. It was necessary, therefore, to write all procedures into supported types.

The default values for the kinds yield double precision, default real, and default integer numbers. They can be tailored to extend the precision. Note, however, that *dpk*, and *spk* must correspond to different precisions to avoid clashes in overloading resolution. The FORTRAN 90 standard ensures that at least two different kinds of reals are provided by the compiler. Multiple definitions of these kinds can be eliminated by modifying the module to inherit the kinds from another or export them outside *deriv_class* by changing the access attribute. By default, these and all "internal" variables and functions are of PRIVATE access. Note that **complex variables are not supported**.

There is a number of variables to be specified at run-time, before the computation is enabled. These are the required order of differentiation (*drvtv*) and the independent variables. Two subroutines are provided, *derivative* and *independent*, to manipulate them from the user's routine.

The subroutine *derivative* accepts an integer argument and assigns it to *drvtv*. It should be either 0, 1 or 2. All derivatives with order less or equal to this number will be evaluated (considering the value of the function as the zeroth derivative). An argument different than 0, 1 or 2 results in computing only the value. The interface is:

SUBROUTINE derivative(der)
IMPLICIT NONE
INTEGER, **INTENT** (**in**) :: der
END SUBROUTINE derivative

The subroutine *independent* is used for declaring a TYPE (func) variable as independent in the mathematical sense. The routine accepts three arguments: the variable, a REAL (*dpk*) value and an integer i. It zeroes the derivatives of the independent variable except the ith component of the first derivative, which is set to unity. It also assigns to the appropriate component of the TYPE (func) variable the supplied real value. This routine should be repeatedly called for all independent variables. Its interface is:

SUBROUTINE independent(i, x, val)
IMPLICIT NONE
INTEGER, **INTENT** (**in**) :: i
TYPE (func), **INTENT** (**out**) :: x
REAL (dpk), **INTENT** (**in**) :: val
END SUBROUTINE independent

The module *deriv_class* provides the subroutine *extract* to "decode" a TYPE (func) variable. It breaks it up into a real number (for the value), and two optional rank–1 arrays for the derivatives. There is a number of routines to extract them separately (under the generic names *value, FD, SD*) but normally they need not be used; therefore, they are private to the module. The interface of *extract* is:

SUBROUTINE extract(x, val, Dx, DDx)
IMPLICIT NONE
TYPE (func), **INTENT** (**in**) :: x
REAL (dpk), **INTENT** (**out**) :: val
REAL (dpk), **INTENT** (**out**), **OPTIONAL** :: Dx(n), DDx(n∗(n+1)/2)
END SUBROUTINE extract

5.5.1 Supported F90 Intrinsics

The module was designed in such a way that any intrinsic function or subroutine in standard F90 that can be applied to a real number can also accept a TYPE (func) variable and give the expected result. For example, a statement

```
f = SIN(y),
```

where f and y are of TYPE (func), amounts to three statements, when *drvtv*=2, (the FORTRAN 90 array notation is used)

$$\begin{aligned} \texttt{f\%value} &= \texttt{SIN(y\%value)} \\ \texttt{f\%x} &= \texttt{COS(y\%value) * y\%x} \\ \texttt{f\%xx} &= -\texttt{SIN(y\%value) * y\%x} \otimes \texttt{y\%x + COS(y\%value) * y\%xx}. \end{aligned}$$

The product of two arrays, y%x⊗y%x, in the last expression is the tensor product. It produces a higher order tensor (the Hessian), which is stored in a rank–1 array as in eq. (5.1). As operations involving intrinsic types can not be redefined, we should use a function (*tensor*) or define a new operator (`.tensor.`), as we chose in *deriv_class*, to compute this special product.

In order to localize all references to the exact representation of TYPE (func), we introduce several functions under the generic names *value*, *FD*, *SD*, and *val_assign*, *FD_assign*, *SD_assign*. They provide the value, the first and the second derivatives, and assign them to the components of a TYPE (func) variable. They are not meant to be used outside the module so they are declared as PRIVATE. Extensive use of pointers keep them very simple and it should be a relatively easy task for a compiler with inlining capabilities to integrate them in a code without the overhead of a function call. We anticipate that no loss in efficiency is introduced by this practice while it adds considerably to the maintainability of the code. The only binding to the

internal representation of TYPE (func), remains the assumption that the derivatives are stored in rank–1 arrays; all pointers are declared as such. Unless type aliasing is introduced in FORTRAN, this limitation can not be waived. We could have declared the derivatives as new user-defined types to solve it but by this we would make the code more complex and, possibly, less efficient.

Care was taken that all meaningful for numerical calculations intrinsic functions and every built-in operator of FORTRAN 90 are overloaded appropriately. Fully supported are all expressions involving the following routines: ABS, ATAN, CEILING, COS, COSH, DIGITS, DIM, DOT_PRODUCT, EPSILON, EXP, EXPONENT, FLOOR, FRACTION, HUGE, KIND, LOG, LOG10, MATMUL, MAXEXPONENT, MINEXPONENT, MOD, MODULO, NEAREST, PRECISION, RADIX, RANGE, RRSPACING, SCALE, SET_EXPONENT, SIGN, SIN, SINH, SPACING, TAN, TANH, TINY. Certain others are not fully overloaded; details on them are presented in the following paragraph.

5.5.2 Limitations

As we can not implement the *kind* as an argument, required by AINT, ANINT, INT, NINT, their overloaded functions simply do not accept this argument. They can transform only to the default kinds defined by *dpk* and *ik*.

A very serious limitation stems from the lack in FORTRAN 90 of user–defined elemental functions. An expression like `y = SIN(x)` where `y, x` are conformable arrays, is accepted by FORTRAN 90 if the array elements are of a built-in type. Unfortunately, this does not hold for user–defined types. The multitude of definitions that must be added to AUTO_DERIV in order to provide a similar behavior for them, would make the code very complicated. The user is, therefore, required either to make explicit the loop or loops implied in his/her code or, a better solution, to enhance *deriv_class* by adding to it only the exact instance of the function needed. This normally means that the programmer should copy the function accepting scalars, rename it, change the type of the arguments to make them arrays of the required rank, and add the function name to the corresponding public interface provided by the module.

A similar problem arises for intrinsic functions accepting arrays (SUM, PRODUCT, MAXLOC, MINLOC, MAXVAL and MINVAL). AUTO_DERIV overloads these functions to accept arrays of rank–1 only of TYPE (func) elements. If the user wishes to apply any of the above functions to arrays of different rank, he/she should add to the module the appropriate version of the function with the dimensions of the array arguments altered.

FORTRAN does not provide functions a mechanism to accept variable number of arguments. Therefore, the implementation of overloaded functions for MAX/MIN is inherently incomplete. The number of arguments must be fixed, while the not overloaded versions can have arbitrary. *deriv_class* provides MAX/MIN that accept two or three arguments. If the user needs a MAX/MIN with more, the appropriate instance has to be added and overload MAX/MIN by including its name to the relevant interface.

Note that in the implementation of MAX, MIN and MAXVAL, MINVAL we use MAXLOC, MINLOC; finding only the maximum/minimum *value* does not suffice. As MAXLOC, MINLOC do not accept the optional argument *DIM* in FORTRAN 90, the

four functions above can not be implemented efficiently to accept it either; we chose not to support the optional argument in them.

A serious mathematical problem arises in cases where we have discontinuity or when $0/0$ is encountered; for example, in ABS(x) at $x = 0$, or when the derivatives of $\sqrt{f(x)}$ at $x = 0$ are required and $f(0) = f'(0) = 0$. Care was taken when only the denominator in a fraction equals to zero; this case is avoided, unless the user in the code performs an illegal operation (which would show up even without using *deriv_class*). But "undefined" situations as the above, may appear in ACOS, ASIN, ATAN2, SQRT. In such cases, $0/0$ is arbitrarily resolved to 0; admittedly this is not correct. The user should either modify the code or not depend on AUTO_DERIV in such situations. Note that even computing by other means the analytic expressions for the derivatives would lead to this problem. A newer version of AUTO_DERIV than the published one, sets the module variable *ad_error* to *.TRUE.* enabling the user to check whether such problematic cases were encountered.

5.6 Tests

We conducted certain tests to measure the efficiency of AUTO_DERIV. We have calculated the elapsed time during the computation of the value and the derivatives of functions for which the corresponding analytic expressions were known. In each test we used a version of the FORTRAN 90 code with the derivatives computed analytically, "by hand," and another incorporating AUTO_DERIV.

Potential	Compiler	Order of derivatives		
		0	1	2
HCP (analytic)	NAG	0.626	1.155	2.612
HCP (AUTO_DERIV)	NAG	8.465	38.147	83.975
HCP (analytic)	PGI	0.712	1.217	2.451
HCP (AUTO_DERIV)	PGI	9.105	355.795	807.796
HCP (analytic)	Fujitsu	0.690	1.270	2.703
HCP (AUTO_DERIV)	Fujitsu	10.279	66.731	142.812
HCP (analytic)	Absoft	0.667	1.288	2.973
HCP (AUTO_DERIV)	Absoft	16.075	68.494	156.458
HF dimer (analytic)	NAG	0.071	0.752	-
HF dimer (AUTO_DERIV)	NAG	1.807	5.302	14.250
HF dimer (analytic)	PGI	0.152	0.518	-
HF dimer (AUTO_DERIV)	PGI	1.142	39.513	103.397
HF dimer (analytic)	Fujitsu	0.075	0.596	-
HF dimer (AUTO_DERIV)	Fujitsu	1.903	9.335	23.231
HF dimer (analytic)	Absoft	0.086	1.315	-
HF dimer (AUTO_DERIV)	Absoft	3.174	10.434	22.812

Table 5.1: Elapsed times during the calculations of the derivatives of Potential Energy Surfaces for the molecular systems HCP and HF–dimer. Time quoted in ms.

The first mathematical function we used is the potential for the HCP molecule [143]. It is a realistic example of a function depending on three variables and it is

sufficiently complex for exhibiting the capabilities of AUTO_DERIV. Another test was made with a potential for the HF–dimer [144], a function of six variables. For this we have calculated analytically only the first derivatives. In table (5.1) we present the elapsed time, averaged over a thousand evaluations, during the computation of each potential and for the two versions (analytic derivatives and using AUTO_DERIV). The results are tabulated for the compilers we had available. The standard DATE_AND_TIME subroutine was employed. The tests were performed on a PC with an Intel Pentium II processor at 450 MHz, running the Linux Operating System. We have also compiled and run the programs on IBM RS/6000 and HP machines with the systems' compilers; these results are not presented here. In the test we used the F90/95 compilers shown in table (5.2); the options chosen should be the optimal ones. The required memory during the tests, naturally, depends on the specific function differentiated. As we use a TYPE (func) variable holding $(1+n+n\,(n+1)/2)$ REAL (dpk) numbers for each REAL (dpk) mathematical variable in the original code we expect a roughly proportional increase in memory used by the program.

COMPILER	OPTIONS
NAGWare f95 Rel. 4.0(185) gcc 2.95.1	−Ounroll=1 −O4 −Wc,−funroll-loops,−O3,−fforce-mem −Wc,−fforce-addr,−march=i686
Portland Group, Inc. pgf90 v3.0	−fast −tp p6
Fujitsu F90	−O3 −Kfast,eval,PENTIUM_PRO −AR
Absoft Pro Fortran 6.0 f90 v2.1	−B100 −O

Table 5.2: FORTRAN 90/95 compilers used for the test runs.

5.7 Discussion

AUTO_DERIV was designed to make the evaluation of accurate analytic first and second derivatives feasible; computing them "by hand" is, in realistic cases, too time consuming and highly error prone. The emphasis was not on implementing it optimally. Efficiency is, for the most part, hampered by the primitive support FORTRAN 90 offers for value–oriented programming. Most important was to make it work, requiring as little change in user's code as possible. We can see from the tests in the last section that AUTO_DERIV should not be considered as an option when the derivatives are, or can easily be, available analytically. However, it is a valuable tool when we deal with complicated mathematical functions with no derivatives available. We anticipate that as the compilers evolve and support more efficiently the advanced features of FORTRAN 90, this disproportionality in performance between our package and the analytic derivatives shrinks and programmers will not be deterred from using it.

We may ask whether it is possible to compute higher order derivatives from the first and second ones. Recursive functions could be used in order to compute derivatives of arbitrarily high order. We leave such extensions for future upgrades.

The current standard [145] of FORTRAN 95 provides a few extra facilities (among others the ELEMENTAL attribute of subroutines and functions) which would enable

us to provide a much "cleaner" and more powerful implementation. However, the relative scarcity of FORTRAN 95 compilers led us to postpone these modifications for future upgrades. Care was taken that the array notation provided by F90 is used throughout the code. It might assist a compiler to optimize, or, even, parallelize it. Unfortunately, the current definition (version 2.0) of High Performance Fortran (HPF) does not support distribution onto multiple processors of arrays of a derived type; otherwise, compiler directives could be inserted to indicate to the HPF compiler possible parallelisms. When FORTRAN 95 compilers become widespread, and, most importantly, when the expected major revision, unofficially known as FORTRAN 2000, is standardized, some of the above limitations in the package can be overcome. We plan to follow closely all enhancements in the language and incorporate them to AUTO_DERIV.

Chapter 6

Spectroscopy of phosphaethyne (HCP) and deuterated phosphaethyne (DCP)

6.1 Introduction

As mentioned in the introductory chapter, an important research area for modern spectroscopists is the isomerization process in small molecules, and, especially, its manifestation in the experimental and the theoretical rovibrational spectrum. Isomerization is the transformation of a molecule from a stable configuration to another stable, or, more loosely, metastable arrangement. In a broad sense, any substantial change in the molecular configuration, such as the large-amplitude bending motion we will analyze below, can be considered as equivalent to isomerization and is equally interesting.

The triatomic monohydrides, molecules of the HAB form, can exhibit the simplest kind of isomerization reaction, the hydrogen migration process: HAB↔ABH. These molecules are fundamental in experimental and theoretical studies and serve as prototypes—especially those containing a carbon atom such as *hydrogen cyanide (HCN)* and *phosphaethyne (HCP)*. Their small size and the single and triple bonds involved make them ideal benchmark molecules. The basic chemical interest of their electronic structure, the profound change in nature of the bonds the hydrogen atom participates in during the isomerization reaction, and the dynamics exhibited, motivated their study. Moreover, apart from HCN which for decades is the subject of intense research by astrophysicists and environmental scientists, HCP is also of astrophysical relevance: According to Turner *et al.* [146], thermochemical equilibrium calculations show that all gas-phase phosphorus in the interstellar medium should be in the form of HCP. As a consequence, many spectroscopic studies are available on HCP and its isotopomers: high resolution spectra from microwave to infrared region have been recorded [147–159] and various Potential Energy Surfaces have been determined [143, 150, 160–166].

Our group was interested in studying among others, the HCN, HCP and its isotopic variant, *deuterated phosphaethyne (DCP)*, molecules. The electronic ground state $1\,^1\Sigma^+(1\,^1A')$ for the HCP/DCP molecules possesses, as will be explained below,

one stable minimum at the linear configuration (H/D–CP) and a saddle point at the other linear form (CP–H/D), in contrast to HCN where the isomers are the two linear configurations. Strictly speaking, isomerization can not occur in HCP/DCP in their ground electronic state; nevertheless, with sufficiently high energy, the bending amplitude of the H/D–CP bond can grow and the molecule can approach the metastable configuration in a process resembling isomerization.

Isotopic substitution is a well-established spectroscopic method for identifying and interpreting spectral features of molecules. The replacement of a particular atom in a molecule by its isotope affects only the kinetic part of the Hamiltonian and, consequently, it modifies the fundamental frequencies and the zero-point energy of the system. As a consequence, we can anticipate a quantitative change, a shift of the vibrational levels, in the lower energy region without significant modification in the overall spectral patterns. At higher energies, where the coupling terms in the kinetic energy between various degrees of freedom grow strong, we can expect a substantial deviation in the spectra of the isotopic variants. However, in the case where an anharmonic resonance controlled by the atomic masses governs the phase space of the molecule, qualitative changes can be observed even at low energies. Naturally, the larger the mass variation is, the stronger these changes are.

In this chapter we will present our research results on two of the most extensively studied species, HCP and DCP, elucidate the analysis of their classical phase space in the ground electronic state for zero total angular momentum and relate the findings to the quantum mechanical picture. We will show how the different facets of the features of a molecular system are encoded in the experimental, quantum and classical results, and relate to each other. The emphasis will be given in the classical analysis. We will thus develop a way to predict characteristic features of the quantum and experimental spectra through the classical picture. This, hopefully, is a valuable assistance in larger molecules, where the full quantum treatment is practically inapplicable while the classical one we present for triatomic molecules can be rather trivially extended.

Let us just note at this point that recently, a simple, qualitative model for HCP and other similar bond-breaking isomerizing systems has been developed by Jacobson and Child [167]. It consists of a spherical pendulum coupled to a harmonic oscillator and admits analytical treatment.

We begin the chapter with an overview of related experimental results, followed by a brief review of the available potential energy surfaces derived in the literature for HCP/DCP. We also outline the construction of the potential energy surface we used. Then, the detailed analysis of the classical phase space of HCP and DCP is given. It is followed by a presentation of the related quantum picture for each molecule, along with a discussion of the analogies between the classical and quantum treatment. The chapter concludes with an overview of our findings. Preliminary results for HCP were presented in a review paper [168], while for the DCP molecule our work was published in [169]. Additionally, our team calculated the analytical form of the first and second derivatives of the potential we used, a very complex function fitted to ab initio points.

6.2 Experiment

HCP has been the subject of pioneering experiments since the early 1960's when it was first synthesized by Gier [170]. Various spectroscopic techniques were since employed to investigate its microwave, ultraviolet, and, recently, infrared spectra and reveal the dynamics encoded in them. While HCN is the most examined molecule for signatures of isomerization in the vibrational spectrum, no experimental observation for its isomerization states exists yet. The excited electronic states of HCN from which highly excited vibrational levels of the ground state can be accessed, lie in the vacuum ultraviolet wavelength region and, as most of such states rapidly predissociate, it is difficult to employ present experimental techniques to high energies. The spectroscopic conditions for observing indications of isomerization in the form of hydrogen migration, are more favorable for HCP than HCN. The isomerization process or large amplitude bending motion in HCP has been studied experimentally by Lehmann *et al.* [150], Chen *et al.* [151] and later by Ishikawa and co-workers [154, 156–158].

The first group studied the vibrational levels of the $\widetilde{X}$ (ground) electronic state up to 16917 cm^{-1} above the zero-point energy (with zero angular momentum) in the Dispersed Fluorescence (DF) $\widetilde{A}\ ^1A'' \rightarrow \widetilde{X}\ ^1\Sigma^+$ spectrum. They assigned the observed states as combinations of the bend (v_2) and the CP stretching (v_3) modes, $(0, v_2, v_3)$. The Stimulated Emission Pumping (SEP) experiment of the second group probed the highly excited vibrational levels at 16000 cm^{-1}–19000 cm^{-1} above zero-point energy in the ground electronic state. They found a predominantly bending character in these states with very small differences in the rotational constants. Both teams found the overall vibrational spectrum surprisingly harmonic even at the high energies probed. This indicates that the observed states do not actually follow the isomerization path as they would access significantly anharmonic region of the potential on it. The third group has recorded the $\widetilde{A}\ ^1A'' \rightarrow \widetilde{X}\ ^1\Sigma^+$ and $\widetilde{C}\ ^1A' \rightarrow \widetilde{X}\ ^1\Sigma^+$ SEP and DF spectra for HCP in an attempt to access high lying bending vibrational states ($\widetilde{A}$ and $\widetilde{C}$ have significantly bent equilibrium geometries, roughly 130° and 113° respectively). The former band is believed to follow the pure bending overtones $(0, v_2, 0)$, with v_2 ranging from 26 to 42, in the $\widetilde{X}$ state; it covers an energy regime up to 25315 cm^{-1} above the ground vibrational state, that is, roughly 3.139 eV above zero-point energy (which is ~ 0.3684 eV above the potential minimum). The latter band sampled vibrational levels in the interval of 22500 cm^{-1} to 23200 cm^{-1} above the ground state. As we will see below, the energy difference of the two linear configurations is calculated to be ca. 3.39 eV and therefore, the energy interval probed in the experiment is sufficiently wide to allow the observation of large-amplitude motion of H around CP, provided the atoms move along the minimum energy path. By fitting the spectra to well known spectroscopic models for linear molecules, they, too, established that the spectra are quite regular, despite the molecule being highly excited. Nevertheless, three important observations, among others, were made: First, perturbations of the pure bending overtones appear with $v_2 \geq 32$ which were absent at lower excitations. Second, the rotational and vibrational fine structure constants of the $(0, v_2, 0)$ levels change abruptly around $v_2 = 36$. Third, anomalously large rotational constants are exhibited by some of the vibrational levels in the $\widetilde{C} \rightarrow \widetilde{X}$ spectrum. These were considered as indica-

tions of a change in the character of the H–CP stretch from predominantly H–C to H–P motion. Thus, the onset of perturbations and the abrupt changes of the fine structure constants were suggested as diagnostic of the onset of isomerization. Subsequent SEP experiments by Ishikawa *et al.* [156] on the $\widetilde{C} \rightarrow \widetilde{X}$ transition, focused on the energy region of 13400 cm^{-1} to 17500 cm^{-1} above the ground state. Motivated by qualitative results of Farantos *et al.* in [171], they found strong evidence corroborating the existence of two distinct families of bending states, attributed to normal-mode and isomerization-type states.

No states with excitation in the HC stretch mode (v_1) were observed in the DF or SEP spectra by any group as the HC distance does not change significantly in the transitions they studied. A recent experiment using IR-UV-SEP triple resonance spectroscopy by Ishikawa and co-workers [158] managed to access some levels with one quantum in the HC mode around 16000 cm^{-1}. Additionally, of the third pure progression, $(0, 0, v_3)$, only states up to $v_3 = 3$ have been observed due to unfavorable Franck–Condon factors: the $(0, 0, v_3)$ states are centered around 180° whereas the $\widetilde{A}$ and $\widetilde{C}$ electronic states are significantly bent.

In contrast to HCP, experimental information on the vibration–rotation spectrum of DCP is sparse (see [163] and references therein). The transition energies of the lowest states have been measured [172–174]. The pure rotational spectrum of DCP is better studied, especially on the ground and the lower excited vibrational states [153, 159]. High resolution Fourier Transform IR spectra of DCP were also recorded in various energy windows from 400 cm^{-1} to 5500 cm^{-1} and spectroscopic constants, including Fermi-resonance parameters of the effective Hamiltonian, were calculated by Jung in [175].

6.3 Potential Energy Surface

Various forms for the Potential Energy Surface (PES) of the ground electronic state for HCP/DCP were reported in literature. Lehmann and co-workers in [150], fitted a rigid bender Hamiltonian to experimental data they measured, thereby determining the bending potential over a broad range of the bending angle. In the same work, an ab initio potential was also calculated using Møller–Plesset perturbation theory (MP4), in excellent agreement with the empirical one in the areas they coincided. Their prediction was that the linear CP–H configuration corresponds to a saddle point with the curvature of the potential energy along the bending coordinate changing almost 90°; subsequent calculations by other groups confirmed this. Another PES was produced by Chen and Chong [162], fitted to ab initio DFT points. Puzzarini *et al.* in [163], used internally contracted MRCI from CASSCF reference wave functions with large orbital expansions, to develop another potential for HCP, adjusted to reproduce experimental data. Koput and Carter [165] employed a coupled–cluster variant, CCSD(T), with basis sets of triple- to quintuple-zeta quality to derive a potential energy surface. Schinke and co-workers in [164], computed a number of points by ab initio methods on the MRCI level with singly and doubly excited reference wave functions obtained by CASSCF calculation. The points were fitted to an analytical expression of the Sorbie–Murrell form (§3.5.6). The same team produced an improved and more accurate global PES in [143]. Though it does

not describe properly the H+CP dissociation channel, it was designed for the study of the isomerization process; therefore, we based on it our classical analysis of the phase space. We will outline below the procedure they employed. Since our work in HCP/DCP, another ground state potential energy surface has been developed by Nanbu *et al.* [166].

Surfaces for excited electronic states have also been produced through ab initio MRCI calculations by various groups [160, 161, 166]. It turns out that some of the potentials exhibit interesting topographical features such as multiple minima. Various other groups have reported ab initio calculations for specific geometries of the molecule or experimental results aiming mainly to determine the equilibrium structure.

The potential energy surface we employed was calculated using the internally contracted multi-reference configuration interaction method with Davidson correction (icMRCI+Q) (§3.5.3); the number of contracted configurations in the CASSCF calculation was such that the total energies were determined to an accuracy better than 10^{-8} hartree. All calculations were performed with the MOLPRO program [85]. More than one thousand points were computed, scattered on a grid covering the full range of the $\widehat{HCP}$ bond angle; R_{HC}, R_{CP} varied from 2.5 α_0 to 4.0 α_0. Additional points were calculated in the vicinity of the isomerization path. The calculated points encompass an energy range of about 5 eV with respect to the global minimum, way above the metastable configuration and close to the dissociation threshold.

The ab initio points were fitted to an analytical function of the form (cf. fig. (6.1) for the notation on coordinates)

$$v = \sum_{i=0}^{5}\sum_{j=0}^{6}\sum_{k=0}^{6}\left[a^C_{ijk}\,\eta^i_C\,P_j(\cos\phi_C)\,\mu_C + a^P_{ijk}\,\eta^i_P\,P_j(\cos\phi_P)\,\mu_P\right] r^k\,\mu_{asy}$$

with $i+j+k \le 6$. The functions η^i_C, η^i_P are

$$\eta_C = 1 - e^{-b_1(R_{HC}-b_2)}, \qquad \eta_P = 1 - e^{-b_3(R_{HP}-b_4)},$$

and P_j are the Legendre polynomials. The μ functions are

$$\begin{aligned}\mu_C(x) &= \frac{1-\tanh[b_5(x-b_6)]}{2},\\ \mu_P(x) &= 1-\mu_C(x),\\ \mu_{asy}(R) &= \frac{1-\tanh[b_7(R-b_8)]}{2},\end{aligned}$$

where $x = R\cos\gamma$. The parameters a^C_{ijk}, a^P_{ijk}, b_i were determined by fitting the function v to the ab initio points. Two independent fits were performed, one (V_1) to approximate best the region below 2.25 eV above the minimum, and the other (V_2) to reproduce accurately higher energies. The final expression for the PES is

$$V = V_1(1-\lambda_1) + V_2\lambda_1 - \delta V\lambda_2 + V_0$$

where

$$\lambda_1 = \frac{1+\tanh(4V_2+12)}{2}, \qquad \lambda_2 = \frac{1-\tanh(12V_2+15.6)}{2}.$$

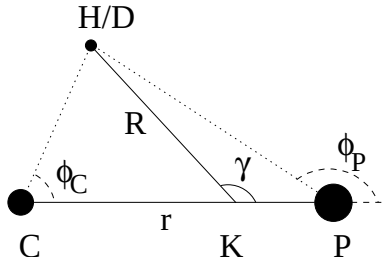

Figure 6.1: Coordinates for the HCP/DCP molecules. K indicates the C–P center-of-mass.

The correction term is of the form

$$\delta V = c_0 + \sum_{m=1}^{381} c_m \, e^{-\left(\frac{R_{HC}-q_{HC}}{p_{HC}}\right)^2} e^{-\left(\frac{R_{CP}-q_{CP}}{p_{CP}}\right)^2} \left[e^{-\left(\frac{\alpha-q_\alpha}{p_\alpha}\right)^2} + e^{-\left(\frac{2\pi-\alpha-q_\alpha}{p_\alpha}\right)^2} \right],$$

with $\alpha \equiv \phi_C$, the $\widehat{HCP}$ bond angle in rad. The parameters in this term were chosen to minimize the differences between the original energies and those obtained from the analytical expression. V_0 is a constant with its value chosen to adjust the energy of the minimum to the value of the energy minimum predicted by the potential in [171]. A discrepancy between the fundamental frequency for the CP stretching mode and certain experimental results lead Schinke and co-workers to scale the R_{CP} coordinate by 1.01. The final expression of the PES contains also several cut-off functions in order to eliminate unphysical structures in regions not covered by the original ab initio points.

The topographical analysis of the potential in the physically relevant region reveals a global minimum of $V_{min} = -5.2362$ eV at $R = 2.1750$ Å, $r = 1.53065$ Å, $\gamma = \pi$ rad in Jacobi coordinates. The CP–H/D configuration at $R = 1.8783$ Å, $r = 1.6040$ Å, $\gamma = 0$ rad is a saddle point; the potential value there is -1.8438 eV. Contour plots of cuts of the potential on the minimum are given in fig. (6.2) and fig. (6.3). We notice the "peanut"-like structure reflecting the different "radii" of the carbon and phosphorus atoms. A projection of the minimum energy path is given in fig. (6.4). This path consists of the points where the potential is minimum with respect to R and r for successive fixed values of the angle γ. A drastic slope change around $\gamma \simeq 130°$ at roughly -3.05 eV is exhibited on the potential "waist;" towards the CP–H/D region the potential becomes quite anharmonic.

6.4 Analysis of the Classical Phase Space

In our calculations in both HCP and DCP molecules we employed the Jacobi coordinate system, fig. (4.1)(I), as more appropriate to study the large-amplitude bending motion of H/D. The values for the masses we used are $m_{\rm H} = 1.00783$ u, $m_{\rm D} = 2.01566$ u, $m_{\rm C} = 12.0$ u, $m_{\rm P} = 30.9810343$ u. The total angular momentum of both molecules was zero.

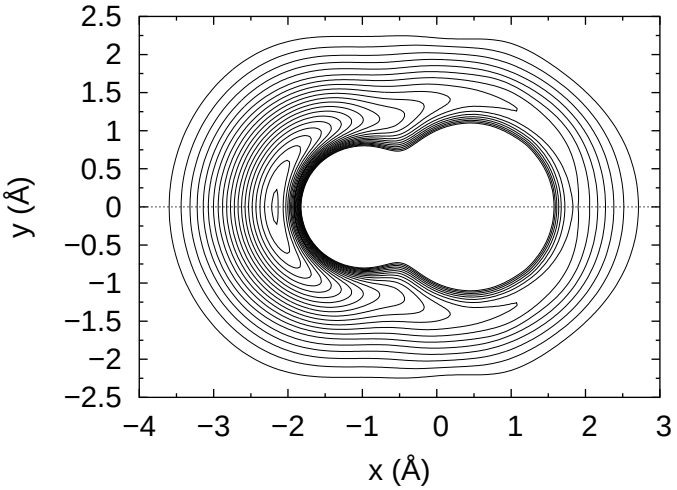

Figure 6.2: Contour plot of the HCP/DCP ground-state potential energy surface for $r \equiv R_{CP}$ at the equilibrium value of 1.53065 Å. x, y are the coordinates of H/D with respect to the CP center of mass. The 21 contours start from −5.2 eV and increase by 0.25 eV.

6.4.1 HCP

The Continuation/Bifurcation (C/B) diagram for the HCP molecule is given in fig. (6.5). It depicts the periodic orbit families we located, plotting their period (measured in time units of $\sim$ 10.18 fs) with respect to their energy (in eV). For clarity it is split in two, one graph comprising the principal families and their bifurcations, and another consisting of the saddle–node orbits. Energy plays the role of the "external" parameter which causes the bifurcations. There is little point in showing the C/B diagram in a more traditional form in terms of a coordinate with respect to energy as in fig. (2.1) and fig. (2.2); in our case of multidimensional periodic orbits it would not be unique, while all information on the bifurcations can be inferred from the Energy–Period plot.

Three principal families emerge deep in the potential well. The orbits just above the energy minimum have periods very close to those predicted through the harmonic expansion (Weinstein theorem, cf. §2.3.2) and exhibit predominant excitation in each of the normal modes. The calculated periods of the classical harmonic oscillators are 0.9802 t.u., 2.5524 t.u., and 4.7774 t.u.. The first two modes are of pure stretching nature, mainly in R and r respectively, while the last period corresponds to the pure bending mode. Notice the approximate 2:5:10 resonance among them; this inherent to the system 1:2 relation of periods for the r- and γ-oscillators is the one which influences decisively the classical phase portrait and the quantum spectrum of HCP, as we will see below. We denote the principal families by **R**, **r**, and **B** to indicate their primary character (B stands for bending). Their detailed evolution is as follows:

The **R** family is remarkably stable up to relatively high energy; at roughly −2.590 eV and at a period of 1.285 t.u. it loses its stability through a period–doubling bifurcation, giving birth to a new family, **R1**, with initial period around 2.571 t.u.. Stability is regained at (−2.056 eV, 1.384 t.u.) through another period–

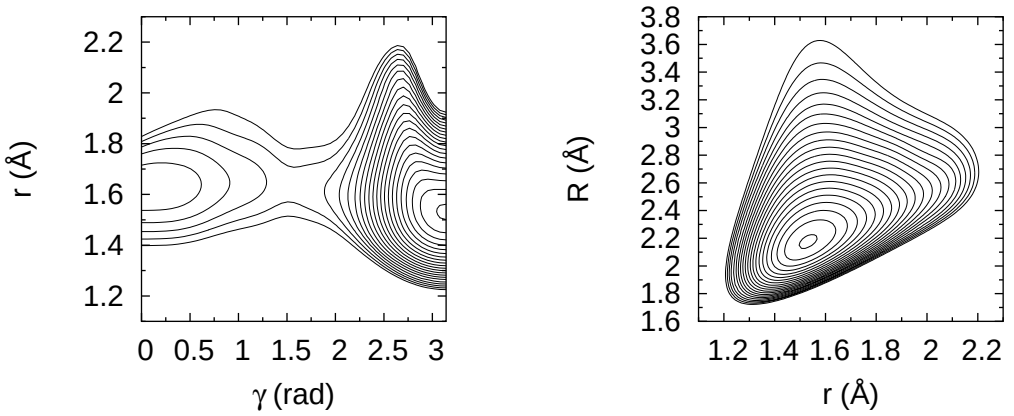

Figure 6.3: Contour plots of the HCP/DCP ground-state potential energy surface for $R = 2.1750$ Å (left) and $\gamma = \pi$ rad (right). The 21 contours start from -5.2 eV and increase by 0.25 eV.

doubling bifurcation. A family of unstable orbits, denoted by **R2**, branches off there. If we examine the real pair of the Floquet multipliers in the interval of instability, we notice that the largest in absolute value does not exceed 1.12; the **R** family, therefore, behaves as relatively stable at least up to dissociation. **R1** is stable until -0.57 eV where a period–doubling bifurcation takes place. We notice that the periods of the orbits in the **R1** family are roughly the "eigenperiod" of the r-oscillator enabling a resonance through which energy is transfered to it. This justifies the stability of **R1** even in high energies as it deposits a large part of the excess energy on the less stiff r-oscillator, which is essentially unexcited in the parent family **R** prior to the birth of **R1**. The same reasoning extends to the orbits of **R2** which preserve their unstable character with minor alterations. Plots of representative orbits of these families at various energies are depicted in fig. (6.6); their energies, periods and sets of initial conditions are given in table (6.1).

The **r** family starts at the predicted period of 2.552 t.u. and is stable up to (-3.434 eV, 2.819 t.u.) where it undergoes a period–doubling bifurcation. Above this point, the family is mildly unstable apart from a small interval between -1.06 eV and -1.00 eV where the real eigenvalues of the monodromy matrix return briefly to the unitary circle. The family becomes stable again through a period–doubling bifurcation at (0.242 eV, 2.99 t.u.). The stable family that branches off at the main period–doubling bifurcation is denoted by **r1**. Its first located orbit has a period of 5.637 t.u. at -3.434 eV. The family is stable throughout its life apart a very brief interval around (-1.231 eV, 6.535 t.u.) where a "collision" of the Floquet multipliers on the unit circle in a Hopf bifurcation renders it temporarily complex unstable. The **r1** family recombines with the principal family at (-1.0 eV, 6.475 t.u.) in the vicinity of the stability interval of **r**. This interval gives also birth to another family with γ excitation through a period–doubling bifurcation; we denote it by **r2**. It starts at (-1.06 eV, 6.489 t.u.) and while it appears in the diagram as the continuation of **r1** it is different in character. **r2** family has not been continued above -0.623 eV,

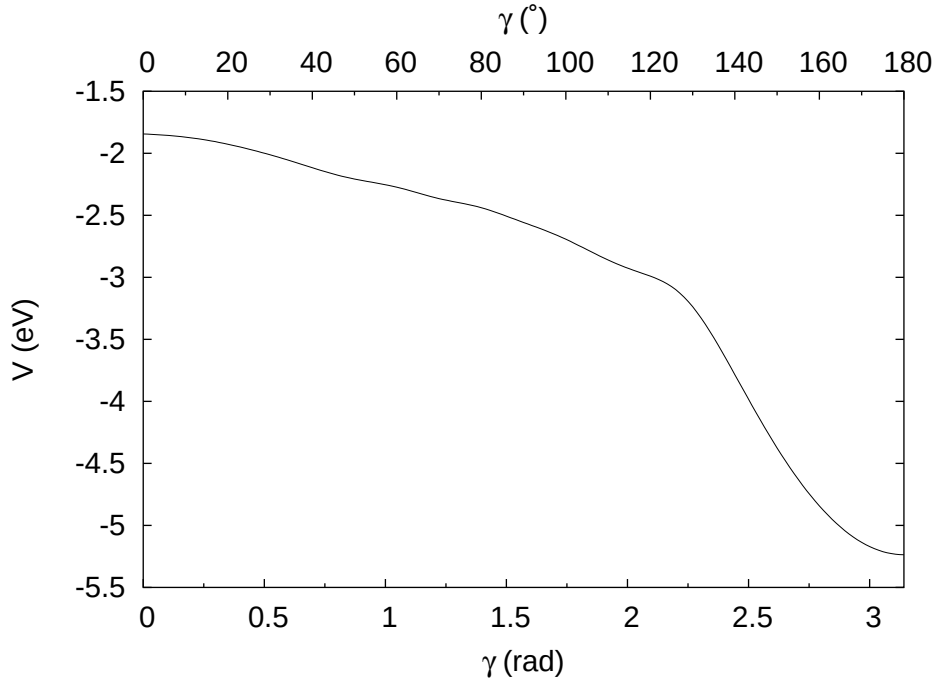

Figure 6.4: Potential energy as a function of γ along the minimum energy path. The potential is minimized in R and r for specific γ. The kink exhibited at roughly -3.05 eV relates to the birth of saddle–node bifurcations and isomerization states.

as numerical difficulties due to nearby orbits there prevented the convergence of the algorithms we used. In fig. (6.6) the evolution of **r** family is depicted by plots of three of its orbits covering the energy range of this family. Similarly, orbits of the **r1** and **r2** families are plotted in fig. (6.7). Their initial conditions, periods, and energies are given in table (6.1).

The orbits of the **R**, **R1**, **R2**, and **r** families are effectively restricted on the $\{R, r\}$ plane due to the linearity of HCP at the equilibrium point, whereas the **r1**, **r2** families exhibit a small bending vibration; the orbits of the latter families have the appropriate period to resonate with the γ-oscillator. Nevertheless, the predominant character of all of them is the stretch in R and r.

The principal family of primarily bending nature is denoted with **B**. The first located orbit in it is at -5.213 eV and has a period of 4.786 t.u., quite close to the expected by the harmonic approximation. The initial stability is lost around (-3.910 eV, 5.190 t.u.) but is quickly regained at -3.866 eV and is kept even above dissociation. During the instability interval of **B**, a conjugate pair of Floquet multipliers leaves and, in a slightly higher energy, re-enters the unit circle at 0°. The two successive bifurcations appear to give birth to the **B1** and **B2** families. The first orbit of **B1**, which inherits the stability, has the same period as the corresponding orbit of **B**, 5.191 t.u.. The family becomes unstable at -2.75 eV. Orbits of the **B1** family are quite complicated; they are not symmetric with respect to $\gamma = \pi$ rad line and, therefore, we can deduce that their "reflections" are also periodic orbits and that their influence on the quantum behavior is limited. The **B2** family starts off as unstable; it changes through a steady–state bifurcation at (-2.763 eV, 5.525 t.u.)

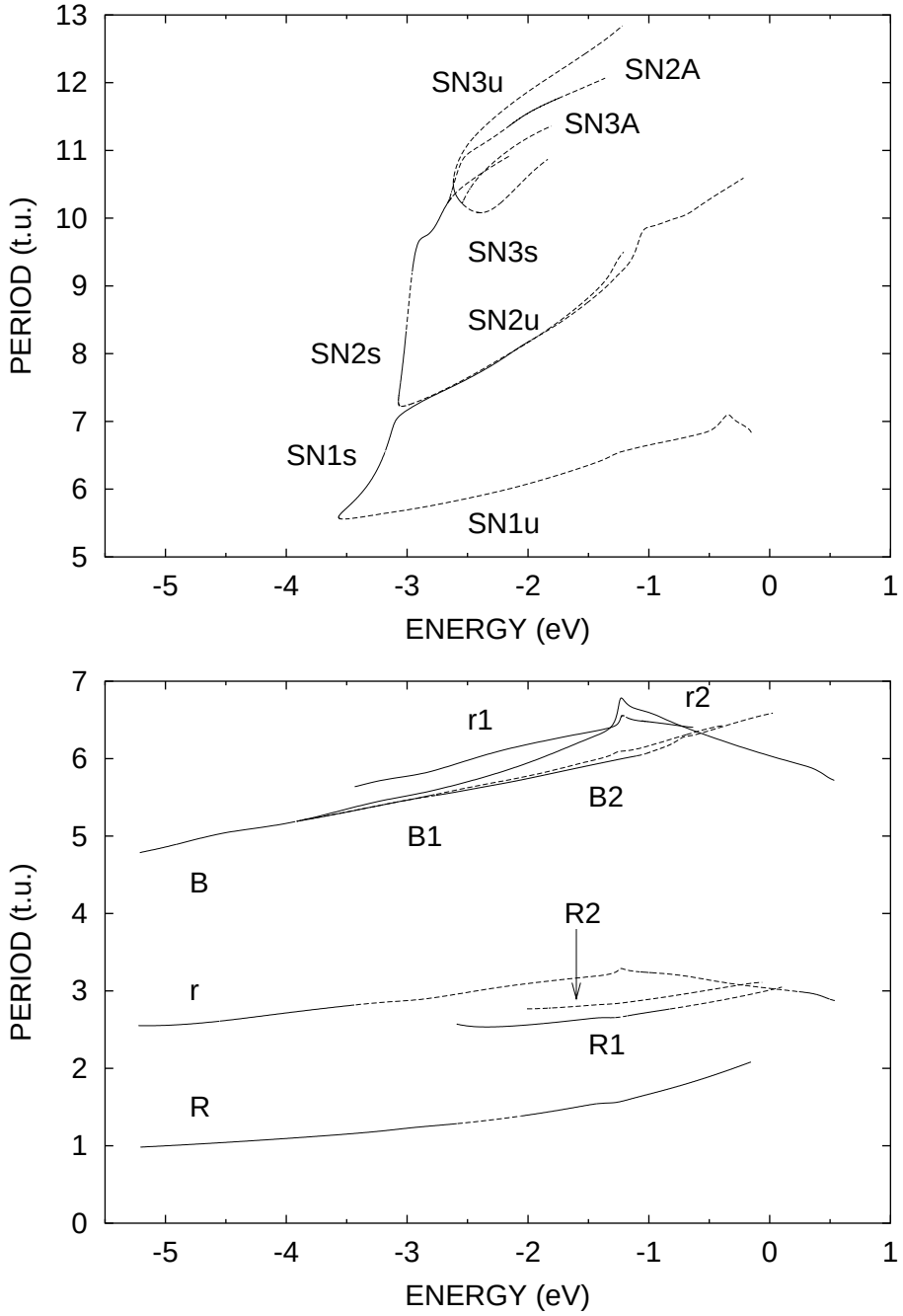

Figure 6.5: Continuation/Bifurcation Diagram for HCP: fundamental families (lower figure) and saddle–node families (upper figure). All periods are measured in time units of ~ 10.18 fs. Continuous lines represent stable families of periodic orbits; dashed ones indicate instability.

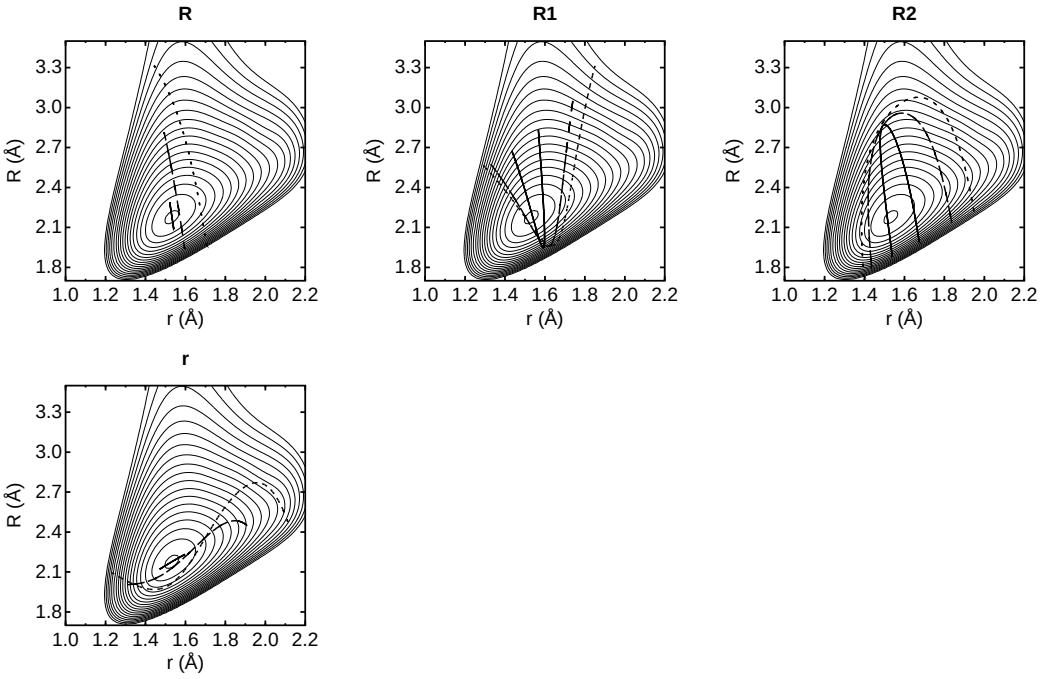

Figure 6.6: Projections in the $\{R, r\}$ plane of orbits at low (solid line), medium (dashed line), and high (dotted line) energies of the **R**, **r**, **R1**, and **R2** families in HCP, superimposed on the potential contours for $\gamma = \pi$ rad. The inner contour is at -5.2 eV and the increment is 0.3 eV.

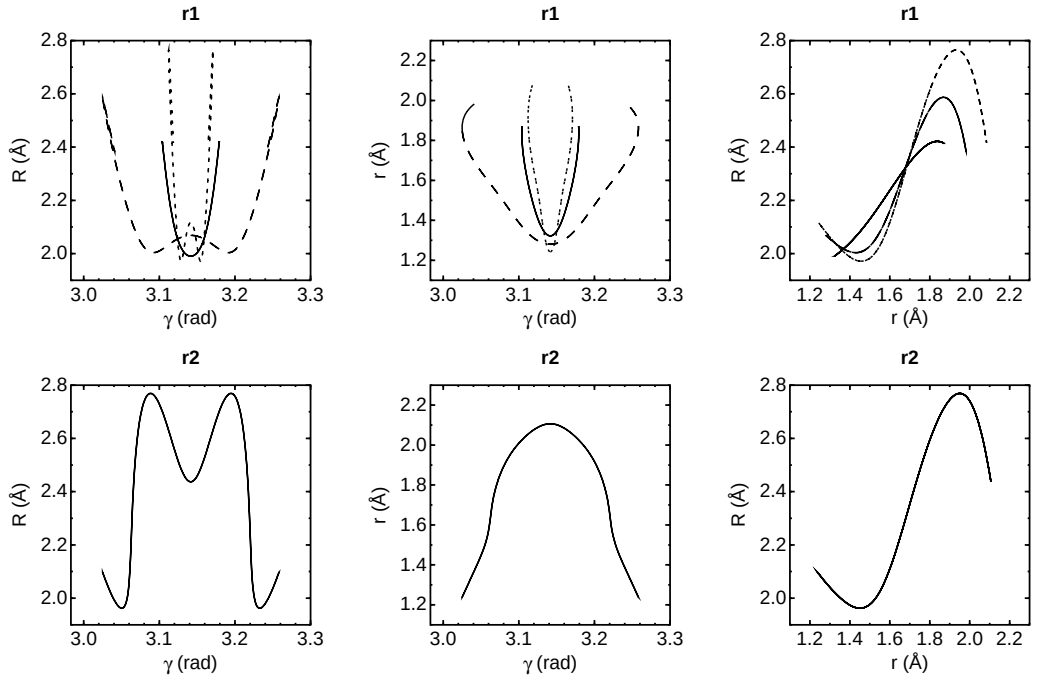

Figure 6.7: Projections of orbits in HCP, given at table (6.1), of **r1** (upper row) and **r2** (lower row). Solid, dashed, and dotted lines on the same plot represent orbits of increasing energy.

remaining stable up to −1.102 eV where it undergoes a period–doubling bifurcation. It is quite intricate but symmetric with respect to $\gamma = \pi$ rad. In fig. (6.8) representative orbits of the **B**, **B1**, and **B2** families are given; their energies, periods and initial conditions are given in table (6.1).

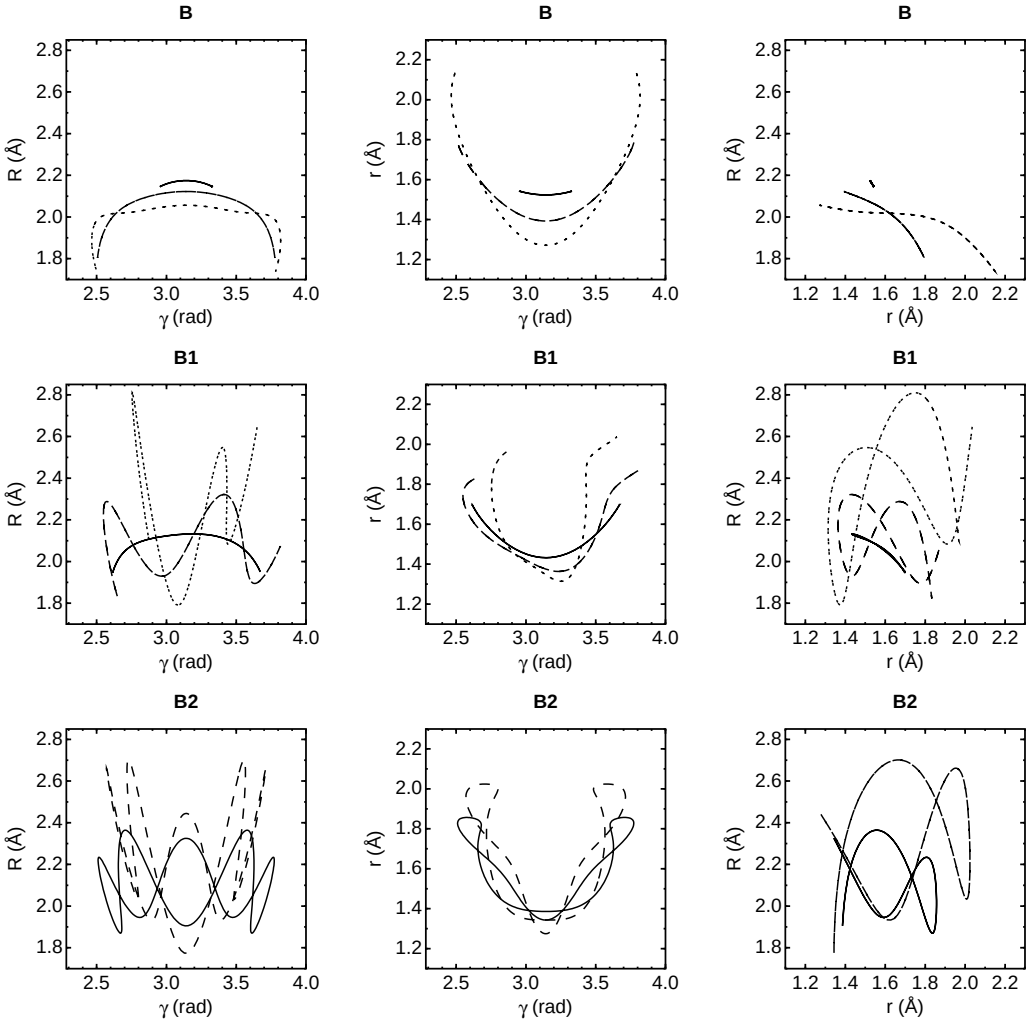

Figure 6.8: Projections of orbits in HCP, given at table (6.1), of the **B** family (upper row), the **B1** family (middle row), and the **B2** family (lower row). Solid, dashed, and dotted lines on the same plot represent orbits of increasing energy.

Quite interesting is the "peak" exhibited by **B** at −1.23 eV. The energy accumulated in the bending mode is such that angle γ reaches there 2.4 rad, very close to the onset of strong anharmonicity of the potential, as judged by the minimum energy path, fig. (6.4). This fact makes, eventually, the γ-oscillator resonate primarily with r and, in a lesser extent, with R, resulting in the onset of excitation of higher harmonic terms of these modes. It is important to note that the orbits of the **B** family are thus confined, regardless the energy, in relatively small bending angles between 2.4 rad and 3.88 rad around the equilibrium geometry. Moreover, their shape is not the appropriate one to penetrate towards CP–H. This behavior

is counterintuitive: one would expect that orbits in **B** family explore deeper and deeper the isomerization path with increasing energy. As it turns out, the excess energy is deposited in the other two modes enlarging primarily the CP stretching and making H approach CP. One could attribute this confinement to an effective barrier due to the 1:2 resonance of the r- and γ-oscillators, and, in a lesser degree, to the 1:5 resonance of R and γ. A similar "kink" is exhibited by the **r** and **r1** families at the same energy and can be explained by the resonance with R. The descending segment of **r** and, consequently, **B**, above the onset of resonance is due to the steep region of the potential which is explored by r in high energies.

Apart from the orbits in the fundamental **B** family and its bifurcations, other orbits exist which exhibit a large bending vibration, extending on the isomerization path towards the CP–H side of the PES at gradually higher angles. They are born through saddle–node bifurcations. The first bifurcation of this kind we located occurs at (−3.5673 eV, 5.5855 t.u.) and the emerging family is denoted by **SN1**. Its stable branch, **SN1s**, undergoes a steady–state bifurcation at (−1.978 eV, 8.196 t.u.) through which it loses its stability for the rest of the energy region we traced it. As we can see in fig. (6.9), the r-oscillation changes considerably as energy increases. The orbits of the family exhibit gradually smaller r–amplitude up to (−3.1 eV, 7.0 t.u.); at this point of the C/B diagram, fig. (6.5), a significant change in the slope takes place. Above −3.1 eV the family grows in parallel to the **r** family, an observation which corroborates that the resonance with the r-oscillator is reestablished and that the excess in energy is deposited there; the other two modes, R and γ, do not change their quite large amplitude considerably. Nevertheless, the variation in the r coordinate is small, much smaller than in the **B** family. In fig. (6.10) the evolution of the unstable branch **SN1u** of the first saddle–node family is depicted. It exhibits a much larger r-oscillation and its Period–Energy relation resembles that of **r**. The data of the orbits plotted are given in table (6.2).

Two interesting observations can be made on **SN1**: First, none of its orbits extends more than roughly 60° from the equilibrium, even at high energies; they barely exceed the angle where the "kink" in the minimum energy path is exhibited (cf. fig. (6.4)). Therefore, these too support the regularity of the system and cannot influence the isomerization quantum states. Second, we notice that a saddle–node bifurcation occurs at the vicinity of the rather abrupt change in the slope of the **SN1** family. The emerging family, denoted by **SN2**, has a stable branch which, in a sense, "inherits" and continues the steep segment of **SN1s**.

SN2 is born at (−3.0723 eV, 7.2932 t.u.); notice that the minimum energy path depicted in fig. (6.4) at this energy exhibits the most notable "kink". Its stable branch, **SN2s**, undergoes a series of steady–state bifurcations at −3.007 eV, −2.958 eV, and −2.656 eV which alternate the stability. The last bifurcation gives birth to a family we denote by **SN2A** and renders **SN2s** unstable for the rest of the energy region we covered. The unstable branch, **SN2u**, was continued up to −1.21 eV; it consists of orbits with very small r-vibration and it is "parallel" to the similar in character segment of **SN1s**. The segment of **SN2A** we located starts at 10.2522 t.u. and is unstable. In fig. (6.11) representative orbits of the **SN2** family and its bifurcation are depicted; their data are given in table (6.2). We also give there an initial condition for an orbit belonging to a bifurcation of **SN2A** (**SN2AA**)

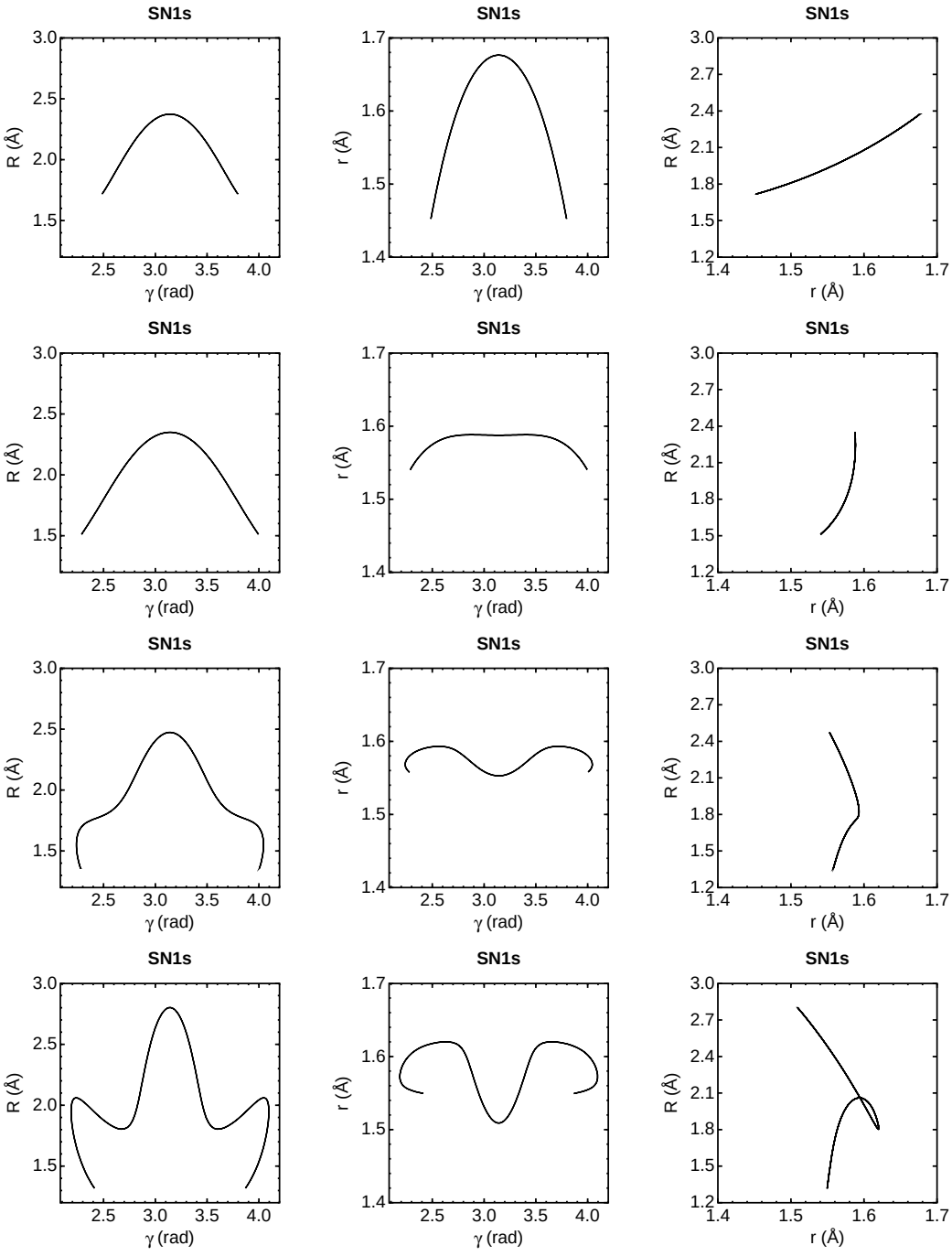

Figure 6.9: Projections of orbits of the **SN1s** family of HCP from low (upper row) to high (lower row) energies. Their data are given in table (6.2).

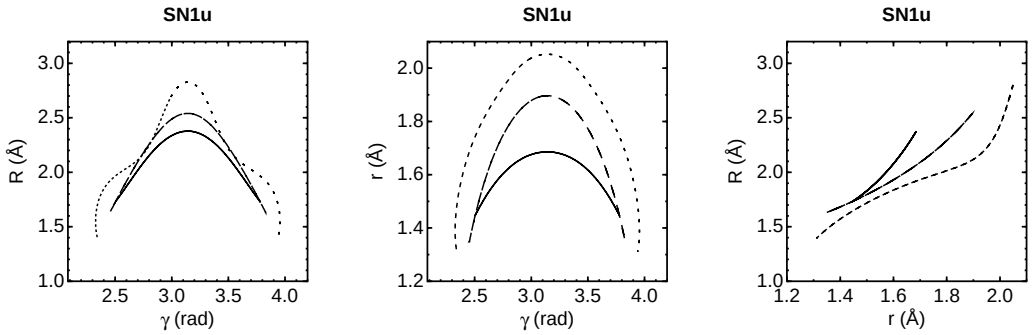

Figure 6.10: Projections of orbits of the **SN1u** family of HCP at low, medium, and high energies (solid, dashed, and dotted lines respectively). Their energies, periods and initial conditions are given in table (6.2).

we located but we were not interested in continuing. As we can see, the orbits of the **SN2** family extend to large angles on the isomerization path. On the other hand, while some of them have enough energy to reach the saddle point at $\gamma = 0°$, the CP–H configuration, none of them does.

At (−2.6179 eV, 10.5163 t.u.) another saddle–node bifurcation was located. It gives birth to the **SN3** family. The stable branch of this family, **SN3s**, becomes unstable at (−2.545 eV, 10.2176 t.u.) and the **SN3A** family emerges with the same period. As the energy increases, **SN3s** becomes highly unstable. The unstable branch, **SN3u**, undergoes a steady–state bifurcation at −2.6078 eV and gains stability; 3 meV above this energy it becomes complex unstable. **SN3A** starts at −2.5447 eV having an initial period of 10.22 t.u.. It quickly loses the initial stability through a bifurcation at (−2.535 eV, 10.258 t.u.) which renders it complex unstable. The orbits in this family are not symmetric with respect to $\gamma = \pi$ rad. Initial conditions for representative orbits of the **SN3** and **SN3A** families are given in table (6.2); they are plotted in fig. (6.12).

As we can see in the relevant plots, the families emanating from saddle–node bifurcations comprise of orbits which extend progressively deeper on the minimum energy path, exploring areas where the potential is gradually flatter; this has a direct impact on their periods, which strongly increase with energy. One can surmise the birth of more saddle–node families in higher energies which penetrate deeper and deeper into the CP–H hemisphere of the PES. Such families are born in predominantly chaotic phase space regions making quite problematic the attempts to locate them. The overall dynamical behavior of HCP, as deduced from the C/B diagram and elaborated in this section, is rather regular despite the resonance between the r- and γ-oscillators. Instability is developed in relatively high energies primarily when the bending angle extends significantly towards the CP–H side of the potential.

6.4.2 DCP

The Continuation/Bifurcation (C/B) diagram for the DCP molecule is given in fig. (6.13). It depicts the various periodic orbit families we located, plotting their period (measured in time units of ~ 10.18 fs) with respect to their energy (in eV). For clarity it is split in two, one graph comprising the principal families and their

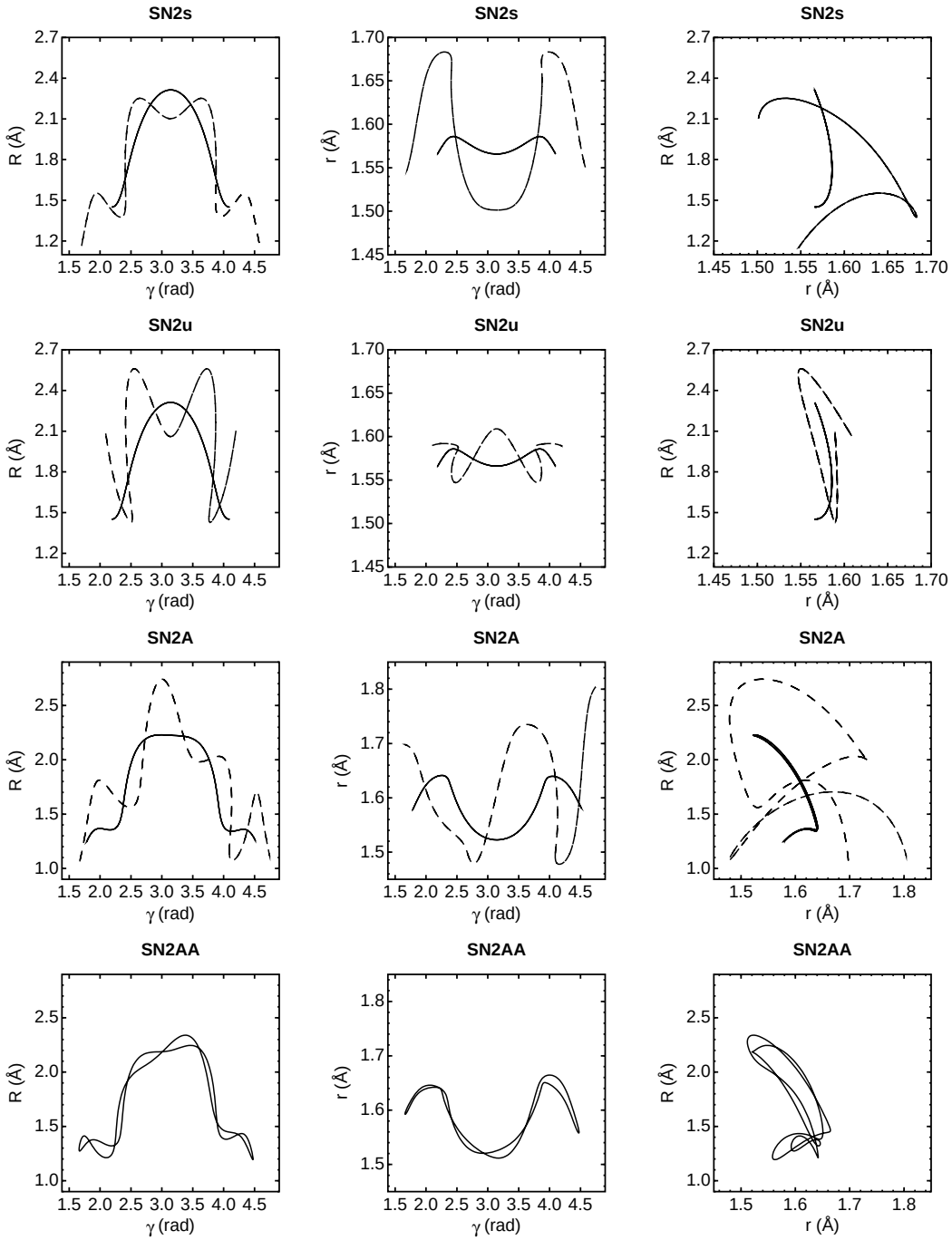

Figure 6.11: Projections of orbits in HCP, given at table (6.2), of the **SN2s** family (first row), the **SN2u** family (second row), the **SN2A** family (third row), and the **SN2AA** family (fourth row). Solid and dashed lines on the same plot represent orbits of low and high energy respectively.

FAMILY	ENERGY	PERIOD	R	r	γ	P_R	P_r	P_γ
R	−5.0098	0.9983	2.1705368	1.5332104	3.1415927	0.6389897	−0.5598528	0.0000000
R	−2.3162	1.3313	2.6001818	1.5229558	3.1415927	1.4524385	−1.6490115	0.0000000
R	−0.2670	2.0183	3.3145125	1.4434516	3.1415927	−0.0900473	0.3483874	0.0000000
r	−5.1234	2.5510	2.2140031	1.5751685	3.1415927	0.0899993	0.9865916	0.0000000
r	−2.8806	2.8920	2.4839796	1.8584142	3.1415927	−0.0574219	2.9866601	0.0000000
r	−0.7623	3.2059	2.5661655	2.0886143	3.1415927	−1.0018651	2.6280334	0.0000000
R1	−2.5126	2.5499	2.5668581	1.5798056	3.1415927	1.6361441	−0.6598344	0.0000000
R1	−1.1881	2.6749	2.6607958	1.7063780	3.1415927	1.9950884	1.3549628	0.0000000
R1	−0.0281	3.0008	2.6273117	1.7551437	3.1415927	2.4215264	2.4216273	0.0000000
R2	−1.9580	2.7695	2.8682244	1.5091001	3.1415927	0.1802383	−1.7892894	0.0000000
R2	−0.9999	2.8910	2.9255071	1.5294985	3.1415927	−0.5176192	−3.8664846	0.0000000
R2	−0.0619	3.1100	2.8906712	1.4927549	3.1415927	−1.2002971	−4.5177393	−0.0000000
B	−5.1188	4.8172	2.1713515	1.5260363	3.0751511	−0.0231203	0.1395135	−0.8712665
B	−3.0262	5.5120	2.0576730	1.5547816	2.7194877	−0.2304032	4.0192122	−2.1384678
B	−0.1718	6.1190	1.9577462	1.9172224	2.4805928	−0.3512663	5.6610266	−0.6598103
r1	−3.3589	5.6670	2.4214516	1.8344177	3.1038761	−0.0098072	−2.2337193	0.0022235
r1	−2.2135	6.1070	2.5818014	1.8466184	3.0252364	−0.2020402	−3.8449667	0.0563229
r1	−1.0372	6.4814	2.6162899	1.8017968	3.1138363	−1.1656462	−5.0896702	0.0841787
r2	−0.8375	6.4450	2.6459270	1.8273452	3.2103002	−1.0589544	−5.1706911	0.3024545
B1	−3.9150	5.1906	2.1118184	1.4836535	2.9039403	−0.0894932	2.3285745	−2.2803901
B1	−2.1287	5.7350	2.2249154	1.5900134	2.6468523	0.6622198	3.9468271	−2.2085247
B1	−0.3924	6.4250	2.7829180	1.8039032	2.7542308	−0.4849770	4.0701720	0.1954621
B2	−2.0417	5.7300	1.9881869	1.3923209	3.2756894	1.1246462	0.9327665	3.1895797
B2	−0.0194	6.5730	2.6423173	1.5514969	3.5214523	0.7135468	5.9905620	1.4535095

Table 6.1: Initial conditions for representative periodic orbits of the fundamental families in HCP. Lengths are measured in Å, the angle in rad, the energy in eV, the period in t.u. (~ 10.18 fs) and the momenta in the appropriate derived units.

FAMILY	ENERGY	PERIOD	R	r	γ	P_R	P_r	P_γ
SN1s	−3.5654	5.5990	2.3572747	1.6727386	3.2327680	0.2422886	0.4737776	−3.0437798
SN1s	−3.2301	6.3530	2.2892723	1.5880821	2.9414508	−0.4963087	0.0201634	−3.5273220
SN1s	−2.9192	7.2530	1.9478342	1.5894576	2.7000495	−1.0456749	0.4238239	−2.5354168
SN1s	−1.7067	8.4930	2.0548677	1.5986606	2.2610834	0.1831446	−0.6754577	−1.6030482
SN1u	−3.5669	5.5800	2.3587295	1.6811276	3.2376681	0.2555370	0.5525874	−2.9729164
SN1u	−2.0383	6.0596	2.5305324	1.8932820	3.0805099	−0.1919586	−0.5942143	−3.2051082
SN1u	−0.3212	7.0751	2.6705887	2.0335874	2.9820089	−1.0557121	−1.1199029	−3.0830399
SN2s	−3.0723	7.2952	1.8505315	1.5848498	2.5108383	0.9544847	−0.1416566	1.6534220
SN2s	−2.1563	10.9152	1.7550253	1.6479578	3.8773122	−1.5491234	1.4804235	0.0229162
SN2u	−3.0723	7.2872	1.8472872	1.5847833	2.5084183	0.9579566	−0.1359420	1.6309519
SN2u	−1.2281	9.4592	2.0646599	1.6085427	3.1784142	0.3721073	−0.3073531	4.6437097
SN2A	−2.6558	10.2512	2.1942439	1.5445073	2.7422249	0.3463885	−0.9967600	3.5629546
SN2A	−1.3741	12.0572	1.1813492	1.4962802	4.0917646	−1.1688671	−1.5857644	−0.1162055
SN2AA	−2.5546	10.6720	2.1583824	1.5293722	2.6875499	−0.2967319	0.7055814	−3.4690283
SN3s	−2.6179	10.5160	2.2720696	1.5186431	2.9974888	0.2270871	−0.5351478	4.2884328
SN3s	−1.8363	10.8691	2.5072967	1.4750895	3.2539312	−0.5883798	1.1607422	3.8187099
SN3u	−2.6179	10.5203	2.2720195	1.5183739	2.9995815	0.2223120	−0.5277718	4.2925473
SN3u	−1.2174	12.8400	1.7822931	1.8059597	3.8843145	−1.0178905	3.9534564	0.4452245
SN3A	−2.5292	10.2800	2.2396688	1.5410660	3.3811208	0.6521617	−1.0736049	−4.0432614

Table 6.2: Initial conditions for periodic orbits of saddle–node families in HCP. Lengths are measured in Å, the angle in rad, the energy in eV, the period in t.u. (~ 10.18 fs) and the momenta in the appropriate derived units.

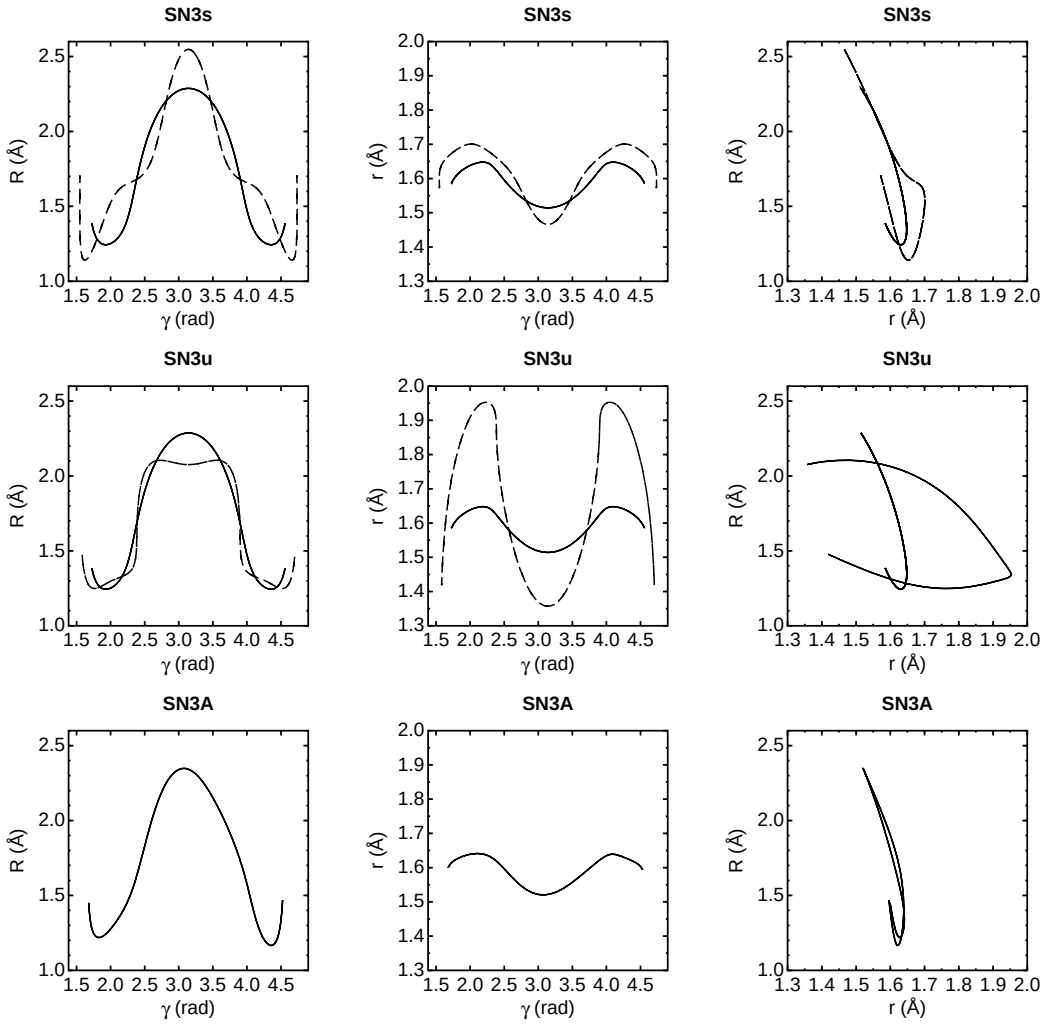

Figure 6.12: Projections of orbits in HCP, given at table (6.2), of **SN3s** (upper row), **SN3u** (middle row), and **SN3A** (lower row). Solid and dashed lines on the same plot represent orbits of low and high energy respectively.

bifurcations, and another depicting the saddle–node orbits.

As expected, three principal families emerge deep in the potential well. The orbits just above the energy minimum have periods, as shown below, very close to those predicted through the harmonic expansion and exhibit predominant excitation in each of the normal modes. The calculated periods of the classical harmonic oscillators are 1.3138 t.u., 2.6628 t.u., and 6.1534 t.u.. The first two modes are of pure stretching nature, mainly in R and r respectively, while the last period corresponds to the pure bending mode. Due to the significant change in one of the atomic masses from the HCP case we examined above, a 1:2 Fermi resonance is now exhibited between the stretching modes, while the bending one does not participate in a low order resonance. We denote the principal families by **R**, **r**, and **B** to indicate their primary character (B stands for bending). Their detailed evolution is as follows:

The first orbit we located from the **R** family, in the vicinity of the potential

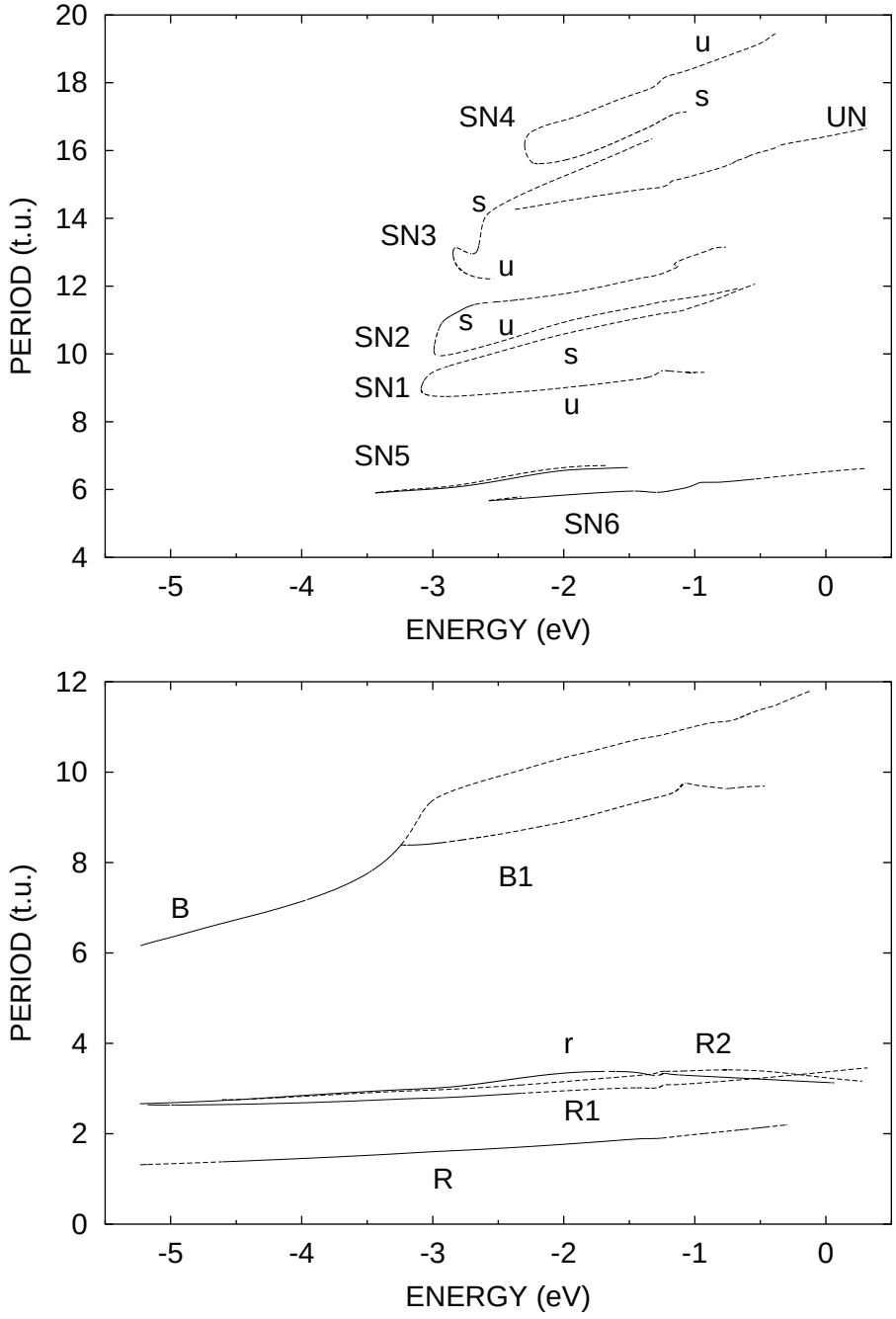

Figure 6.13: Continuation/Bifurcation Diagram for DCP: fundamental families (lower figure) and saddle–node families (upper figure). All periods are measured in time units of ~ 10.18 fs. Continuous lines represent stable families of periodic orbits; dashed ones indicate instability.

minimum, has a period of 1.314 t.u.. At (−5.1760 eV, 1.3195 t.u.), just 0.06 eV above the minimum, the **R** family undergoes a period–doubling bifurcation through which it loses stability and gives birth to the **R1** family. Stability is regained at (−4.6115 eV, 1.378 t.u.) through another period–doubling bifurcation; the instability is inherited by the **R2** family born at this point. Above this bifurcation, the **R** family is remarkably stable up to at least −0.3 eV, which is the energy we ended its continuation. **R1** starts at a period of 2.639 t.u.; its initial stability is lost through a period–doubling bifurcation at (−2.3218 eV, 2.8957 t.u.). The first orbit we located from the **R2** family is at 2.7567 t.u.; the family is unstable in the energy region we traced it.

The **r** family starts with a period of 2.663 t.u. and remains stable up to 0.04 eV where it undergoes a period–doubling bifurcation. Representative orbits of the **R**, **R1**, **R2** and **r** families depicting their evolution are given in fig. (6.14). The orbits are confined on the $\{R, r\}$ plane at $\gamma = 180^\circ$ and they are overlaid on the relevant potential contour plot. Their data are given in table (6.3). As we can see from

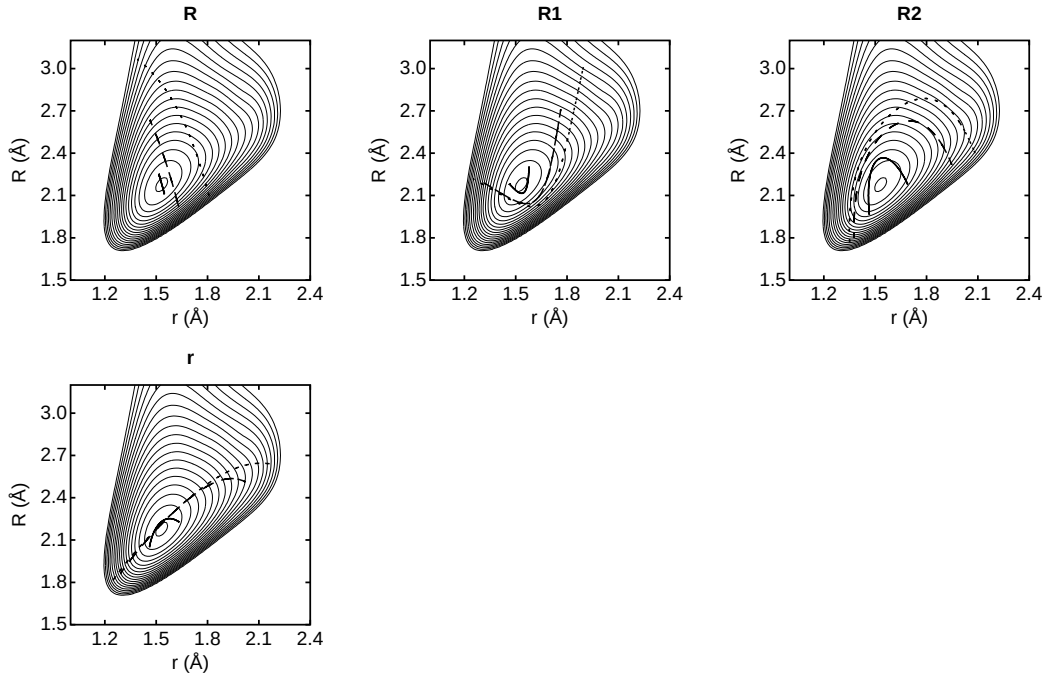

Figure 6.14: Projections in the $\{R, r\}$ plane of orbits at low, medium, and high energies of the **R**, **R1**, **R2**, and **r** families in DCP, superimposed on the potential contours for $\gamma = \pi$ rad. The inner contour is at −5.2 eV and the increment is 0.3 eV.

the plot, the families **R1** and **R2** exhibit substantial oscillation in both R and r coordinates. We will relate them below to certain progressions of quantum states which have similar behavior.

Let us note that at −1.3 eV a sharp dip followed by an equally sharp peak at −1.23 eV is exhibited by **r**, and, as it turns out, by other families (**B1**, **SN1u**,**SN4u**). The peak occurs at the same energy as in HCP and can be attributed to a very acute resonance with R, while the plunge in the period prior to it indicates that the relevant orbits started to explore a quite steep region of the potential.

B, the principal family exhibiting excitation in the γ-oscillator, starts with a period of 6.16 t.u.. As energy increases, the eigenvalues of the monodromy matrix come very close to ± 1 but do not leave the unit circle apart from a brief interval of complex instability between -3.4815 eV and -3.4626 eV. A steady–state bifurcation prior to reaching (-3.2424 eV, 8.39 t.u.) gives birth to the **B1** family which inherits the stability. The **B** family becomes more unstable as energy grows and undergoes another bifurcation at -0.709 eV becoming doubly unstable. **B1** starts at 8.388 t.u. and undergoes two successive Hopf bifurcations at -2.9323 eV and 2.8676 eV which render it temporarily complex unstable. Two successive period–doubling bifurcations at -2.8666 eV and -2.4213 eV make it singly and doubly unstable, respectively, at least up to the final energy we continued it. Plots of various orbits of the **B** and **B1** families are given in fig. (6.15).

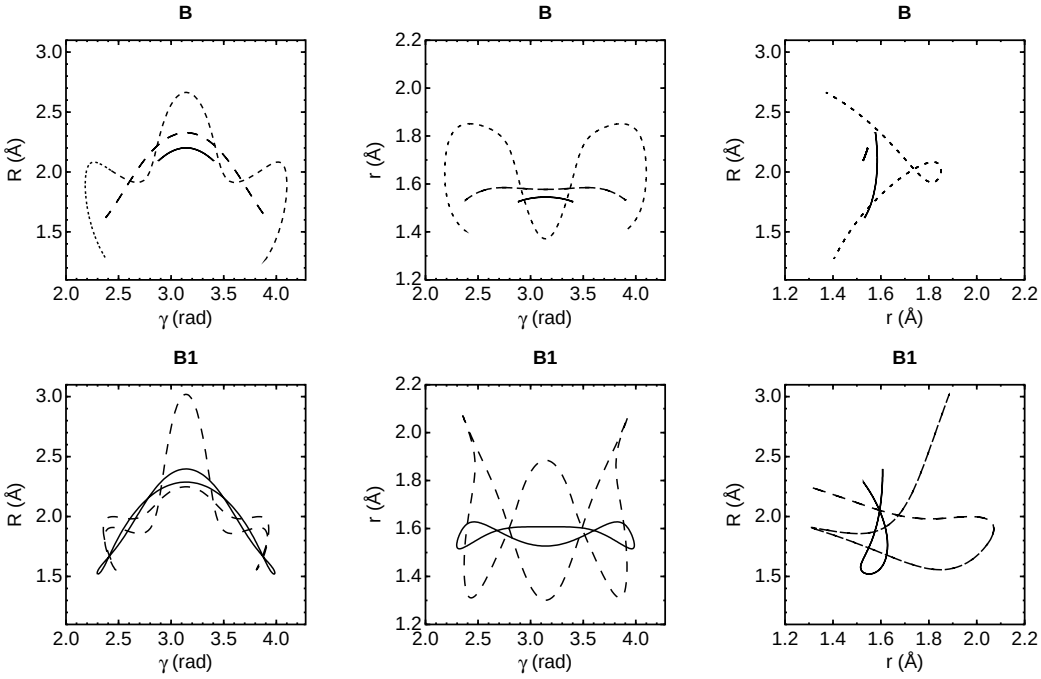

Figure 6.15: Projections of various orbits in DCP from the **B** family (upper figures) at low (solid line), medium (dashed line), and high (dotted line) energies, and the **B1** family (lower figures) at low (solid line) and high (dashed line) energies. Their data are given in table (6.3).

A similar observation for the bending orbits we made in the HCP case holds also for the DCP phase space. The orbits of the **B** and **B1** families go deeper on the isomerization path but are still confined, even at high energies, in angles ± 1 rad around the equilibrium geometry. Although they do have the proper shape, they do not probe deeper and deeper the CP–D hemisphere with increasing energy as one might expect but, rather, they deposit the excess energy in the other two modes. This is intriguing as the γ-oscillator does not take part, at least initially, in a low-order resonance with the others; we attributed the confinement in HCP to such a resonance. The solution lies in the significant anharmonic character of the bending mode in contrast to the other two (and to the **B** family in HCP). γ gradually tunes

at high energies into a resonance with the R- and r-oscillators, effectively confining the **B** and **B1** families to small deviations from equilibrium.

Many saddle–node families have been located in the DCP phase space. The first such family is born at (−3.0895 eV, 8.9660 t.u.) and is denoted by **SN1**. Its orbits do not extend more than 1 rad away from the equilibrium. It is not symmetric with respect to $\gamma = \pi$ rad so we expect its "mirror" family to exist; both play a limited, if any, role in the quantum picture. The stable branch **SN1s** undergoes a Hopf bifurcation at −3.065 eV which renders it complex unstable. Around −2.91 eV it regains stability through another Hopf bifurcation, losing it shortly afterwards at (−2.88 eV, 9.64 t.u.) through a period doubling bifurcation. Another period–doubling bifurcation at −2.725 eV renders **SN1s** doubly unstable. The unstable branch, **SN1u**, undergoes at −2.012 eV a period–doubling bifurcation. The two eigenvalues that leave the unitary circle at this energy return at −1.126 eV. Representative orbits of **SN1** are given in table (6.4) and plotted in fig. (6.16).

A saddle–node bifurcation at (−2.991 eV, 10.107 t.u.) gives birth to the **SN2** family. The two branches can be characterized as stable and unstable in a reduced phase space judging from the position of one pair of eigenvalues on the unitary plane. The second free-to-move pair makes both unstable. **SN2s** undergoes successively in an energy region from −2.96 eV to −2.34 eV a cascade of period–doubling and Hopf bifurcations which, apart a very small region of stability, render it as complex unstable. There is an indication that this branch incorporates the branches of another saddle–node bifurcation at (−1.1572 eV, 12.647 t.u.) but we could not isolate it. The initially doubly unstable branch, **SN2u**, undergoes two period–doubling bifurcations at −2.985 eV and −1.033 eV; in this region it is singly unstable. The orbits of **SN2** are also non-symmetric with respect to $\gamma = \pi$ rad. Interestingly enough, the orbits of **SN2u** tend to be symmetric with increasing energy; this is achieved above −1.93 eV. The evolution of **SN2** is depicted by representative orbits in fig. (6.16); their data are given in table (6.4).

Another saddle–node bifurcation was located at (−2.8456 eV, 12.9731 t.u.). The family emanating from it is denoted with **SN3**. Its stable branch, **SN3s**, undergoes a series of Hopf bifurcations at −2.8375 eV, −2.681 eV, −2.648 eV which toggle the stability, leaving the family doubly unstable. In the region between −2.3 eV and −1.527 eV a pair of eigenvalues return and remain on the unitary circle. the largest of the eigenvalues grows steadily in magnitude, making the family highly unstable. As we can see in fig. (6.17), the orbits of **SN3** are symmetric with respect to $\gamma = \pi$ rad and probe the isomerization path deeper than the previous saddle–node families.

SN4 is born at (−2.2985 eV, 16.1594 t.u.). Both branches of it are, as in the case of **SN2**, unstable. The family undergoes a series of bifurcations none of which changes it qualitatively. The shape of its orbits is depicted in fig. (6.17); they are non-symmetric.

At (−3.4363 eV, 5.9033 t.u.) another saddle–node bifurcation occurs and **SN5** is born. This family is robust in the sense that its branches do not alter their stability at least up to −1.51 eV where our data end. Another saddle–node bifurcation was located at (−2.5722 eV, 5.6741 t.u.). The family emanating from it is denoted with **SN6**. The stable branch undergoes a bifurcation only at −0.53 eV through which it

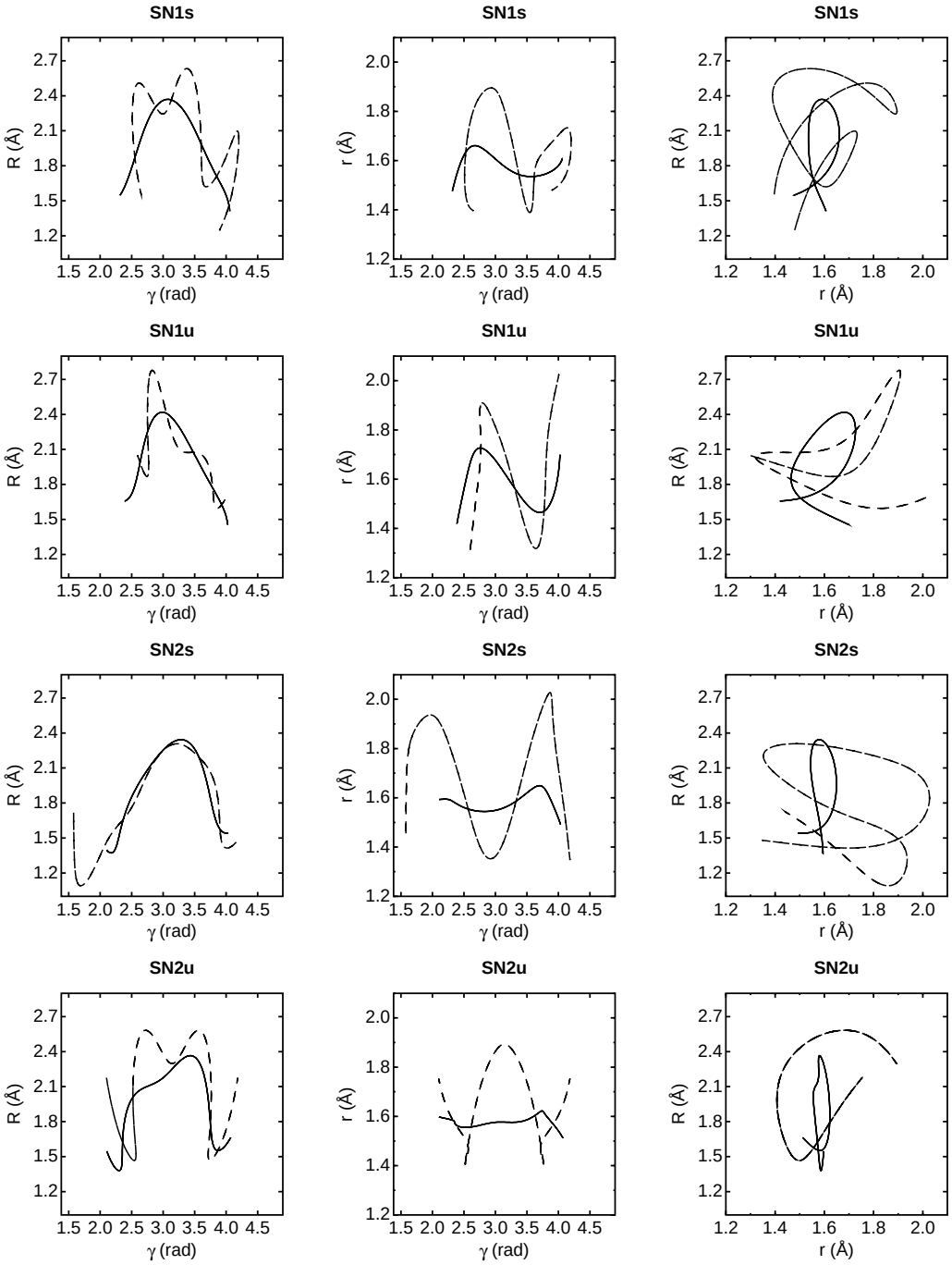

Figure 6.16: Projections of orbits from the stable (first row) and unstable (second row) branches of **SN1** and the stable (third row) and unstable (fourth row) branches of **SN2** families in DCP at low (solid line) and high (dashed line) energies. Their data are given in table (6.4).

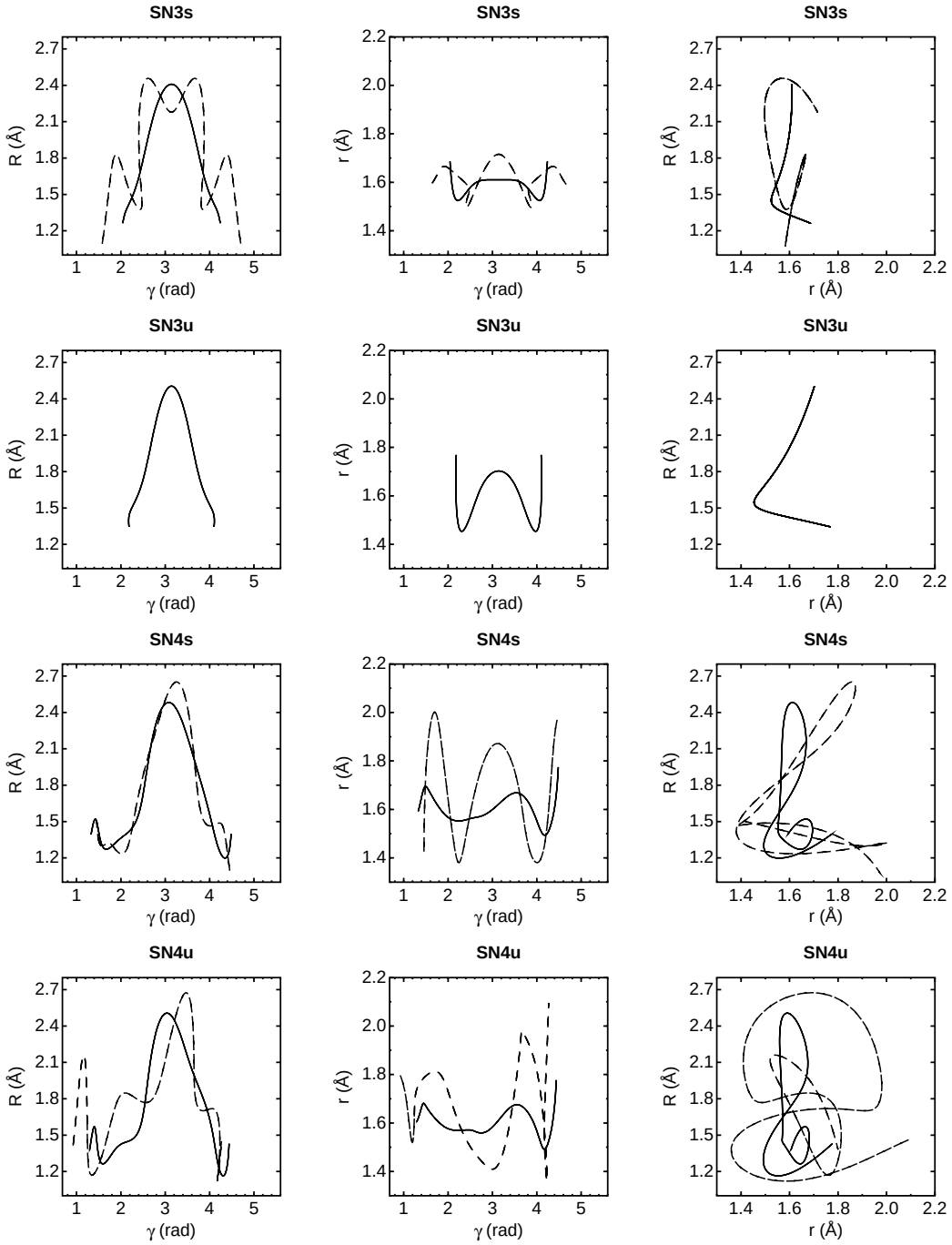

Figure 6.17: Projections of orbits from the stable (first row) and unstable (second row) branches of **SN3** and the stable (third row) and unstable (fourth row) branches of **SN4** families in DCP at low (solid line) and high (dashed line) energies. Their data are given in table (6.4).

loses stability. We were not able to continue the unstable branch above -2.325 eV; it appears to head towards a bifurcation which will stabilize it. Plots of representative orbits of **SN5** and **SN6** are plotted in fig. (6.18); their data are given in table (6.4). We can see that the orbits of both families are symmetric with respect to $\gamma = \pi$ rad.

We have also located another family of periodic orbits which we were not able to identify as a bifurcating branch of any family. The first orbit from the denoted with **UN** we found is at (-2.3736 eV, 14.2665 t.u.); we have continued the **UN** family well above the dissociation limit. In the energy region we have data for, the family is unstable. Its evolution is depicted in fig. (6.19).

Notice that the orbits from the saddle–node families we located are either non-symmetric with respect to $\gamma = \pi$ rad (**SN1**, **SN2**, **SN4**), or their shape is not the appropriate one to explore the isomerization path (**SN5**, **SN6**). The **SN3** family, which lack these limitations, is highly unstable and, therefore, is unable to induce localization of wave functions. There seem to be no families to facilitate the transition of the molecule from D–CP to CP–D in contrast to the HCP case we examined in the previous section.

6.5 Quantum Treatment and Discussion

The quantum mechanical study of HCP has been presented in [143] by Beck *et al.*, while for DCP it was published by Bredenbeck *et al.* in [169]. We review and augment them below.

6.5.1 HCP

The quantum treatment of HCP was performed for $J = 0, 1, 2$; it was treated in in Jacobi coordinates and the corresponding Hamiltonian operator is given in eq. (4.1). The nuclear wave function was expanded on a set of basis functions for the angular motion, represented by the three Euler angles χ, ϕ, θ and the Jacobi angle γ, while the two stretching coordinates were treated by the discrete variable representation (DVR). 116 products of the Wigner functions $D^J_{KM}(\chi, \phi, \theta, \gamma)$ with the associated Legendre polynomials $P_{\ell K}(\gamma)$ were used as basis functions for the angular part; equidistant grids with 42 and 45 nodes were used for R and r respectively. The initial set of 219240 direct product basis functions was drastically contracted in a sequence of diagonalizations and truncations leaving a manageable optimized basis set of ca. 9500 functions; in this basis, the Hamiltonian was diagonalized to produce the energies and wave functions. For non-zero angular momentum, this procedure was repeated for every allowed value of K and for the final step, the Coriolis coupling was introduced and parity was taken into account. The calculations were deemed fairly accurate as the energies deviated by less than 0.1 cm^{-1} in the energy window of interest, compared to the same procedure with a different cut-off energy.

The classical harmonic expansion of the potential around the equilibrium provided us with the oscillator periods. From them we can estimate the quantum vibrational frequencies of the normal modes, once we clarify a point.

The deviation of the C–P bond, during the molecular vibrations, from the closest principal axis at the equilibrium configuration is small, due to the small mass and

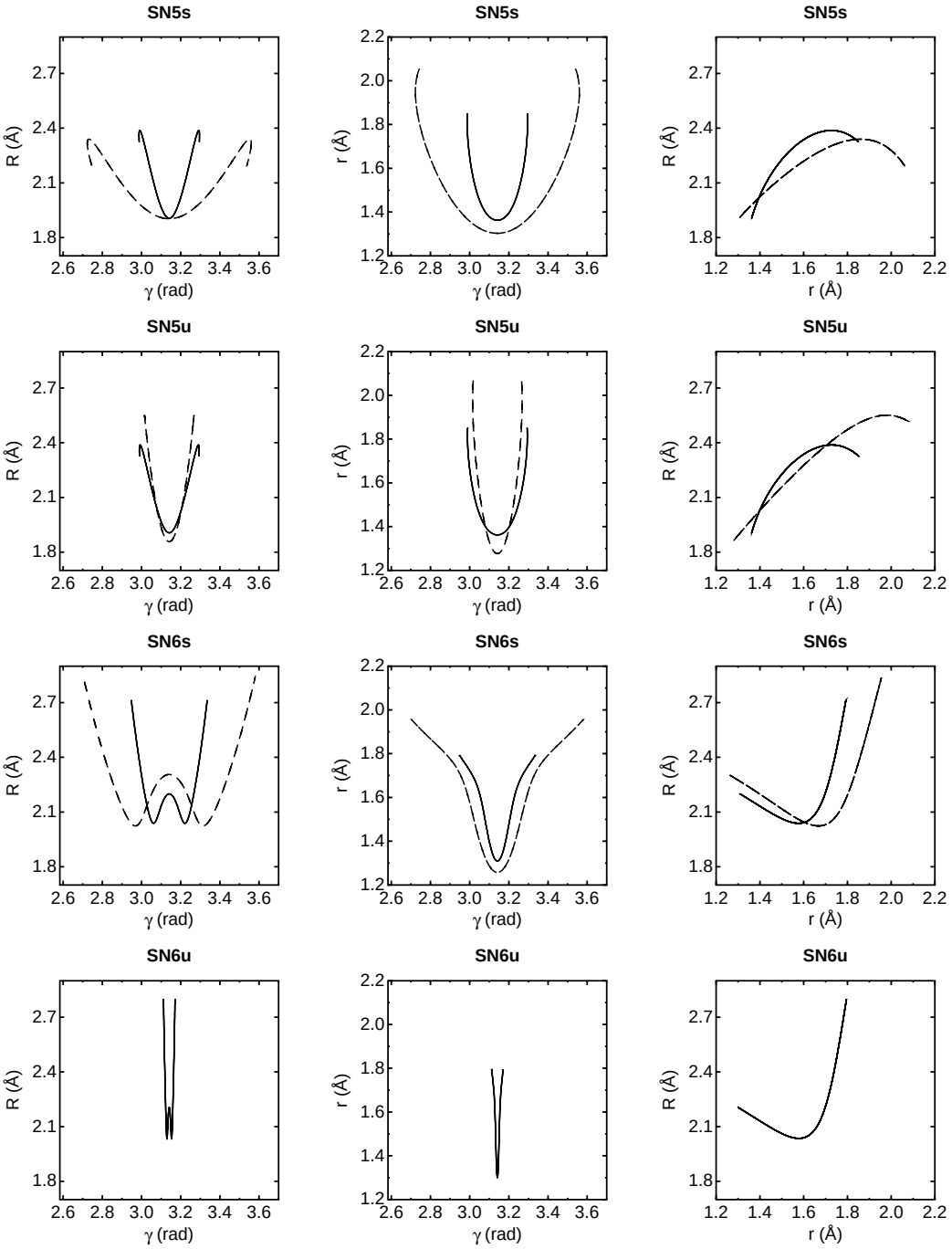

Figure 6.18: Projections of orbits from the stable (first row) and unstable (second row) branches of **SN5** and the stable (third row) and unstable (fourth row) branches of **SN6** families in DCP at low (solid line) and high (dashed line) energies. Their data are given in table (6.4).

FAMILY	**ENERGY**	**PERIOD**	R	r	γ	P_R	P_r	P_γ
R	−5.1003	1.3268	2.2273687	1.5214012	3.1415927	−0.4782257	0.5092888	0.0000000
R	−2.9765	1.6060	2.3714688	1.5461717	3.1415927	−2.2675684	2.8123480	0.0000000
R	−0.3438	2.1820	2.1208529	1.8033018	3.1415927	−2.1695934	2.1591702	0.0000000
R1	−5.0333	2.6353	2.2621841	1.5761610	3.1415927	−0.6175855	−0.1357361	0.0000000
R1	−2.8958	2.8003	2.5273027	1.7384145	3.1415927	−1.8453430	−1.1790147	0.0000000
R1	−0.8804	3.1396	2.4996629	1.8030716	3.1415927	−3.0466529	−2.5999908	0.0000000
R2	−4.3863	2.7680	2.3214988	1.4926914	3.1415927	−0.8612334	−1.8301493	0.0000000
R2	−2.0506	3.1402	2.5307423	1.8484531	3.1415927	1.2451399	−3.9122003	0.0000000
R2	−0.6785	3.4110	2.6143676	1.9953149	3.1415927	1.6540375	−3.8901253	0.0000000
r	−4.9606	2.6900	2.2292667	1.6320185	3.1415927	0.1036897	−0.5609911	0.0000000
r	−2.1915	3.2842	2.5361241	1.9389049	3.1415927	−0.0111790	−3.1515895	0.0000000
r	−0.5852	3.2210	1.8889490	1.2914384	3.1415927	−1.5717710	−4.4170844	0.0000000
B	−5.0062	6.3400	2.1535920	1.5373171	2.9685295	−0.2052299	−0.1659303	−1.2167127
B	−3.5012	7.7550	1.6354504	1.5368249	2.3927095	−0.2636214	−0.3331103	−0.4887950
B	−0.6867	11.1700	2.0107943	1.8512616	2.4312595	−0.7393502	−0.0918696	4.1273203
B1	−3.1941	8.3861	1.5208009	1.5461873	2.3013416	−0.0406436	1.0648523	0.2355702
B1	−0.4668	9.6900	1.8275395	2.0619105	2.3618707	1.0770120	1.1428557	−0.5869025

Table 6.3: Initial conditions for representative periodic orbits of the fundamental families in DCP. Lengths are measured in Å, the angle in rad, the energy in eV, the period in t.u. ($\sim$ 10.18 fs) and the momenta in the appropriate derived units.

FAMILY	ENERGY	PERIOD	R	r	γ	P_R	P_r	P_γ
SN1s	−3.0895	8.9760	2.3693828	1.5889036	3.0801728	−0.0219529	−1.2253630	4.8463924
SN1s	−0.9172	11.5060	1.8797413	1.4929573	3.6065259	−3.1151192	4.0224487	0.2779638
SN1u	−2.9131	8.7453	2.4178266	1.6784751	2.9941691	−0.0460034	−1.6347977	4.4625792
SN1u	−1.0033	9.4380	2.7274377	1.9085369	2.7825650	0.9685827	0.2922084	1.7030140
SN2s	−2.9910	10.1170	1.3819965	1.5935884	2.1304594	0.1036559	−0.0219305	−0.3975258
SN2s	−0.8642	13.1070	1.1176613	1.8147427	1.6367395	−0.7510942	3.0236058	0.6679760
SN2u	−2.8085	10.0304	1.4070718	1.5903374	2.2327248	−0.4944988	−0.1871978	1.1977582
SN2u	−0.6735	11.9304	2.1165717	1.4129348	2.5215535	2.6602865	1.1434884	0.3588949
SN3s	−2.8267	13.1331	1.2624105	1.6862939	2.0439904	0.0030314	−0.0167837	0.0017113
SN3s	−1.3333	16.3300	1.8051870	1.6649135	1.9478711	−0.5289868	−0.1949035	1.7109558
SN3u	−2.5587	12.2131	1.3763453	1.7010516	2.1761329	−0.2213092	2.1687719	0.0533989
SN4s	−2.2985	16.1494	1.4399776	1.6095782	1.3518811	0.3974407	0.7248303	0.3803573
SN4s	−1.1369	17.1015	1.3343786	1.7698387	1.5051346	−0.3684400	4.1771486	0.4589119
SN4u	−2.2544	16.5294	1.5029406	1.6313129	1.3494232	0.5559545	0.6792178	0.5022181
SN4u	−0.4417	19.3000	1.6187653	1.6333020	1.2397503	−2.3679562	2.4929954	0.1716384
SN5s	−3.4363	5.9032	2.3572961	1.8151762	2.9872208	−0.3632237	2.2613527	0.0056375
SN5s	−1.6113	6.6366	2.2029959	2.0562071	2.7434976	0.3022827	−0.8166277	−0.3089998
SN5u	−3.4360	5.9040	2.3582824	1.8156101	2.9888705	−0.3590358	2.2569597	0.0050691
SN5u	−1.7505	6.7042	2.5237141	2.0687197	3.0180893	0.1686834	−1.2068364	−0.0720976
SN6s	−2.5235	5.6820	2.6380467	1.7817087	2.9563406	−1.2029041	−0.8339630	0.6521618
SN6s	−0.3451	6.3900	2.3943967	1.8563982	2.8128237	−2.5741959	−2.8349772	3.0777531
SN6u	−2.3355	5.7854	2.6769965	1.7794002	3.1140773	−1.5552622	−0.9496759	0.1230657
UN	−2.3579	14.2725	2.1333298	1.6814832	3.2664908	1.4886997	4.5433776	−1.3073484
UN	−0.4293	16.0255	3.1221978	1.8917499	3.1437628	0.0821346	0.0800814	−1.1919754

Table 6.4: Initial conditions for representative periodic orbits of the saddle–node families in DCP. Lengths are measured in Å, the angle in rad, the energy in eV, the period in t.u. (~ 10.18 fs) and the momenta in the appropriate derived units.

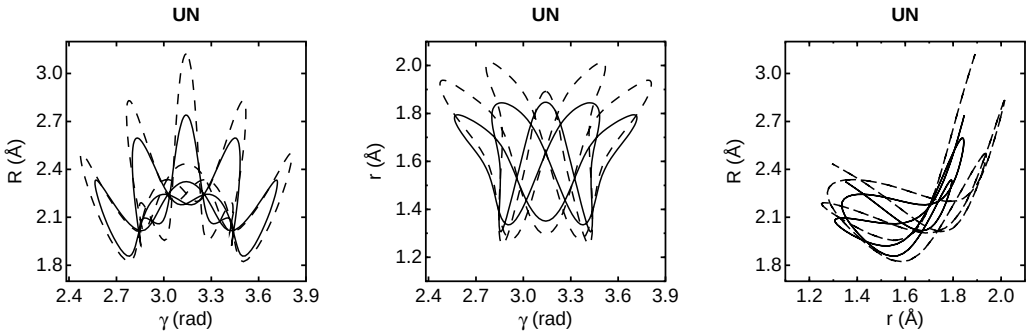

Figure 6.19: Projections of orbits from the **UN** family in DCP at low (solid line) and high (dashed line) energies. Their data are given in table (6.4).

distance from C–P of H/D. Therefore, we can regard the C–P bond as the molecule-fixed z-axis. This choice offers the advantage of rendering the Coriolis coupling, the terms with the raising/lowering operators, very small. This coupling spoils the conservation of the eigenvalues $K\hbar$ of $\widehat{\mathscr{J}_z}$ (which are also eigenvalues of $\widehat{\ell_z}$ with our choice for the z-axis) by mixing states with adjacent K; making the coupling small allows us to regard K as a good quantum number. This K in spectroscopic literature is called the vibrational angular momentum quantum number.

The second normal mode has almost pure bending character. Since the equilibrium structure of the HCP $\widetilde{X}$ electronic state is linear, the bending vibration is doubly degenerate. This leads to the restriction that the eigenvalues of $\widehat{\mathscr{J}_z}$, $K\hbar$, satisfy $|K| = v, v-2, \ldots$ and 0 or 1 for even or odd bending quantum number v respectively. The total angular momentum J must be larger or equal to K. As we treat classically the molecule as having $J = 0$, it follows that K is zero and v must be even; therefore, the quanta of the bending mode are twice the classically estimated. With the above in mind, the quanta of the normal modes are calculated from classical data to be 0.4144 eV (3342.68 cm^{-1}), 0.1592 eV (1283.67 cm^{-1}), and 0.1701 eV (1371.67 cm^{-1}) for the R, r and bending modes respectively. The fundamental frequencies as determined by the quantum calculations are 3216.56 cm^{-1}, 1274.58 cm^{-1} and 1333.74 cm^{-1} respectively, while the experimental values (from [155]) are 3216.889 cm^{-1}, 1278.278 cm^{-1} and 1334.980 cm^{-1}. The quantum and experimental results are in very good agreement (as the PES was appropriately modified to achieve this), while the slight discrepancy exhibited in the classical values can be accounted for: the frequencies of the classical oscillators were computed at the minimum of the potential while the quantum treatment incorporates the zero-point energy. From the classically estimated quanta we can compute the ground-state energy at -4.86435 eV, in excellent agreement with the correct value of -4.86776355 eV.

The principal feature of the HCP quantum phase space is, as in the classical analysis, the pronounced 2:1 anharmonic resonance between the bending and r normal modes, i.e. $2v_2 = v_3$. This resonance leads to a quasi-degeneracy of eigenstates with the same *polyad number* $P = v_2 + 2v_3 = 0, 1, 2 \ldots$ (and the same v_1). The quantum states are organized in well-defined "clusters" termed as *polyads*, which, in the low energy regime are far from each other. We will use the notation $[[v_1, P]]$

for each polyad; the states can be assigned as $(v_1, P-2v_3, v_3)$. There are $(P+2)/2$ and $(P+1)/2$ individual states in each polyad for even and odd values of P respectively. In low energies the pure v_2 overtones $(0, v_2, 0)$ lie at the top of the polyad whereas the pure v_3 overtones $(0, 0, v_3)$ lie at the bottom. The characteristics of the polyads are generally the same up to [[0,16]]. Qualitative changes occur above this "cluster," starting from the bottom states which gradually assume the character of isomerization states.

The first mode essentially represents the H–CP stretch. It is weakly coupled to the other two modes and due to its large quantum, few members of its pure progression lie in the energy window of interest and were unambiguously identified. Those wave functions which were visually assigned to the $(v_1, 0, 0)$ states can be shown to be scarred by periodic orbits of the **R** family with appropriate energies, that is, their energy above the potential minimum is roughly equal to the excitation energy of the wave functions.

The members of the $(0, v_2, 0)$ progression start out as true bending states at the bottom of the energy-level spectrum, that is, they exhibit excitation predominantly on the bending angle. Due to the resonance, however, they gradually evolve towards larger CP bond distances as v_2 increases. As we can see in fig. (6.20) [R. Schinke, personal communication] where representative members of the pure bending progression are depicted, the series acquires a CP stretch character and, as a consequence, its members, even at high energies, are confined to angles $\pm 40°$ around the HCP equilibrium. They do not follow the isomerization path from H–CP to CP–H as

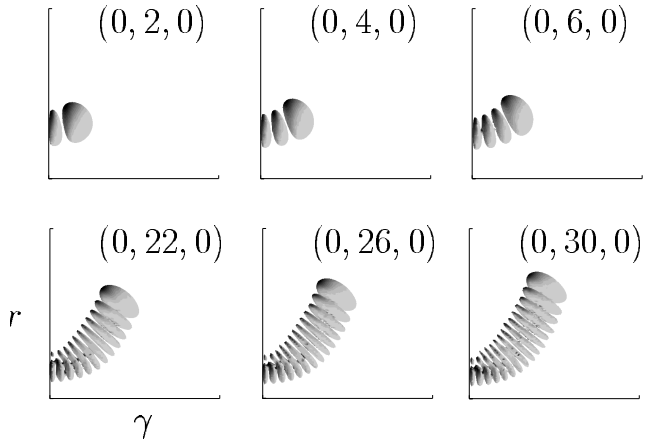

Figure 6.20: Various members of the $(0, v_2, 0)$ progression in HCP. Shown is one particular contour $R^2 r^2 \sin\gamma |\Psi(R, r, \gamma)|^2 = \text{const.}$. The plots are viewed along the R axis in the direction perpendicular to the $\{r, \gamma\}$ plane. The r axis ranges from 2.4 α_0 to 4.0 α_0 and the γ axis ranges from 180° to 100°. Due to the $\sin\gamma$ factor, a node at the linear configuration exists irrespective of whether v_2 is even or odd.

one would expect through a normal mode analysis, even when their energies lie well above the energy where the minimum energy path departs from the potential well around the equilibrium and levels off to the CP–H side. The $(0, v_2, 0)$ states are very robust in the sense that they form regular series easily recognizable up to very high energies where many other states are unassignable due to strong mixing with their neighboring states. Wave functions of this progression do not alter their

general shape; with increasing energy more nodes build up. If we recall the shape and the almost continuous stability of the periodic orbits comprising the **B** family, we can clearly consider them as backbones of the $(0, v_2, 0)$-type wave functions. As will be shown below, there is also a quantitative match between **B** and the bending progression.

The third pure progression $(0, 0, v_3)$ comprises wave functions which evolve along the CP stretching coordinate, r. They are also robust and easily identified even at high energies. As inferred by fig. (6.21) [R. Schinke, personal communication] and fig. (6.6), they are obviously scarred by orbits of the **r** family.

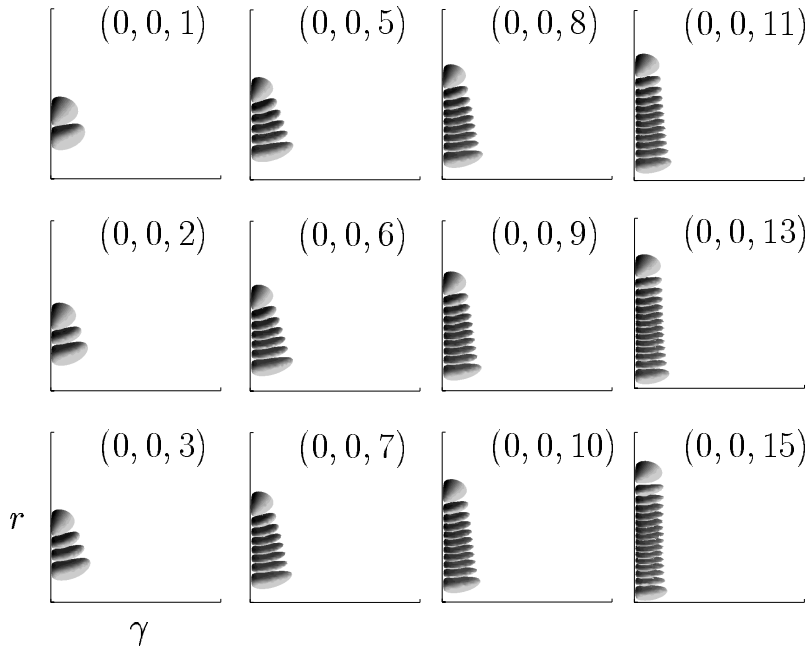

Figure 6.21: Various members of the $(0, 0, v_3)$ progression in HCP. The r axis ranges from 2.4 α_0 to 4.0 α_0 and the γ axis ranges from 180° to 100°.

A remark pertaining to all wave functions of the pure progressions is that the quantum numbers in their assignment are consistent with the number of nodes along the corresponding scarring periodic orbits and not necessarily along the coordinate axes. This distinction is not that prominent in the HCP case we examine here, as the fundamental periodic orbit families follow the R, r and γ oscillators, at least in low energies; it is very clear, though, in the DCP spectrum as we will explain in the following section.

States which exhibit large-amplitude bending motion of the hydrogen atom around CP emerge rather abruptly at high energies. The so called "isomerization states" appear as mutations of the lowest states in the polyads from $P = 18$ onwards, and gradually their neighboring states also acquire a true bending character, replacing the regular states. As we can see in fig. (6.22) [R. Schinke, personal communication], the isomerization states, parametrized by the polyad number and denoted by $(0, P, 0)_I$, are not confined to angles close to linearity as the members of the bending progression are. Due to the substantial change in the slope of the potential along the minimum energy path towards the CP–H region, the $(0, P, 0)_I$

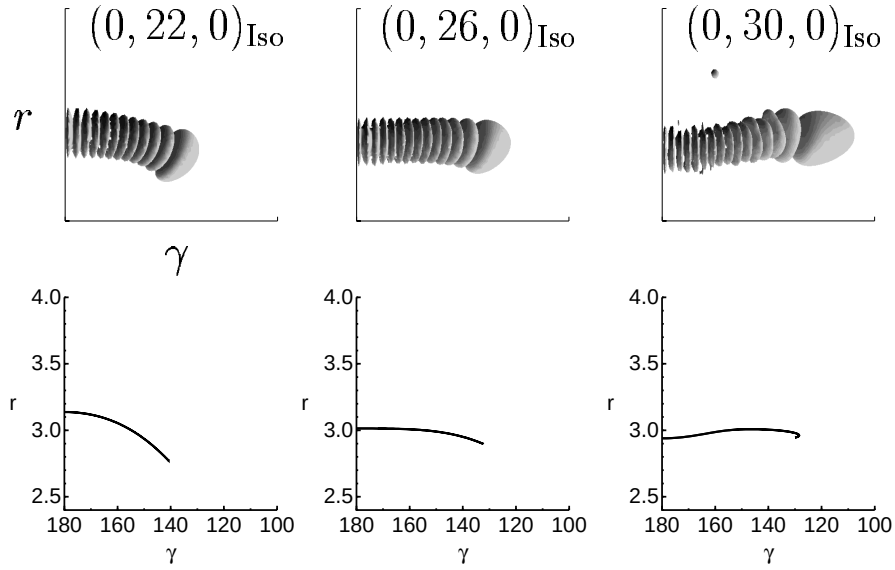

Figure 6.22: Upper row: Isomerization states in HCP. Lower row: Corresponding classical periodic orbits. The r axis ranges from 2.4 α_0 to 4.0 α_0 and the γ axis ranges from 180° to 100°.

progression is considerably more anharmonic than the pure v_2 progression. This causes neighboring polyads to overlap, making the energy spectrum complicated and confusing. The first wave function clearly assigned as an isomerization state, $(0,22,0)_I$, appears at -3.203 eV or 1.664 eV above the zero-point energy. At almost exactly (within 5×10^{-3} eV) this amount of energy above the potential minimum the first saddle–node bifurcation occurs; naturally, **SN1** also influences lower quantum states. Recall that the orbits in the steep segments of **SN1** and **SN2** exhibit excitation primarily in γ; the resonance skews the branches and increases the amplitude of r. We can therefore consider the orbits in the steep segments as the backbones of the pure $(0,P,0)_I$ progressions. This is verified in the lower row of fig. (6.22) where the "corresponding" periodic orbits are plotted. Their energy above minimum roughly equals the excitation energy (i.e. above zero-point energy) of the depicted isomerization states.

In fig. (6.23) a striking evidence of the correspondence of quantum and classical results is depicted. In the upper part of the figure, reprinted from [168], the calculated [168] and the experimental [150,154,155] energy differences between neighboring quantum states of the progressions $(0,P,0)$, $(0,0,P/2)$ and $(0,P,0)_I$ versus the polyad quantum number P are plotted. In the lower part, the classical equivalent is given: the frequencies of the periodic orbits of the **B** (multiplied by 2), **r**, and **SN** (multiplied by 2) families are plotted against the polyad number P as inferred by the classical energy E. In the harmonic approximation, the classical energy above minimum is proportional to the classical action; this in turn relates linearly to the quantum numbers via the EBK quantization rule, eq. (2.22). Exact quantitative correspondence of course cannot be expected, nevertheless, all the features of the system as exhibited in the quantum diagram are present in the classical one: kinks and "dips" or minima of interpolyad level spacings appear also on the periodic orbit

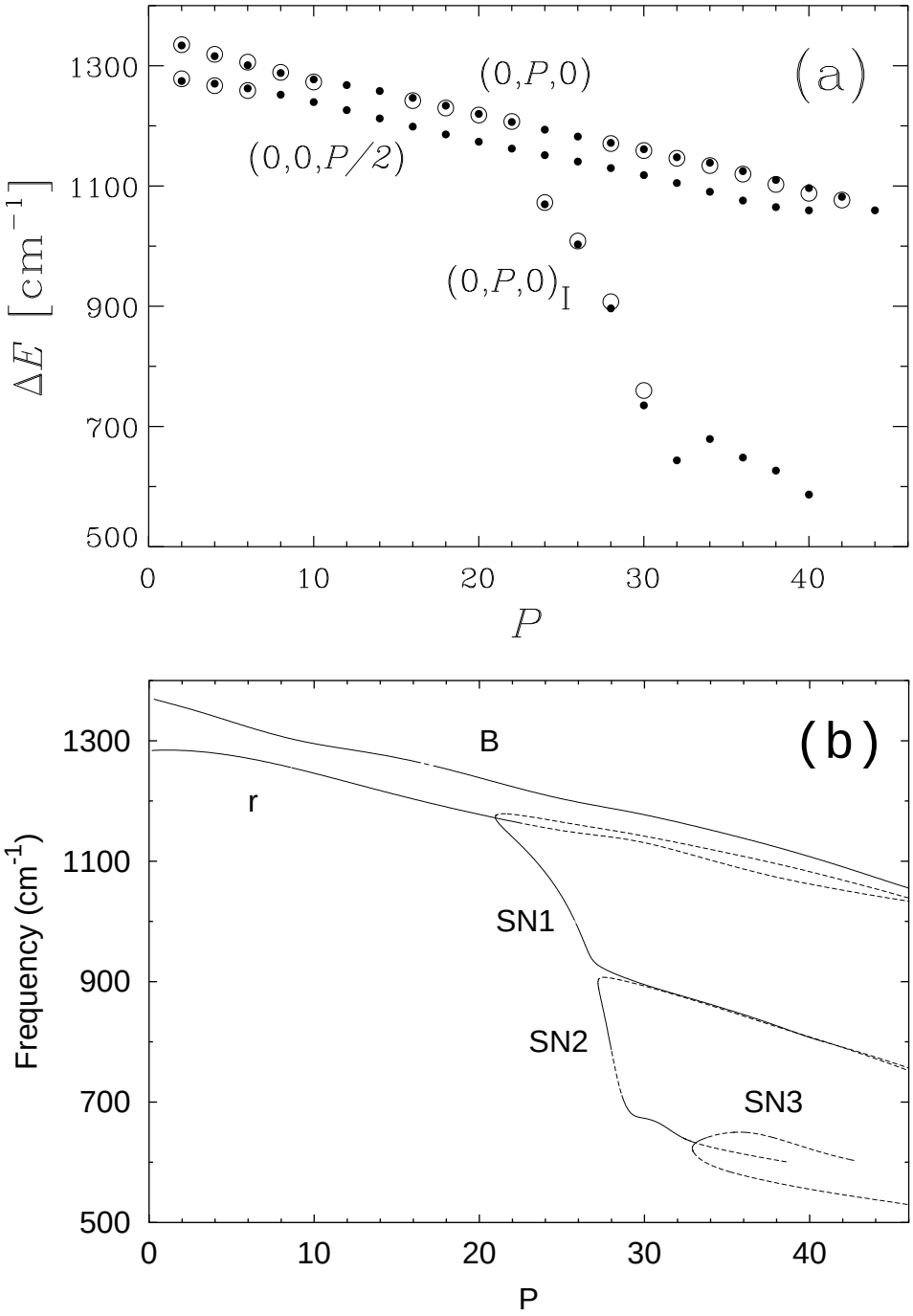

Figure 6.23: (a) Energy differences between neighboring states of the $(0, P, 0)$, $(0, 0, P/2)$ and $(0, P, 0)_I$ progressions versus polyad number P in the HCP spectrum. Dots indicate quantum mechanical calculations and are plotted at the higher state, open circles show the experimental results. (b) Classical frequencies of the **B**, **r**, and the saddle–node families versus a classically estimated polyad number (see text). The linetype changes with the stability.

families, the convergence of $(0, P, 0)$ and $(0, 0, P/2)$ progressions at high energies is exhibited by the **B** and **r** families which correspond to these progressions. We also note that the behavior of the quantum isomerization states, which exhibit small r excitation, is reflected in the steep segments of the saddle–node states; once they level off due to the onset of resonance with r, one can surmise that they influence the $(0, v_2, v_3)$ progressions.

Svitak and co-workers [176] showed that characteristic patterns in the spectrum of a pair of resonant modes are associated with the structure of the corresponding classical phase space. According to them, a "dip" or minimum of interpolyad level spacings implies a separatrix, a structure in the classical phase space that contains an unstable periodic orbit. More complicated phase space structures which involve more than one periodic orbit, e.g. those formed after a saddle–node bifurcation, can give rise to more complex spectral patterns. Joyeux *et al.* in [177] examine such patterns in the energy spacing between adjacent levels in the HCP spectrum.

6.5.2 DCP

All quantum calculations for DCP assumed a non-rotating molecule. The Hamiltonian for DCP, eq. (4.1), was represented in a highly contracted-truncated three-dimensional basis in a similar manner to the HCP case. The initial 322770 functions were shrunk to 12087; tests were performed with different cut-off energies to assess the error of the variational calculations and ensure the accuracy of the results. The uncertainty for the energies of the less satisfactory converged progression is of the order of 1 cm^{-1} while for most states the accuracy is much higher. It is worth noting that the agreement between the quantum calculations of the transition energies and the limited experimental results is excellent.

The classical harmonic expansion of the potential around the equilibrium provided us with the oscillator periods. From them we can calculate the quanta of the normal modes to be 0.3092 eV (2493.87 cm^{-1}), 0.1526 eV (1230.80 cm^{-1}) and 0.1320 eV (1064.65 cm^{-1}) for the R, r and bending modes respectively, keeping in mind the remark on the bending frequency we elucidated in the HCP case. The fundamental frequencies as determined by the quantum calculations are 2419.44 cm^{-1}, 1228.68 cm^{-1} and 1037.17 cm^{-1} respectively. We notice the very good agreement of classical and quantum frequencies although they are not supposed to be directly comparable. One could attribute the more accurate, than in HCP, classical predictions to the larger mass of D compared to H; it makes the molecule more suitable for classical treatment. The ground-state energy is classically estimated at -4.9393 eV, while the correct quantum value is -4.9410 eV.

As expected by the classical analysis, the quantal spectrum of DCP is governed by a 1:2 anharmonic resonance between the two stretching modes v_1 and v_3. This resonance leads to a quasi-degeneracy of eigenstates with the same *polyad quantum number* $P = 2v_1 + v_3 = 0, 1, 2 \ldots$ (and the same bending quantum number v_2). The bending degree of freedom is—at least in the low and intermediate energy regimes—relatively weakly coupled to the two stretching degrees of freedom. The spectrum is structured in terms of polyads; we will denote them with $[[v_2, P]]$. Up to [[0,15]] the polyads are distinct and the assignment in terms of v_1 and v_3 is generally straightforward; above $P = 15$ the polyads overlap making the identification more

and more cumbersome. It turns out that the pure v_3 overtones $(0,0,v_3)$ always lie at the top of their polyads whereas the pure v_1 overtones $(v_1,0,0)$ lie at the bottom.

The particular resonance appearing in DCP leads to a substantial mixing of the R and r modes. As a consequence, the pure v_1 and v_3 progressions are not localized parallel to the R and r axes but they develop along the **R** and **R1** periodic orbit families following them up to high energies; the assignment reflects the number of nodes along the corresponding scarring orbits. Recall that the **R1** family is born roughly 0.06 eV above the minimum, well below the quantum zero-point energy (0.29517 eV). In fig. (6.24) we present contours of members of the v_1 and v_3 progressions exhibiting this particular behavior. We can describe the $(v_1,0,0)$ over-

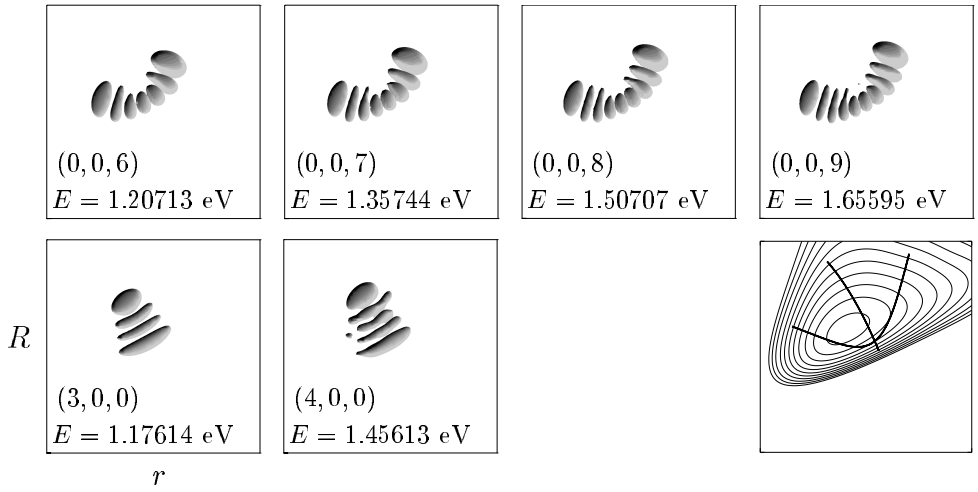

Figure 6.24: Selected wave functions of the $(0,0,v_3)$ and $(v_1,0,0)$ progressions in DCP. Shown is one particular contour $R^2r^2\sin\gamma|\Psi(R,r,\gamma)|^2 = \text{const.}$. The plots are viewed along the γ axis in the direction perpendicular to the $\{R,r\}$ plane. The lower rightmost panel shows the potential energy surface and representative orbits of the **R** and **R1** families. The R axis ranges from 2.2 α_0 to 5.5 α_0 and the r axis ranges from 2.2 α_0 to 3.9 α_0. The referenced eigenenergies are measured from the potential minimum.

tones as D–CP stretching states; a similar classification of the $(0,0,v_3)$ overtones as CP stretching states would certainly be inappropriate. Instead, another group of quantum states exhibits a predominant CP stretch.

An examination of the quantum results shows that a few states with $v_2 = 0$ do not clearly fall into the v_1 and v_3 pure progressions or their combinations but, instead, form different classes. The states assigned as $(v,0,v)$ with $v = 3,4,\ldots$ $(P = 9,12,\ldots)$ judging by their position in the spectrum, are the clearest examples. They gradually develop a new type of shape with increasing v. Their "backbone" is strongly curved in the $\{R,r\}$ plane, too, but in the opposite direction than observed for the v_3 progression. Recalling the shape of the orbits in the **r** family one can relate the new class to these and assign them as $(0,0,P)_r$ to distinguish them from the $(0,0,v_3)$ states. The number of nodes along the backbones of the $(0,0,P)_r$ wave functions is identical to the polyad number P. Notice that states of the new class can be found in higher polyads with P a multiple of 3. In other polyads there are states with similar, but not as clear, character as $(v,0,v)/(0,0,P)_r$; however, in their

assignment v_1 and v_3 must differ by one, i.e. $v_1 - v_3 = \pm 1$. A careful inspection of the $(v, 0, v \pm 1)$ and the low $(v, 0, v)$ levels reveals that these are mixtures of the $(0, 0, v_3)$ and $(0, 0, P)_r$ wave functions. Therefore, the $(0, 0, P)_r$ wave functions do exist in lower energies but are obscured; in higher energies, the mixing decreases and the $(0, 0, P)_r$ character emerges. In fig. (6.25) the wave functions of few $(v, 0, v \pm 1)$ and $(v, 0, v)/(0, 0, P)_r$ states are depicted.

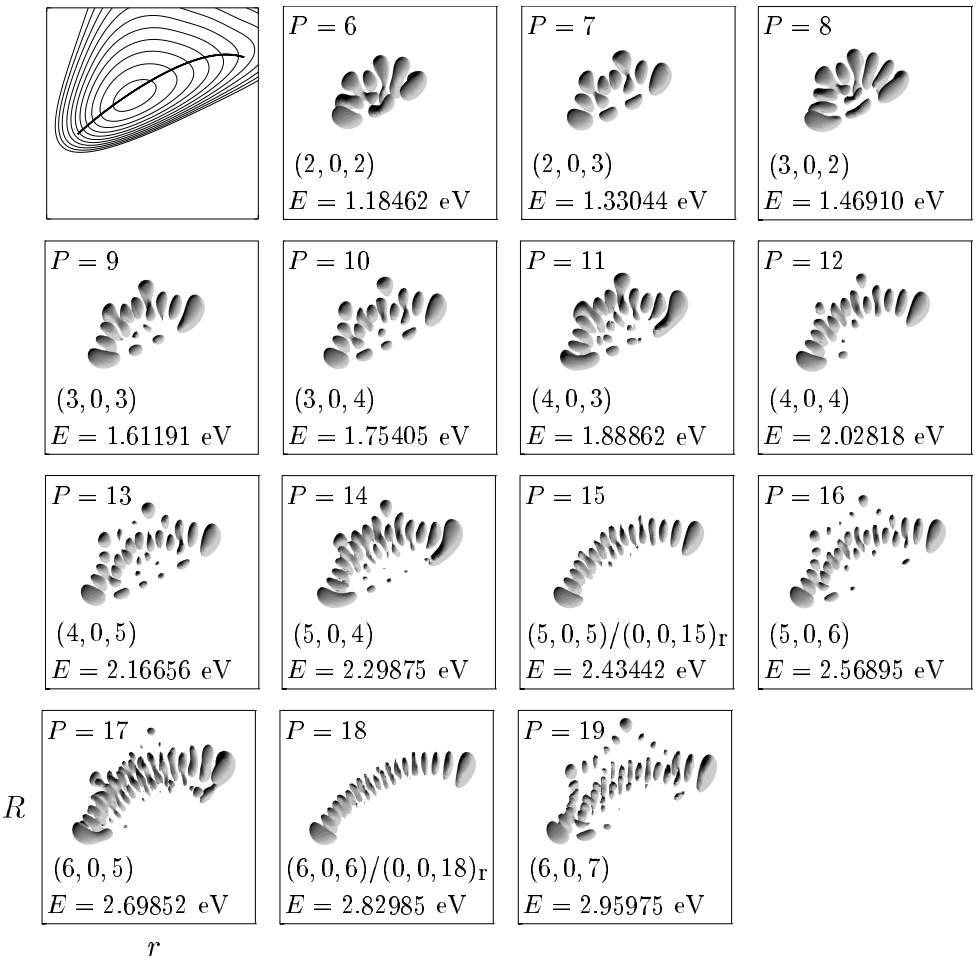

Figure 6.25: Wave functions of the form $(v, 0, v)$ and $(v, 0, v \pm 1)$ in DCP. The first panel shows the potential energy surface and a representative periodic orbit of the **r** family. The axes and the plots are as in fig. (6.24).

The qualitative relation of the three progressions $(v_1, 0, 0)$, $(0, 0, v_3)$ and $(0, 0, P)$ with the corresponding periodic orbit families, **R**, **R1** and **r** can be also exhibited in terms of the energy dependent transition frequencies i.e. the energy differences between adjacent levels, and their relation to the classical frequencies as depicted in fig. (6.26). The energies for the $(v_1, 0, 0)$ progression are divided by 2 because of the 2:1 resonance and the energies of the $(0, 0, P)_r$ progression are divided by 3 as there is one entry for every third polyad. The frequencies of the **R** family are also divided by 2 to follow the $(v_1, 0, 0)$ progression. Additionally, the classical energies with respect to minimum are shifted by the quantum zero-point energy.

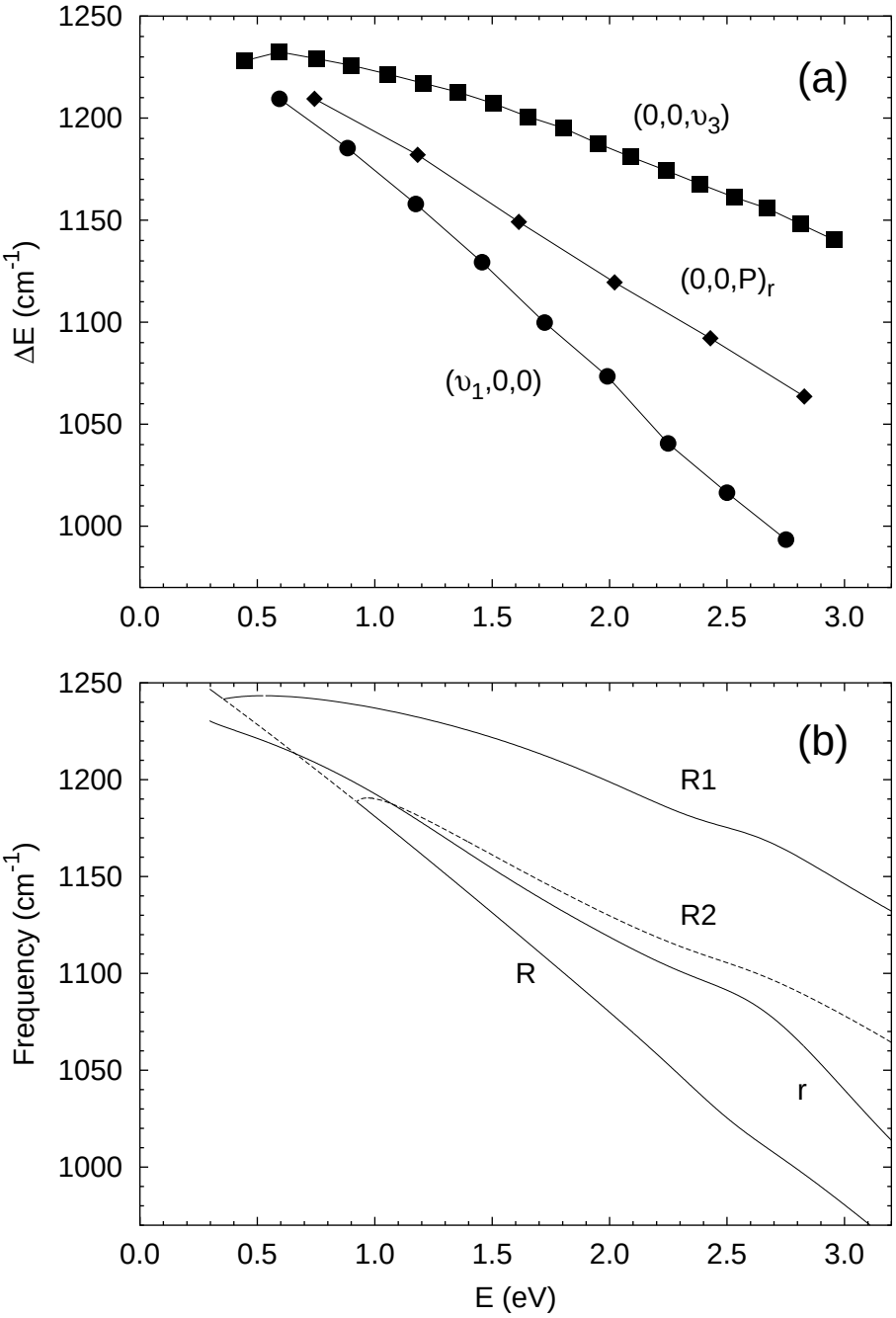

Figure 6.26: (a) Transition energies, i.e. energy differences between neighboring levels, for the three progressions $(v_1, 0, 0)$ (divided by 2) (●), $(0, 0, v_3)$ (■), and $(0, 0, P)_r$ (divided by 3) (♦), in the DCP spectrum. Each symbol is plotted at the energy of the upper state. (b) Frequencies of the periodic orbits of the families **R** (divided by 2), **R1**, **R2** and **r**. The energy of each orbit with respect to minimum is shifted by the zero-point energy. Solid lines represent stable families; dashed ones indicate instability.

At low energies, the transition frequencies for all three progressions are very close together, which implies that here the mixing of modes is strongest. Due to the different anharmonicities of the three progressions, the gap between the transition energies widens. This means that the energy range over which a polyad spreads, increases with energy, which in turn may explain why the mixing between the states $(0,0,v_3)$ and $(0,0,P)_r$ gradually diminishes in the higher polyads. In this respect, there is one detail worth mentioning: The transition energy of the $(0,0,v_3)$ progression first *increases* with v_3 rather than decreases as expected for a vibrational progression. This indicates that the $(0,0,1)$ state is not a true member of the $(0,0,v_3)$ progression; this is actually confirmed by examining the particular wave function. It appears to fit better into the $(0,0,P)_r$ progression rather than the $(0,0,v_3)$ series.

One could expect that the fundamental progression $(0,0,v_3)$ follows the **r** principal family of periodic orbits and not the **R1** bifurcation. There is no apparent reason within the classical framework why this happens. A semiclassical analysis though, provides an explanation to this (cf. Sec. V of [169]).

The bending dynamics of DCP is quite different than what we encountered in HCP. The bending mode is not involved in an low-order anharmonic resonance with any of the other two modes but is more or less separated. The corresponding wave functions $(0,v_2,0)$ are not hindered to evolve along the minimum energy path in γ. The quantum analysis reveals that up to $v_2 = 34$ the wave functions do not show distortions and are easy to locate in the spectrum. The corresponding energy is roughly where the **B** family becomes unstable. At higher energies, the bending states become more difficult to assign and the wave functions show gradually more admixtures of other states. As we can infer from fig. (6.27) where selected states of the pure bending progression are plotted, and the plots of the classical orbits with bending excitation, the $(0,v_2,0)$ states are scarred by orbits of the stable segment of the **B** family. In higher energies, additional contributions from orbits in the saddle-node families, most probably **SN3**, justify the complexity of the evolution towards CP–D on the isomerization path. It is a fact that no clear-cut isomerization quantum states have been found.

6.6 Conclusion

We showed above how powerful the classical phase space analysis can be. In the case of HCP, the abrupt onset of perturbations observed in the experimental SEP spectra, the substantial change of the rotational and vibrational fine structure constants of the bending states above a particular energy, and the anomalously large rotational constants of certain vibrational levels are consistent with the existence of the quantum "isomerization" states; these in turn have been shown to relate in terms of shape and transition energies to the saddle–node families of periodic orbits. The overall regularity of the spectrum is reflected in the stability of the fundamental families and their bifurcations. In DCP, the existence and the characteristics not only of the fundamental progressions but also of a special class of wave functions is accurately encoded in the classical phase space. Moreover, the lack of periodic orbits that would support a definite isomerizing transition is consistent with the quantum calculations. The crucial role of the periodic orbit analysis in the identification pro-

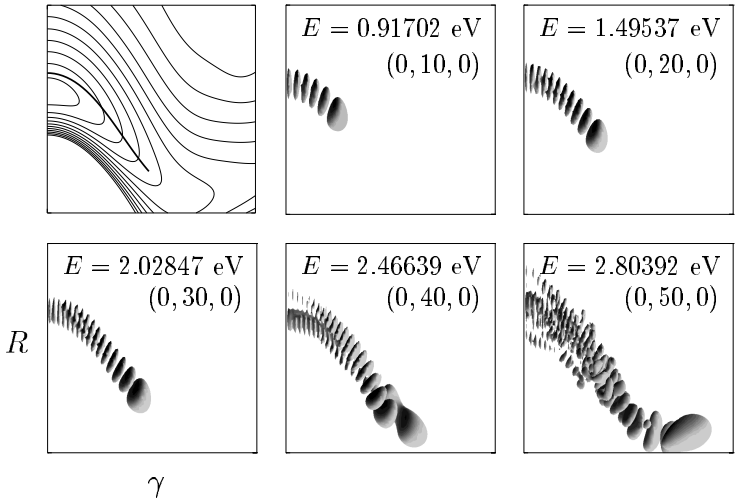

Figure 6.27: Selected wave functions of the pure bending progression in DCP. The vertical axes range from 2.2 α_0 to 5.5 α_0 and the horizontal axes range from 180° to 80°. The first panel shows the potential energy surface and a representative periodic orbit of the **B** family.

cess of the quantum wave functions with appropriate characteristics and, even, the fairly accurate—due to the regularity of the spectrum—quantitative predictions it provided are desirable properties of a technique extensible to larger molecules for which a complete quantum treatment is infeasible.

Chapter 7

Spectroscopy of formyl radical (HCO) and deuterated formyl radical (DCO)

7.1 Introduction

When a molecule is excited above its lowest dissociation threshold, it will ultimately fragment into the various possible products through the energetically accessible channels. This process, the *unimolecular dissociation*, is of fundamental importance to physical chemistry and chemical physics [178]; its implications are key topics in atmospheric and astrophysical sciences. One might expect that the possibility of a molecule to dissociate rises monotonically with the energy above threshold, and so is the rate of fragmentation. This is mostly correct, except when resonance states are encountered. Their dissociation rate may differ by orders of magnitude from those of neighboring ordinary continuum states. The advances in modern spectroscopic methods, such as the Stimulated Emission Pumping (SEP) and Dispersed Fluorescence (DF), allow the preparation of a system in a particular resonance state, at least in principle, enabling the experimentalists to determine its energy and width, along with the distribution of internal quantum states of the products. In practice, it is possible to record a large number of resonance energies and widths in the spectrum of few small molecules which have a sufficiently low density of states. This characteristic is necessary to avoid averaging as the energy resolution that can be achieved in present experiments is not arbitrary. The identification of a large number of resonances can provide valuable insight of the internal dynamics of a system prior to fragmentation.

The formyl radical, HCO, is among the important molecules in combustion [179], atmospheric chemistry [180] and astrophysics [181]. In addition to its practical implications, the very rich resonance structure has attracted a lot of research efforts, both experimental and theoretical, on HCO and especially on its dissociation into H+CO. Comprehensive references can be found in [182–184]. Its deuterated isotopomer, DCO, has also been under investigation [115, 184–186]. As we will see below, a very shallow potential well (~ 0.84 eV) characterizes these molecules; resonances are mainly built on excitation of the CO stretching mode. The wealth

of spectroscopic data for extended energy regions available for HCO and DCO, combined with theoretical calculations based on accurate global ab initio potentials [114, 187–189] make these molecules prototype systems for studies of radical spectroscopy and unimolecular reactions. Numerous calculations have been made to reconstruct the experimental data, and several theoretical techniques, both established and innovative ones, have been tested on them.

In this chapter we will present our research results on HCO and DCO based on the analysis of their classical phase space in the ground electronic state for zero total angular momentum. The qualitative behavior of the molecules will be derived from the classical picture and checked against the accurate quantum predictions. Also, we will elaborate on the applicability of the classification scheme of quantum states based on classical periodic orbits; it is a superior alternative to the traditional normal mode assignment which can reveal specific patterns in the organization of quantum states.

We begin the chapter with a concise review of the available potential energy surfaces derived in the literature for HCO/DCO. We also outline the construction of the one we used. Then, the detailed analysis of the classical phase space of HCO and DCO is given. It is followed by a presentation of the quantum picture for each molecule, along with a discussion of the analogies between the classical and quantum treatment. The chapter concludes with an overview of our findings. The presentation here is a revised and expanded version of the analysis we published in [190].

7.2 Potential Energy Surface

The first and, for many years, the only global Potential Energy Surface (PES) for the ground electronic state of HCO/DCO was developed by Bowman, Bittman and Harding (BBH) [187] and reformulated via a Legendre polynomial fit by Romanowski, Lee, Bowman, and Harding (RLBH) [188]. The potentials were the result of extensive—at that time—ab initio calculations fitted via a novel method to a global function. These surfaces reproduce quite accurately all special features (wells, barriers, saddle points, etc.) of the actual potential and are, in general, realistic descriptions for it. However, the comparison of the calculated bound states of HCO [187] with low-resolution measurements by Murray *et al.* [191], indicated that the BBH potential was not adequately accurate. Bowman and Gazdy in [192] employed a coordinate scaling to the BBH potential to bring the theoretical predictions in agreement with the experimental results by Murray *et al.* and with newer ones by Sappey and Crosley [193]. This scaling applied to RLBH potential proved to be a significant improvement as it gave a PES which produced more accurate energies for the bound states and resonances of HCO and DCO [194, 195] in comparison to experimental observations [182, 185, 191, 193, 196–198]. Notwithstanding the modification, the BBH and RLBH surfaces did not satisfactorily reproduce the more recent spectroscopic data for HCO [199, 200] and DCO [185, 186]. The inherent drawback is that both potentials use spline fits of the ab initio points, something which results in very slight, unphysical wiggles in significant regions of the PES. These, in turn, compromise the accuracy of the calculations, primarily on resonance energies and

widths. On the other hand, scattering cross sections for H+CO are relatively less sensitive on them and are quite accurate.

Another potential energy surface for HCO/DCO has been developed by Cho *et al.* [201]. It is an analytical fit of experimental vibrational energies and reproduces the general topography of the actual surface. It has the advantage, with respect to an ab initio PES, that the parameters of the potential can be easily varied. This allows to assess how each feature of the surface influences the quantitative results. An alternative potential function has been derived by Murrell and Rodriguez [202] for the ground-state surface of HCO/DCO, which reproduces the spectroscopic properties of the molecule at equilibrium and the results of ab initio calculations at other stationary points on the surface.

To cope with the need of a state-by-state comparison between theory and experiment—in view of the large density of states, especially in DCO—Werner, Keller, and Schinke developed another PES for the lowest two singlet states, $\widetilde{X}\ ^2A'$ and $\widetilde{A}\ ^2A''$, based on more accurate than ever ab initio calculations. Its preliminary version [189] covered the configuration space only partially ($\widehat{HCO} > 60^\circ$) and used a threefold 1D spline interpolation scheme. Nevertheless, its predictions were in better agreement with experimental data for HCO [193] than the BBH results. The ab initio calculations were extended to cover all relevant configuration space and a new interpolation scheme was used in the newest version of the potential, the WKS surface [114]. This is the PES we employed in our calculations; we will describe it briefly below.

A total of ca. 1000 ab initio energies were calculated for various points, primarily the nodes of a three-dimensional grid defined by the two stretching coordinates, R_{HC} and R_{CO}, and the $\widehat{HCO}$ bond angle. The grid covered the entire region important for the fragmentation into H and CO, the main dissociation channel. The other channels require the breaking of the CO bond which, in turn, demands a substantial amount of energy; they were not taken into account. All calculations were performed with the MOLPRO package [85] using the internally contracted multireference configuration interaction method with Davidson correction (icMRCI+Q) (§3.5.3). The potential is written as a sum of diatomic and triatomic terms. The diatomic potentials for R_{HO} and R_{HC} are of the form of the extended Rydberg functions (§3.5.6) fitted on specific spectroscopic data, while the CO potential is a rational function constructed to have the appropriate R_{CO}^{-6} asymptotic behavior. The three-body term is a rational function of complex expansions on primitive polynomial bases. The potential for the ground state incorporates a term to account for the conical intersection at $\widehat{HCO} = 180^\circ$ with another electronic state of the same symmetry; the intersection at $\widehat{HCO} = 0^\circ$ was not treated in any special way as it is much higher in energy and, therefore, less important for the H+CO dissociation. Numerous modifications in the general form were made in order to avoid unphysical behavior. The few hundred parameters of the potential function were determined through a complicated optimization procedure. Dynamical calculations on the resulting PES gave theoretical estimates with systematic deviations from the experimental results; the necessary modifications to correct them were introduced in the potential, and the new parameters were fitted to reproduce mainly the spectroscopic data of Tobiason *et al.* [200]. It should be noted that our group computed the analytical first derivatives of the WKS potential.

The topographical analysis of the physically relevant region of the potential reveals a global minimum of -0.833884 eV at $R = 3.02150\ \alpha_0$, $r = 2.23253\ \alpha_0$, $\gamma = 2.52822$ rad in Jacobi coordinates, cf. fig. (7.1). The potential is zero for infinitely

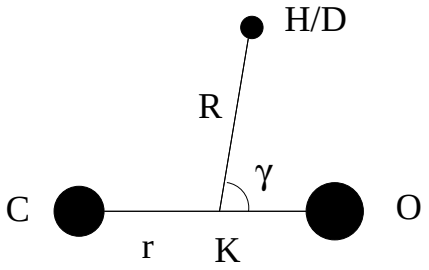

Figure 7.1: Coordinates for the HCO/DCO molecules. K indicates the C–O center-of-mass.

separated H/D and CO with CO at its equilibrium distance of $2.13942\ \alpha_0$. The dissociation energy is not zero: a barrier of 0.125406 eV exists at $R = 4.23411\ \alpha_0$, $r = 2.14885\ \alpha_0$, $\gamma = 2.30282$ rad. There also exists a linearization barrier of 0.26807 eV at $R = 3.29158\ \alpha_0$, $r = 2.24855\ \alpha_0$, $\gamma = \pi$ rad. Local minima much higher than the main well were found but they are not expected to influence the dissociation of HCO/DCO. Representative cuts of the WKS surface for the ground state at the primary equilibrium are given in fig. (7.2); in the same figure a projection of the minimum energy path is plotted. This path consists of the points where the potential is minimum with respect to r and γ for successive fixed values of the H–CO distance R.

7.3 Analysis of the Classical Phase Space

In our calculations in HCO and DCO molecules, we employed the Jacobi coordinate system as more appropriate for studying the primary dissociation channel of H/D+CO. The values for the masses we used are $m_{\mathrm{H}} = 1.00783$ u, $m_{\mathrm{D}} = 2.01566$ u, $m_{\mathrm{C}} = 12.0$ u, and $m_{\mathrm{O}} = 15.99491$ u. The total angular momentum of both molecules was $J = 0$.

7.3.1 HCO

The Continuation/Bifurcation (C/B) diagram for the HCO molecule is given in fig. (7.3). It depicts the periodic orbit families we located, plotting their period (measured in time units of ~ 5.387 fs) with respect to their energy (in eV). For clarity it is split in two, one graph comprising the principal families and their bifurcations, and another consisting of the saddle–node orbits. Energy plays the role of the "external" parameter which causes the bifurcations.

Three principal families emerge deep in the potential well. The orbits just above the energy minimum have periods very close to those predicted through the harmonic expansion (Weinstein theorem, cf. §2.3.2) and exhibit predominant excitation in each of the normal modes. The calculated periods of the classical harmonic oscillators are 2.2799 t.u., 3.2791 t.u., and 5.5761 t.u.. The first two are of stretching nature, initially at least, mainly in R and r respectively, while the last one corresponds to

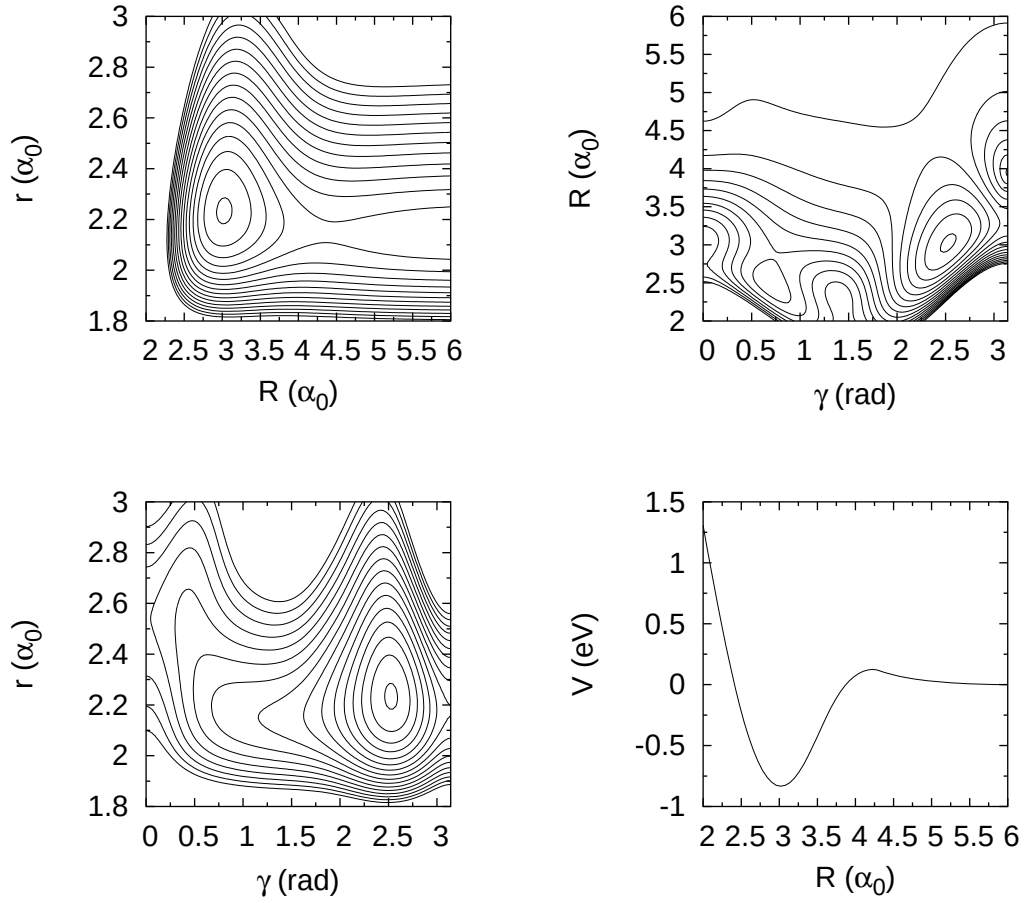

Figure 7.2: Contour plots of the WKS potential energy surface for the ground state of HCO/DCO. On each plot, one coordinate is fixed at the corresponding primary equilibrium value. The 16 contours start from -0.8 eV and increase by 0.25 eV. The lower right panel depicts the potential energy as a function of R along the minimum energy path. The potential is minimized in r and γ for specific R.

the bending mode. The periods of the three modes are quite incommensurate; they do not participate initially in a low-order resonance. We denote the principal families by **R**, **r**, and **B** respectively to indicate their primary character (B stands for bending). Below we present their detailed evolution; unfortunately, the numerically evaluated Jacobian of the Hamilton equations is not accurate enough to provide reliable eigenvalues of the monodromy matrix especially at high energies and therefore the stability analysis is somewhat vague.

The **R** family is quite anharmonic; it undergoes a period–quadrupling bifurcation—two eigenvalues of the monodromy matrix pass through $(0, \pm i)$—around -0.5884 eV and the **R1** family is born. **R** is stable up to (-0.2665 eV, 2.818 t.u.) where a period–doubling bifurcation occurs and **R2** branches off. At (1.385 eV, 3.348 t.u.) there is indication that stability is regained through another period–doubling bifurcation. The first orbit we located from **R1** is at (-0.5841 eV, 9.816 t.u.) and is stable. The family loses its stability at 0.757 eV through a period–doubling bifurcation. The **R2**

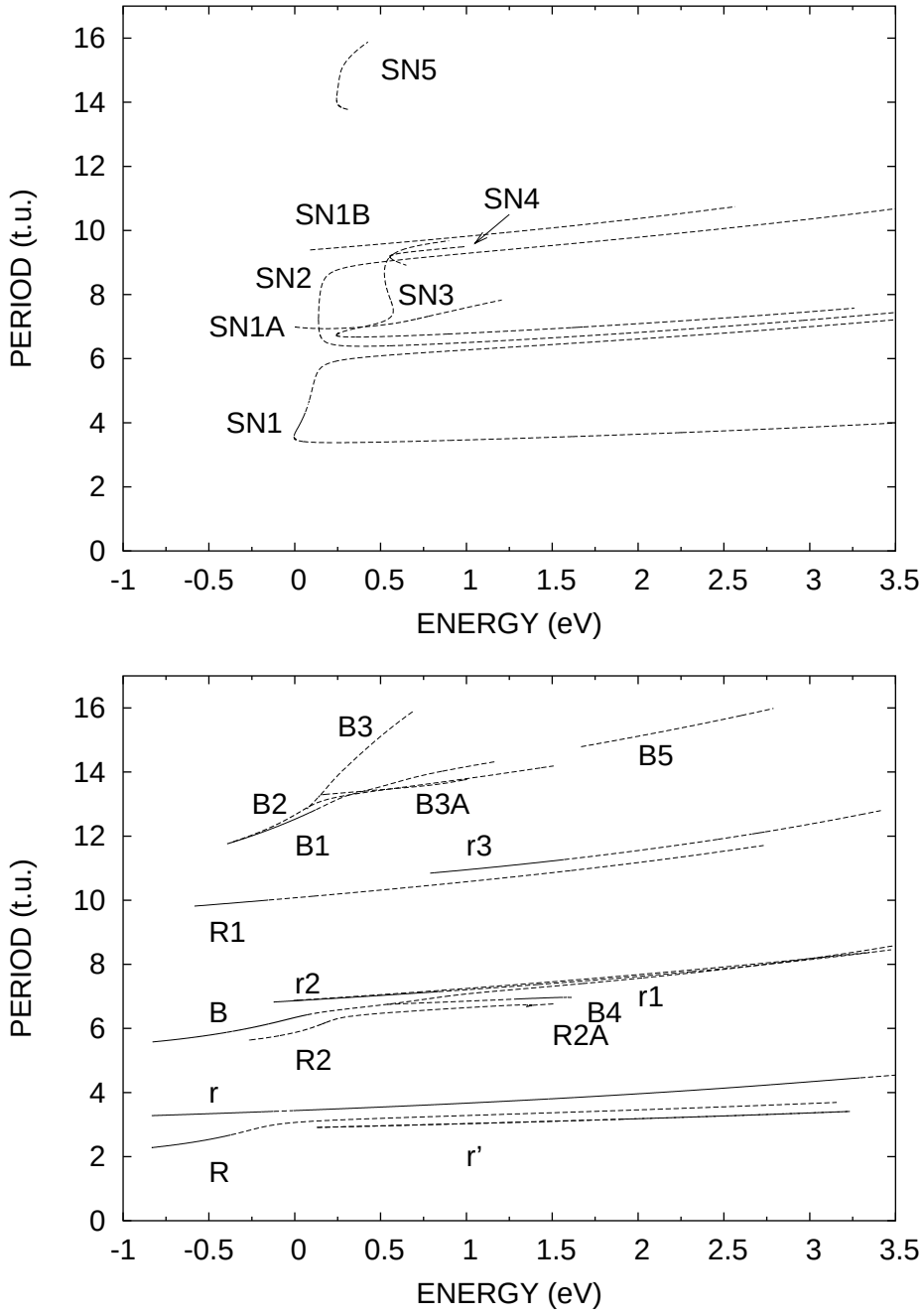

Figure 7.3: Continuation/Bifurcation Diagram for HCO: fundamental families (lower figure) and saddle–node families (upper figure). All periods are measured in time units of ~ 5.837 fs. Continuous lines represent stable families of periodic orbits; dashed ones indicate instability.

family starts with a period of 5.636 t.u.. Its birth can be attributed to the interaction between the R- and γ-oscillators as the gradually tune into a 1:2 resonance. There is indication that the family loses its initial stability around 1.08 eV. It seems it merges with a saddle–node family born around 1.3808 eV. At this energy, a bifurcation gives birth to the **R2A** family. Representative orbits of the **R** family and its bifurcations are given in fig. (7.4); their initial conditions, energies, and periods are given in table (7.1).

The **r** family starts with the expected period of 3.2792 t.u. and is stable up to well above 3.2 eV with the exception of a narrow energy window between (−0.1235 eV, 3.4117 t.u.) and (−0.0097 eV, 3.435 t.u.). At these energies, two period-doubling bifurcations destabilize the family, giving birth to **r1** and **r2** respectively. Around 0.785 eV, a "period–tripling" bifurcation occurs, that is, a pair of Floquet multipliers becomes equal to $e^{\pm i2\pi/3}$ and a family we denote by **r3** is born. **r1**, which inherits the stability of **r**, undergoes a Hopf bifurcation at 0.837 eV; the two pairs of eigenvalues of the monodromy matrix which collided and left the unitary circle do not return, at least before the last orbit we located at 3.5 eV. The **r2** family starts with a period of 6.8707 t.u. and is unstable through all its located segment. The first orbit of **r3** was located at (0.7892 eV, 10.846 t.u.) and is stable. The family undergoes a series of period–doubling bifurcations (at 1.567 eV, 2.665 eV, 3.150 eV and 3.390 eV) which alternate its stability. Representative orbits of the **r** family and its bifurcations are given in fig. (7.5); their initial conditions, energies, and periods are given in table (7.1).

The **B** family is stable up to (−0.395 eV, 5.88 t.u.) where a family, denoted by **B1**, branches off with twice the period. Two other period–doubling bifurcations, at (−0.359 eV, 5.91 t.u.) and (0.07 eV, 6.423 t.u.), toggle the stability and give birth to **B2** and **B3** respectively, leaving the **B** family permanently unstable. A pair of eigenvalues of the monodromy matrix becomes real passing through +1 at (0.533 eV, 6.75 t.u.) and an orbit with the same period was located in the vicinity of **B** at this point. The family born is denoted by **B4**. Two period–doubling bifurcations take place at 1.172 eV and 1.655 eV. Through the first, the **B** family recombines with the **B1** branch while the second generates the **B5** family. No other qualitative change of **B** takes place up to at least 3.5 eV. The **B1** family starts with a period of 11.76 t.u. and is stable up to 0.122 eV where a period–doubling bifurcation occurs. At (0.42 eV, 13.43 t.u.) a pair of Floquet multipliers leave the unitary circle through +1 and re-enter around (1.06 eV, 14.22 t.u.). As mentioned, the family merges with **B**. **B2** starts at (−0.359 eV, 11.825 t.u.) and is unstable. It undergoes two period–doubling bifurcations at 0.725 eV and 1.482 eV. The **B3** family is born at (0.071 eV, 12.85 t.u.) as stable. Between 0.81 eV and 0.135 eV it is complex unstable. At 0.151 eV the family becomes singly unstable and the **B3A** family is born. **B3** undergoes at 0.46 eV a period–doubling bifurcation. **B3A** starts at (0.151 eV, 13.289 t.u.) and soon becomes complex unstable. The first orbit of the **B4** family has a period of 6.7509 t.u. and is unstable. The family stabilizes around (1.27 eV, 6.911 t.u.) through a period–doubling bifurcation. **B4** merges with a bifurcation of the saddle–node family **SN3** we will see below, around 1.6137 eV. The first orbit we located from the **B5** family is at (1.668 eV, 14.79 t.u.); the whole segment is highly unstable. Representative orbits of the **B** family and its bifurcations are depicted in fig. (7.6) and fig. (7.7); their initial conditions, energies, and periods

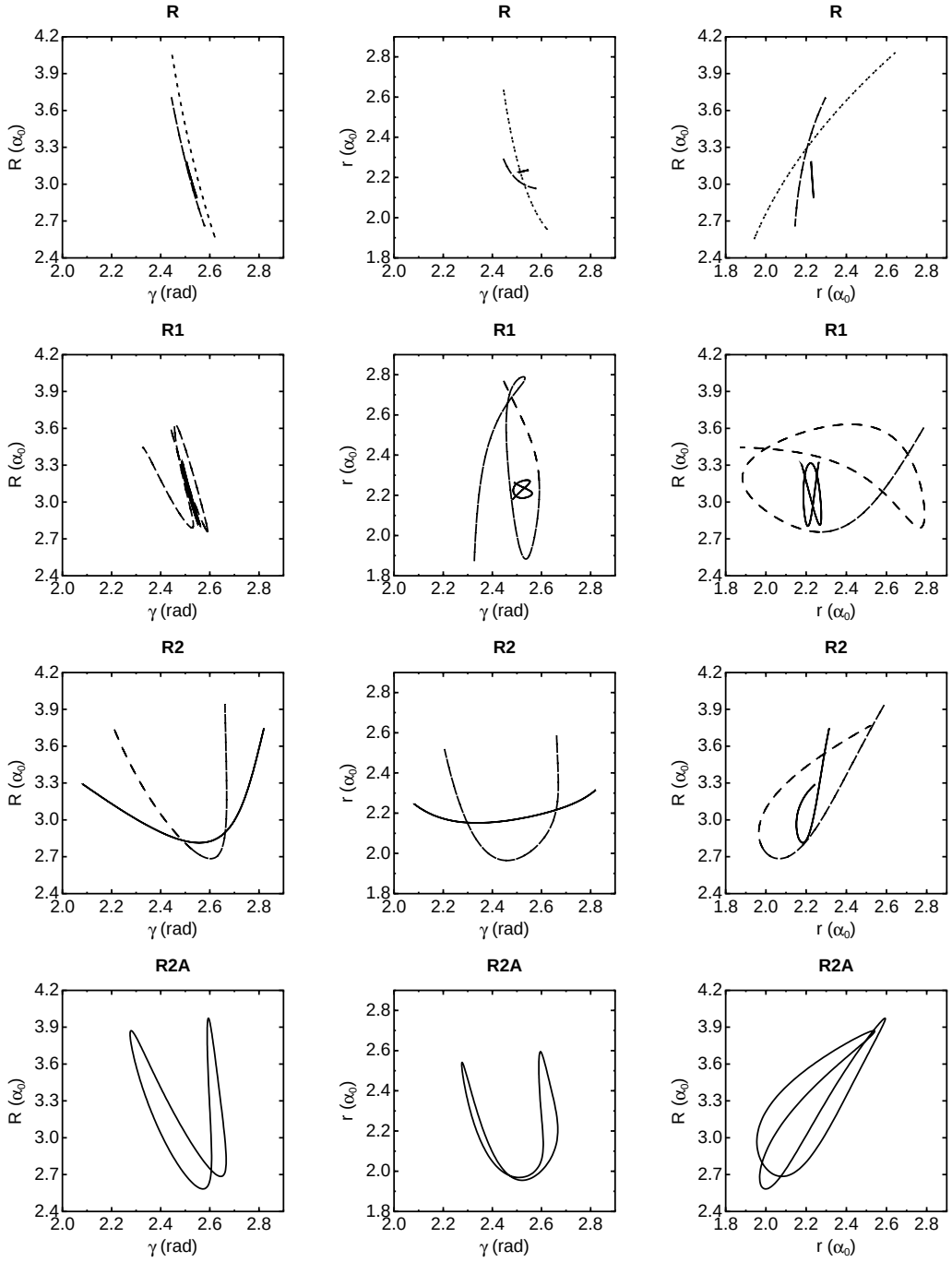

Figure 7.4: Projections of representative orbits of the **R**, **R1**, **R2**, **R2A** families in HCO at various energies. The data are given in table (7.1). Solid, dashed, and dotted lines on the same plot represent orbits of increasing energy.

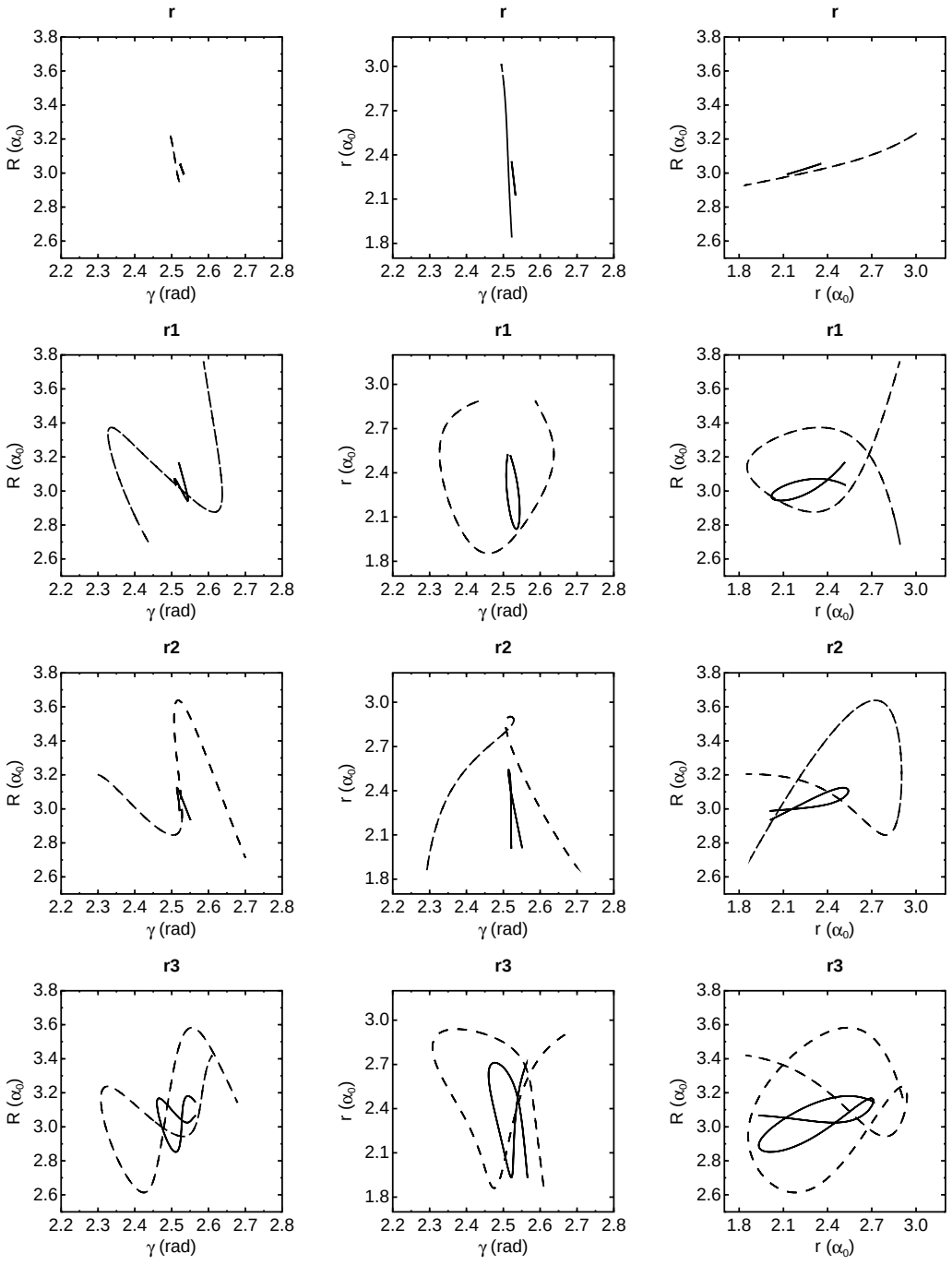

Figure 7.5: Projections of representative orbits of the **r**, **r1**, **r2**, **r3** families in HCO at low (solid line) and high (dashed line) energies. The data are given in table (7.1).

are given in table (7.1).

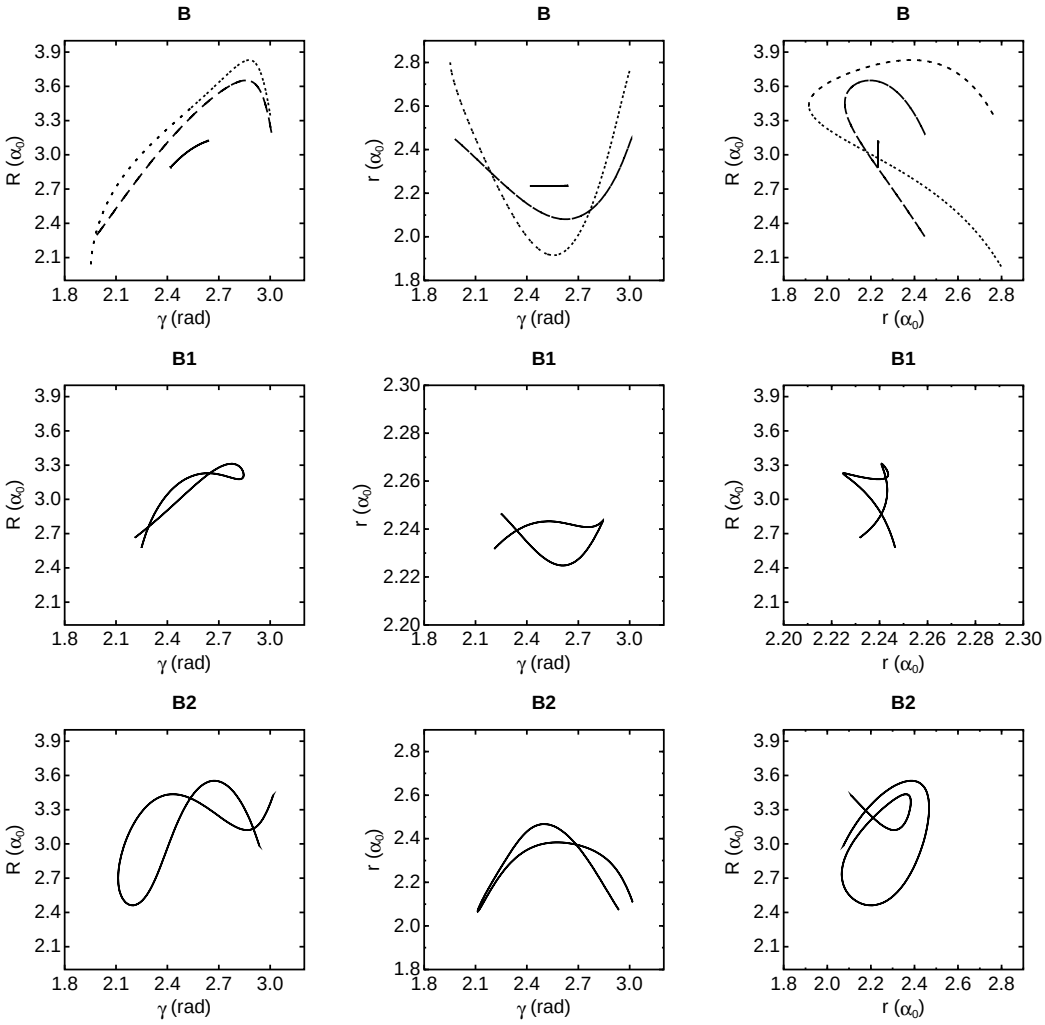

Figure 7.6: Projections of representative orbits of the **B**, **B1**, **B2** families in HCO at various energies. The data are given in table (7.1). Solid, dashed, and dotted lines on the same plot represent orbits of increasing energy. Note that the r-range in the **B1** plots has been adjusted for clarity.

One family of periodic orbits originating at the dissociation barrier has been located. It is denoted by $\mathbf{r}'$ to indicate the primary excitation, which is in r as this is the (only) stable direction in the saddle point at the barrier. It starts at (0.1299 eV, 2.911 t.u.) and, naturally, is unstable. Representative orbits from it are plotted in fig. (7.8) while their data are given in table (7.1).

A cascade of saddle–node bifurcations was also located. The lowest family energy-wise is born just below the threshold at (−0.0046 eV, 3.564 t.u.); it is denoted by **SN1**. Its main feature is a prominent excitation in R. The stable branch, **SN1s**, grows towards higher periods and soon it undergoes two Hopf bifurcations at 0.062 eV and 0.079 eV, which render it temporarily complex unstable. Stability is eventually lost at (0.085 eV, 4.695 t.u.) through a period–doubling bifurcation which

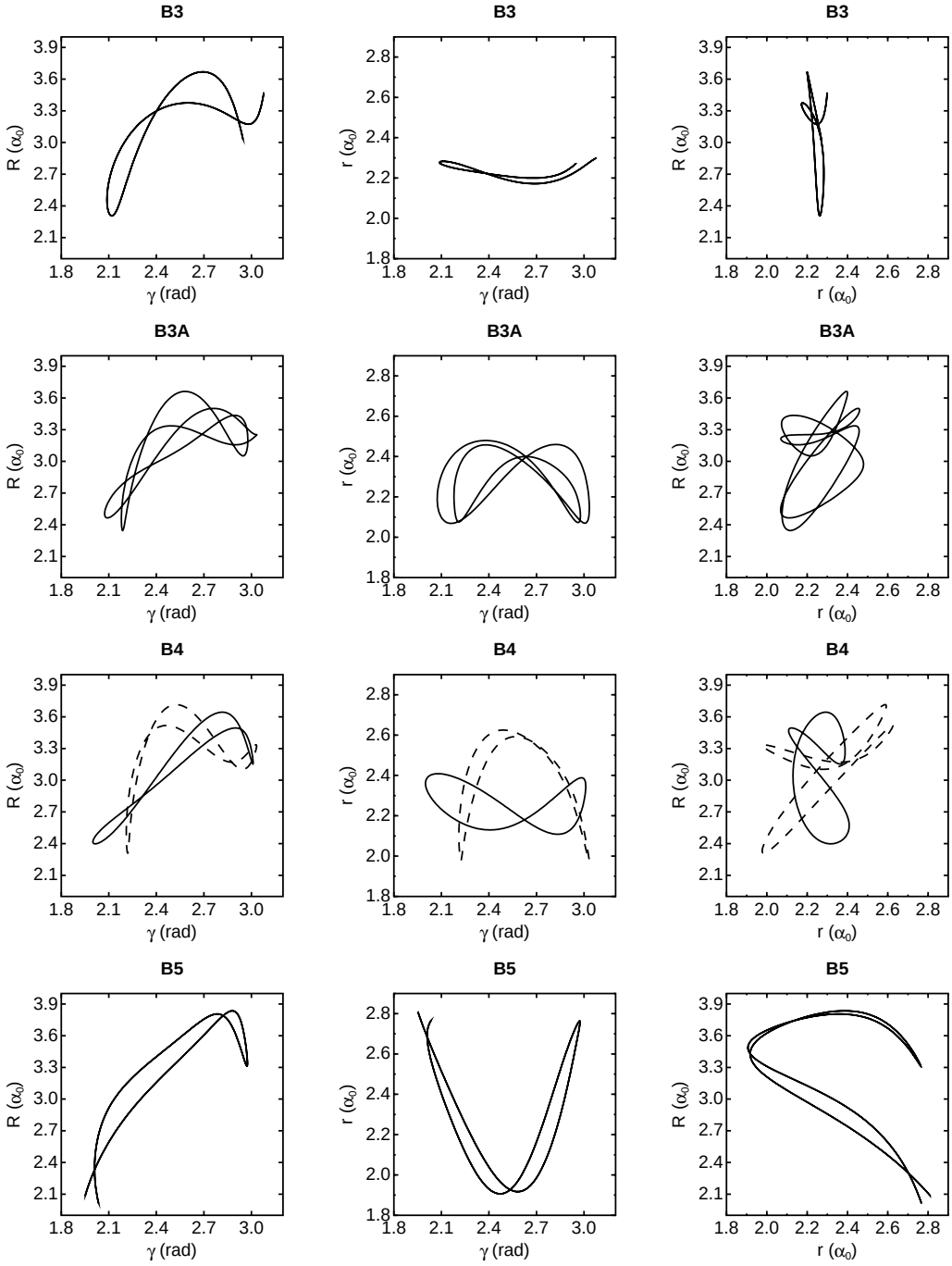

Figure 7.7: Projections of representative orbits of the **B3**, **B3A**, **B4**, **B5** families in HCO at various energies. The data are given in table (7.1). Solid and dashed lines on the same plot represent orbits of low and high energy respectively.

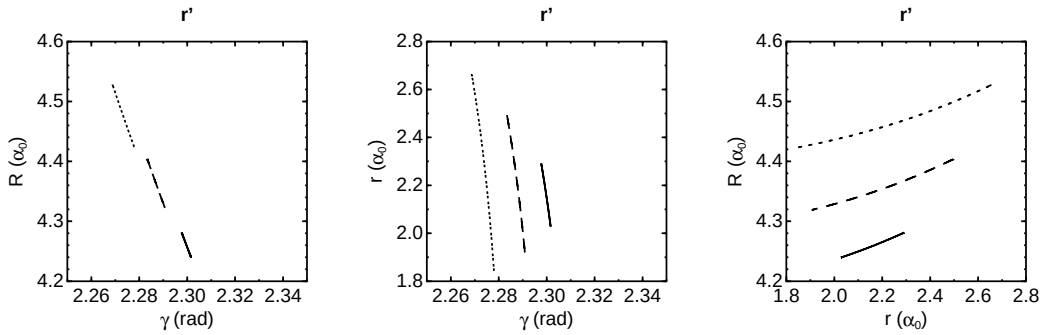

Figure 7.8: Projections of representative orbits of the $\mathbf{r}'$ family in HCO at low (solid line), medium (dashed line), and high energies (dotted line). The data are given in table (7.1).

generates **SN1B**. The unstable branch of **SN1**, **SN1u**, undergoes a period–doubling bifurcation at 0.001 eV which gives birth to **SN1A**; the naming of the bifurcations follows their relative energies. Another period–doubling bifurcation for the unstable branch of **SN1** occurs too high, at 2.14 eV. **SN1A** has initial period of 6.9885 t.u. and is unstable throughout its lifetime. **SN1B** starts at 9.391 t.u.; its initial stability is lost almost immediately through a Hopf bifurcation. Representative orbits of the **SN1** and its bifurcations are plotted in fig. (7.9); their data are given in table (7.2). As we can tell from the C/B diagram and these plots, the orbits of the stable branch of **SN1** acquire a significant excitation in r above 0.23 eV. This qualitative change can be attributed to the fact that at this energy the ratio of the periods of **SN1** and the r-oscillator reaches a low order of resonance, 3:5. Above this resonance, the r-oscillator absorbs the excess amount of energy, making the family behave as quite harmonic, resembling the **r** family. On the other hand, the immediate 1:1 resonance of the unstable branch of **SN1** with r shows up in the evolution of the whole branch.

A saddle–node bifurcation was located close to the "kink" of the **SN1** family, at (0.1384 eV, 7.2300 t.u.). The family born is denoted by **SN2**. The two branches can be characterized as stable and unstable in a reduced phase space judging from the position of one pair of eigenvalues on the unitary plane. The second free-to-move pair makes both unstable. The evolution of both branches exhibits no interesting features other than the onset around 0.3 eV of a 2:5 resonance with the r-oscillator for the upper, "unstable" branch. The consequent excitation of r above this energy is evident in fig. (7.10) where representative orbits of the **SN2** are plotted.

At (0.24287 eV, 6.7356 t.u.) a saddle–node family is born; it is denoted by **SN3**. The stable "upper" branch **SN3s**, undergoes a period–doubling bifurcation at 0.310 eV where it merges with a branch of another saddle–node family, **SN5**. **SN3s** heads towards two successive saddle–node bifurcations at 0.574 eV and 0.522 eV. Around (0.7 eV, 9.5 t.u.) a qualitative change is evident. The apparent 8:3 resonance with the r-oscillator at this point affects the evolution in higher energies in the usual pattern. The unstable branch **SN3u** undergoes two period–doubling bifurcations at 0.885 eV and 1.152 eV. It becomes stable at (1.6137 eV, 6.967 t.u.) where it meets the **B4** family and destabilizes again through a Hopf bifurcation at 1.68 eV.

The next saddle–node bifurcation we located is at (0.5544 eV, 9.178 t.u.). It gives

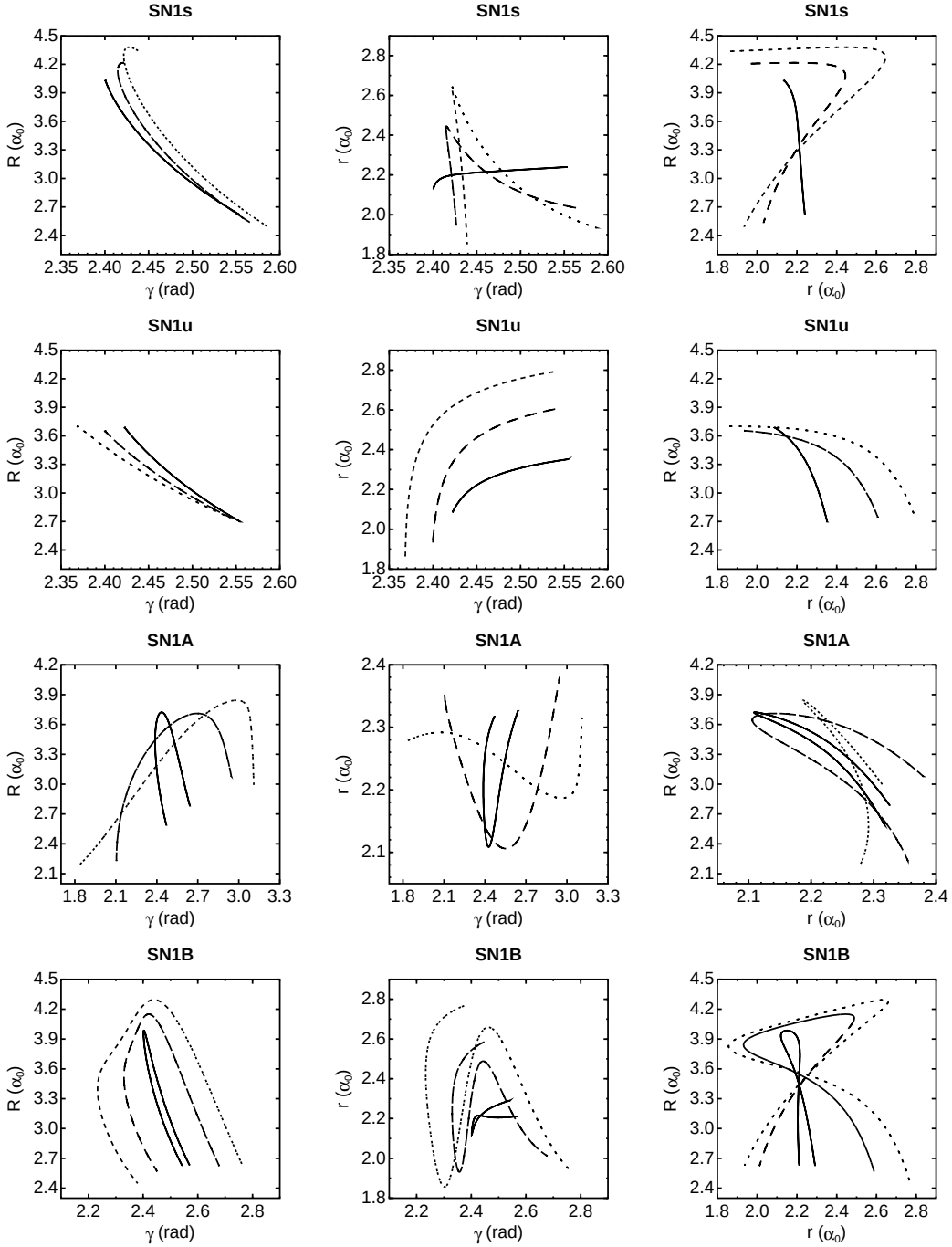

Figure 7.9: Projections of representative orbits of the **SN1**, **SN1A**, and **SN1B** families in HCO at low (solid line), medium (dashed line), and high energies (dotted line). The data are given in table (7.2).

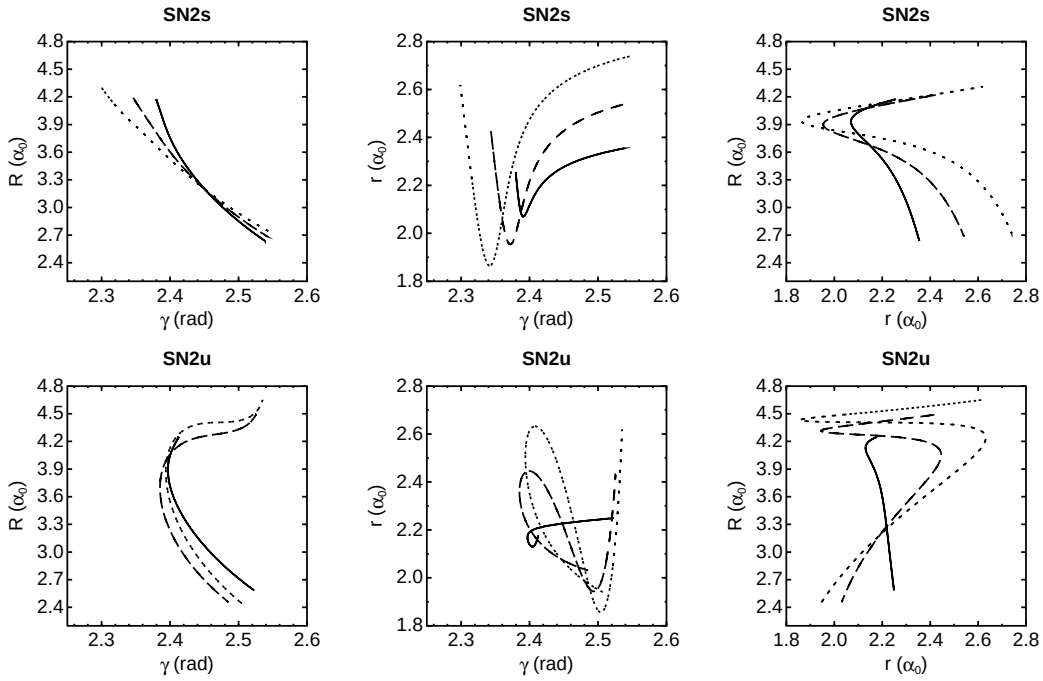

Figure 7.10: Projections of representative orbits of the **SN2** family in HCO at low (solid line), medium (dashed line), and high energies (dotted line). The data are given in table (7.2).

birth to the **SN4**. It comprises highly unstable orbits on which stability analysis could not be performed reliably. Another saddle–node family, the **SN5**, is born at (0.2437 eV, 14.094 t.u.). It has no interesting features. Representative orbits of the **SN3**, **SN4**, and **SN5** families are plotted in fig. (7.11). Their data are given in table (7.2).

7.3.2 DCO

The Continuation/Bifurcation (C/B) diagram for the DCO molecule is given in fig. (7.12). It depicts the periodic orbit families we located, plotting their period (measured in time units of ~ 5.387 fs) with respect to their energy (in eV). For clarity it is split in two, one graph comprising the principal families and their bifurcations, and another consisting of the saddle–node orbits. Energy plays the role of the "external" parameter which causes the bifurcations.

Three principal families emerge deep in the potential well. The orbits just above the energy minimum have periods very close to those predicted through the harmonic expansion. The calculated periods of the classical harmonic oscillators are 3.06226 t.u., 3.34940 t.u., and 7.19393 t.u.. The first two families are of mainly stretching nature with roughly equal amplitudes in R and r and similar periods. We, therefore, describe them as consisting of Antisymmetric Stretch (AS) and Symmetric Stretch (SS) orbits, respectively, according to the relative phases of the R- and r- oscillators. The third period corresponds to an orbit with mainly bending (B) excitation. Below we present their detailed evolution.

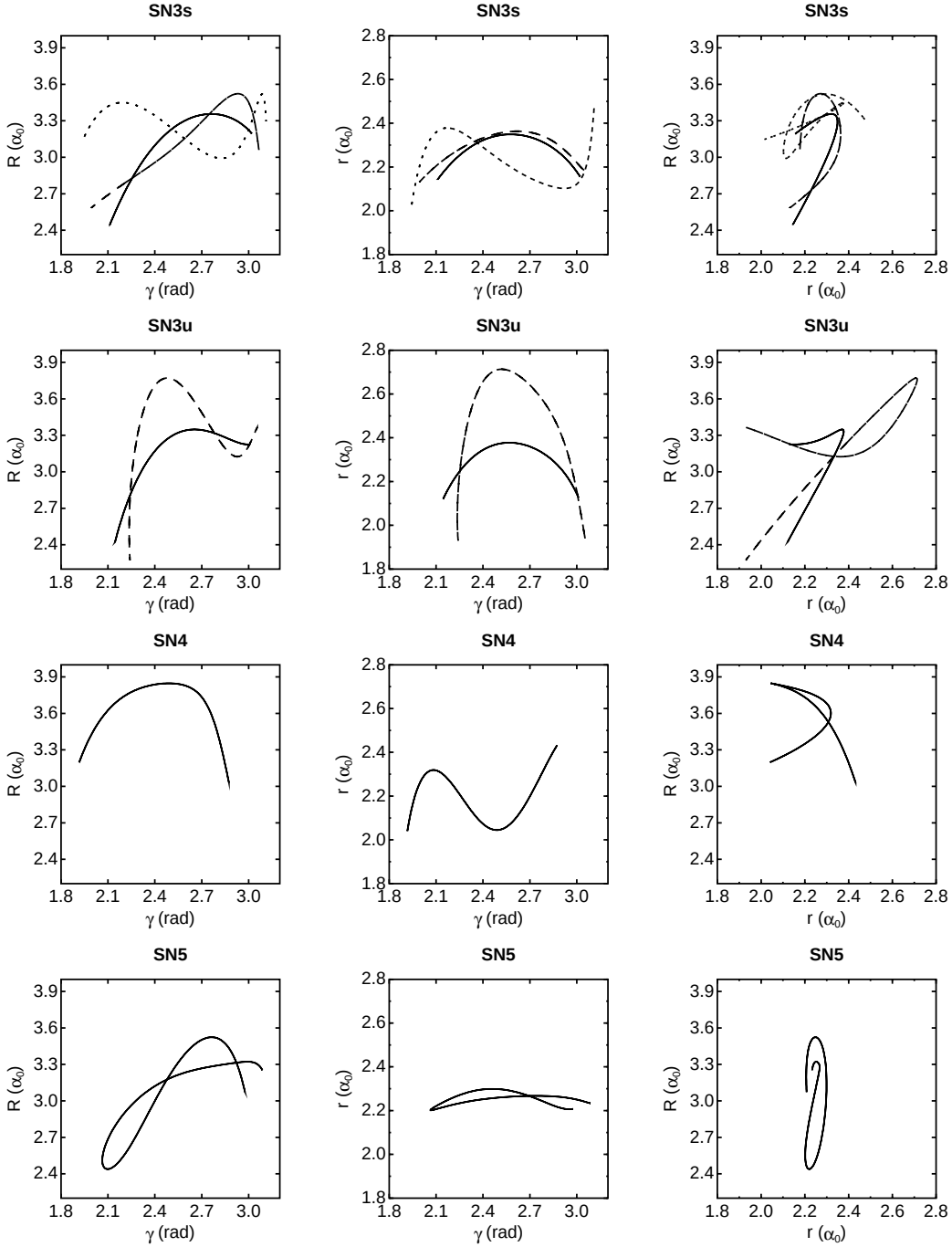

Figure 7.11: Projections of representative orbits of the **SN3s**, **SN3u**, **SN4**, and **SN5** families in HCO. Solid, dashed, and dotted lines on the same plot represent orbits of low and medium and high energy respectively. The data are given in table (7.2).

FAMILY	ENERGY	PERIOD	R	r	γ	P_R	P_r	P_γ
R	−0.7439	2.3360	3.0131614	2.2315834	2.5281369	−0.3866342	0.1164887	0.4092423
R	−0.0287	3.0770	2.6709585	2.1453525	2.5764477	−0.3523696	−0.1061235	0.3564254
R	2.0010	3.4580	2.5763093	1.9475757	2.6191460	0.5571225	1.0208775	−0.4905930
R1	−0.5606	9.8260	2.9563839	2.1887300	2.5367418	−0.6196737	0.1960107	0.6635109
R1	1.9930	11.1700	2.7557613	2.2797968	2.5904178	0.0419445	5.5360882	−0.2615622
R2	−0.2238	6.2650	2.8195380	2.1924764	2.5882896	−0.1764140	−0.9433830	−2.9198211
R2	1.3413	6.7360	2.7520801	1.9907788	2.5322987	0.6271803	−1.9396660	−2.3452014
R2A	1.4375	6.7410	2.8118188	1.9763435	2.5738472	0.8571774	−1.8166311	−1.9801406
r	−0.6641	3.3090	3.0286993	2.2625522	2.5267823	0.0565625	1.4662804	−0.0695591
r	2.4560	4.1200	3.1536134	2.8332421	2.5030774	0.2025122	3.5869391	−0.1479690
r1	−0.0602	6.8435	3.0708484	2.3568890	2.5079591	−0.0189468	2.8590598	−0.0280622
r1	2.4345	7.8325	2.8490366	2.8515197	2.4007854	−0.8678252	1.7722162	1.3644768
r2	0.0188	6.8800	3.0183488	2.3539874	2.5204975	0.0689015	3.0691284	−0.0149949
r2	2.4224	7.8800	2.9419820	2.8750751	2.5281960	0.7303092	1.4682089	0.0895420
r3	0.9014	10.9000	3.0253169	2.4746985	2.5387920	0.0272827	3.9652117	−0.4068236
r3	2.4623	11.8980	3.0345021	2.9041064	2.4515784	0.4693540	1.5641681	−2.1472487
B	−0.7693	5.6096	3.1212443	2.2345495	2.6348582	−0.0212676	−0.0094533	−0.3139554
B	0.8795	6.9996	3.6044667	2.1186179	2.7643506	−0.3082401	−1.4852835	−3.3597856
B	2.4608	7.8200	3.4059824	1.9170687	2.5335098	−0.6593413	0.5962042	−3.9639148
B1	−0.3356	11.8560	3.1826047	2.2359024	2.7911151	0.0710806	−0.1721983	−1.5287238
B2	0.5812	13.4900	3.2959922	2.3785523	2.6519019	0.4820799	0.3977611	−3.9135487
B3	0.3677	14.4900	3.5684905	2.2060683	2.5448822	−0.4490701	0.2009650	−3.2328700
B3A	0.6586	13.5200	3.4219787	2.1859144	2.8531707	−0.1685296	2.4750767	−2.4835914
B4	0.6129	6.7668	3.5368108	2.2065051	2.6780910	−0.5048384	−1.4285997	−3.4640482
B4	1.5990	6.9694	3.3952802	2.3964973	2.3449178	−0.9244773	−3.3520149	−2.0331294
B5	2.3829	15.5180	3.0917694	2.0930486	2.3571910	−0.7645938	4.6040532	−3.5194616
r′	0.3996	2.9460	4.2811063	2.2912204	2.2977216	−0.0015999	−0.0617934	0.0018168
r′	1.4184	3.0900	4.4030642	2.4932730	2.2834311	−0.0144867	−0.5241720	0.0170347
r′	2.4858	3.2660	4.5263003	2.6482608	2.2689922	−0.0316339	−1.1557558	0.0386079

Table 7.1: Initial conditions for representative periodic orbits of the fundamental families in HCO. Lengths are measured in α_0, the angle in rad, the energy in eV, the period in t.u. (~ 5.387 fs) and the momenta in the appropriate derived units.

FAMILY	ENERGY	PERIOD	R	r	γ	P_R	P_r	P_γ
SN1s	0.1033	5.0850	3.9420561	2.1654372	2.4044291	−0.2425281	0.4177403	0.1260396
SN1s	1.0243	6.2800	4.1374133	2.4322816	2.4147747	−0.2701715	0.8869005	−0.0128632
SN1s	2.2692	6.7100	4.2553264	2.6449226	2.4217828	−0.3869462	−0.2384980	0.0600802
SN1u	0.0503	3.4135	3.6904165	2.0855809	2.4223332	0.0030195	−0.0166253	−0.0024681
SN1u	1.1167	3.4819	3.6546364	1.9334511	2.3998482	0.0061655	−0.2754262	−0.0054800
SN1u	2.2532	3.6931	3.7013863	1.8633053	2.3683329	−0.0025177	1.3981862	0.0078630
SN1A	0.0306	6.9710	2.9861926	2.2766421	2.4138208	1.1207363	−0.9765929	−0.8416538
SN1A	0.6034	7.1208	2.4360023	2.3379621	2.1111017	0.8984211	−0.5920079	0.2944673
SN1A	1.2062	7.8300	2.4609804	2.2906749	2.0074054	0.7809926	0.1026656	2.3233624
SN1B	0.1079	9.4000	3.8964308	2.2055570	2.4133466	−0.2848791	0.3584611	0.2680649
SN1B	1.2414	9.9400	4.0979605	2.4878263	2.4468270	−0.2739578	−0.2263617	0.9246230
SN1B	2.3562	10.5990	4.1402832	2.5947560	2.5100339	−0.5298186	−2.2328071	1.6844199
SN2s	0.2631	6.4100	4.0552040	2.1166244	2.3851602	0.2179693	1.2243857	−0.1049558
SN2s	0.9946	6.5000	4.0699641	2.1250995	2.3565007	0.2735861	3.3722942	−0.2616089
SN2s	2.1337	6.8650	4.1464264	2.2250597	2.3157144	0.2950870	5.0834118	−0.3755579
SN2u	0.1408	7.6400	4.2426491	2.1720681	2.4121839	0.0336312	0.2031004	0.0282138
SN2u	1.0721	9.3200	4.3794400	2.0790648	2.5125549	−0.1538684	−3.3199461	−0.3358088
SN2u	2.2122	9.9000	4.4910110	2.0437398	2.5213905	−0.1717142	−5.0100750	−0.3528326
SN3s	0.2429	6.7387	2.9784237	2.2952134	2.3283274	−0.6630513	−1.1418318	−2.5720372
SN3s	0.5139	7.1570	2.7946572	2.2661813	2.2153627	−0.3871093	−1.4381869	−2.8420372
SN3s	0.8986	9.6790	3.4476774	2.3783527	2.1642519	−0.0549802	−0.0869452	−2.5855486
SN3u	0.2998	6.6778	3.0584250	2.3131481	2.3381199	−0.6814667	−1.3885682	−2.4465716
SN3u	2.3580	7.2155	3.2573681	2.4012646	2.2826546	−1.1744705	−4.4235471	−1.3605948
SN4	0.7493	9.3730	3.4339074	2.2622975	1.9972244	−0.3440329	−1.5118477	−1.2890144
SN5	0.2449	14.2000	2.6285736	2.2689932	2.2422690	−0.7021868	−0.6426818	−1.9482475

Table 7.2: Initial conditions for representative periodic orbits of the saddle–node families in HCO. Lengths are measured in α_0, the angle in rad, the energy in eV, the period in t.u. (~ 5.387 fs) and the momenta in the appropriate derived units.

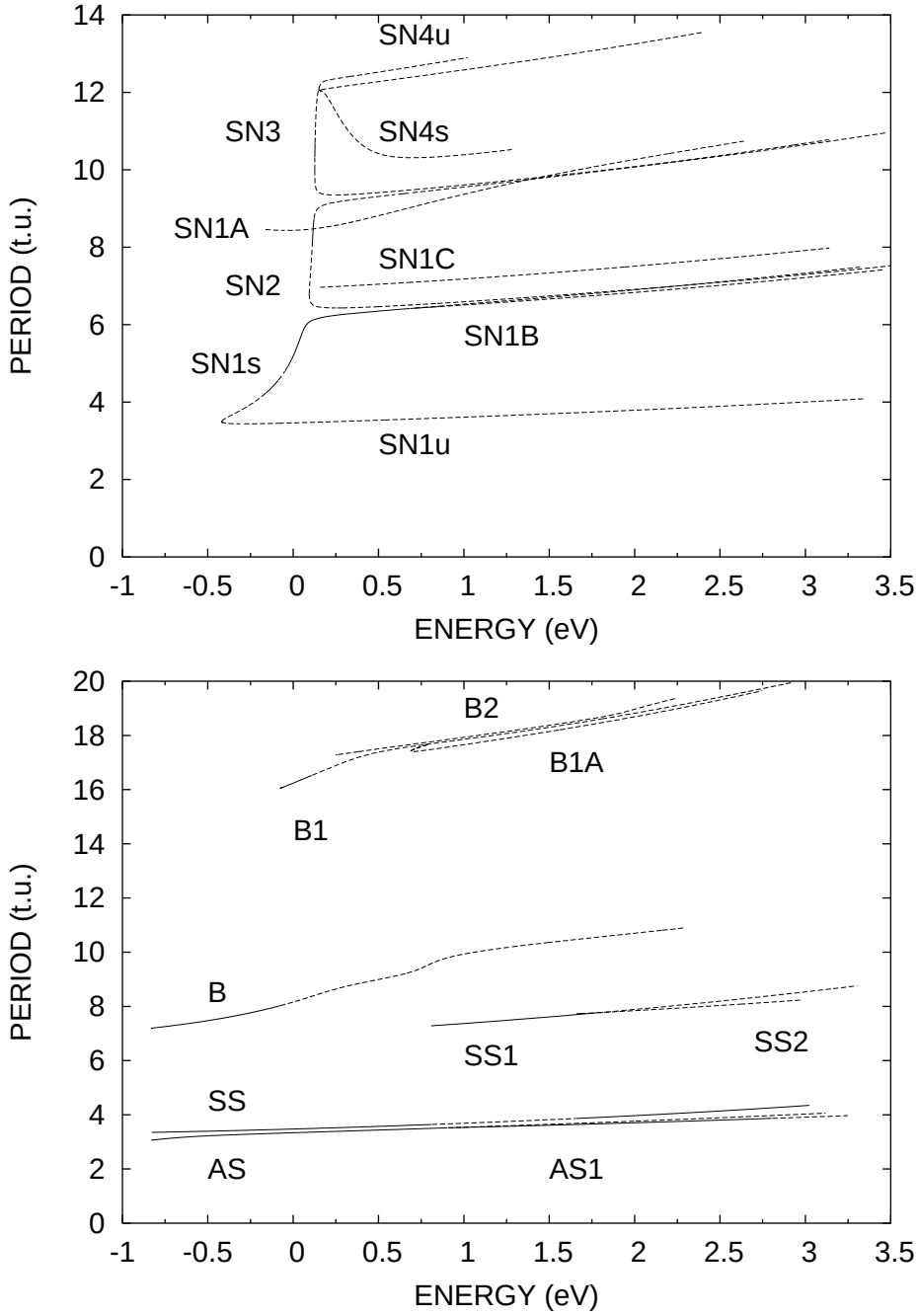

Figure 7.12: Continuation/Bifurcation Diagram for DCO: fundamental families (lower figure) and saddle–node families (upper figure). All periods are measured in time units of ~ 5.837 fs. Continuous lines represent stable families of periodic orbits; dashed ones indicate instability.

The first orbit of the **AS** family we located is at (−0.8328 eV, 3.063 t.u.). It is stable up to (0.905 eV, 3.52 t.u.) where a bifurcating family is born with the same period, inheriting the stability. This new family, **AS1**, destabilizes through a Hopf bifurcation at 2.805 eV and remains complex unstable well above 3.2 eV. Representative orbits of the **AS** and **AS1** families at various energies are given in fig. (7.13); their data are presented in table (7.3).

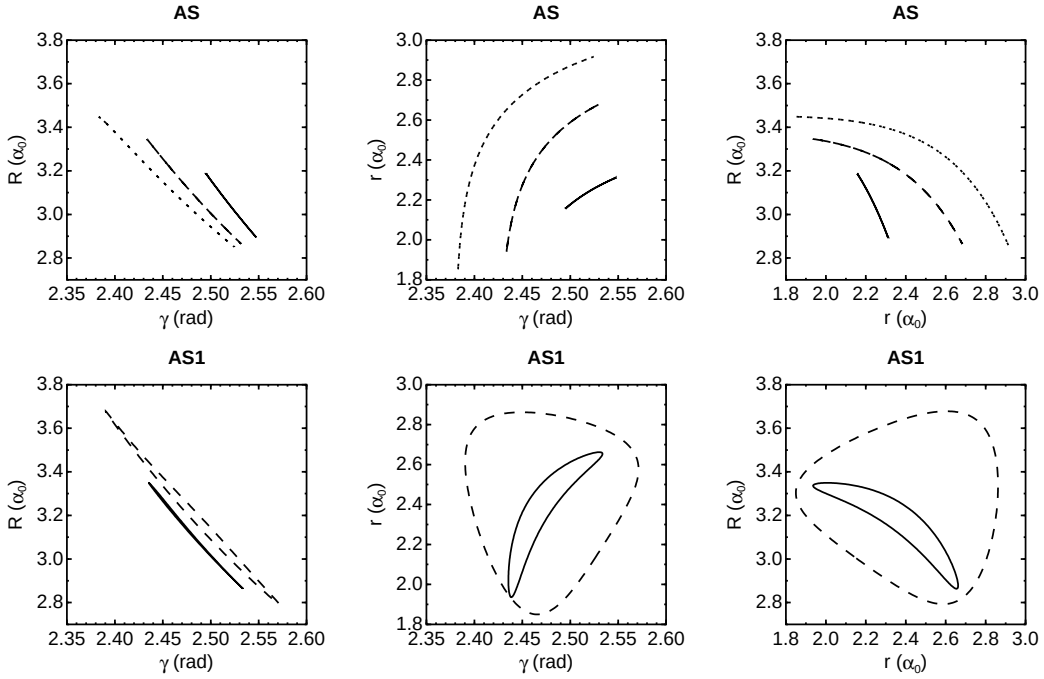

Figure 7.13: Projections of representative orbits of the **AS** and **AS1** families in DCO at various energies. The data are given in table (7.3). Solid, dashed, and dotted lines on the same plot represent orbits of increasing energy.

The **SS** family is stable up to (0.808 eV, 3.642 t.u.) where a period-doubling bifurcation gives birth to **SS1**. Stability is restored at (1.658 eV, 3.864 t.u.) through another period-doubling bifurcation, generating **SS2**, and is kept even above 3 eV. **SS1** starts at a period of 7.284 t.u.. It loses its initial stability at (1.78 eV, 7.763 t.u.) through a period-doubling bifurcation. The other two free-to-move Floquet multipliers collide at +1 and become real at 1.94 eV. Another period-doubling bifurcation occurs at 2.05 eV but it is too high to interest us. **SS2** starts with a period of 7.7283 t.u. and is twice unstable. At (1.801 eV, 7.775 t.u.) a period-doubling bifurcation occurs and the family becomes singly unstable. Representative orbits of the **SS**, **SS1**, and **SS2** families at various energies are given in fig. (7.14); their data are presented in table (7.3).

The principal family with prominent bending character, **B**, is stable up to (−0.078 eV, 8.022 t.u.) where a period-doubling bifurcation generates **B1**. A series of additional period-doubling bifurcations can be identified at 0.2488 eV, 0.272 eV, and 0.665 eV before the high instability of **B** prohibits a meaningful construction of the monodromy matrix. The family born at the first bifurcation is denoted by **B2**. **B1** starts at a period of 16.044 t.u. and is stable up to (0.111 eV, 16.525 t.u.)

where a period-doubling bifurcation occurs. At 0.79 eV the family is rendered doubly unstable through a steady–state bifurcation. The bifurcating branch is **B1A** and undergoes a saddle–node bifurcation around 0.6889 eV. The first located orbit of the **B2** family is at (0.2498 eV, 17.281 t.u.). The whole branch is unstable; there are indications that two steady–state bifurcations take place at 0.92 eV and 1.5 eV. Representative orbits of the **B** family and its bifurcations are plotted in fig. (7.15); their data are presented in table (7.3).

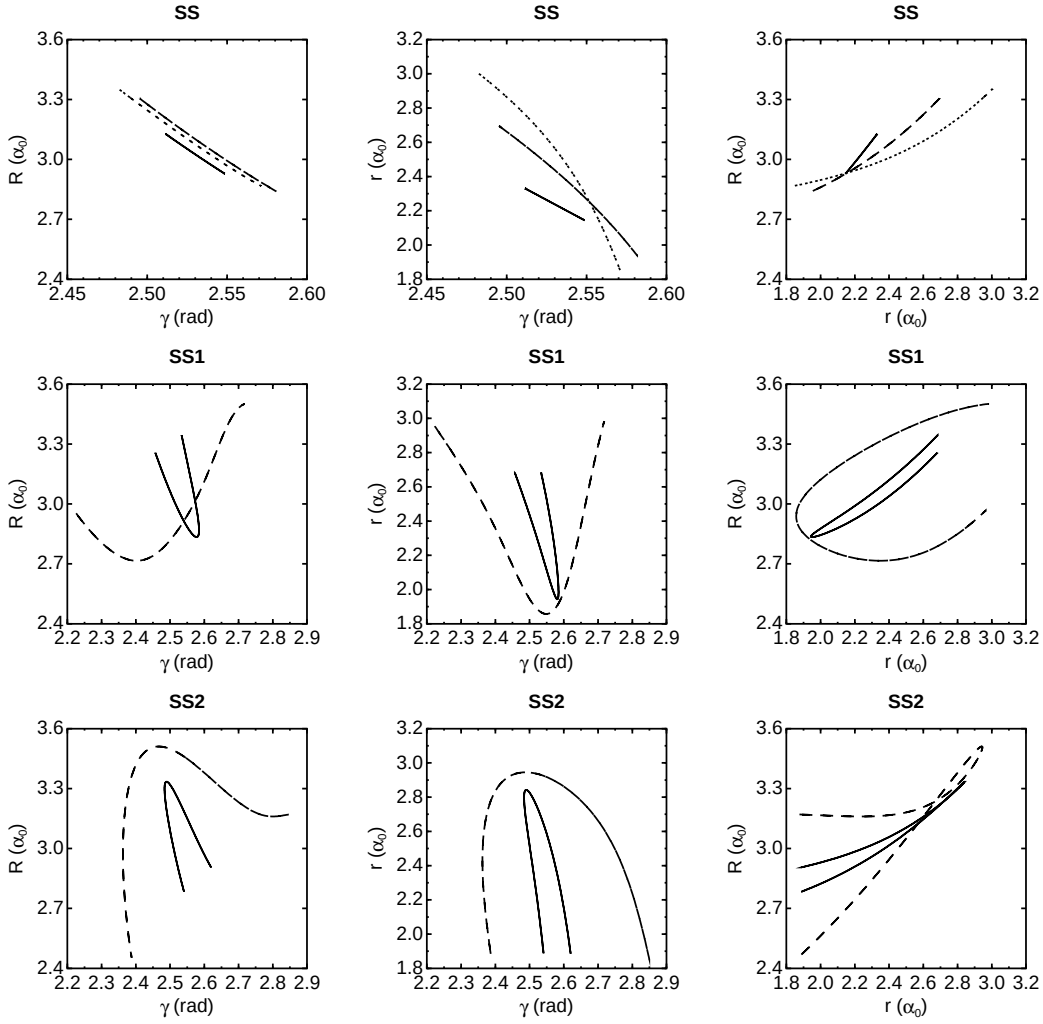

Figure 7.14: Projections of representative orbits of the **SS**, **SS1**, and **SS2** families in DCO at various energies. The data are given in table (7.3). Solid, dashed, and dotted lines on the same plot represent orbits of increasing energy. The narrower γ-range in the **SS** plots than in the others was chosen for clarity.

One family of periodic orbits originating at the dissociation barrier has been located. It is denoted by $\mathbf{r}'$ to indicate the primary excitation. It starts at (0.12569 eV, 2.9134 t.u.) and, naturally, is unstable. Representative orbits from it are plotted in fig. (7.16) while their data are given in table (7.3).

A series of saddle–node families has been located for DCO. Their overall pattern is

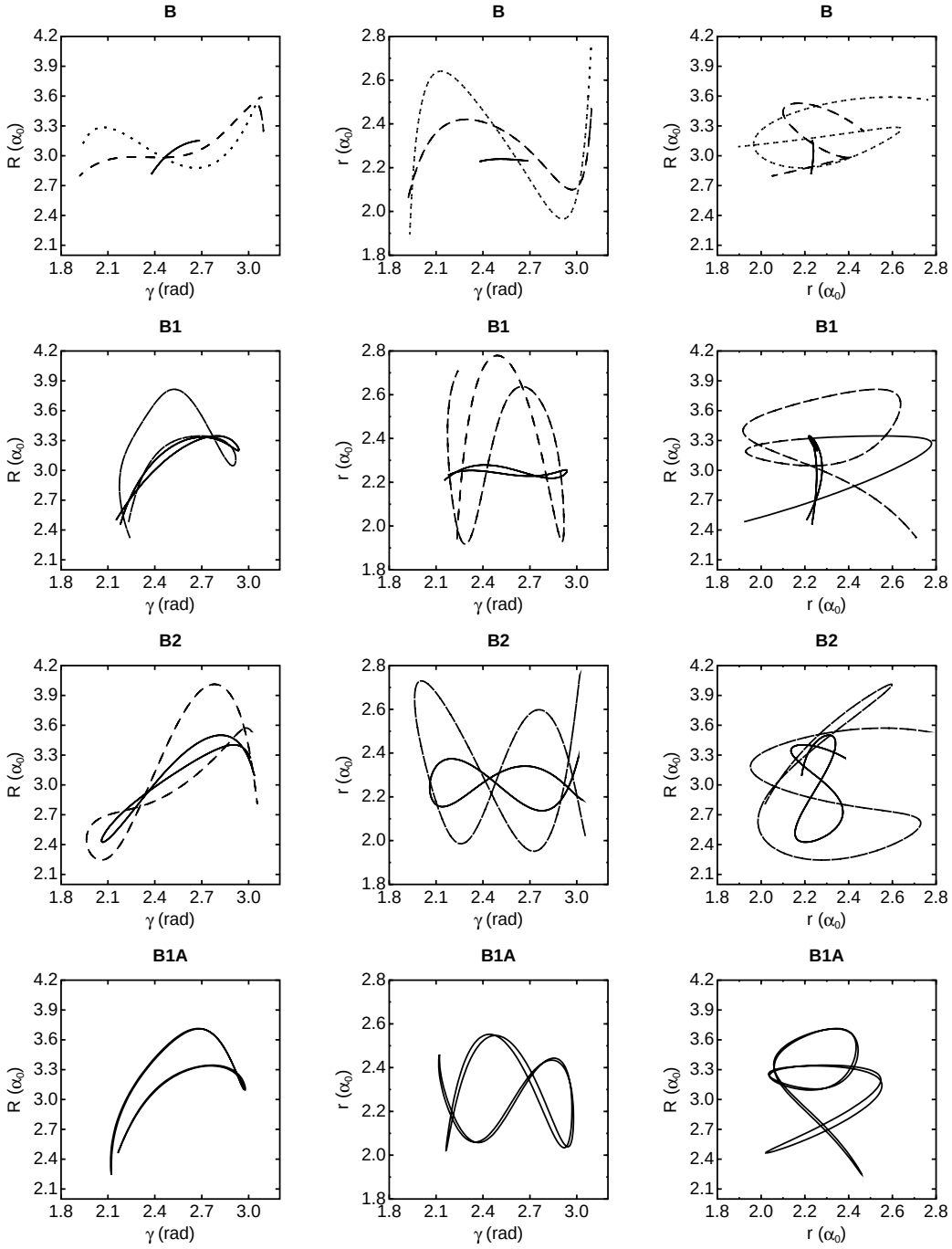

Figure 7.15: Projections of representative orbits of the **B**, **B1**, **B2**, and **B1A** families in DCO at various energies. The data are given in table (7.3). Solid, dashed, and dotted lines on the same plot represent orbits of increasing energy.

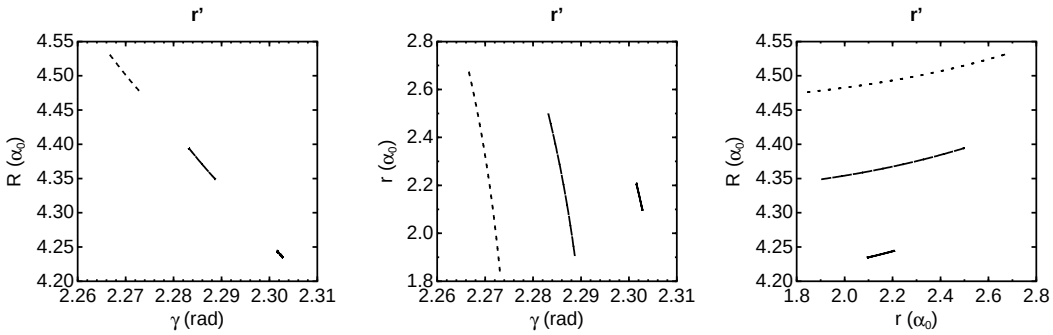

Figure 7.16: Projections of representative orbits of the $\mathbf{r}'$ family in DCO at low (solid line), medium (dashed line), and high energies (dotted line). The data are given in table (7.3).

the familiar one: each has a quite anharmonic segment which, when conditions allow a low-order resonance with r, changes its slope in the C/B diagram dramatically and evolves almost parallel to the fundamental stretching families. At the vicinity of the point where the slope changes for each family, its "successor" is born inheriting the anharmonic behavior. The detailed evolution of the saddle–node families is as follows.

SN1 is born at (−0.4185 eV, 3.4973 t.u.). Both its branches start as unstable; they can be characterized as stable (**SN1s**) or unstable (**SN1u**) in a reduced space. The "stable" is the one rising in period. At −0.1608 eV it undergoes a period–doubling bifurcation and stabilizes; the branching family there is denoted by **SN1A**. Two Hopf bifurcations, at −0.087 eV and −0.058 eV, and two period–doubling ones, at −0.048 eV and −0.034 eV, destabilize it briefly. Stability is eventually lost at a steady–state bifurcation around 0.688 eV where **SN1B** is born. The "unstable" branch, **SN1u**, undergoes a period–doubling bifurcation at 0.157 eV which generates **SN1C**. **SN1A** is born with an initial period of 8.4583 eV and inherits the instability of **SN1s**. Two period–doubling bifurcations have been recorded at 0.02 eV and 0.532 eV but the stemming branches were not followed. The first orbit of **SN1B** we located is at 6.4185 t.u.. It is stable up to 0.858 eV where a period–doubling bifurcation occurs. **SN1C** starts with a period of 6.965 t.u.. It is unstable and no qualitative changes of it take place. Representative orbits of the **SN1** family and its bifurcations are plotted in fig. (7.17) and fig. (7.18). Their data are given in table (7.4).

SN2 is born at (0.0944 eV, 6.7889 t.u.). The "stable" branch **SN2s** grows steeply towards higher periods. A series of period–doubling bifurcations around 0.11 eV at various periods (7.77 t.u., 8.02 t.u., 8.73 t.u.) is characterized by a window of stability between the last two. Another small stable segment is found between 0.615 eV and 0.68 eV before the branch becomes highly unstable. The unstable branch, **SN2u**, exhibits no qualitative changes. Quite interesting, though, is the fact that it is not parallel to **SN1s** but it crosses it at a point—unlike the saddle–nodes in HCO and other molecules we studied where each SN family is, in a sense, bounded by the neighboring ones. It turns out that a crossing occurs also between the **SN2s** and **SN3** families.

SN3 is born at (0.1262 eV, 9.993 t.u.). The upper branch, nominally denoted by

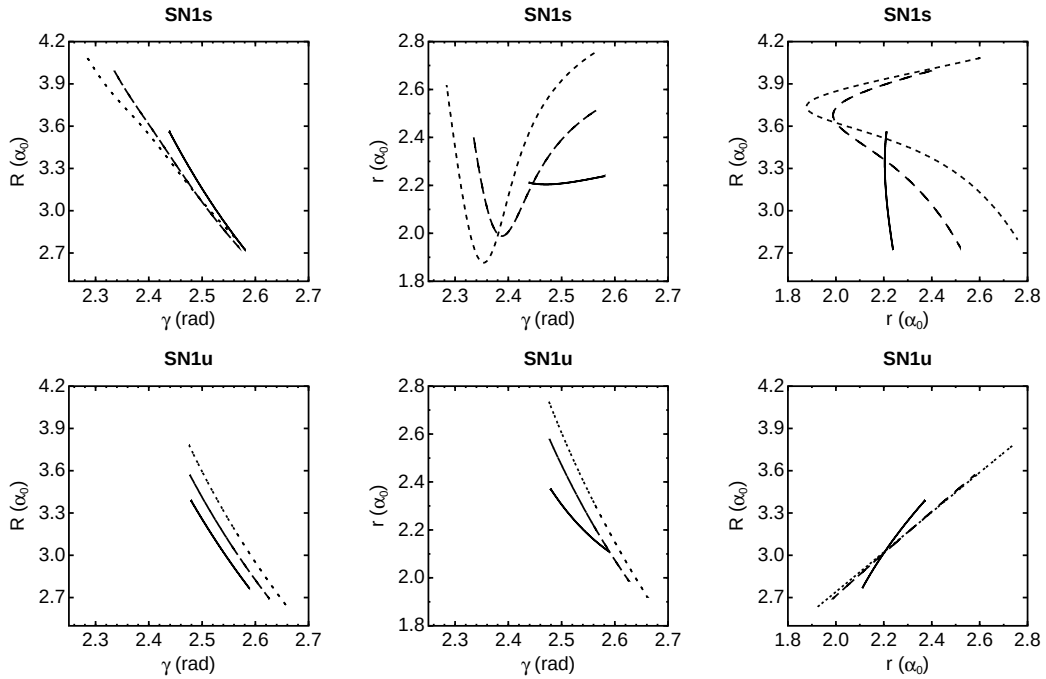

Figure 7.17: Projections of representative orbits of the **SN1** family in DCO at various energies. The data are given in table (7.4). Solid, dashed, and dotted lines on the same plot represent orbits of increasing energy.

SN3s, is quite steep and all interesting features occur around the energy mentioned. Its initial complex instability is lost at 10.313 t.u.. A period–doubling bifurcation at 10.683 t.u. ends the small stable segment. A steady–state bifurcation also takes place at 0.136 eV. The lower branch, **SN3u**, is highly unstable in the energy region we traced it. Representative orbits of the **SN2** and **SN3** families are plotted in fig. (7.19). Their data are given in table (7.4).

Another saddle–node family we located is at (0.1503 eV, 12.087 t.u.), denoted with **SN4**. It is born extremely close to the point where the upper branch **SN3** skews. The family is too unstable to construct a meaningful monodromy matrix and analyze it. The two branches, as we traced them, show the "reverse" behavior of the expected; one of them (denoted by **SN4s**) is quite steep but plunges in period until a resonance levels it, while the other (**SN4u**) evolves parallel to **SN3s**. Representative orbits of the **SN4** family are plotted in fig. (7.20).

7.4 Quantum Treatment and Discussion

The main quantum mechanical studies for the unimolecular dissociation of HCO and DCO we will refer to, have been presented by Keller *et al.* in [114] and [115] respectively, based on the WKS surface. Recent, and generally more accurate, results on resonances and widths of HCO have also been obtained by Poirier and Carrington in [118], on the same surface via another technique. We will review them below in order to relate them to our findings. Let us mention here that, since the work of Keller *et al.*, resonances of HCO for various values of the total angular momentum

FAMILY	ENERGY	PERIOD	R	r	γ	P_R	P_r	P_γ
AS	−0.6560	3.1650	3.0165207	2.2563368	2.5245714	0.5547972	−0.9970125	−0.6138411
AS	1.0496	3.5500	3.2346281	2.3155559	2.4538671	0.6416789	−4.4802130	−0.8207996
AS	2.4986	3.8900	3.4199483	2.1910495	2.3905728	0.2760014	−6.1924747	−0.4503949
AS1	0.9428	3.5255	3.1460518	2.3231218	2.4744072	0.7863873	−4.3714599	−0.9956587
AS1	2.6014	3.8250	3.0101842	2.1418158	2.5271885	1.1538631	−6.2832180	−1.3767704
SS	−0.6908	3.3680	3.1277752	2.3306421	2.5114482	−0.0043838	−0.0141953	0.0050842
SS	0.9063	3.6650	3.2981318	2.6866773	2.4964121	−0.1833982	−0.7563638	0.2309318
SS	2.4993	4.1400	3.3094632	2.9502013	2.4892793	−0.4042056	−1.9035480	0.5513256
SS1	0.8459	7.3000	3.2491088	2.6736846	2.4584717	−0.1771574	−0.7325674	0.2746527
SS1	2.5080	8.2000	2.8728632	2.8365639	2.2626159	−0.5221438	−2.9030235	1.6910972
SS2	1.6824	7.7360	3.3284639	2.8363702	2.4956253	−0.1573889	−0.6238618	0.7336360
SS2	2.7453	8.1350	3.4532939	2.9202747	2.5464429	−0.5293966	−1.2622128	3.7398831
B	−0.7052	7.2900	3.1472808	2.2330816	2.6607098	0.0385477	−0.0341072	0.9683388
B	0.9573	9.8760	3.4095105	2.3549850	3.0824211	0.7495842	−2.3969022	−0.6295446
B	2.1660	10.8120	3.5858420	2.5188121	3.0729394	−0.1213357	−3.9819708	−0.8219986
B1	−0.0555	16.1000	3.2362551	2.2418909	2.9307658	0.2991345	−0.3325327	−0.7110939
B1	1.7605	18.5600	3.3184369	2.2102500	2.8106161	0.2290862	5.0425718	−2.7394607
B1A	0.7875	17.6748	3.2914596	2.0511022	2.8868505	0.3380276	1.3372625	−2.4695383
B2	0.3711	17.3900	3.2766451	2.3789658	3.0099499	0.1728907	−0.5283114	−0.3725815
B2	2.0197	19.0000	3.5463204	2.3771512	2.9497909	−0.3399156	−4.5904658	−2.1754490
r′	0.1777	2.9200	4.2444894	2.2081444	2.3015433	0.0001934	0.0074751	−0.0002210
r′	1.4401	3.0950	4.3942708	2.4977284	2.2831952	−0.0141393	−0.4838340	0.0169530
r′	2.6077	3.2890	4.5308052	2.6664400	2.2666968	−0.0333414	−1.1713558	0.0415248

Table 7.3: Initial conditions for representative periodic orbits of the fundamental families in DCO. Lengths are measured in α_0, the angle in rad, the energy in eV, the period in t.u. (~ 5.387 fs) and the momenta in the appropriate derived units.

FAMILY	ENERGY	PERIOD	R	r	γ	P_R	P_r	P_γ
SN1s	−0.2396	3.9673	3.2539408	2.2049102	2.4842595	1.1425474	−0.0883595	−1.2041647
SN1s	0.7411	6.4373	3.9939475	2.3999928	2.3350206	−0.0020912	−0.0162302	0.0027878
SN1s	2.0214	6.9073	4.0793436	2.5925580	2.2856900	−0.1464541	−1.4150824	0.2273819
SN1u	−0.2611	3.4386	3.0238756	2.2032935	2.5397231	1.0864585	1.5974579	−1.1753299
SN1u	0.8306	3.5830	3.0636871	2.2329902	2.5562789	1.4849283	3.6346744	−1.5978425
SN1u	1.9994	3.7900	3.1824576	2.3129604	2.5609094	1.8467394	4.7532475	−1.9796628
SN1A	−0.1235	8.4460	3.3619626	2.2141492	2.3972206	1.0221516	0.0272229	−0.0877811
SN1A	1.5060	9.8600	3.6573821	2.3560169	2.4739746	0.6153082	−2.2457994	5.3544111
SN1B	0.7305	6.4305	3.9928518	2.3856923	2.3373658	−0.0555564	−0.8665139	0.0835710
SN1B	1.9988	6.8315	4.1302069	2.5395617	2.3286987	−0.0339948	−2.4718883	0.0872660
SN1C	0.3158	7.0000	3.0052885	2.2365978	2.4740690	1.1333303	2.8695016	−2.0773030
SN1C	1.9706	7.5000	3.0469641	2.4146703	2.2587203	1.1446160	4.1755984	−2.9783777
SN2s	0.1006	7.2689	3.9318028	2.1735320	2.3842781	0.3559370	−0.1504588	−0.2761834
SN2s	0.6987	9.4089	4.1289322	1.9887098	2.3179147	−0.0091583	−0.8643715	0.0087524
SN2s	1.5031	9.8089	4.1563566	1.9070038	2.2808688	0.0126299	0.9834283	−0.0091154
SN2u	0.2634	6.4312	3.1550528	2.2001837	2.4949976	1.7527238	0.9503130	−1.7272273
SN2u	1.6164	6.7800	2.8850796	2.1100046	2.5650395	2.1142962	3.2413383	−1.9773195
SN3s	0.1262	10.0830	4.1989560	2.1618919	2.3805393	−0.0176114	−0.0483726	−0.0034971
SN3s	0.6081	12.3430	4.1920576	2.0059674	2.3172430	−0.0869946	−1.0526937	0.0885767
SN3s	1.8624	13.1530	4.1844374	1.9378634	2.2346811	0.0105554	3.2916467	0.2319310
SN3u	0.2088	9.3530	4.1949749	2.2250227	2.3900331	0.0381427	0.3837374	−0.0101779
SN3u	1.2606	9.7220	4.3317531	2.3237861	2.4301660	0.2004460	3.1609126	−0.0471170
SN4s	0.1514	12.1170	4.2982419	2.1468290	2.4677834	−0.0732237	−0.1381367	−0.2539369
SN4s	1.0222	12.8970	4.3228756	1.9845383	2.6580260	−0.1325362	−1.5120815	−1.2903334
SN4u	0.1637	12.0340	4.3117607	2.1562701	2.5004700	−0.0616983	0.1772634	−0.3225672
SN4u	1.2814	10.5237	4.1160658	2.2249012	2.8856853	0.2953924	2.6230476	−1.9584393

Table 7.4: Initial conditions for representative periodic orbits of the saddle–node families in DCO. Lengths are measured in α_0, the angle in rad, the energy in eV, the period in t.u. (~ 5.387 fs) and the momenta in the appropriate derived units.

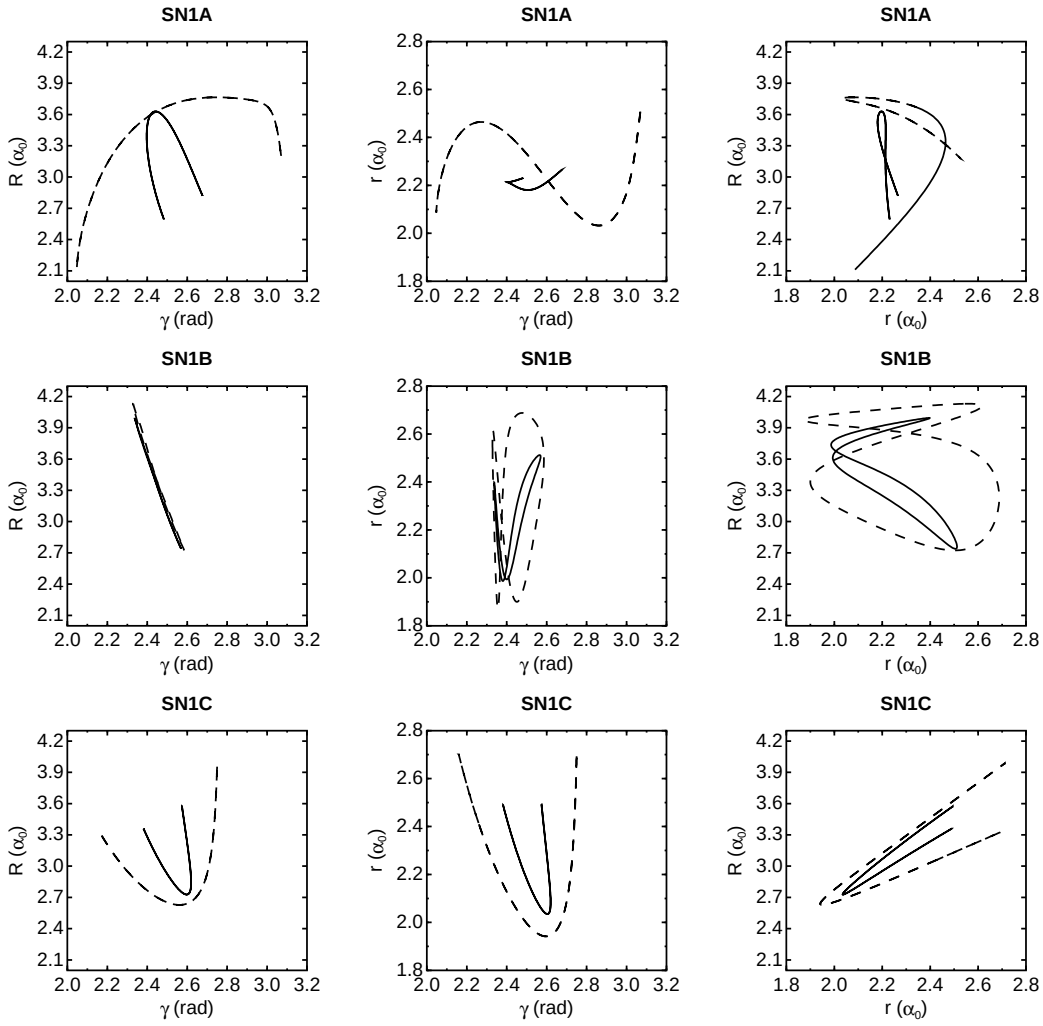

Figure 7.18: Projections of representative orbits of the located bifurcations of the **SN1** family in DCO at various energies. The data are given in table (7.4). Solid, dashed, and dotted lines on the same plot represent orbits of increasing energy.

have been calculated by Whittier and Light [117] on the RLBH surface.

The dynamical calculations by Keller *et al.* were performed in Jacobi coordinates, fig. (7.1); the Hamiltonian is the one given in eq. (4.1) as the total angular momentum J was zero for both molecules. There were also calculations for $J = 1$ in the case of DCO, which do not concern us. The group followed a modification of the log-derivative version of the Kohn's variational principle, outlined in §3.6, to solve the time-independent Schrödinger equation $(\widehat{\mathscr{H}} - E)\Psi_E^{(n,j)} = 0$ for the partial wave functions $\Psi_E^{(n,j)}$ subject to the appropriate boundary conditions for the fragmentation into H/D+CO(n, j). The quantum numbers (n, j) indicate the final vibrational and rotational state of CO respectively. The resonances show up as sharp structures in any quantity containing the wave functions; Keller *et al.* calculated an

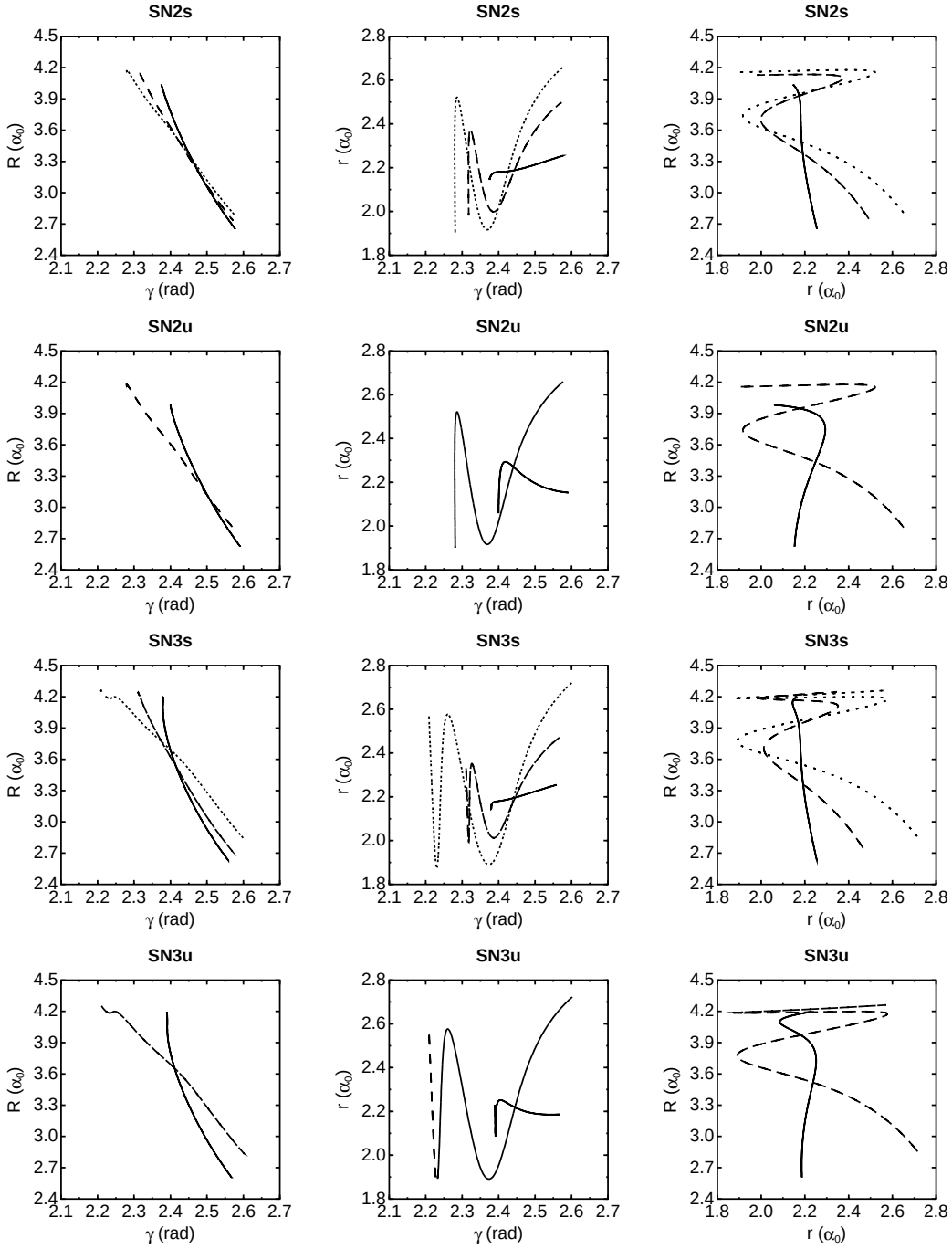

Figure 7.19: Projections of representative orbits of the **SN2** and **SN3** families in DCO at various energies. The data are given in table (7.4). Solid, dashed, and dotted lines on the same plot represent orbits of increasing energy.

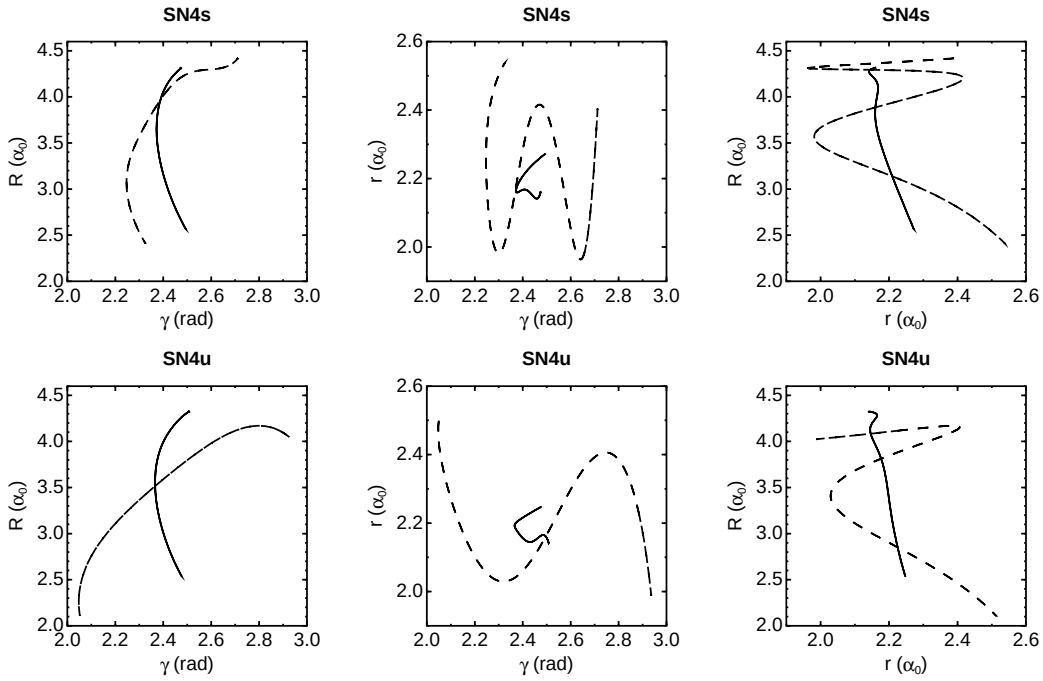

Figure 7.20: Projections of representative orbits of the **SN4** family in DCO at low (solid line), medium (dashed line). The data are given in table (7.4).

absorption-type cross section,

$$\sigma_{abs}(E) = \sum_{n,j} \left| \left\langle \chi_0 \middle| \Psi_E^{(n,j)} \right\rangle \right|^2,$$

as a sum over all open product channels (n, j). χ_0 was arbitrarily chosen to be a three-dimensional Gaussian function appropriately localized and extended in order to give good Franck–Condon overlap with many resonance states. Information on resonance energies and widths was extracted through a fit of a Lorentzian at the peaks of the lifetime function

$$\tilde{\tau}(E) = \frac{||\Psi_E||^2}{4\ \sigma_{abs}(E)}.$$

Ψ_E is the total wave function, the one we will plot later on for various resonances, a particular superposition of all partial wave functions for a given energy,

$$\Psi_E = \sum_{n,j} \left| \Psi_E^{(n,j)} \right\rangle \left\langle \Psi_E^{(n,j)} \right| \chi_0.$$

Its norm is computed over the region where the coupling of the various vibrational–rotational channels of CO is not negligible.

7.4.1 HCO

The quantum calculations estimated the ground energy of the HCO system to be -0.48685 eV, and provided the fundamental excitation energies of the three normal

modes at 2437.2 cm^{-1}, 1865.0 cm^{-1}, 1079.3 cm^{-1} for the HC stretch, CO stretch and $\widehat{HCO}$ bending modes respectively. The corresponding experimental values [203] are 2434.5 cm^{-1}, 1868.2 cm^{-1}, and 1080.8 cm^{-1}. Given the periods of the classical oscillators we can estimate the corresponding frequencies to be 2715.79 cm^{-1}, 1888.23 cm^{-1}, and 1110.40 cm^{-1} respectively, while the ground-state energy is classically derived at -0.47963 eV. The quantum and experimental results are in very good agreement as the PES was appropriately modified to achieve this, while the slight discrepancy exhibited in the classical values for the frequencies of the CO stretch and bending modes can be accounted for: the frequencies of the classical oscillators were computed at the minimum of the potential while the quantum treatment incorporates the zero-point energy. The substantial deviation of frequencies in the HC stretch reflects the large anharmonicity of this mode, evident in the C/B diagram, fig. (7.3), and corroborated by the significantly lower second excitation energy in the HC progression. We will denote by (v_1, v_2, v_3) a state with v_1, v_2, v_3 quanta in the HC stretch, CO stretch, and bending modes respectively.

The analysis of the lifetime function provided 15 true bound states and 123 resonances up to 2 eV. Bound states are these with energy below the ground state of the isolated CO, at 0.135 eV; the resonance states with energy below the dissociation barrier (including the zero-point energy in r and γ) at 0.27 eV, are blocked by a dynamical barrier and decay via tunneling. Let us note that Poirier *et al.* in [118] calculated additional resonances up to 1.11 eV, interspersed among those derived by Keller *et al.*.

As we see in the potential cuts, fig. (7.2), the two primary dissociation channels, H+CO and HC+O, are almost perpendicular to each other; r- and γ-oscillators are also largely independent. These imply a weak coupling of the CO stretching mode to the coordinates of H. The quantum mechanical calculations validate this conclusion as Keller and coworkers managed to identify unambiguously all eleven members of the $(0, v, 0)$ progression falling into the energy window they studied. The patterns of the corresponding wave functions were clear and their energies indicated a very regular progression. It is also corroborated by the C/B diagram fig. (7.3) and the relevant plot, fig. (7.5), as the family denoted by **r** exhibits an almost pure CO excitation—and, therefore, scars the $(0, v, 0)$ progression, has a slightly ascending period, and is stable almost throughout the energy region we probed. Similarly, progressions with excitation in r and few quanta on one of the other two modes exhibit a clear nodal structure up to their high overtones.

The fundamental excitation energies are initially quite different and no mixing effects appear. As the quantum calculations showed, the pure $(v, 0, 0)$ progression is substantially anharmonic and, at some energy, the HC stretch tunes into resonance with the similarly—but in a lesser degree—anharmonic bending mode and approaches the period of CO stretch. This is also evident in the classical bifurcation diagram: just above the dissociation threshold, the **R** and **B** families come very close to a 1:2 resonance which is approximately retained in the rest of the energy region we studied. The fact that two quanta of the bending mode roughly equal one of the HC stretch led Keller and coworkers to categorize the quantum states according to their *polyad number* $P = 2v_1 + v_3$ (and their CO stretch quantum number v_2). At low energies, where the states with the same P and v_2 are energetically far from each other, the polyad members exhibit clear nodal patterns. At higher energies, the resonance

sets in and the approximately degenerate states mix substantially; the assignment in terms of normal modes is, in cases, rather ambiguous and, even, meaningless and infeasible. Certain wave functions were identified against their nodal pattern, based solely on their position in their polyads, while others were left "unnamed." Let us note that Tobiason *et al.* in [200] provided an assignment based on a Dunham expansion fit of the experimental energies which generally agrees with the one by Keller *et al.*, derived by the visual inspection of each wave function. Of course, states with more than one quanta on the dissociation mode, the HC stretch, were not measured experimentally as they turned out to have a very short lifetime. The theoretical computations had the same problem for overtones with more than two quanta on HC stretch; they were rather broad for a definite identification and those located were mixed, due to the resonance, and assigned an ambiguous label. The overall agreement between experiment and theory on the positions of the resonances is excellent; the estimated rms deviation is 17 cm^{-1}.

An alternative assignment of the quantum states, based on the structure of the classical phase space and its periodic orbits, can elucidate the mixing due to resonances and guide the identification of the members of a progression. Periodic orbits are governed by the same resonances of a quantum system albeit in a classical way; they have a distinct advantage over the presumed independent normal modes and are not tied to a particular coordinate system. In fig. (7.21) the $\{R, \gamma\}$ projections of selected wave functions with excitation in R and γ are presented, plotted on the corresponding in shape periodic orbits. In the upper right corner of each panel, their energy (in cm^{-1}) above zero-point and the normal mode assignment are given. The assignment in parentheses, $(2, 0, 1)$, is determined by the position in a polyad, and, therefore, is in some cases, ambiguous. As we can see, the wave functions of the pure $(0, 0, v)$ progression possess a very clear nodal pattern which, despite the assignment, is not aligned with the γ axis. They are obviously scarred by orbits of the **B** family and the nodes are arranged on them. In fact, all wave functions presented, develop along the periodic orbit (or combination of periodic orbits) which scars them and not necessarily according to their "name." Therefore, the $(2, 0, 0)$, $(1, 0, 1)$ and $(2, 0, 1)$ states are all scarred by the **R2** family (the first one might have a contribution from **R**), and, according to our analysis, are related. On the other hand, the $(1, 0, 0)$ state is scarred by **R** while $(3, 0, 0)$ is localized mainly along a **SN1** orbit, something which explains the large anharmonicity of the $(v, 0, 0)$ progression.

Keller and coworkers did not succeed in determining overtones higher than $(3, 0, 0)$ and $(0, 0, 7)$, at 0.744 eV and 0.875 eV above zero-point energy, respectively. This can be justified in the classical framework: stability of the corresponding periodic orbit families is lost at 0.896 eV and 0.905 eV above minimum; the corresponding actions are 3.33 $\hbar$ and 7.0 $\hbar$. Higher overtones in HC stretch and bending modes fall into the region where the classical orbits of **SN1** and **B** are unstable.

In fig. (7.22) the energy differences between successive members of the pure progressions is plotted against the energy of the higher state in each pair. The points are overlayed on the plot of the frequencies of the relevant periodic orbits vs. their excitation energy. The classical energies with respect to the potential minimum are shifted by the zero-point energy. As we can see, the transition energies follow the frequencies of the corresponding periodic orbit families with the exception of the last point of the $(v, 0, 0)$ progression which is influenced by **SN1** and **R2**. Nevertheless,

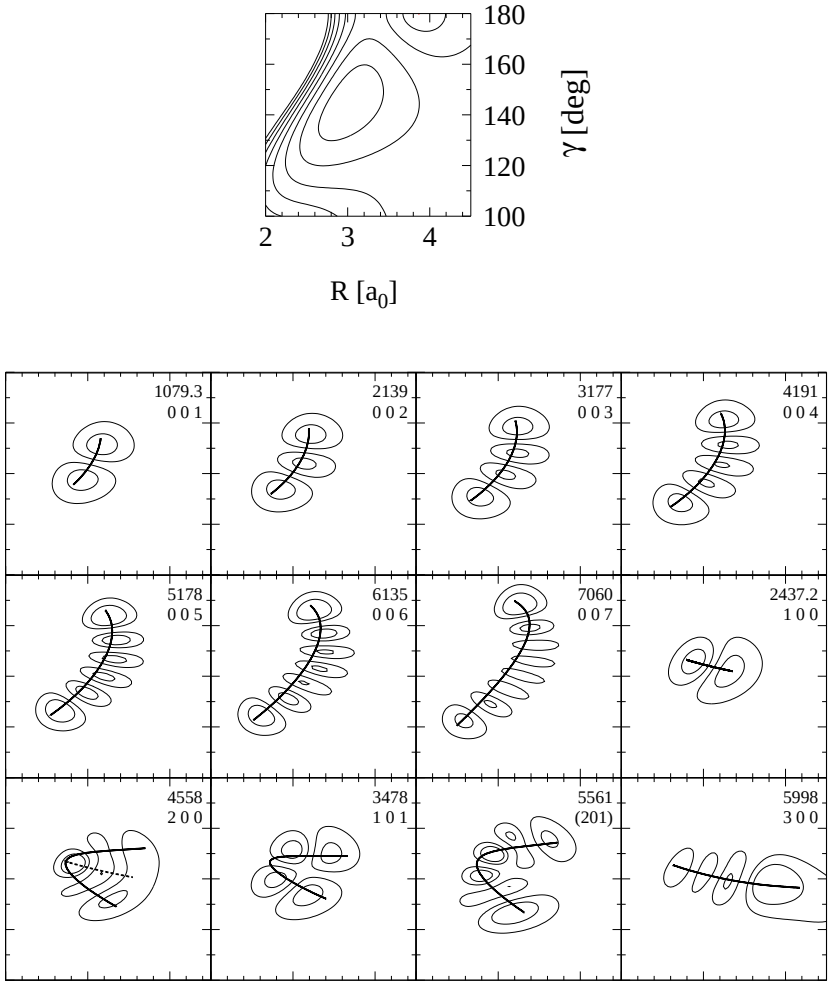

Figure 7.21: Contour plots of the modulus square of selected eigenfunctions in the $\{R, \gamma\}$ plane in HCO, superimposed on the corresponding periodic orbits that scar them. The normal mode assignment and the energy in cm^{-1} above the ground state are given for each. Shown separately is the relevant potential cut at minimum.

the trend indicated by the steep segments of **R** and **SN1** is reflected in the evolution of the transition energies in the pure HC stretch progression.

7.4.2 DCO

The ground state of DCO was calculated to be -0.54465 eV. The quantum treatment provided the fundamental excitation energies of the three normal modes at 1804.8 cm^{-1}, 1900.6 cm^{-1}, and 843.8 cm^{-1} for the two stretching and $\widehat{DCO}$ bending modes respectively. The corresponding experimental values [186] are 1795.0 cm^{-1}, 1910.2 cm^{-1}, and 846.5 cm^{-1}. Given the periods of the classical oscillators we can estimate the corresponding frequencies to be 1848.6 cm^{-1}, 2021.9 cm^{-1}, and 860.7cm^{-1} respectively, while the ground-state energy is classically derived from them at -0.54059 eV. The quantum values are in very good agreement with the experimental results in view of the fact that the WKS PES was adjusted to repro-

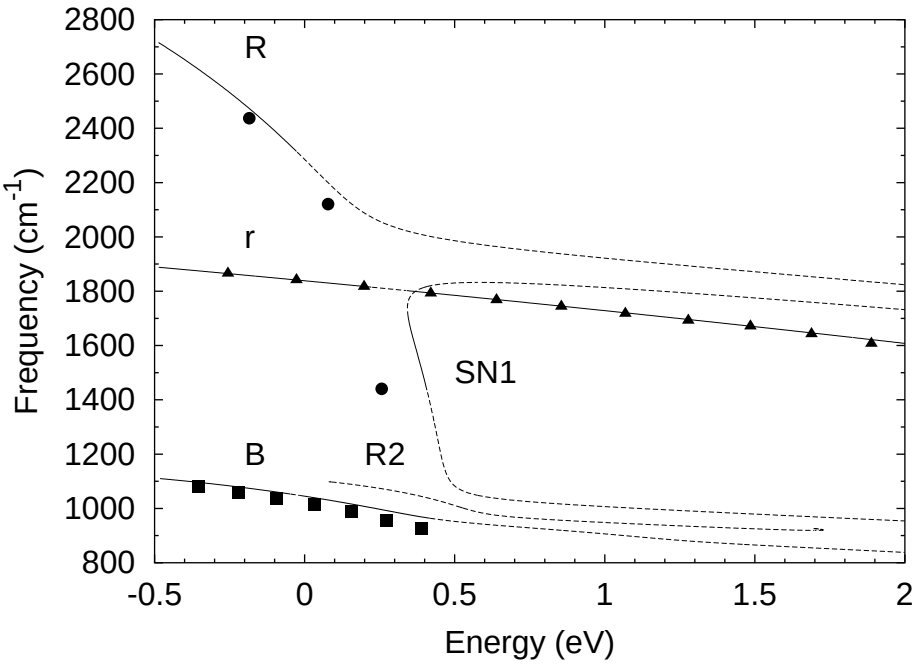

Figure 7.22: Transition energies, i.e. energy differences between neighboring levels, for the three progressions $(v,0,0)$ (●), $(0,v,0)$ (▲), and $(0,0,v)$ (■) in the HCO spectrum. Each symbol is plotted at the energy of the upper state and is overlayed on the frequency curves of the periodic orbits of the **R**, **SN1**, **R2**, **B** and **r** families. The energy of each orbit above minimum is shifted by the zero-point energy. Solid lines represent stable families; dashed ones indicate instability.

duce experimental HCO spectra and was not modified for the DCO analysis. The relative deviation of the classical from the quantum values in the bending mode is comparable to the corresponding one in the HCO case. Recall that in HCO the classical frequencies of other two modes, the harmonic CO stretch and the quite anharmonic HC stretch, exhibited respectively a small and a large deviation from the quantum excitation energies. In the DCO case, this difference in magnitude is smoothed out: both stretch modes are mildly anharmonic.

In all experimental, quantum, and classical results, the accidental 1:1:2 approximate resonance is evident. Due to this resonance and the strong coupling of R and r, the two stretching modes cannot be characterized of primarily DC or CO stretch but, instead, can be described as symmetric and antisymmetric combinations of them. The mixing between modes can be demonstrated by varying a parameter in the Hamiltonian and investigating how this change affects the energies of the modes. The easiest way to introduce a parameter without a modification of the potential is a multiplicative factor on the mass of the hydrogen atom. It can be shown quantum mechanically [115] as well as classically fig. (7.23) that the almost pure HC and CO stretch modes we saw in HCO undergo an avoided crossing and mix—or, in classical terms, the corresponding oscillators gradually tune into resonance—when the mass of the light atom varies continuously from $1m_{\mathrm{H}}$ to $2m_{\mathrm{H}}$. The classical harmonic approximation estimates that the mixing is maximal around $2.1m_{\mathrm{H}}$, not far from

what the accurate quantum treatment predicts ($\approx 1.9 m_{\rm H}$). On the other hand, the bending mode is not involved in the mixing and remains relatively intact.

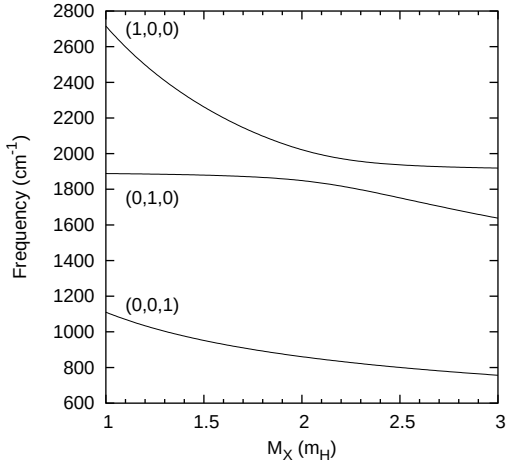

Figure 7.23: Fundamental frequencies of the three normal modes in the XCO molecule as a function of the mass of X. The upper two curves are the stretching modes; the lower is the bending mode.

Keller and coworkers have located in DCO 29 bound states, that is, with energy less than the ground state of the free CO (0.135 eV), and 144 resonances up to 1.5 eV. The agreement with the experiment [186] on the energies was deemed excellent with an rms deviation of 16 cm^{-1}; the widths were not reproduced with the same accuracy. The 1:1 resonance and the strong coupling between the DC and CO stretches prevented a meaningful identification for the majority of the wave functions. The assignment (v_1, v_2, v_3) with v_1, v_2, v_3 quanta in the DC stretch, CO stretch, and bending modes respectively, was straightforward mostly for overtones of the pure bending mode and for few states with excitation in the other two. In fig. (7.24) [reprinted from [115]], contour plots in the $\{R, r\}$ plane of all calculated states assigned as $(v_1, v_2, 0)$ are depicted, labeled with their nominal normal mode assignment. Visual inspection cannot justify the identification for some of them in this figure; striking examples are the states labeled with $(0, 1, 0)$ and $(1, 0, 0)$ which actually reflect the assignment of the HCO states they evolve into when the light atom mass is varied from $m_{\rm D}$ to $m_{\rm H}$.

The fact that one quantum in DC stretch roughly equals a quantum in CO stretch or two quanta in the bending mode facilitates the organization of the quantum states into polyads according to their polyad number $P = v_1 + v_2 + v_3/2$. Within each polyad there are states which participate in an avoided crossing. The most prominent coupling exists between states assigned as $(0, v_2, v_3)$ and $(1, v_2 - 1, v_3)$ where one quantum is transferred from DC stretch to CO stretch and vice versa. Among others, states which exchange two quanta between these modes were found to mix, as the $(0, v_2, v_3)$ and $(2, v_2 - 1, v_3 - 2)$ states do, due to the strong coupling between the coordinates of the light atom. Note that the assignments above refer to the corresponding states away from the crossings, that is, either in HCO or TCO. An alternative way to label a state is through a decomposition in terms of basis wave functions. As we mentioned, the mere visual identification of the mixed states in DCO in terms of normal modes is problematic.

The analysis of the classical phase space offers another means to classify most quantum states into progressions without the shortcomings of the assignment based

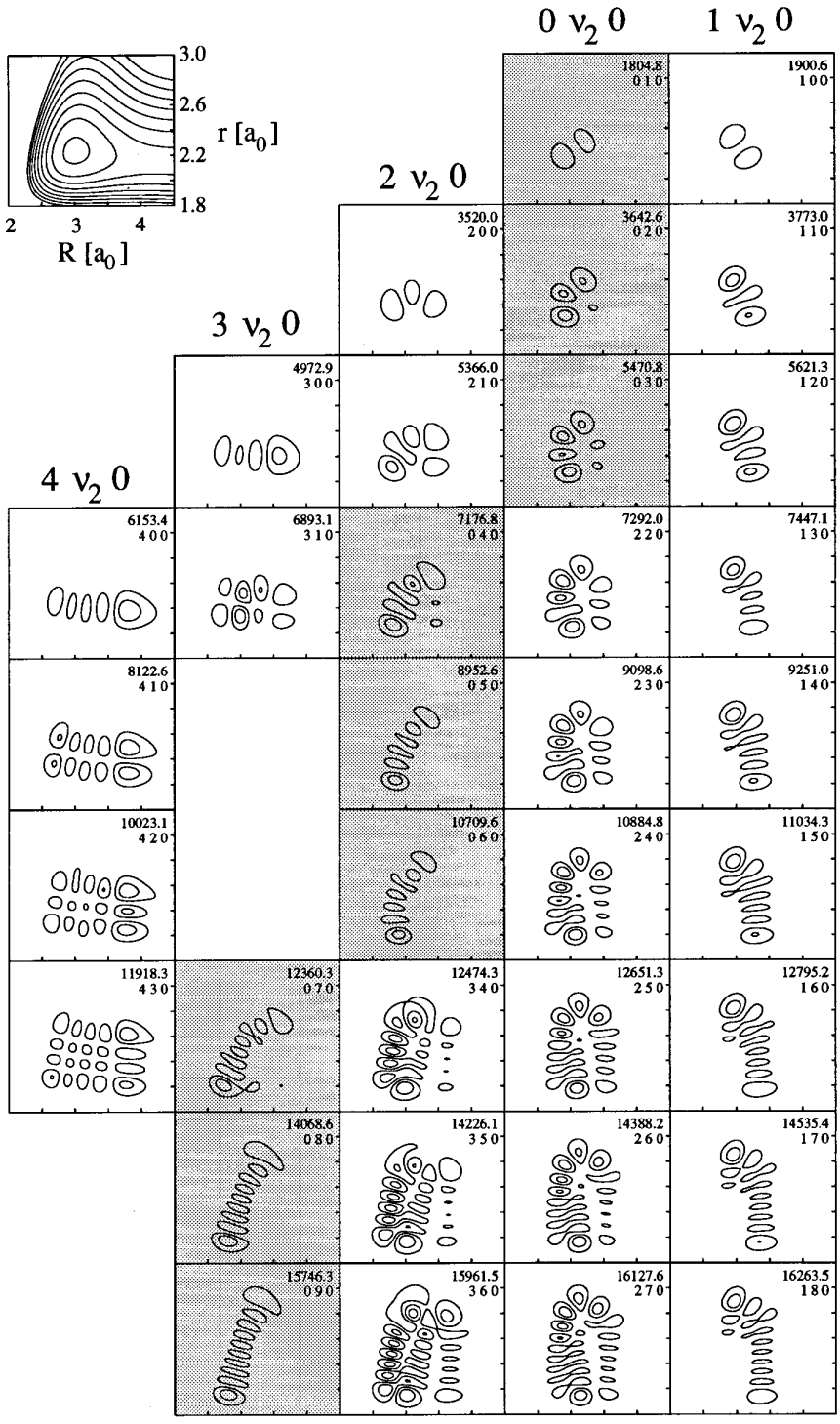

Figure 7.24: Contour plots in the $\{R, r\}$ plane of all calculated states by Keller *et al.* assigned as $(v_1, v_2, 0)$ in DCO. [Fig. 11 of [115]].

on normal modes. We notice in fig. (7.24) that there are groups of wave functions which form pure progressions, that is, their maxima and minima align incrementally along a line in one direction without excitation perpendicular to it. Such a group is the progression identified as $(1, v_2, 0)$; another comprises the $(0, v_2, 0)$ states although one could seriously question the assignments of the $(0, 2, 0)$, $(0, 3, 0)$ and $(0, 7, 0)$ states and their fundamental difference from e.g. $(2, 2, 0)$. The $(2, 0, 0)$, $(3, 0, 0)$, and $(4, 0, 0)$ states (but not the $(1, 0, 0)$ one) appear to form another progression. In fig. (7.25), the members of these progressions are overlaid on the corresponding—with respect to excitation energy—periodic orbits of specific families. The $(1, v_2, 0)$

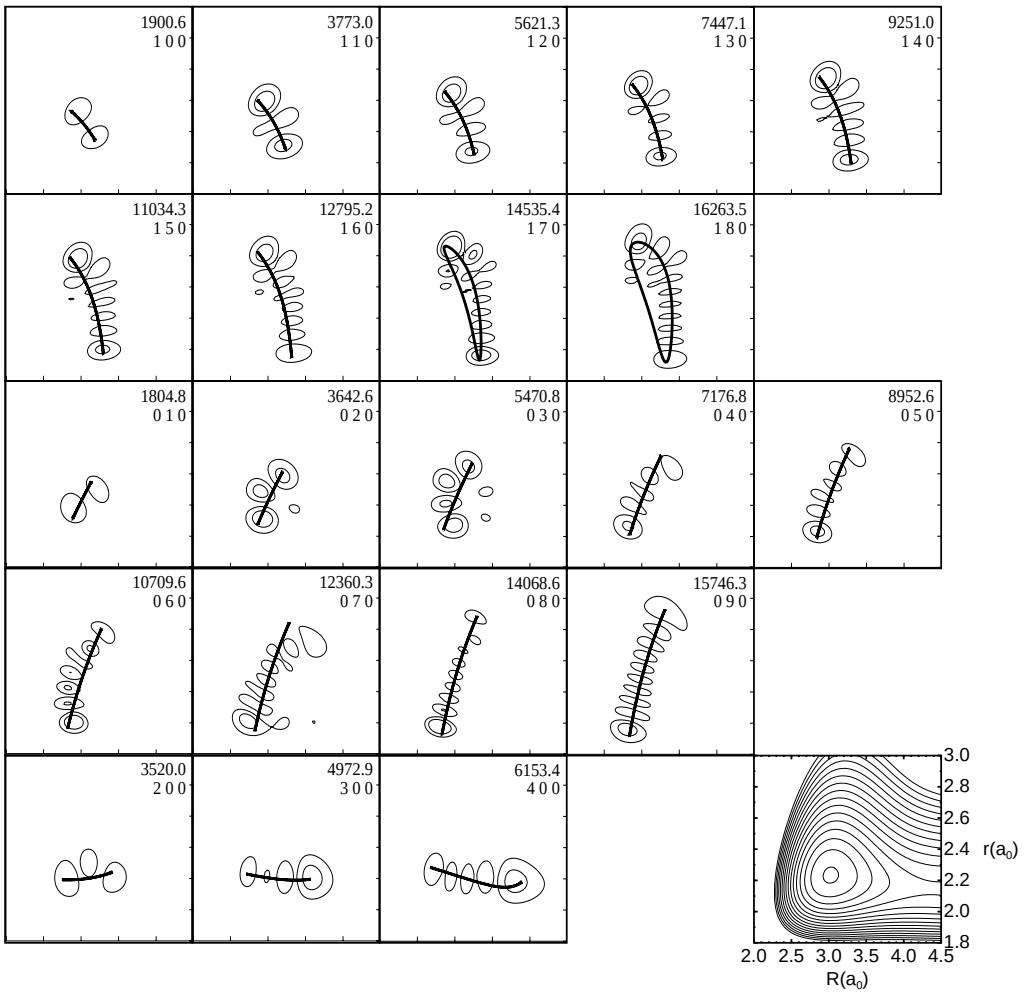

Figure 7.25: Contour plots in the $\{R, r\}$ plane of the modulus square of the wave functions of the $(1, v, 0)$, $(0, v, 0)$, $(v, 0, 0)$ progressions in DCO, superimposed on periodic orbits of the **AS** and **AS1**, **SS**, and **SN1** families respectively that scar them. The normal mode assignment and the energy in cm^{-1} above the ground state are given for each. The relevant potential cut at minimum is also shown.

states are scarred by the **AS** family; the last two members of the progression are more appropriately superimposed on orbits of the **AS1** family which is the stable branch with almost exactly the same period with the corresponding segment of the

AS family. The $(0, v_2, 0)$ states are localized on orbits of the **SS** family while **SN1** scars the $(v_1, 0, 0)$, $v_1 = 2, 3, 4$ progression.

Although two plots only are available to us from the pure bending progression, fig. (7.26), the relation of $(0, 0, v_3)$ states to the classical **B** family can be verified through their energies, as shown below.

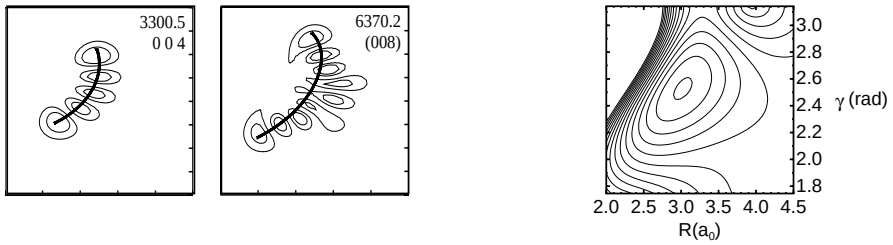

Figure 7.26: Contour plots in the $\{R, \gamma\}$ plane of the modulus square of the wave functions of $(0, 0, 4)$ and $(0, 0, 8)$ states in DCO, superimposed on corresponding periodic orbits of the **B** family. The normal mode assignment and the energy in cm^{-1} above the ground state are given for each. The relevant potential cut at minimum is also shown.

The qualitative relation of the four progressions mentioned above with the corresponding periodic orbit families, can also be demonstrated through the dependence of their transition frequencies, i.e. the energy differences between adjacent levels, on energy and their relation to the classical frequencies, fig. (7.27). The oscillations observed in the $(0, v_2, 0)$ transition energies and the fact that the backbones of some members do not follow the orbits (cf. fig. (7.25)) can be attributed to a substantial mixing with other states or, even, an inappropriate assignment. It is no surprise, from a classical point of view, that no states in the pure progressions with more quanta have been located; the corresponding classical families are unstable at the energies where the higher members would lie, and no similar and stable periodic orbits exist there to localize the wave functions. Especially for levels above $(4, 0, 0)$, the dissociation barrier has been reached and their lifetimes are too small to allow identification.

Fig. (7.25) and fig. (7.27) make clear beyond doubt that all states but the first, characterized as of DC stretch character, $(v_1, 0, 0)$, correspond to the saddle–node periodic orbits of **SN1** while $(1, 0, 0)$ is fundamentally different and should be attributed to an **AS** orbit. The saddle–node orbits appear just before the next excited level and mark the domains in phase space where eigenfunctions localized along the R coordinate can be found. Orbits of the **SN1** family also play important role in the localization of other states with substantial excitation in R and few quanta on r. According to the assignment based on periodic orbits, the $(1, v_2, 0)$ states comprise, despite their "name," a pure progression which should be labeled as **AS**. Most members of $(0, v_2, 0)$ should unambiguously be assigned as **SS** states while there is doubt whether the remaining levels in this progression according to the normal mode decomposition do actually belong to it. On the other hand, the assignment of the $(0, 0, v_3)$ states—which do not participate considerably in any mixing—is clearly justified by the classical analysis.

It is worth noting that Tobiason *et al.* in [185] performed an assignment based on a Dunham fit of the energy differences measured in their dispersed fluorescence ex-

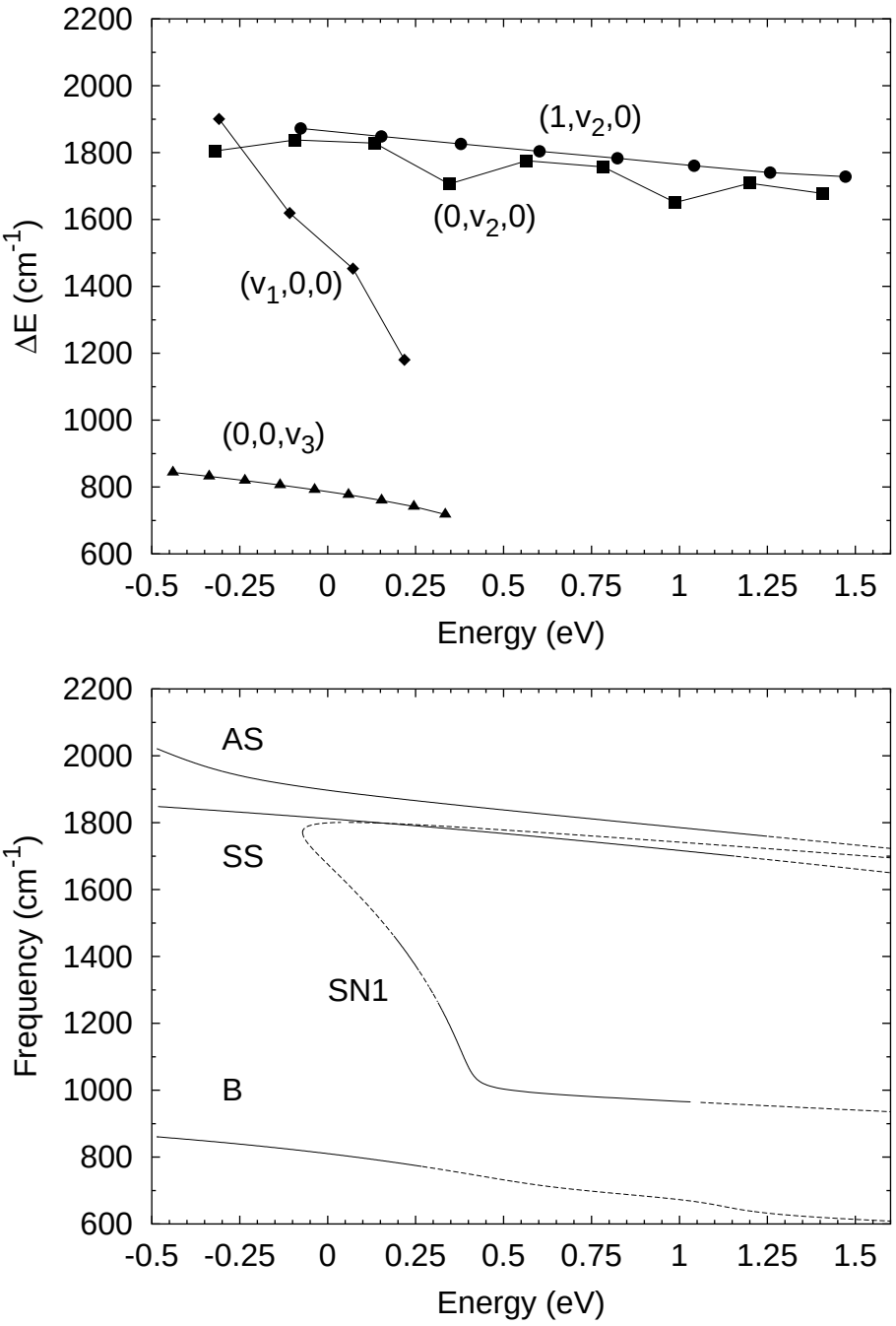

Figure 7.27: (a) Transition energies, i.e. energy differences between neighboring levels, for the four progressions $(v_1, 0, 0)$ (♦), $(0, v_2, 0)$ (■), $(0, 0, v_3)$ (▲) and $(1, v_2, 0)$ (●) in the DCO spectrum. Each symbol is plotted at the energy of the upper state. (b) Frequency curves of the periodic orbits of the **AS**, **SS**, **SN1**, and **B** families. The energy of each orbit above minimum is shifted by the quantum zero-point energy. Solid lines represent stable families; dashed ones indicate instability.

periment. Their labeling of many states does not agree with the one by Keller *et al.*; in fact, the assignment of $(2, 2, 0)$ is attributed to $(0, 4, 0)$ and vice versa, state $(0, 7, 0)$ by Keller *et al.* is $(2, 4, 2)$ according to Tobiason *et al.*, etc..

7.5 Conclusion

The analysis presented above of the HCO and DCO quantum spectra demonstrates the general scope of the assignment based on periodic orbits: it is applicable to both spectra, providing consistent labeling of states, whether the normal mode assignment suffices (as in HCO case) or is inadequate (as in DCO). The Fermi resonance between two or more modes may prevent a meaningful assignment, while, as seen here, it is predicted and embodied naturally in the shape of the scarring periodic orbits. Moreover, the number and the evolution of the pure progressions is correctly deduced through the classical analysis avoiding the distortions imposed by the assignment based on the normal modes.

Chapter 8

Spectroscopy of hypochlorous acid (HOCl)

8.1 Introduction

Hypochlorous acid, HOCl, is one of the molecules drawing considerable research efforts, both experimental and theoretical, into its spectroscopy and dynamics, mainly due to its role in the chemistry of the upper atmosphere. It acts as a reservoir of OH and chlorine [204] while its photodissociation via the three available channels (OH+Cl, HCl+O, OCl+H) gives reactive species of atmospheric relevance [205]. Moreover, HOCl was proposed to play an important role in the balance of stratospheric ozone in the polar regions; it contributes to the conversion of relatively stable chlorine reservoir compounds into more reactive species via heterogeneous chemistry on polar stratospheric clouds [206]. A detailed understanding of the infrared spectrum of HOCl facilitates, among others, the monitoring of its concentration in the atmosphere, a crucial factor in its implications. HOCl is also much studied due to its pure scientific interest. It is a prototype system for investigating bond breaking on ground-state Potential Energy Surfaces (PES) which lack reaction barriers; intense research focused on this [207].

The spectroscopy [208] and dissociation [209] of HOCl are the target of recent experimental interest. However, due to experimental limitations (vibrational overtone spectroscopy), only states in the vicinity of overtones of the HO bond are considered—out of the $\tilde{8}00$ bound states merely 2%-3% have been experimentally analyzed.

In this chapter we will present our research results on HOCl. We will mainly focus on the analysis of the classical phase space and study the influence of saddle–node bifurcations on the level pattern and morphology of the quantum states. This process helps us test, validate and expand our approach in deducing quantum features based on classical analysis. We begin with an exposition of the potential energy surface we employed, followed by the detailed analysis of the classical phase space regarding the organization of periodic orbits. The subsequent section presents a review of the behavior of the quantum eigenstates in terms of their shape and energy distribution along with a detailed cross-reference to classical features. The presentation here is a revised and expanded version of the analysis we published in [210].

8.2 Potential Energy Surface

Various groups have proposed functional forms representing the potential of the HOCl electronic ground state, mainly in the vicinity of the equilibrium, either empirically, (Escribano *et al.* [211]), or through ab initio calculations: Halonen and Ha [212] used third order Møller–Plesset method, Peterson [213] and Koput and Peterson [214] employed CCSD(T), a variant of Coupled Cluster method, to calculate high quality ab initio values. The last two potentials were very accurate in reproducing the experimentally known overtones and combination bands up to energies of about 10000 cm^{-1}. However, the study of high overtones of the HO stretching mode and the fragmentation into HO and Cl requires a global function covering at least the HO+Cl channel. Skokov, Peterson, and Bowman [215] extended the calculations of Peterson and constructed such a global surface. Our group also derived a suitable PES [210], with comparable accuracy in the ab initio level to their version. Skokov *et al.* however, performed a more elaborate scaling procedure and therefore their PES reproduces the experimentally known vibrational energies slightly better than our surface. The general topographies of the two potential functions are very similar. We will describe below the details of our potential which, of course, is the one employed in our classical and quantum treatment.

The total energies of hypochlorous acid are calculated using the internally contracted multi-reference configuration interaction method with Davidson correction (icMRCI+Q) (§3.5.3). The one-particle basis set employed in the calculation is the correlation-consistent polarized set of quintuple-zeta quality, cc-pV5Z. The cc-pV5Z basis set consists of a $(20s12p4d3f2g1h)/[7s6p4d3f2g1h]$ set for chlorine, a $(14s8p4d3f2g1h)/[6s5p4d3f2g1h]$ set for oxygen, and a $(8s4p3d2f1g)/[5s4p3d2f1g]$ set for hydrogen, thus resulting in a molecular one-particle basis set of 241 contracted functions. Only the spherical harmonic components of the d through h polarization functions are used. The reference wave function in the icMRCI calculations consists of a full valence complete active space (CAS). The wave function thus includes all excitations of 14 valence electrons in 9 molecular orbitals corresponding to the valence atomic sp orbitals of chlorine and oxygen, and the $1s$ orbital of hydrogen. For each point of the PES, the reference wave function is determined in the complete active space self-consistent field calculation (CASSCF). The molecular $1s$- and $2sp$-like core orbitals of chlorine and the $1s$-like core orbital of oxygen are kept doubly occupied in all the configurations and optimized. In the vicinity of the minimum of the PES, the contribution of the SCF configuration in the CASSCF wave function is determined to be about 0.98 and there are only two excited configurations with coefficients greater than 0.05. The total energy of hypochlorous acid is determined in the subsequent icMRCI calculation, in which all single and double excitations with respect to the reference wave function are included and external configurations are internally contracted. The molecular core orbitals are kept doubly occupied in all the configurations. This results in over one million contracted configurations (in contrast to over 75 million uncontracted configurations). The multi-reference Davidson correction to the calculated energy is then employed to approximately compensate for the effects of higher excitations. The total energies are determined to an accuracy better than 10^{-8} hartree. All calculations were performed using the MOLPRO program [85].

Ab initio calculations were performed on 1234 points scattered on a grid covering most of the energetically accessible configuration space. On this grid, the two bond distances R_{HO} and R_{OCl} and the $\widehat{HOCl}$ bond angle vary from 1.3 α_0 to 3.5 α_0, 2.5 α_0 to 9 α_0, and 20° to 160° respectively. Distances are spaced 0.1 α_0 apart and the angle increases by 10° steps for the largest part of the grid. The mesh is denser around the equilibrium whereas it is coarser at large OCl distances. The dissociation channel to HO+Cl is energetically much more favorable than the others [216, 217] and, therefore, it is the only one sampled.

The analytical function to be fitted on the ab initio points was expressed in bond coordinates in an attempt to make a reasonable extrapolation towards the two linear configurations where no points were calculated. Following Sorbie and Murrell (§3.5.6), the total potential is written as

$$V(R_{\mathrm{OCl}}, R_{\mathrm{HO}}, R_{\mathrm{ClH}}) = V_I(R_{\mathrm{OCl}}, R_{\mathrm{HO}}, R_{\mathrm{ClH}}) + v_{\mathrm{HO}}(R_{\mathrm{HO}}),$$

where V_I goes to zero for large OCl distances. The diatomic term is expressed as a Morse potential, eq. (3.24), with the parameters taken from [218]: $D = 4.621$ eV, $a = 1.2139\ {\alpha_0}^{-1}$, and $R_e = 1.8323\ \alpha_0$. The energy normalization is chosen such that $E = 0$ corresponds to HO+Cl with the HO distance fixed at equilibrium. The "interaction potential" V_I is written as a threefold sum of one-dimensional functions:

$$V_I(R_{\mathrm{OCl}}, R_{\mathrm{HO}}, R_{\mathrm{ClH}}) = \frac{1}{2}\left[1 + \tanh\left(6 - R_{\mathrm{OCl}}\right)\right] \sum_{i=0}^{7}\sum_{j=0}^{7}\sum_{m=0}^{7} \alpha_{ijm} g_i(R_{\mathrm{HO}}) h_j(R_{\mathrm{OCl}}) d_m(R_{\mathrm{ClH}}),$$

with

$$\begin{aligned} g_i(R_{\mathrm{HO}}) &= \left[1 - e^{-k_{\mathrm{HO}}\left(R_{\mathrm{HO}} - \bar{R}_{\mathrm{HO}}\right)}\right]^i \\ h_j(R_{\mathrm{OCl}}) &= \left[1 - e^{-k_{\mathrm{OCl}}\left(R_{\mathrm{OCl}} - \bar{R}_{\mathrm{OCl}}\right)}\right]^{j+1} - 1 \\ d_m(R_{\mathrm{ClH}}) &= \left[1 - e^{-k_{\mathrm{ClH}}\left(R_{\mathrm{ClH}} - \bar{R}_{\mathrm{ClH}}\right)}\right]^m . \end{aligned}$$

The non-linear parameters are: $\bar{R}_{\mathrm{HO}} = 1.85\ \alpha_0$, $\bar{R}_{\mathrm{OCl}} = 3.2\ \alpha_0$, $\bar{R}_{\mathrm{ClH}} = 4.0\ \alpha_0$, $k_{\mathrm{HO}} = 0.3\ {\alpha_0}^{-1}$, $k_{\mathrm{OCl}} = 0.8\ {\alpha_0}^{-1}$, $k_{\mathrm{ClH}} = 0.1\ {\alpha_0}^{-1}$. All $h_j(R_{\mathrm{OCl}})$ functions go to zero as R_{OCl} tends to infinity. The damping factor introduced in V_I suppresses spurious features of the potential at large distances where the ab initio points are scarce.

The linear parameters α_{ijm} are determined using a least-squares fit procedure. Two independent fits $V_I^{(1)}$ and $V_I^{(2)}$ were performed with different weighting factors for the ab initio points: one focuses on the potential well giving smaller weight to points above dissociation while the other provides a better description of the global potential by treating all points equivalently. The final expression for the HOCl ground-state PES is

$$V = (t-1)V_I^{(1)} + tV_I^{(2)} + v_{\mathrm{HO}},$$

where the switching function t is defined by (all energies are in eV)

$$t = \frac{1}{2}\left\{1 + \tanh\left[8\left(V_I^{(2)} + v_{\mathrm{HO}} + 0.8\right)\right]\right\}.$$

The rms deviation of the fit from the ab initio points is of the order of 1meV even well above the $E = 0$ threshold; in the vicinity of the primary equilibrium is even less. In order to improve agreement with experimental data on the overtone frequencies from [209], the two bond distances R_{HO} and R_{OCl} were scaled by 0.996 and 0.998 respectively. The modified PES agrees favorably in all its features with relevant experimental results.

The analysis of the surface reveals a global minimum of -2.524756 eV at $R = 3.24077\ \alpha_0$, $r = 1.82848\ \alpha_0$, $\gamma = 1.81650$ rad in Jacobi coordinates, cf. fig. (8.1). This particular choice is the appropriate one for studying the dissociation of HOCl into HO and Cl: R is the distance from Cl to the center of mass of HO, r is the HO bond distance, and γ is the angle between the two vectors $\vec{R}$ and $\vec{r}$; $\gamma = 180^\circ$ corresponds to linear HOCl.

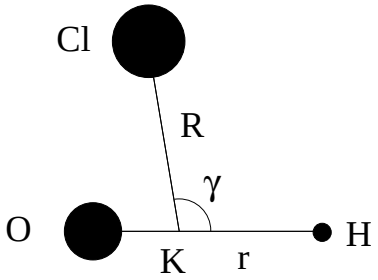

Figure 8.1: Coordinates for the HOCl molecule. K indicates the H–O center-of-mass.

Fig. (8.2) depicts the equipotential contour plots of the PES at minimum. In the same figure we also depict a projection of the minimum energy path towards the HO+Cl channel; the potential is minimized in r and γ for successive specific values of R. From the first plot is evident that there is no barrier in the HO+Cl exit channel. Moreover, from the orthogonality of the two channels $R \to \infty$ and $r \to \infty$ we can infer the (approximate) independence of R and r. In the linear geometry, $\gamma = 180^\circ$, two conical intersections exist, caused by interaction with higher electronic states [215]. The first one is estimated to occur near $R = 4.03\ \alpha_0$, $r = 1.85\ \alpha_0$ at 0.449 eV and is attributed to an interaction of the $1\,^1A'$ and $2\,^1A'$ states, which vanishes for linear configurations where these states are of $^1\Sigma^+$ and $^1\Pi$ symmetry. It is essentially the crossing between the Σ^+ and Π states of OH as Cl is relatively far. The second conical intersection is located at $R = 3.26\ \alpha_0$, $r = 3.14\ \alpha_0$ at 2.29 eV; it can be regarded as the crossing between the Σ^+ and Π states of OCl. Both intersections occur at relatively high energies and are not expected to influence significantly the bound and low resonance states. Recall that the potential for geometries close to linearity is evaluated by extrapolation and, thus, is only qualitatively correct. Based on this remark, certain features of the potential—such as a spurious saddle point at $R = 3.15\ \alpha_0$, $r = 1.78\ \alpha_0$, $\gamma = 180^\circ$ where $V = -0.44$ eV—which are not present in the Skokov *et al.* PES should be treated with caution. Nevertheless, they do influence the quantum states, even bound ones.

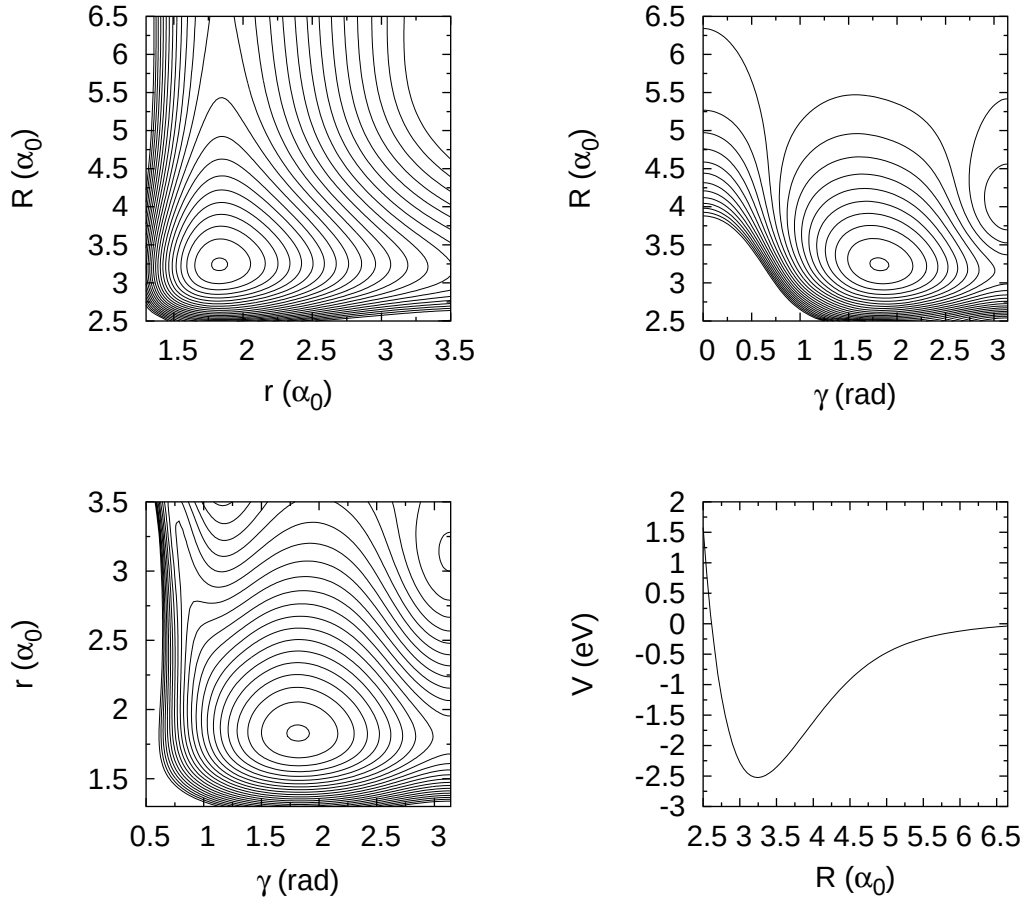

Figure 8.2: Contour plots of the HOCl ground-state potential energy surface at minimum. On each plot, one coordinate is fixed at the corresponding value at minimum. The 23 contours start from -2.5 eV and increase by 0.25 eV. The lower right panel depicts the potential energy as a function of R along the minimum energy path. The potential is minimized in r and γ for specific R.

8.3 Analysis of the Classical Phase Space

The classical treatment of HOCl was performed in Jacobi coordinates, fig. (4.1)(I). The angular momentum was taken to be zero. The values for the masses we used are $m_{\mathrm{O}} = 15.99494$ u, $m_{\mathrm{H}} = 1.00777$ u, and $m_{\mathrm{Cl}} = 35.44594$ u.

The Continuation/Bifurcation (C/B) diagram for the HOCl compound is given in fig. (8.3). It depicts the periodic orbit families we located, plotting their period (measured in time units of ~ 5.387 fs) with respect to their energy (in eV). For clarity it is split in two, one graph comprising the principal families and their bifurcations, and another consisting of the saddle–node orbits. Energy plays the role of the "external" parameter which causes the bifurcations.

Three principal families emerge deep in the potential well. The orbits just above the energy minimum have periods very close to those predicted through the harmonic expansion (Weinstein theorem, cf. §2.3.2). The calculated periods of the

classical harmonic oscillators are 8.3499 t.u., 1.6330 t.u., and 4.8571 t.u.. The first corresponds to an orbit with predominant Cl–OH stretching and substantial γ excitation; the family starting with it will be denoted by **R**. The second period is of an orbit of pure OH stretching; its family is labeled with **r**. The third period corresponds to an orbit exhibiting mainly bending character but with non-negligible R amplitude; **B** stands for its family. Below we present their detailed evolution.

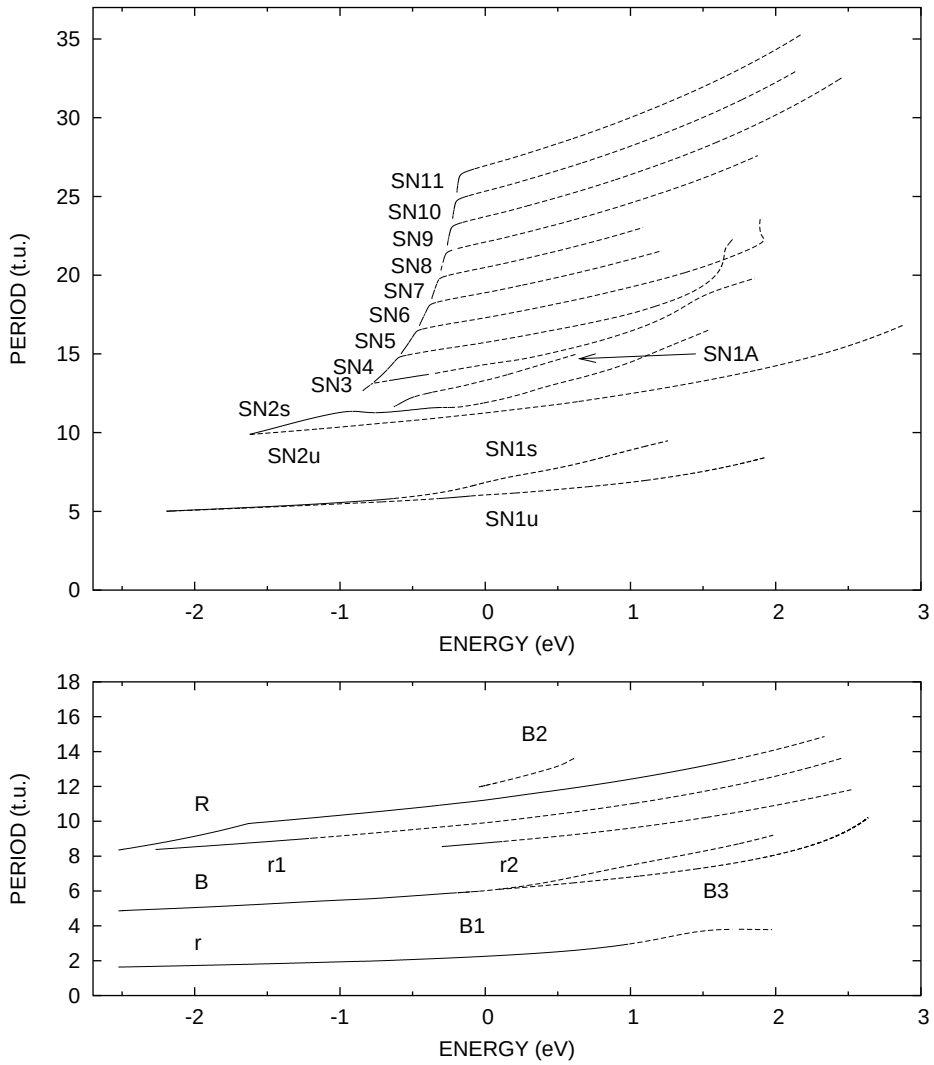

Figure 8.3: Continuation/Bifurcation Diagram for HOCl: fundamental families (lower figure) and saddle–node families (upper figure). All periods are measured in time units of ~ 5.837 fs. Continuous lines represent stable families of periodic orbits; dashed ones indicate instability.

The **R** principal family is initially stable and quite anharmonic compared to the other fundamental families. At (-2.064 eV, 9.0300 t.u.) it comes very close to a period–doubling bifurcation but does not destabilize. At (-1.6290 eV, 9.8700 t.u.) **R** exhibits an abrupt change in its slope in the C/B diagram and at the same point the Floquet multipliers indicate that a steady–state bifurcation is imminent.

As we will see below, at the vicinity of this point the **SN2** saddle–node family is born. This behavior is the most clear example we have encountered so far of an "avoided" pitchfork bifurcation, cf. fig. (2.3). The **R** family becomes less anharmonic and retains its stability up to (1.687 eV, 13.5 t.u.) where it undergoes a period–doubling bifurcation. The skew marks the onset of a 1:6 resonance between R- and r-oscillators. As we can see in fig. (8.4) where orbits of **R** at low, medium, and high energies from table (8.2) are plotted, the amplitude in r is negligible before the skew but grows considerably afterwards. The fact that the excess energy is deposited in the r-oscillator contributes to the stabilization of **R** and makes it follow the evolution of the more harmonic **r** family we will examine below.

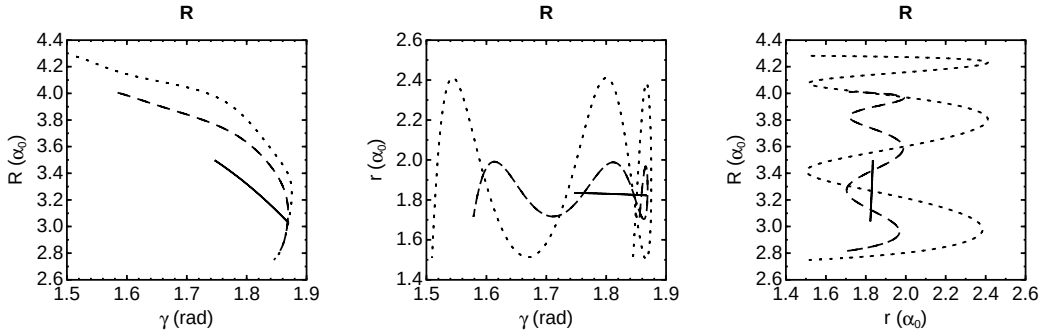

Figure 8.4: Projections of representative orbits of the **R** family at low (solid line), medium (dashed line), and high energies (dotted line). Their data are given in table (8.2).

The **r** family is remarkably stable in a wide range of energies and exhibits an almost pure OH stretching character. It undergoes a period–doubling bifurcation around (0.9933 eV, 2.96 t.u.) where it loses stability. However, before this point two branching families of **r** have been located: one with five times the period of the orbit at (−2.2695 eV, 1.676 t.u.) of **r** and the other with four times the period at (−0.2994 eV, 2.1367 t.u.); at these energies, a pair of eigenvalues of the monodromy matrix reaches $e^{\pm 2\pi i/5}$ and $e^{\pm 2\pi i/4}$ respectively. The first one, denoted by **r1**, starts with a period of 8.38 t.u. and is stable up to (−1.205 eV, 9.02 t.u.) where it undergoes a period–doubling bifurcation. The second, denoted by **r2**, starts with a period of 8.5465 t.u.. It is destabilized at (0.125 eV, 8.845 t.u.) through a period–doubling bifurcation. Such a bifurcation also occurs at 1.88 eV, rendering the family twice unstable. Representative orbits of the **r**, **r1**, and **r2** families are plotted in fig. (8.5); their initial conditions, energies, and periods are given in table (8.2).

The **B** family loses its initial stability at (−0.1894 eV, 5.901 t.u.). A steady–state bifurcation there gives birth to **B1** which, in its short lifetime, evolves exactly as **B** before it merges with it at −0.101 eV thereby restoring the stability of **B**. A period–doubling bifurcation finally renders the bending family unstable at (−0.0437 eV, 5.985 t.u.) where **B2** is born. Another steady–state bifurcation at 0.09 eV renders the **B** family twice unstable and **B3** branches off. **B2** is also short-lived as it merges with **B** at 0.611 eV. Representative orbits of the **B** family and its bifurcations are plotted in fig. (8.6); their data are given in table (8.2).

A large number of saddle–node families have been located in the classical phase space of HOCl. The first one, **SN1**, is born at (−2.1945 eV, 5.0093 t.u.); its stable

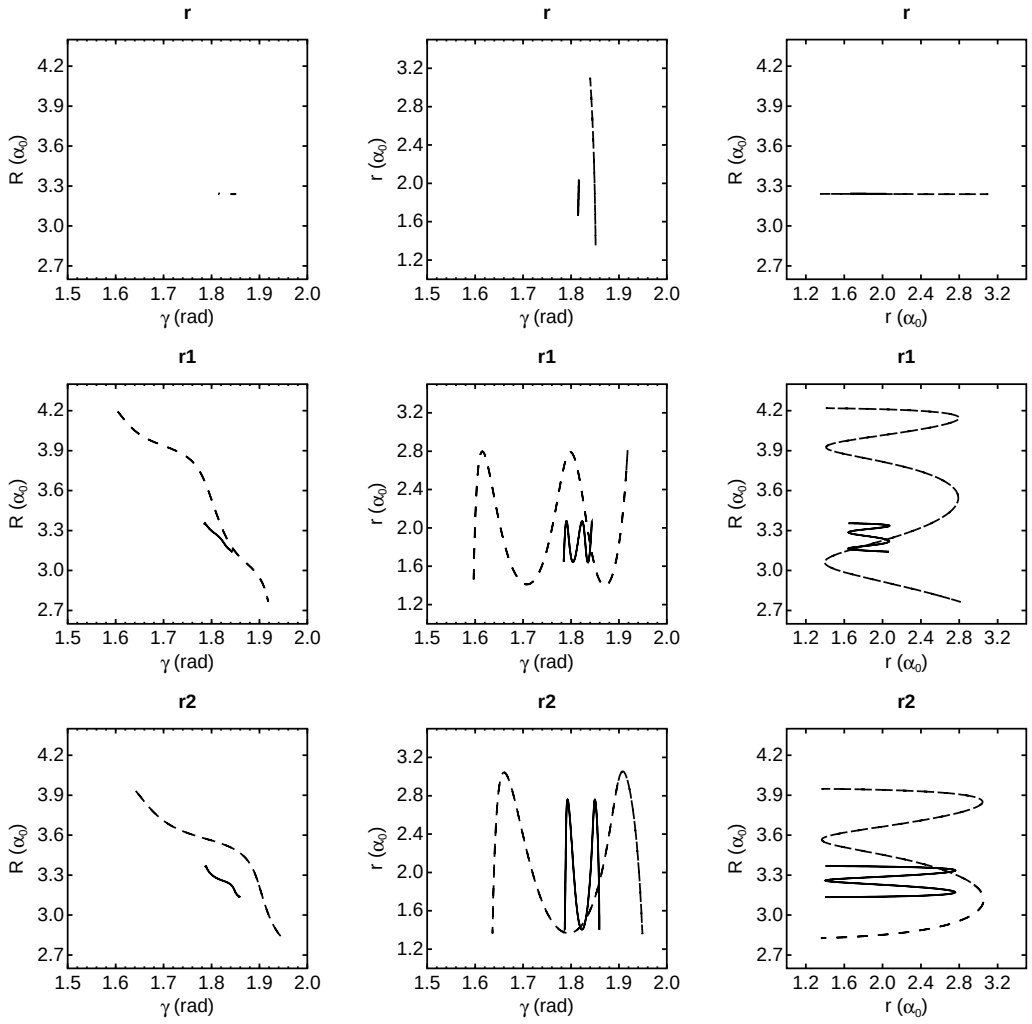

Figure 8.5: Projections of representative orbits of the **r**, **r1**, and **r2** families at low (solid line) and high (dashed line) energies. Their data are given in table (8.2).

branch, **SN1s**, undergoes a period–doubling bifurcation at −0.6291 eV where **SN1A** is born. The unstable branch, **SN1u**, exhibits a brief window of stability among two steady–state bifurcations at −0.3188 eV and −0.102 eV. **SN1u** is quite harmonic in the located segment, following closely the evolution of **B**. On the other hand, **SN1s** deviates from harmonicity above roughly −0.5 eV. **SN1A** alternates in stability through a series of bifurcations before it becomes highly unstable. Representative orbits of the **SN1** and **SN1A** families are plotted in fig. (8.7); their data are given in table (8.3).

At (−1.6213 eV, 9.8894 t.u.), exactly at the point where **R** skews, another saddle–node family is born; it is denoted by **SN2**. The evolution of its stable branch initially mimics the one of the steep segment of **R**; around −0.91 eV **SN2s** skews and becomes more harmonic due to a resonance with r. It loses its initial stability around −0.245 eV. Orbits of the **SN2** family are depicted in fig. (8.8); their data are given in table (8.3).

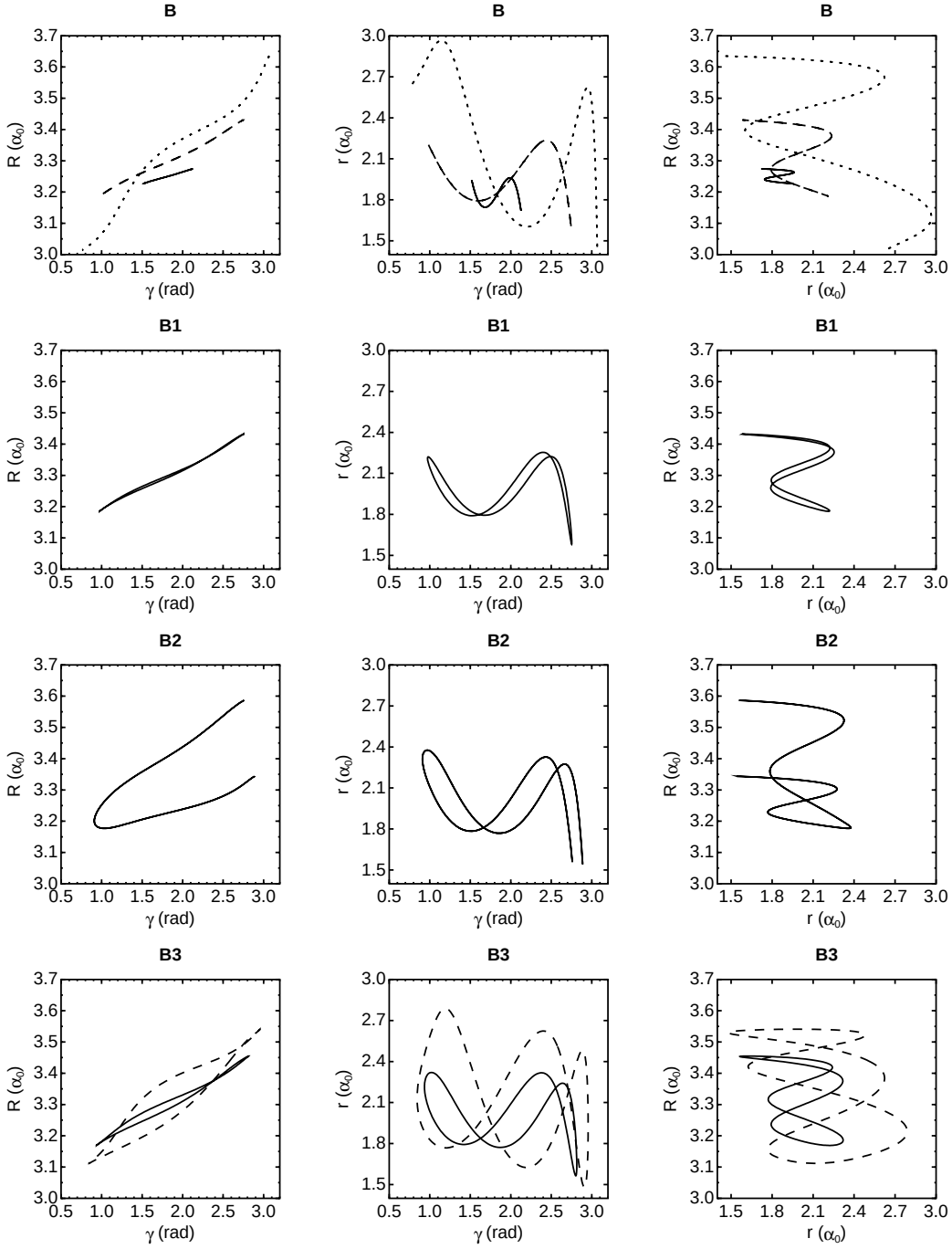

Figure 8.6: Projections of representative orbits of the **B**, **B1**, **B2** and **B3** families at various energies. Solid, dashed, and dotted lines on the same plot represent orbits of increasing energy. Their data are given in table (8.2).

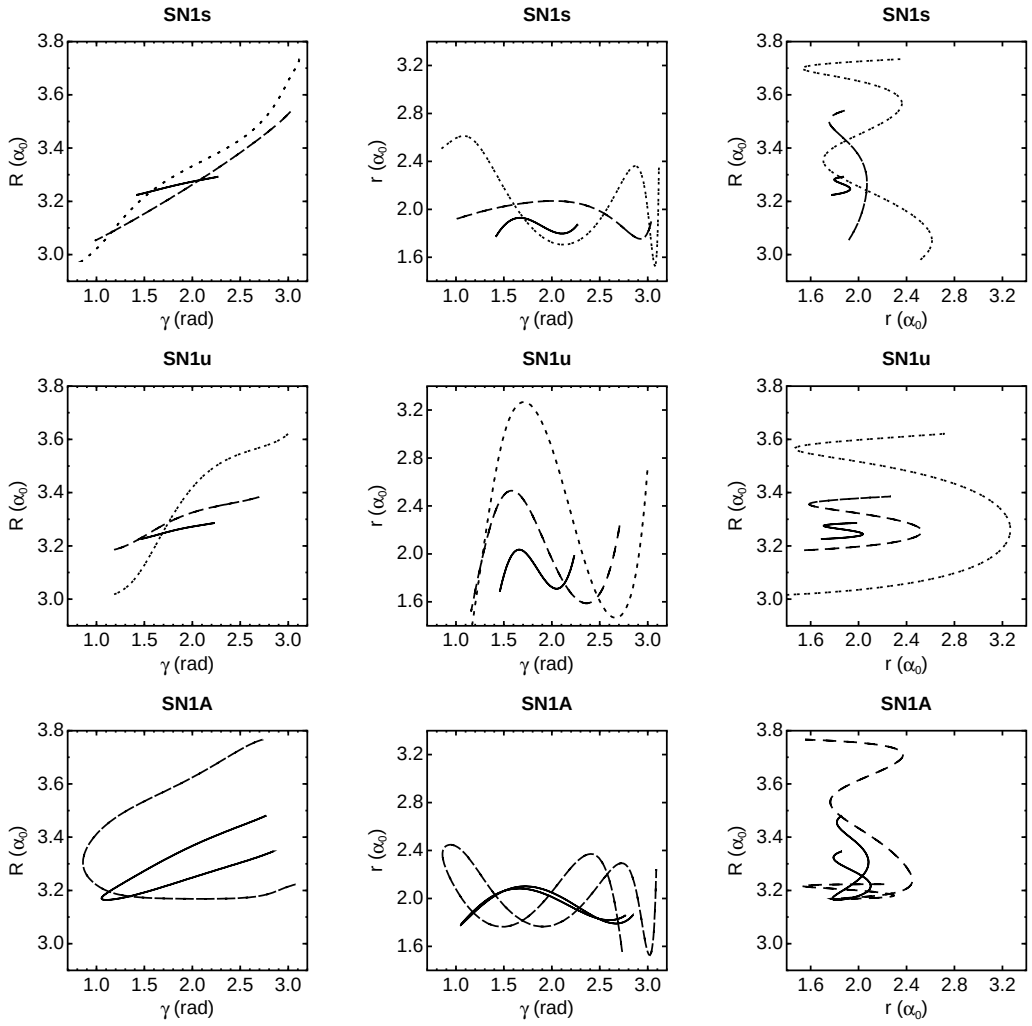

Figure 8.7: Projections of representative orbits of the **SN1** and **SN1A** families at various energies. Solid, dashed, and dotted lines on the same plot represent orbits of increasing energy. Their data are given in table (8.3).

A cascade of saddle–node families which all behave in a similar manner, has also been located. They are denoted by **SN3**, **SN4**,. . . ,**SN11**. The general pattern is the following: the stable branch of each family comprises of orbits with a predominant OH–Cl stretching character and initially evolves quite steeply. At a certain point a resonance (1:8, 1:9,. . .) between the R- and r-oscillators kicks in and the family changes slope dramatically; soonly afterwards the stability is lost. At the vicinity of the point where the skew takes place, the next member of this series of saddle–node families is born and the behavior is replicated. In table (8.1) we present the pairs of energy and period where each bifurcation takes place. Plots of representative orbits of the families born are given in fig. (8.9), fig. (8.10), and fig. (8.11). Their data are presented in table (8.4).

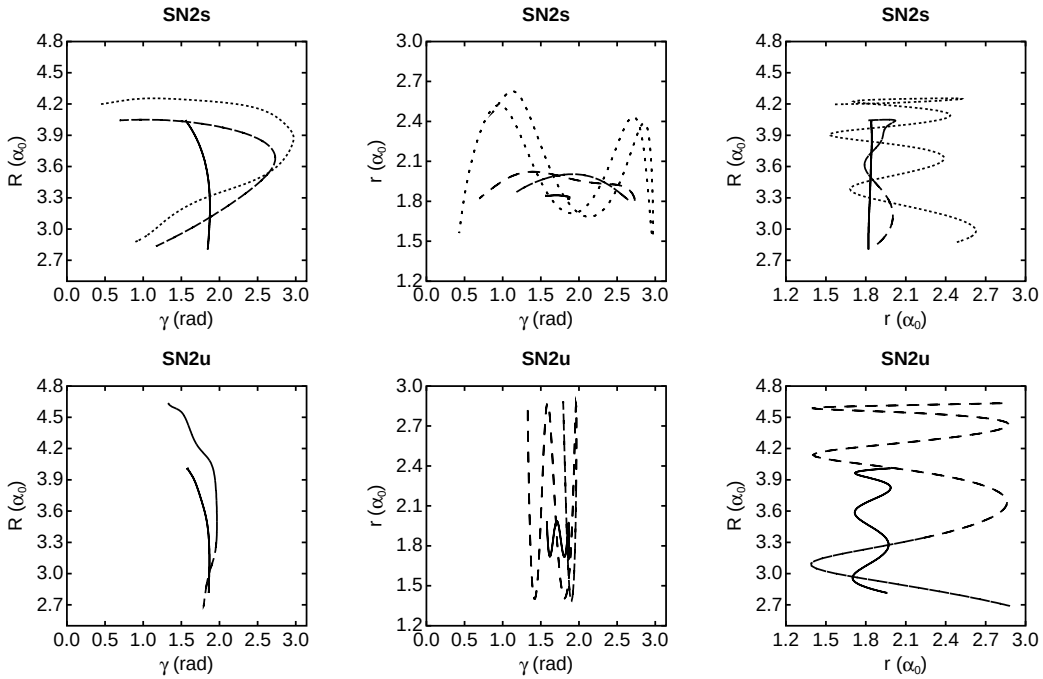

Figure 8.8: Projections of representative orbits of the **SN2** family at various energies. Solid, dashed, and dotted lines on the same plot represent orbits of increasing energy. Their data are given in table (8.3).

FAMILY	**ENERGY** (eV)	**PERIOD** (t.u.)
SN3	−0.842419	12.6434
SN4	−0.766117	13.1940
SN5	−0.578109	14.9941
SN6	−0.452732	16.7664
SN7	−0.367191	18.4922
SN8	−0.305820	20.1970
SN9	−0.259752	21.8900
SN10	−0.223688	23.5750
SN11	−0.194331	25.2542

Table 8.1: Origins of the saddle–node families comprising the cascade in the classical phase space of HOCl.

FAMILY	ENERGY	PERIOD	R	r	γ	P_R	P_r	P_γ
R	−2.3562	8.5800	3.2217560	1.8280933	1.8253287	−1.9448048	−0.0044853	0.1290049
R	−1.4476	10.0050	2.9553919	1.9684176	1.8659058	−3.6642362	−0.0257347	−0.0479985
R	0.0080	11.2250	2.7625823	1.6833615	1.8482363	−1.5640392	−1.3880059	−0.0747409
r	−2.2834	1.6740	3.2425564	1.6622809	1.8148814	0.0011373	−0.0534184	−0.0006120
r	−0.6699	2.0120	3.2459256	1.5564874	1.8197935	−0.0263899	1.4533773	0.0071072
r	0.5680	2.5600	3.2395464	2.1465222	1.8483791	−0.0419776	2.2204553	−0.0546352
r1	−2.1815	8.4300	3.2002122	1.9911098	1.8271105	−0.8233637	−0.5385360	0.0485526
r1	−0.6503	9.4100	3.0449863	1.5118531	1.8641343	−3.2084465	−0.6599871	0.1085215
r1	1.0222	11.0250	2.8089959	2.5994615	1.9155008	−2.4281054	1.0097069	0.0856067
r2	−0.2212	8.6000	3.2400614	1.6937378	1.8356527	−1.0157476	1.9975759	0.1163562
r2	0.6005	9.2250	3.2704377	2.3616818	1.8741333	−3.3062779	1.7097059	0.2653474
r2	1.2725	9.9100	3.2260261	2.9566835	1.8988441	−4.3128908	0.6409771	0.2538041
B	−2.2006	4.9770	3.2489794	1.8106247	1.8027864	0.3346573	0.3625772	1.2233751
B	−0.1724	5.9100	3.3599566	2.1938796	2.3174038	1.1900406	0.3798888	2.9912183
B	1.8152	8.8440	3.6348245	1.4636219	3.0670530	−0.0663968	0.4747120	−0.0312754
B1	−0.1492	5.9220	3.3534359	2.2125130	2.2710387	1.2483525	0.3782376	3.1094685
B2	0.2712	12.6100	3.5428848	2.2873231	2.5278891	1.1620437	−0.4025280	2.2493748
B3	0.1418	6.1220	3.3609700	2.3030825	2.3030152	1.4263177	0.2283183	3.2425694
B3	1.2464	7.0390	3.4386740	2.5089522	2.5778832	1.7448932	−0.6667957	2.7066498

Table 8.2: Initial conditions for representative periodic orbits of the fundamental families in HOCl. Lengths are measured in α_0, the angle in rad, the energy in eV, the period in t.u. (~ 5.387 fs) and the momenta in the appropriate derived units.

FAMILY	**ENERGY**	**PERIOD**	R	r	γ	P_R	P_r	P_γ
SN1s	−2.0365	5.0773	3.2595713	1.8953038	1.8158638	0.4926694	−0.1909156	1.6856846
SN1s	0.0299	6.8993	3.4591446	1.8203911	2.7828728	1.7839014	−0.3541039	1.6688190
SN1s	1.2580	9.4813	3.7339362	2.3474531	3.1168603	−0.0414803	−0.1467540	−0.0128330
SN1u	−1.9731	5.0900	3.2579692	1.9264437	1.8062274	0.4455380	−0.5143090	1.5323982
SN1u	−0.0683	6.0000	3.3528723	1.5964612	2.3109724	0.8538805	−0.3384979	2.4364270
SN1u	1.9373	8.4400	3.6203587	2.6968123	2.9972405	−0.1112613	−0.2735790	−0.1850673
SN1A	−0.6200	11.6850	3.3825772	1.9751765	2.0946861	1.5867416	−0.3377231	3.1248690
SN1A	0.5113	14.6650	3.7665515	1.5536202	2.7338075	0.0131867	−0.0682418	0.0256958
SN2s	−1.5198	10.1294	3.6708049	1.8400329	1.7990251	−3.6448794	−0.0095224	0.3774511
SN2s	0.0801	12.0560	3.4763493	1.8493310	2.5623461	−4.2720939	0.2397414	−1.6863140
SN2s	1.5498	16.5550	2.9376903	2.6029205	1.0461981	−2.4514783	−0.2231733	−2.5880422
SN2u	−1.4595	10.0000	3.6645463	1.7761658	1.7783853	−3.5014234	−0.4132479	0.3631362
SN2u	1.7413	13.7170	3.3452905	2.2422836	1.9620951	−6.2077638	−1.8256415	−0.1733081

Table 8.3: Initial conditions for representative periodic orbits of some of the saddle–node families in HOCl. Lengths are measured in α_0, the angle in rad, the energy in eV, the period in t.u. (~ 5.387 fs) and the momenta in the appropriate derived units.

FAMILY	ENERGY	PERIOD	R	r	γ	P_R	P_r	P_γ
SN3	−0.8036	12.9434	3.3597631	1.8394964	1.7090992	−5.9668363	−0.0077558	0.8381454
SN3	0.0139	14.3434	3.0970949	2.1352403	1.9970885	−5.4318411	0.6643118	1.8326138
SN4	−0.7158	13.6240	3.4158025	1.8436669	1.7188791	−6.1440643	−0.0075992	0.6679427
SN4	0.0242	15.7640	2.8830353	2.1499077	1.9537836	−5.4848853	−0.2950883	0.5144572
SN5	−0.5677	15.1641	3.4641025	1.8513711	1.7403326	−6.3897106	0.0024449	0.5312860
SN5	0.8663	18.9441	2.6697088	1.5277153	2.0102698	−1.0055820	−0.8574325	0.0586649
SN6	−0.4377	17.1064	3.6353701	1.8485141	1.7133641	−6.2622500	0.0239473	0.4452869
SN6	0.4154	19.6864	3.0307802	2.2076370	1.9070941	−6.7296939	0.3961209	0.4963994
SN7	−0.3648	18.6122	3.6575031	1.8477990	1.7169302	−6.3409796	0.0533573	0.4290768
SN7	0.4089	21.3422	3.0393731	2.1765703	1.9011386	−6.8552030	0.4482575	0.4696030
SN8	−0.2853	20.9970	3.6187822	1.8523471	1.7333801	−6.5822560	−0.0371474	0.4268499
SN8	0.9020	24.2970	3.2004952	2.1653411	1.8788485	−7.2021566	1.0438079	0.5819453
SN9	−0.2588	22.0000	4.0860152	1.8337617	1.6267818	−5.2480382	−0.0529049	0.3225367
SN9	0.8526	25.9300	3.3553637	1.7977152	1.8350556	−7.2023024	1.3800762	0.6258051
SN10	−0.2234	23.6350	4.0475104	1.8282514	1.6395471	−5.4488738	−0.0401571	0.3416530
SN10	0.8798	27.7950	3.1928498	2.1439909	1.8776841	−7.2872950	1.0238450	0.5640253
SN11	−0.1912	25.5742	4.0092766	1.8307987	1.6536159	−5.6403744	0.0177661	0.3582131
SN11	0.8770	29.5742	3.1531234	2.1963682	1.8851134	−7.2844343	0.8647773	0.5503912

Table 8.4: Initial conditions for representative periodic orbits of the saddle–node families participating in the cascade in HOCl. Lengths are measured in α_0, the angle in rad, the energy in eV, the period in t.u. (~ 5.387 fs) and the momenta in the appropriate derived units.

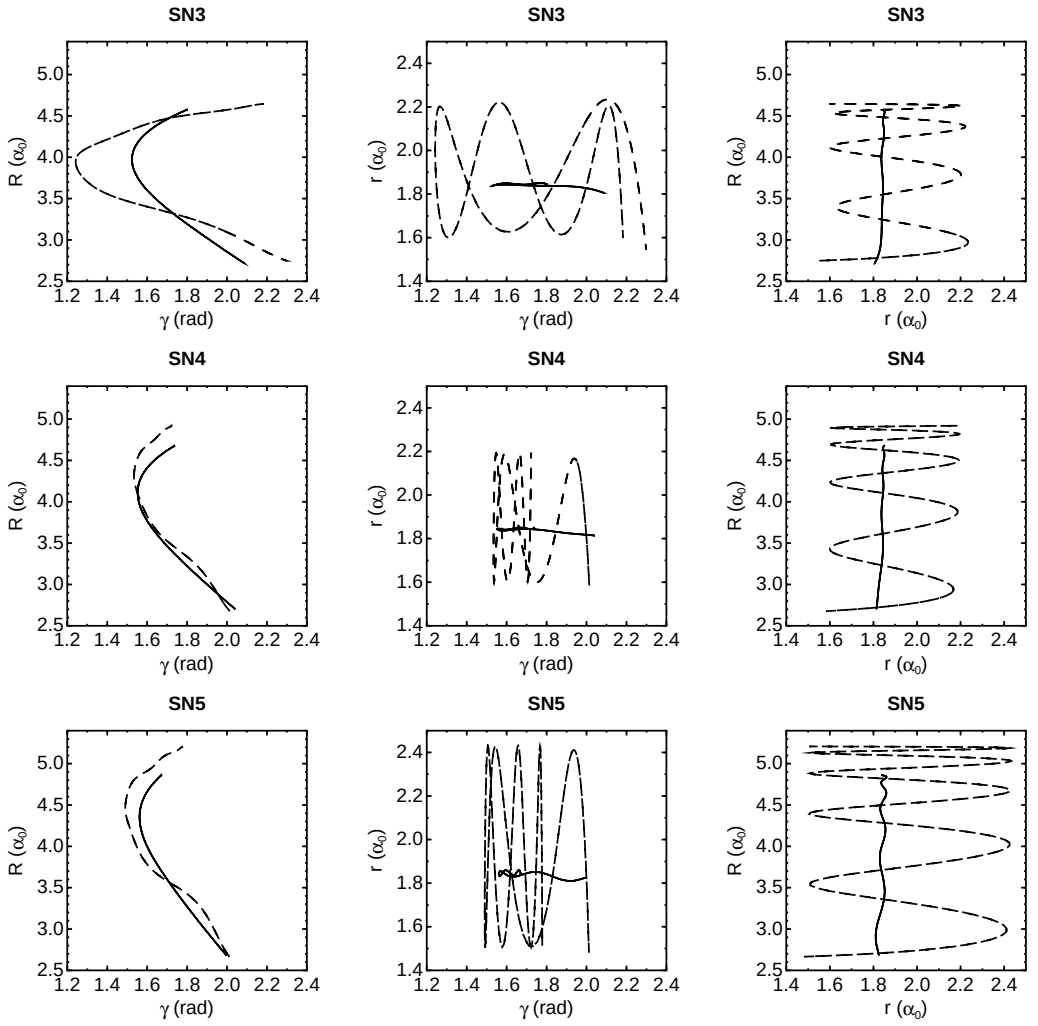

Figure 8.9: Projections of representative orbits of the **SN3**, **SN4**, and **SN5** families at low (solid line) and medium (dashed line) energies. Their data are given in table (8.4).

8.4 Quantum Treatment and Discussion

All dynamics calculations were performed using the filter diagonalization method. This technique calls for the construction of optimally adapted basis functions (so-called "window basis functions") φ_i, which span only a relatively small subspace of the whole Hilbert space. These are generated by applying the Green's function $\widehat{\mathscr{G}}^+(E_i) = (E_i - \widehat{\mathscr{H}} + iW)^{-1}$ as a filtering operator onto an initial wave packet χ, $\varphi_i = \mathrm{Im}\widehat{\mathscr{G}}^+(E_i)\chi$, where iW is a complex absorbing potential ($W = 0$ in calculations for bound states). The energies E_i are taken to be equally spaced in the interval $[E_{\min}, E_{\max}]$. The filtering is efficiently performed using the (modified) Chebychev polynomial expansion of the Green's function [219]. In the second step, the eigenstates in the energy window $[E_{\min}, E_{\max}]$ are calculated by diagonalizing the Hamiltonian in the small set of basis functions $\{\varphi_i\}$. The Hamiltonian employed is the one in eq. (4.1) for zero total angular momentum. The imaginary (absorbing)

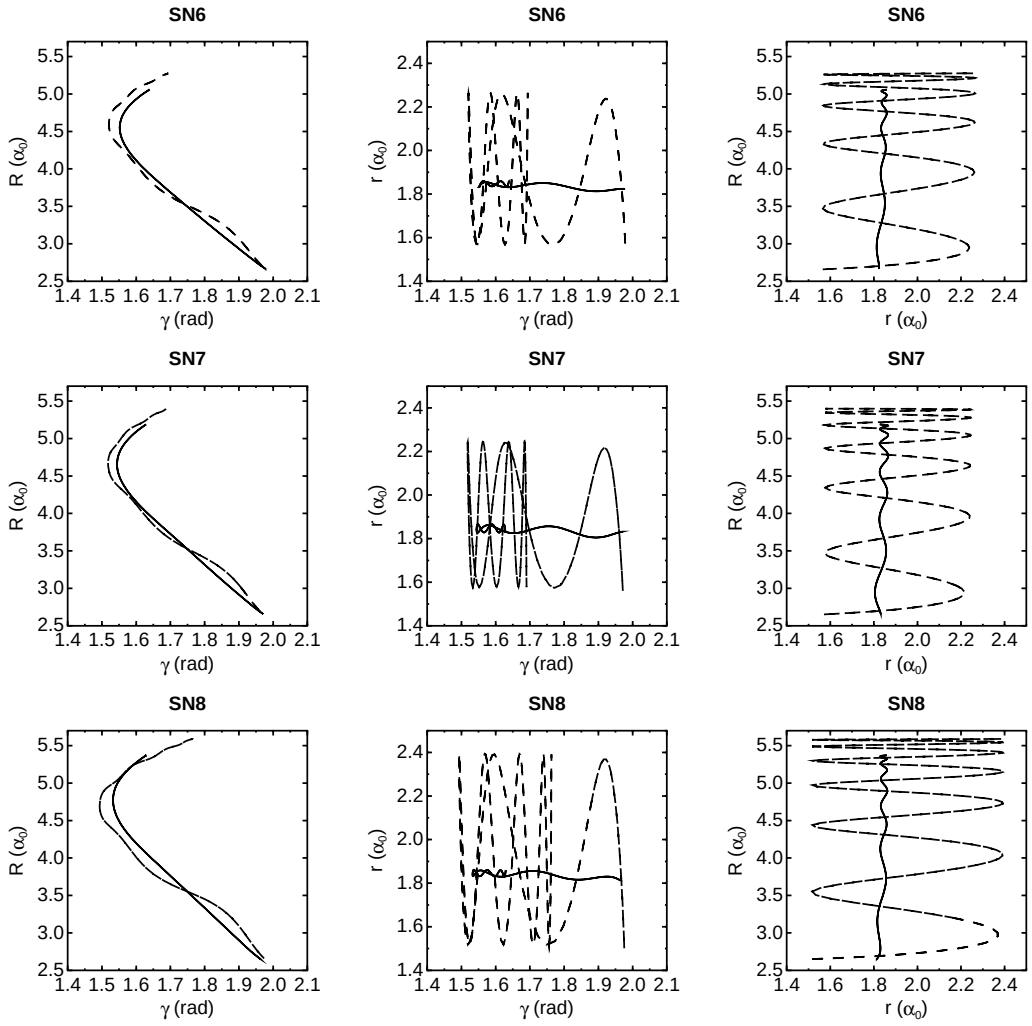

Figure 8.10: Projections of representative orbits of the **SN6**, **SN7**, and **SN8** families at low (solid line) and medium (dashed line) energies. Their data are given in table (8.4).

potential iW in the Green operator for the calculation of the complex resonance energies above the HO+Cl dissociation threshold, enters in the form of a damping factor, $\exp(-\widehat{\gamma}(R))$. Following Mandelshtam and Taylor [219], the coordinate dependent function $\widehat{\gamma}(R)$ was taken to be

$$\widehat{\gamma}(R) = \frac{D_0}{\sqrt{\Delta H}} \left(\frac{R - R_d}{R_{\max} - R_d} \right)^2 \Theta(R - R_d).$$

ΔH (in atomic units) denotes the spectral range of the Hamiltonian and Θ is the Heaviside step function. The three adjustable parameters are the damping strength, D_0, the starting point for the absorbing potential, R_d, and the end point of the grid in the dissociation coordinate, $R_{\max}$. Certain values were chosen for them in order to give tolerable resonance widths.

The quantum calculations estimated the ground energy of the HOCl system to be -2.17028 eV, and provided the fundamental excitation energies of the three nor-

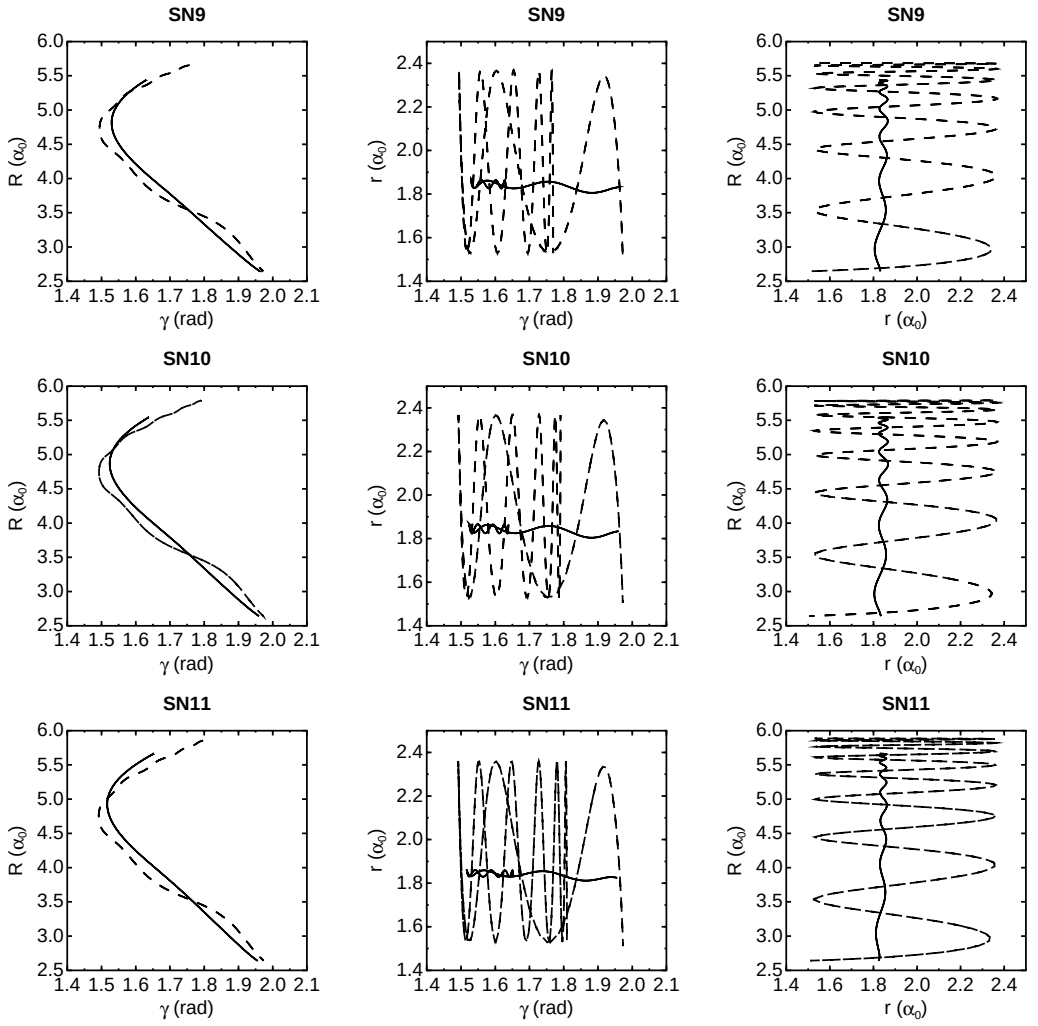

Figure 8.11: Projections of representative orbits of the **SN9**, **SN10**, and **SN11** families at low (solid line) and medium (dashed line) energies. Their data are given in table (8.4).

mal modes at 3602.20 cm^{-1}, 1238.32 cm^{-1}, and 724.61 cm^{-1} for the HO stretching, $\widehat{HOCl}$ bending and OCl stretching modes respectively. The corresponding experimental values [220] are 3609.48 cm^{-1}, 1238.62 cm^{-1}, and 724.36 cm^{-1}, in excellent agreement with the quantum ones. Given the periods of the classical oscillators we can estimate the corresponding frequencies to be 3791.50 cm^{-1}, 1274.77 cm^{-1}, and 741.53 cm^{-1} respectively. The slight discrepancy of a few per cent between classical and quantum values is expected as the frequencies of the classical oscillators were computed at the minimum of the potential while the quantum treatment incorporates the zero-point energy. The ground-state energy is classically estimated by the oscillator frequencies at -2.16472 eV.

The quantum analysis provided 827 bound states and 160 resonances up to 0.30 eV. Bound states are those below the dissociation threshold of 0.22877 eV; this limit incorporates the ground energy of the isolated OH and the zero-point energies of the OCl and bending modes. The narrow energy window in which reso-

nances were sought was sufficient to achieve the goal of elucidating the strong state dependence of the resonance widths. All wave functions were visually inspected and their vast majority was assigned in terms of the normal modes. The labeling was straightforward to about four-fifths of the dissociation limit. Then, however, complications related to saddle–node bifurcations of the corresponding classical phase space arose, making the interpretation quite challenging. In what follows, (v_1, v_2, v_3) designates a state with v_1 quanta in OH stretching, v_2 quanta in bending, and v_3 quanta in Cl–OH stretching modes.

The analysis of the quantum energy spectrum reveals that the same patterns emerge, appropriately shifted, for different values of v_1. It is a clear indication that the coupling between the HO stretch and the other two degrees of freedom is very weak (but, nevertheless, not negligible). This, in addition to the fact that the HO frequency is much larger than the others, results essentially in a separated HO vibration from the Cl motion. Below we will elucidate the distribution and behavior of the states with $v_1 = 0$.

The fact that two quanta of the OCl stretch are roughly equivalent to one quantum of $\widehat{HOCl}$ bending, facilitates the organization of states into clusters, termed as *polyads*. The levels with the same v_1 and *polyad number* $P = 2v_2 + v_3$ have approximately the same energy and comprise the $[[v_1, P]]$ polyad. The polyads are quite broad and overlap even at low energies; this is attributed to the relatively large initial deviation from resonance of the bending and stretching motions of Cl with respect to OH vibration. However, being the dissociation mode, the OCl stretch is much more anharmonic than the bend; this results in a gradual tuning into close resonance of the two modes, destroyed only due to structural changes around -0.5 eV. As the exact resonance sets in, the coupling of R and γ influences the shape of wave functions at least for the highest members in each polyad. As we can see in upper panels of fig. (8.13), the $(0, 0, v_3)$ wave functions become gradually more curved in the $\{R, \gamma\}$ plane. The curvature is present at $v_3 = 12$ but is more pronounced from $v_3 = 16$ and above. This horseshoe-type behavior is typical for systems governed by a 1:2 resonance [221]. Therefore, as a consequence of the mixing, the states which at low energies start out to advance along the dissociation coordinate, R, avoid the dissociation path at high energies (see also fig. (8.12)). We should also note that the $(0, 0, v_3)$ wave functions are localized parallel to the R axis for low energies, thus justifying their initial assignment. On the other hand, for higher energies this is clearly not the case; the identification in terms of the OCl normal mode is meaningless.

Although not shown here, the low members of the pure OCl stretch progression are localized on orbits of the steep segment of the **R** family. Above the point where **R** skews, the localization is controlled by orbits of **SN2**, the family of which the stable branch inherits the behavior of **R** at low energies. In the lower panels of fig. (8.13), the corresponding classical periodic orbits—i.e. the orbits of which the energy above minimum roughly equals the quantum energy above ground state—of the **SN2** family are depicted. It is worth noting that the energy where **SN2** is born corresponds, in the sense above, to an energy less than 0.09 eV below that of the first member ($v_3 = 12$) of the $(0, 0, v_3)$ progression which exhibits a qualitative change in its character. The same factor which affects the $(0, 0, v_3)$ states, namely the R–γ resonance, has analogous effects on the classical orbits. The assignment in

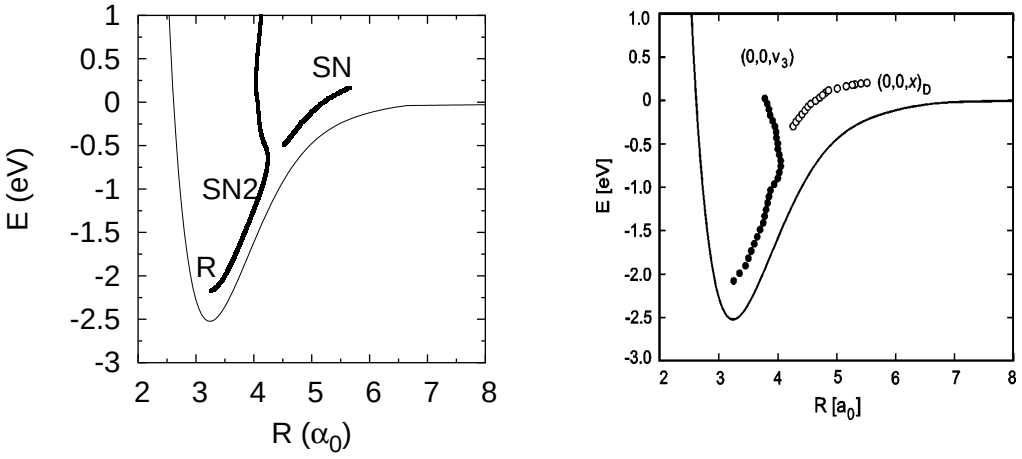

Figure 8.12: The extent of orbits in the **R**, **SN2**, and the cascade saddle–node families (left), and $(0,0,v_3)$ and $(0,0,x)_{\rm D}$ wave functions (right) (see text). The energy of the classical orbits is shifted by the zero-point energy. The symbols are overlaid on the minimum energy path.

terms of the **R** and **SN2** families, which clearly scar the $(0,0,v_3)$ wave functions, is consistent for the whole energy regime; v_3 always reflects the number of nodes along the backbone orbits whether they are parallel to the R axis or not. One might expect that states of the fundamental progression with excitation in R and sufficient energy would explore the HO+Cl channel deeper and deeper. Instead, the analysis reveals that such states bend significantly and remain localized above the potential well irrespective of their energy. This is depicted in the right panel of fig. (8.12), along with the maximum R reached by the corresponding classical orbits (left panel). There is another progression which explores the dissociation path; these D states we will discuss further on, do not come about before -0.5 eV or so.

The wave functions of the $(0,v_2,0)$ progression evolve parallel to the γ axis and retain this shape up to $v_2 = 13$ or so. The weak 1:3 resonance of r and γ is reflected in the undulatory behavior of the wave functions, characteristic for such a resonance [222]. Nevertheless, their backbones are also consistently marked by stable periodic orbits, in this case belonging to the **SN1** family and its bifurcation and in a lesser degree—mainly in low energies—to **B**. This may come as a surprise since **B** does not seem to play the primary role in scarring; nevertheless, the first saddle–node family is born below the quantum ground state and, therefore, exists along with the principal families and can influence from the very beginning the quantum states, as it does. In fig. (8.14), members of the $(0,v_2,0)$ progression are shown along with the corresponding orbits of the **SN1** and **SN1A** families; the role of the latter is explained below.

As mentioned, the pure bending wave functions $(0,v_2,0)$ slightly change their shape at high v_2. While at lower energies the $(0,v_2,0)$ wave functions do not have a node in the R direction, in the high-energy regime they start to develop excitation in R. The energy of the $(0,13,0)$ state is -0.331074 eV which corresponds roughly to -0.685 eV in the classical phase space. The shape the bending wave functions acquire above it resembles a very narrow horse-shoe, see fig. (8.14), a behavior ex-

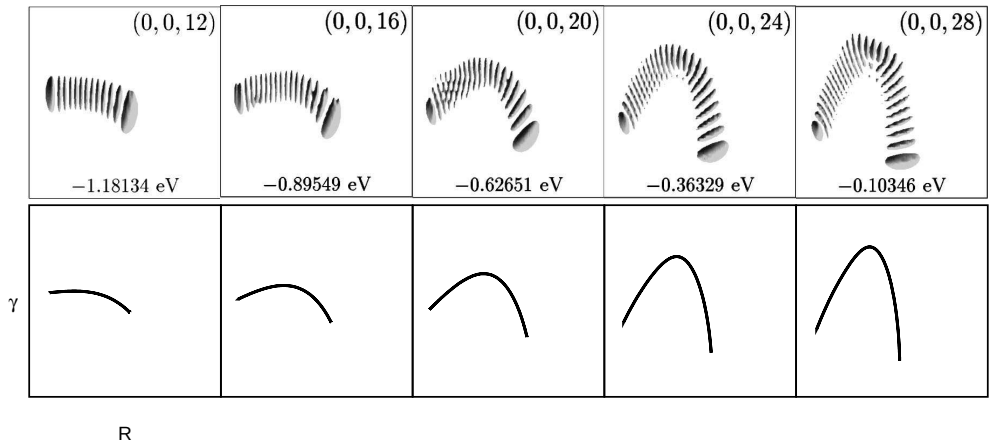

Figure 8.13: Upper row: wave functions of the pure overtone states assigned as $(0, 0, v_3)$. Lower row: corresponding periodic orbits of the **SN2** family. The γ axis ranges from 19° to 179° and the R axis ranges from 2.5 α_0 to 5.42 α_0. In all wave function plots shown is one particular contour $|\Psi(R, r, \gamma)|^2$=const.. The plots are viewed along one coordinate axis, in the direction perpendicular to the plane of the other two coordinates.

pected for a 2:1 resonance. Because of the splitting into two branches, the period of the corresponding orbits, if any, should be about two times longer than the periods of the **SN1** orbits, implying a period-doubling bifurcation. Indeed, these findings are consistent with the birth around −0.63 eV of the **SN1A** family, having twice the period of **SN1**; **SN1A** inherits the stability and, therefore, is the primary localization entity in the relevant phase space region. The **SN1A** family also becomes unstable at higher energies, something which explains the observation that clear-cut $(0, v_2, 0)$ wave functions do not exist in that regime.

The increasing coupling of R and γ with increasing energy and the resulting mixing have another significant implication, this time on the middle members of the high polyads, above $P = 21$. Fig. (8.15) illustrates the changes in the wave function character for selected states belonging to the [[0, 21]] through [[0, 25]] polyads. As we can see, a "backbone" emerges on some wave functions along which the amplitude is maximal. This backbone evolves parallel to the R axis. The change in character can be so dramatic that certain states (e.g. $(0, 8, 8)$, $(0, 9, 7)$) can be given a normal mode assignment based only on their relative position in the polyads and not their shape; they are actually new, independent states. In order to distinguish these new states from the "normal" ones, we can assign them as $(v_1, v_2, x)_{\mathrm{D(P)}}$, where the abbreviation D(P) stands for "dissociation" and the number in parentheses indicates the polyad this state belongs to. With increasing polyad quantum number, combination states of the D type with one, two, and more nodes in the direction perpendicular to the main backbone, i.e. with excitation essentially in the bending mode, come into existence, (e.g. state $(0, 8, 9)$ for polyad $P = 25$). Note that the number of nodes along the backbones of these functions is not identical to the polyad quantum number P. For example, the $(0, 0, x)_{\mathrm{D(24)}}$ wave function for polyad $P = 24$ has only 19 nodes. However, beyond any doubt, it is not a member of polyad $P = 19$. Because of the

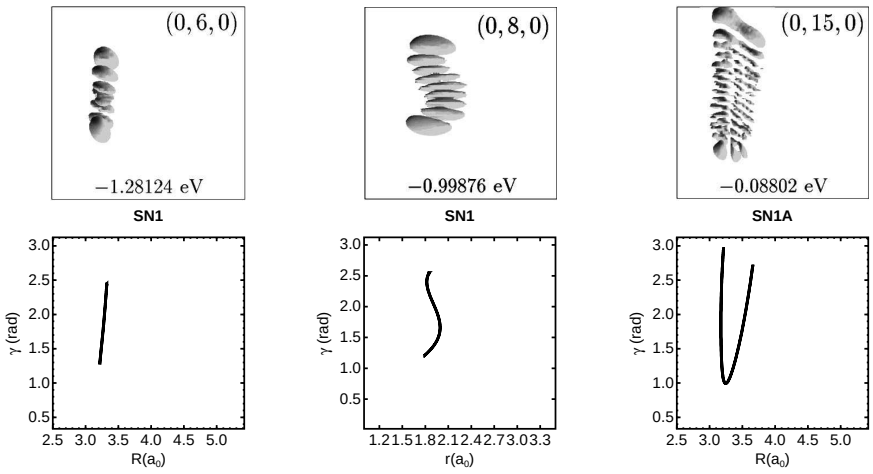

Figure 8.14: Upper row: wave functions of the $(0, v_2, 0)$ states. Lower row: corresponding periodic orbits of the **SN1** and **SN1A** families. The γ axis ranges from 1° to 179°, the R axis ranges from 2.5 α_0 to 5.42 α_0, and the r axis ranges from 1.0 α_0 to 3.5 α_0.

mismatch between the polyad quantum number and the actual number of nodes along the backbone, we replace the quantum number v_3 by x without specifying the value of x. As before, v_1 is the number of HO stretching quanta and v_2 refers to the number of quanta in the direction perpendicular to the backbone, basically the angular coordinate. Notice also another peculiarity: the number of nodes of the D states along their backbones does not necessarily increase by one when going from one polyad to the next higher one. For example, the wave functions for states $(0, 0, x)_{\mathrm{D}(24)}$ and $(0, 0, x)_{\mathrm{D}(25)}$ both have 19 nodes. Moreover, it is possible that the number of nodes along the backbones is identical for states $(0, 0, x)_{\mathrm{D(P)}}$ and $(0, 1, x)_{\mathrm{D(P)}}$. The allocation of such states into particular polyads is based mainly on energy.

The D states clearly follow the dissociation path, i.e. they extend further and further into the HO+Cl fragment channel when the energy increases, see fig. (8.16) and fig. (8.12). They form a new family of states which does not exist at lower energies but is born relatively abruptly at high energies. The birth of the D states leaves the number of states per polyad intact; it is the structure of the individual polyads, i.e. the wave functions and the energy spacings between neighboring states, as elaborated below, that is considerably changed by the D states. The alterations become rapidly more severe with increasing energy.

The first state with a considerable D character is probably $(0, 7, 9)$ at -0.46973 eV. The corresponding classical energy, that is, the one equal to the energy above minimum of the quantum ground state, is -0.8242 eV; it is very close to the point where the cascade of saddle–node families is born in the classical phase space. Orbits in the steep, stable, segments of the **SN3** family and above, penetrate deeper and deeper the dissociation path (cf. fig. (8.12)), show negligible excitation in r and clearly (cf. fig. (8.16)) scar the D states and provide a consistent way to assign these, superior to the problematic in cases, normal mode assignment. On the other hand, the segments after each skew are mainly unstable, exhibit large OH amplitude and,

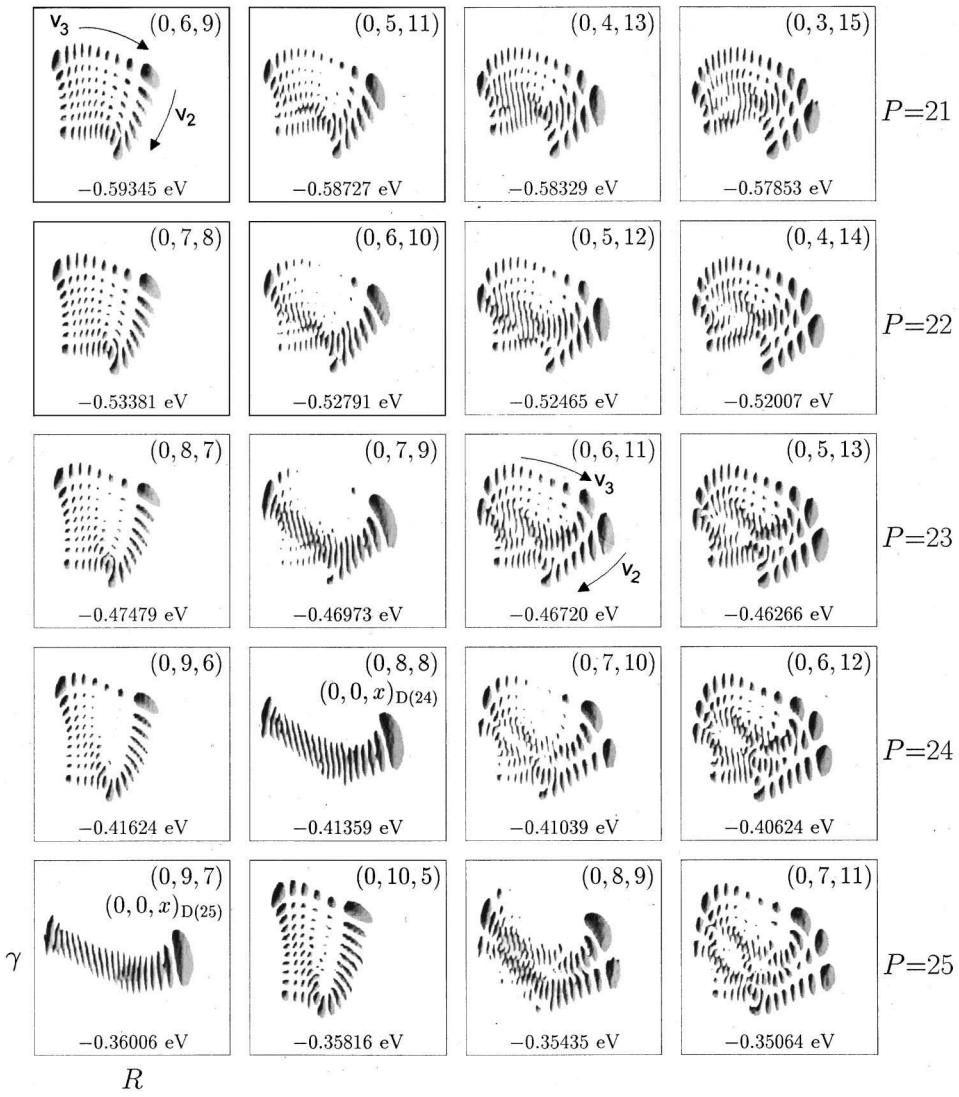

Figure 8.15: Selected wave functions for polyads [[0, 21]]–[[0, 25]] illustrating the gradual distortion of the nodal behavior observed for the lower polyads and the genesis of the $(v1, v2, x)_{\mathrm{D(P)}}$ dissociation states. The R axis ranges from 2.5 α_0 to 5.42 α_0 and the γ axis ranges from 19° to 179°. The assignment reflects the number of nodes on the "axes" indicated in two of the panels.

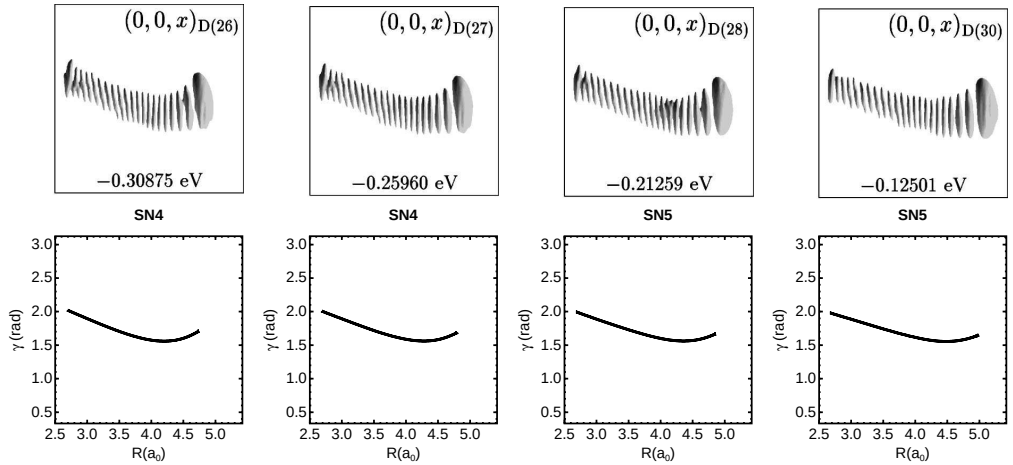

Figure 8.16: Upper panel: wave function plots of selected D states. Lower panel: corresponding periodic orbits of the **SN4** and **SN5** families.

therefore, do not influence the D states.

The quantum analysis we present in [210] focuses on the ramifications of the R and γ resonance on the eigenfunctions and their energies. As we mentioned, OH stretch is effectively independent from the other modes, a fact evident mainly in the quantum picture. A definite series of states, necessarily few due to the large quantum, form the $(v1, 0, 0)$ progression and, although not shown here, are scarred by orbits of the **r** family.

A generic feature of the classical phase space is the major role the resonance of r with R plays: the birth of all but **SN1** saddle–nodes is attributed in a definite way to it. It is intriguing that this resonance affects very slightly the quantum picture. It may be attributed to the large quantum in OH stretch: the energy deposited on the r-oscillator when a resonance condition is met should be quite large in order to have an impact on quantum mechanics, and, in such a case, a large OH amplitude will be accompanied by significant excitations in the other two modes. One can surmise that the harmonic branches of **R** and the saddle–node families, when they are stable, influence states with non-zero quanta in all modes.

The excellent correspondence of classical periodic orbits and quantum wave functions is not limited to their morphology; the transition frequencies, i.e. the energy differences between adjacent levels,[1] are directly comparable to the frequencies of the classical periodic orbits.[2] In the upper panel of fig. (8.17), the transition energies follow closely the frequency curve of **r**. The lower panel depicts the differences of adjacent levels for the $(0, v_2, 0)$, $(0, 0, v_3)$, and $(0, 0, x)_D$ progressions and the frequencies of the corresponding scarring periodic families: **B**, **SN1**, and **SN1A** (multiplied by two) for the first, **R** and **SN2** for the second, and **SN3**–**SN11** for the third progression. Since the D states advance along the dissociation path, they exhibit a considerable anharmonicity as indicated by the energy level spacing between adja-

[1] available from `ftp://ftp.aip.org//epaps/journ_chem_phys/E-JCPSA6-112-009001`
[2] available from the author.

cent $(0,0,x)_{\mathrm{D(P)}}$ states. The curve of transition frequencies for the D states seems to be the continuation of the curve for the $(0,0,v_3)$ states, i.e. the states which in the low energy regime have mainly OCl stretching character.

8.5 Conclusion

The preceding analysis establishes the relation of quantum features to characteristics of the classical phase space in a way that not only qualitative but also quantitative predictions are feasible. The existence and morphology of the fundamental progressions, their energy patterns, the role of the Fermi resonance of R with γ are all accounted for in terms of the shape and frequencies of classical periodic orbits. The fact that the overtones of the Cl–OH stretching mode do not advance along the dissociation path although energetically favored, and the sudden appearance of another progression in high energies which does so are directly reflected to the behavior of the **R** and **SN2** families of periodic orbits and the cascade of saddle–node bifurcations in the classical phase space. Additionally, the organization of quantum states based on their scarring periodic orbits provides a means to assign them consistently from low to high energies avoiding the distortions and unphysical labeling imposed by strict normal mode assignment.

The relation of classical and quantum features developed so far enables us to make valuable predictions on the quantum and actual, experimental behavior of realistic polyatomic molecules based solely on the analysis of periodic orbits. The study of the classical phase space is trivially extensible to systems with more than three, four, or five atoms whereas the detailed quantum analysis is computationally quite challenging if applicable.

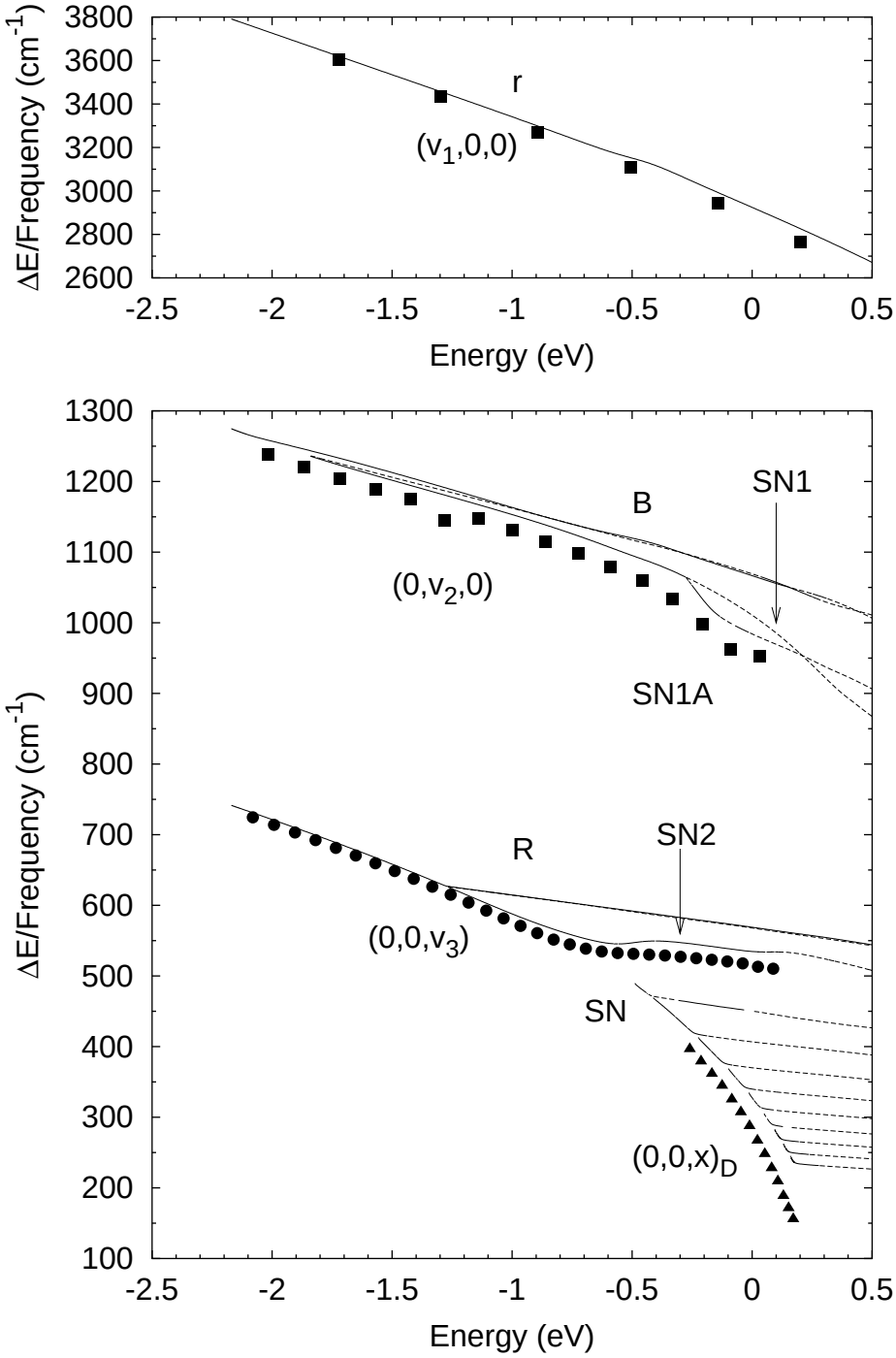

Figure 8.17: Transition energies, i.e. energy differences between neighboring levels, for the progressions $(v_1, 0, 0)$ (upper panel), $(0, v_2, 0)$ (■), $(0, 0, v_3)$ (●), and $(0, 0, x)_D$ (▲) (lower panel) in the HOCl spectrum. Each symbol is plotted at the energy of the upper state and is overlaid on the frequency curves of the periodic orbits of the **r** (upper panel), **B**, **R**, all **SN**, and **SN1A** families. The energy of each orbit above minimum is shifted by the zero-point energy. Solid lines represent stable families; dashed ones indicate instability.

Chapter 9

Conclusions

In the preceding chapters we have presented a detailed analysis of the classical phase space for certain triatomic compounds of environmental or astrophysical interest. We have also showed the wealth of information obtainable through periodic orbit analysis, which, in many cases, is comparable to the results of a full quantum treatment but much less computationally demanding.

It has been established that we can derive, based solely on classical mechanics, many quantum features: the quanta of the normal modes, the ground-state energy, and the morphology of the wave functions, in cases counterintuitive, are among them. Especially the knowledge of the approximate shape of the eigenfunctions is by itself important both for experimentalists and quantum theorists. The former can utilize it to probe successfully specific states by preparing the system in a particular initial state with significant overlap with the desired final one. The latter can employ it as a close initial guess in algorithms that improve a given function to approach the eigenfunction of a Hamiltonian operator, or in other methods, they can use it to construct a limited set of basis functions which reproduces quite closely the wave function sought.

We have also discussed that the organization of periodic orbits into families facilitates the assignment of many quantum states in a manner independent of normal modes and their limitations. Orbits in well-defined segments of one or more closely related families scar specific wave functions. This way, progressions are defined based on similar physical characteristics and morphology of quantum states, whereas the strict normal mode assignment may lead to dubious labelling or even be infeasible. Moreover, the existence and stability analysis of periodic orbit families was shown to provide quite accurate diagnostic indications on the birth and the disappearance of the corresponding scarred progressions, information which is simply unattainable in the quantum mechanics framework.

The correspondence of periodic orbit families and quantum state progressions is not limited to their similarity in morphology. The energy differences among successive members in each progression, that is, the transition energies which are directly or indirectly recorded in experiments, turned out to be in, usually, excellent agreement with the frequencies of the corresponding periodic orbit families. One can get valuable information on the distribution of peaks in a spectrum or the degree of unharmonicity of quantum energy levels by studying a classical Continuation/Bifur-

cation diagram.

In the same context of the relationship of quantum progressions to classical families of periodic orbits, we have also established the important role played by saddle–node bifurcations and the emanating families in clarifying key issues in the experimental and theoretical spectra. We have shown that the birth, morphology and evolution of wave functions which advance further and further on the dissociation or isomerization paths reflect in all their features certain saddle–node families in the classical phase space. These families are born due to resonances between the classical degrees of freedom. In the molecules we studied there is an approximate initial resonance and, additionally, one mode evolves in a more anharmonic fashion compared to the others. This way, two oscillators gradually tune into an almost exact resonance, influencing not only the evolution and the shape of the relevant periodic orbits, but also, giving birth to saddle–node families. Typically, secondary resonances involving the third oscillator are abundant in the classical phase space, with similar ramifications. The coupling between the corresponding degrees of freedom participating in the primary resonance is quite strong and emerges also in the quantum picture; the shape of wave functions changes gradually, reflecting the resonance, and new progressions are born. On the other hand, the secondary resonance is among modes with very weak coupling; dramatic changes due to it occur in the classical phase space where the continuous nature enables the strict resonance conditions to be met, while the discrete quantum mechanics surpasses them.

The work presented in this thesis along with previous studies, enable us to form a systematic method in deriving many useful quantum and, consequently, experimental features of realistic polyatomic systems which may be too large to admit a full, detailed quantum treatment within the present theoretical framework and computational facilities, without resorting, on the other hand, to statistics.

Bibliography

[1] H.-L. Dai and R. W. Field, editors. *Molecular Dynamics and Spectroscopy by Stimulated Emission Pumping*, volume 4 of *Advanced Series in Physical Chemistry*, Singapore, 1995. World Scientific Publ. Co.

[2] Michel Herman, Jacques Lievin, Jean Vander Auwera, and Alain Campargue. Global and Accurate Vibration Hamiltonians from High–Resolution Molecular Spectroscopy. In I. Prigogine and Stuart A. Rice, editors, *Adv. Chem. Phys.*, volume 108, pages 1–431. Wiley–Interscience, New York, 1999.

[3] Mirjana Mladenović. Efficient calculation of rovibrational energy levels of general tetratomic molecules. In Horst Rollnik and Dietrich Wolf, editors, *NIC Symposium 2001, Proceedings*, volume 9 of *NIC Series*, pages 85–94, Jülich, 2002. John von Neumann Institute for Computing.

[4] Mark M. Law, Ian A. Atkinson, and Jeremy M. Hutson, editors. *Rovibrational Bound States in Polyatomic Molecules*, Daresbury, Warrington, WA4 4AD, United Kingdom, 1999. Collaborative Computational Project on Heavy Particle Dynamics.

[5] T. A. Brody, J. Flores, J. B. French, P. A. Mello, A. Pandey, and S. S. M. Wong. Random-matrix physics: spectrum and strength fluctuations. *Rev. Mod. Phys.*, 53(3):385–479, July 1981.

[6] R. D. Levine. In J. Jortner, R.D. Levine, and S.A. Rice, editors, *The Evolution of Dynamic Size Effects*, volume 70, page 53. New York, 1987.

[7] Darin C. Burleigh and Edwin L. Sibert III. A random matrix approach to rotation–vibration mixing in H_2CO and D_2CO. *J. Chem. Phys.*, 98(11):8419, June 1993.

[8] Michael J. Davis. Hierarchical analysis of molecular spectra. *J. Chem. Phys.*, 98(4):2614–2641, February 1993.

Miguel Angel Sepúlveda and Eric J. Heller. Semiclassical analysis of hierarchical spectra. *J. Chem. Phys.*, 101(9):8016–8027, November 1994.

M. J. Davis. Analysis of highly excited vibrational eigenstates. *Int. Rev. Phys. Chem.*, 14(1):15, 1995.

M. J. Davis. Trees from Spectra: Generation, Analysis, and Energy Transfer Information. In H.-L. Dai and R. W. Field, editors, *Molecular Dynamics and*

Spectroscopy by Stimulated Emission Pumping, volume 4 of *Advanced Series in Physical Chemistry*, chapter 23, pages 855–890. World Scientific Publ. Co., Singapore, 1995.

[9] Stephen L. Coy, Matthew P. Jacobson, and Robert W. Field. Identifying patterns in multicomponent signals by extended cross correlation. *J. Chem. Phys.*, 107(20):8357–8369, November 1997.

[10] Matthew P. Jacobson, Stephen L. Coy, and Robert W. Field. Extended cross correlation: A technique for spectroscopic pattern recognition. *J. Chem. Phys.*, 107(20):8349–8356, November 1997.

[11] E. J. Heller. Bound-State Eigenfunctions of Classically Chaotic Hamiltonian Systems: Scars of Periodic Orbits. *Phys. Rev. Lett.*, 53(16):1515–1518, October 1984.

[12] J. M. Gomez Llorente and E. Pollak. Classical Dynamics Methods for High Energy Vibrational Spectroscopy. *Annu. Rev. Phys. Chem.*, 43:91–126, 1992.

[13] Martin C. Gutzwiller. *Chaos in Classical and Quantum Mechanics*, volume 1 of *Interdisciplinary Applied Mathematics*. Springer–Verlag, New York, 1990.

[14] M. Joyeux, S. C. Farantos, and R. Schinke. Highly Excited Motion in Molecules: Saddle–Node Bifurcations and Their Fingerprints in Vibrational Spectra. *J. Phys. Chem. A*, 106(22):5407–5421, 2002.

[15] Stavros C. Farantos. Exploring molecular vibrational motions with periodic orbits. *Int. Rev. Phys. Chem.*, 15(2):345–374, 1996.

[16] Robert L. Waterland, Jian-Min Yuan, Craig C. Martens, Richard E. Gillilan, and William P. Reinhardt. Classical–Quantum Correspondence in the Presence of Global Chaos. *Phys. Rev. Lett.*, 61(24):2733–2736, December 1988.

[17] T. Papenbrock, T. H. Seligman, and H. A. Weidenmüller. Scars of invariant manifolds in interacting few-body systems. *Phys. Rev. Lett.*, 80(14):3057–3060, April 1998.

[18] Donald T. Greenwood. *Classical Dynamics*. Prentice-Hall international series in dynamics. Prentice-Hall, Englewood Cliffs, N.J., 1977. Reprinted by Dover Publications in 1997.

[19] V. I. Arnold. *Ordinary Differential Equations*. Springer–Verlag, Berlin Heidelberg, third edition, April 1992. Translated from the Russian by Roger Cooke.

[20] Morris W. Hirsch and Stephen Smale. *Differential Equations, Dynamical Systems and Linear Algebra*, volume 60 of *Pure and applied mathematics*. Academic Press, New York, second edition, 1997.

[21] Philip Hartman. *Ordinary Differential Equations*. Birkhäuser Press, Boston, second edition, 1982.

[22] V. I. Arnold. *Geometrical Methods in the Theory of Ordinary Differential Equations*. Number 250 in Grundlehren der mathematischen Wissenshaften. Springer–Verlag, New York, second edition, November 1996.

[23] John D. Hadjidemetriou. *Ευστάθεια δυναμικών συστημάτων*. In C. Polimilis, D. Frantzeskakis, and K. Hitzanidis, editors, *Τάξη και χάος στα μη γραμμικά δυναμικά συστήματα*, volume V, pages 35–58, Athens, 1999. G. A. Pnevmatikos.

[24] Lamberto Cesari. *Asymptotic behavior and stability problems in ordinary differential equations*. Springer–Verlag, Berlin Heidelberg, third edition, 1971.

W. Hahn. *Stability of motion*, volume 138 of *Grundlehren Der Mathematischen Wissenschaften Series*. Springer–Verlag, Berlin Heidelberg, January 1968.

[25] Jacob Palis and Wellington deMelo. *Geometric Theory of Dynamical Systems: An Introduction*. Springer–Verlag, New York, 1982.

[26] Ferdinand Verhulst. *Nonlinear Differential Equations and Dynamical Systems*. Universitext. Springer–Verlag, Berlin Heidelberg, second edition, 1996.

[27] Herbert Amann. *Ordinary Differential Equations*. Walter de Gruyter, Berlin, 1990.

[28] A. Weinstein. Normal modes for nonlinear Hamiltonian systems. *Inv. Math.*, 20:47–57, 1973.

[29] J. Moser. Periodic orbits near an equilibrium and a theorem by Alan Weinstein. *Commun. Pure Appl. Math.*, 29:727–747, 1976.

[30] J. A. Montaldi, R. M. Roberts, and I. N. Stewart. Periodic solutions near equilibria of symmetric Hamiltonian systems. *Philos. Trans. R. Soc. London, Ser. A*, 325:237–293, May 1988.

[31] Thomas Bartsch. A generalization of the Weinstein–Moser theorems on periodic orbits of a Hamiltonian system near an equilibrium. *Annales de l'I.H.P. (C) Analyse non Linéaire*, 14(6):691–718, 1997.

[32] John David Crawford. Introduction to bifurcation theory. *Rev. Mod. Phys.*, 63(4):991–1037, October 1991.

[33] J. M. Greene, R. S. MacKay, F. Vivaldi, and M. J. Feigenbaum. Universal behaviour in families of area-preserving maps. *Physica D*, 3:468–486, 1981.

[34] V. A. Yakubovich and V. M. Starzhinskii. *Linear Differential Equations With Periodic Coefficients*. Krieger Publishing Company, Malabar, FL., December 1975.

[35] Henri Poincaré. *New Methods of Celestial Mechanics*, volume 13 of *History of Modern Physics and Astronomy*. Springer–Verlag, New York, September 1992.

[36] A. N. Kolmogorov. On the preservation of quasi–periodic motions under a small variation of Hamilton's function. *Dokl. Akad. Nauk. SSSR*, 98:527, 1954.

[37] J. Moser. On invariant curves of area–preserving mappings on an annulus. *Nachr. Akad. Wiss. Göttingen, Math. Phys. Kl. IIa*, 1:1–20, 1962.

[38] V. I. Arnold. Small denominators and problems of stability of motion in classical and celestial mechanics. *Russ. Math. Surv.*, 18:85–191, 1963.

[39] Henri Poincaré. Sur un théorème Géométrie. *Rendiconti del Circolo Matematico di Palermo*, 33:375–407, 1912.

[40] G. D. Birkhoff. Proof of Poincaré's geometric theorem. *Trans. Amer. Math. Soc.*, 14:14–22, 1913.

[41] R. S. MacKay and J. D. Meiss. *Hamiltonian Dynamical Systems.* Adam Hilger, Bristol, 1987.

[42] S. E. Newhouse. The abundance of wild hyperbolic sets and non-smooth stable sets for diffeomorphisms. *Publ. Math. IHES*, 50:101–151, 1979.

[43] Pankaj Bhatia, Biswajit Maiti, Narayanasami Sathyamurthy, Stamatis Stamatiadis, and Stavros C. Farantos. Exploring molecular motions in collinear HeH_2^+ and its isotopic variants using periodic orbits. *Phys. Chem. Chem. Phys.*, 1(6):1105–1114, March 1999.

[44] V. I. Oseledec. The multiplicative ergodic theorem. The Lyapunov characteristic numbers of a dynamical system. *Trans. Mosc. Math. Soc.*, 19:197–231, 1968.

[45] A. N. Kolmogorov. A metric invariant of transient dynamical systems and automorphisms in Lebesgue spaces. *Dokl. Akad. Nauk. SSSR*, 119:861–864, 1958.

A. N. Kolmogorov. Entropy per Unit Time as a Metric Invariant of Automorphisms. *Dokl. Akad. Nauk. SSSR*, 124:754–755, 1959.

B. V. Chirikov. A Universal Instability of Many Dimensional Oscillator Systems. *Phys. Rep.*, 52:263–379, 1979.

[46] Sofya Kovalevskaya. Sur une propriété du système d' équations différentielles qui définit la rotation d'un corps solide autour d'un point fixe. *Acta Mathematica*, 14:81–93, 1890.

E. Hill. *Ordinary Differential Equations in the Complex Domain*, chapter 3. Wiley–Interscience, New York, 1976.

[47] R. H. G. Helleman and T. Bountis. Periodic Solutions of Arbitrary Period, Variational Methods. In G. Casati and J. Ford, editors, *Stochastic Behaviour in Classical and Quantum Hamiltonian Systems*, volume 93 of *Lecture Notes in Physics*, page 353. Springer–Verlag, Berlin Heidelberg, 1979.

[48] D. W. Noid, M. L. Koszykowski, and R. A. Marcus. Quasiperiodic and stochastic behavior in molecules. *Annu. Rev. Phys. Chem.*, 32:267–309, 1981.

[49] Albert Einstein. Zum Quantensatz von Sommerfeld und Epstein. *Deut. Phys. Ges. Verh.*, 19:82–92, May 1917.

[50] Paul Ehrenfest. Bemerkung betreffs der speziffischen Wärme zweiatomiger Gase. *Deut. Phys. Ges. Verh.*, 15:451–457, 1913.

[51] Karl Sohlberg and Randall B. Shirts. Semiclassical quantization of a nonintegrable system: Pushing the Fourier method into the chaotic regime. *J. Chem. Phys.*, 101(9):7763–7778, November 1994.

[52] G. D. Birkhoff. *Dynamical Systems.* Am. Math. Soc., Providence, RI, revised edition, 1966.

F. G. Gustavson. On constructing formal integrals of a Hamiltonian system near an equilibrium point. *Astron. J.*, 71:670–686, 1966.

R. T. Swimm and J. B. Delos. Semiclassical calculations of vibrational energy levels for nonseparable systems using the Birkhoff–Gustavson normal form. *J. Chem. Phys.*, 71(4):1706–1717, 1979.

T. Uzer, D. W. Noid, and R. A. Marcus. Uniform semiclassical theory of avoided crossings. *J. Chem. Phys.*, 79(9):4412–4425, November 1983.

[53] J. H. Van Vleck. The Coupling of Angular Momentum Vectors in Molecules. *Rev. Mod. Phys.*, 23(3):213–227, July 1951.

[54] Marc Joyeux. Gustavson's procedure and the dynamics of highly excited vibrational states. *J. Chem. Phys.*, 109(6):2111–2122, August 1998.

[55] Anne B. McCoy and Edwin L. Sibert III. Calculation of infrared intensities of highly excited vibrational states of HCN using Van Vleck perturbation theory. *J. Chem. Phys.*, 95(5):3488–3493, September 1991.

[56] R. P. Feynman and A. R. Hibbs. *Quantum Mechanics and Path Integrals.* McG-H, New York, June 1965.

[57] R. Balian and C. Bloch. Distribution of eigenfrequencies for the wave equation in a finite domain I. Three-dimensional problem with smooth boundary surface. *Ann. Phys.*, 60(2):401–447, 1970.

[58] P. Gaspard and D. Alonso. $\hbar$ expansion for the periodic-orbit quantization of hyperbolic systems. *Phys. Rev. A*, 47(5):R3468, May 1993.

[59] Michael V. Berry and Michael Tabor. Calculating the bound spectrum by path summation in action-angle variables. *J. Phys. A*, 10(3):371–379, 1977.

[60] Alfredo M. Ozorio de Almeida. Semiclassical energy spectrum of quasi-integrable systems. In T. Seligman, editor, *Quantum Chaos and Statistical Nuclear Physics*, number 263 in Lecture Notes in Physics, pages 197–211. Springer–Verlag, New York, 1986.

[61] Franz Josef Weiper, Joachim Ankerhold, Hermann Grabert, and Eli Pollak. Semiclassical quantization of nonseparable systems without periodic orbits. *Phys. Rev. Lett.*, 77(13):2662–2665, September 1996.

[62] H. Weyl. Quantenmechanik und Gruppentheorie. *Z. Phys.*, 46:1–46, 1927.

P. Carruthers and F. Zachariasen. Quantum collision theory with phase–space distributions. *Rev. Mod. Phys.*, 55(1):245–285, January 1983.

[63] P. Gaspard, D. Alonso, and I. Burghardt. New ways of understanding semiclassical quantization. In I. Prigogine and Stuart A. Rice, editors, *Adv. Chem. Phys.*, volume 90, pages 105–364. Wiley–Interscience, New York, 1995.

[64] P. Gaspard and I. Burghardt. Emergence of classical periodic orbits and chaos in intramolecular and dissociation dynamics. In Pierre Gaspard, I. Burghardt, I. Prigogine, and Stuart A. Rice, editors, *Adv. Chem. Phys.*, volume 101 of *Chemical Reactions and Their Control on the Femptosecond Time Scale, XXth Solvay Conference on Chemistry*, pages 491–581. Wiley–Interscience, New York, 1997.

[65] Sture Nordholm and Stuart A. Rice. A quantum ergodic theory approach to unimolecular fragmentation. *J. Chem. Phys.*, 62(1):157–168, January 1975.

[66] I. C. Percival. Regular and irregular spectra. *J. Phys. B*, 6:L229–L232, 1973.

[67] L. Kaplan. Scars in quantum chaotic wavefunctions. *Nonlinearity*, 12(2):R1–R40, 1999.

[68] P. Pechukas. Semiclassical approximation of multidimensional bound states. *J. Chem. Phys.*, 57:5577, 1972.

[69] E. P. Wigner. *Ann. Math.*, 53:36, 1951.

[70] L. S. Cederbaum, Th. Zimmermann, H. Köppel, and H.-D. Meyer. Statistical Properties of Energy Levels and Connection to Classical Mechanics. In A. Amann, L. Cederbaum, and W. Gans, editors, *Fractals, Quasicrystals, Chaos, Knots and Algebraic Quantum Mechanics*, volume 235 of *NATO ASI series: Series C, mathematical and physical sciences*, pages 159–173, Dordrecht, The Netherlands, 1988. NATO, Kluwer Academic Publishers. Published in cooperation with NATO Scientific Affairs Division.

[71] Edgar Bright Wilson, Jr., J. C. Decius, and Paul C. Cross. *Molecular Vibrations: The theory of infrared and Raman vibrational spectra.* McGraw-Hill, New York, 1955. Reprinted by Dover Publications in 1980.

[72] B. Podolsky. Quantum-mechanically correct form of Hamiltonian function for conservative systems. *Phys. Rev.*, 32:812–816, 1928.

[73] Daniel C. Harris and Daniel D. Bertolucci. *Symmetry and Spectroscopy: an introduction to vibrational and electronic spectroscopy.* Dover publications, Mineola, N.Y., 1989. Originally publised by Oxford University Press, 1978.

[74] Philip R. Bunker and Per Jensen. *Molecular Symmetry and Spectroscopy.* NRC Monograph Publishing Program. NRC Research Press, Ottawa, Ontario, Canada, second edition, 1998.

[75] G. R. Gunther-Mohr, C. H. Townes, and J. H. Van Vleck. Hyperfine Structure in the Spectrum of $N^{14}H_3$. II. Theoretical Discussion. *Phys. Rev.*, 94(5):1191–1203, June 1954.

[76] G. Herzberg and E. Teller. Schwingungsstruktur der Elektronenübergänge bei mehratomigen Molekülen. *Z. Phys. Chem. B*, 21:410–446, 1933.

[77] Nikos L. Doltsinis. Nonadiabatic Dynamics: Mean-Field and Surface Hopping. In Johannes Grotendorst, Dominik Marx, and Alejandro Muramatsu, editors, *Quantum Simulations of Complex Many-Body systems: From Theory to Algorithms*, volume 10 of *NIC Series*, pages 377–397. John von Neumann Institute for Computing, Jülich, February 2002. Winter School, 25 February - 01 March 2002, Rolduc Conference Centre, Kerkrade, The Netherlands.

[78] R. Renner. Zur Theorie der Wechselwirkung zwischen Elektronen- und Kernbewegung bei dreiatomigen, stabförmigen Molekülen. *Z. Phys.*, 92:172–193, 1934.

[79] H. A. Jahn and E. Teller. Stability of polyatomic molecules in degenerate electronic states. i. orbital degeneracy. *Proc. R. Soc. London, Ser. A*, 161:220–235, 1937.

[80] M. V. Berry. Quantal Phase factors accompanying adiabatic changes. *Proc. R. Soc. London, Ser. A*, 45:392, 1984.

[81] Gerhard Herzberg. *Electronic Spectra and Electronic Structure of Polyatomic Molecules*, volume III of *Molecular Spectra and Molecular Structure*. Krieger Publishing Company, Malabar, FL., second edition, 1989.

[82] M. J. Seaton. Quantum defect theory. *Rep. Prog. Phys.*, 46:167–257, 1983.

[83] K. Bolton, W. L. Hase, and G. H. Peslherbe. Direct Dynamics Simulations of Reactive Systems. In D. L. Thomson, editor, *Modern Methods for Multidimensional Dynamics Computations in Chemistry*, page 143. World Scientific Publ. Co., Singapore, 1998.

[84] M. J. Frisch, G. W. Trucks, H. B. Schlegel, G. E. Scuseria, M. A. Robb, J. R. Cheeseman, V. G. Zakrzewski, J. A. Montgomery, Jr., R. E. Stratmann, J. C. Burant, S. Dapprich, J. M. Millam, A. D. Daniels, K. N. Kudin, M. C. Strain, O. Farkas, J. Tomasi, V. Barone, M. Cossi, R. Cammi, B. Mennucci, C. Pomelli, C. Adamo, S. Clifford, J. Ochterski, G. A. Petersson, P. Y. Ayala, Q. Cui, K. Morokuma, P. Salvador, J. J. Dannenberg, D. K. Malick, A. D. Rabuck, K. Raghavachari, J. B. Foresman, J. Cioslowski, J. V. Ortiz, A. G. Baboul, B. B. Stefanov, G. Liu, A. Liashenko, P. Piskorz, I. Komaromi, R. Gomperts, R. L. Martin, D. J. Fox, T. Keith, M. A. Al-Laham, C. Y. Peng, A. Nanayakkara, M. Challacombe, P. M. W. Gill, B. Johnson, W. Chen, M. W. Wong, J. L. Andres, C. Gonzalez, M. Head-Gordon, E. S. Replogle, and J. A. Pople. *Gaussian 98 (Revision A.11)*. Gaussian, Inc., Pittsburgh, PA, 2001.

[85] R. D. Amos, A. Bernhardsson, A. Berning, P. Celani, D. L. Cooper, M. J. O. Deegan, A. J. Dobbyn, F. Eckert, C. Hampel, G. Hetzer, P. J. Knowles, T. Korona, R. Lindh, A. W. Lloyd, S. J. McNicholas, F. R. Manby, W. Meyer, M. E. Mura, A. Nicklass, P. Palmieri, R. Pitzer, G. Rauhut, M. Schütz, U. Schumann, H. Stoll, A. J. Stone, R. Tarroni, T. Thorsteinsson, and H.-J. Werner. MOLPRO, a package of ab initio programs designed by H.-J. Werner and P. J. Knowles, version 2002.1, 2002.

[86] M. W. Schmidt, K. K. Baldridge, J. A. Boatz, S. T. Elbert, M. S. Gordon, J. H. Jensen, S. Koseki, N. Matsunaga, K. A. Nguyen, S. Su, T. L. Windus, M. Dupuis, and J. A. Montgomery. General Atomic and Molecular Electronic Structure System. *J. Comput. Chem.*, 14:1347–1363, 1993.

[87] Atilla Szabo and Neil S. Ostlund. *Modern Quantum Chemistry: Introduction to Adnvaced Electronic Structure Theory*. Dover publications, New York, 1996.

[88] Tjalling C. Koopmans. Ueber die Zuordaung von Wellenfunktionen und Eigenwerten zu den einzelnen Elektronen eines Atoms. *Physica*, 1(2):104–113, 1934.

[89] C. C. J. Roothaan. New Developments in Molecular Orbital Theory. *Rev. Mod. Phys.*, 23(2):69–89, April 1951.

G. G. Hall. The molecular orbital theory of chemical valency. VIII - A Method of calculating ionization potentials. *Proc. R. Soc. London, Ser. A*, 205:541–552, 1951.

C. C. J. Roothaan. Self-consistent field theory for open shells of electronic systems. *Rev. Mod. Phys.*, 32(2):179–194, April 1960.

[90] Frank W. Bobrowicz and William A. Goddard III. The self-consistent field equations for generalized valence bond and open-shell Hartree-Fock wave functions. In Henry F. Schaefer III, editor, *Methods of Electronic Structure Theory*, volume 3 of *Modern Theoretical Chemistry*, page 79. Plenum Press, New York, 1977.

[91] J. A. Pople and R. K. Nesbet. Self-consistent orbitals for radicals. *J. Chem. Phys.*, 22:571–574, 1954.

[92] J. K. L. MacDonald. Successive Approximations by the Rayleigh–Ritz Variation Method. *Phys. Rev.*, 43(10):830–833, May 1933.

[93] S. R. Langhoff and E. R. Davidson. *Int. J. Quantum Chem.*, 8:61, 1974.

[94] John A. Pople, Martin Head-Gordon, and Krishnan Raghavachari. Quadratic configuration interaction. A general technique for determining electron correlation energies. *J. Chem. Phys.*, 87(10):5968–5975, November 1987.

[95] N. C. Handy, J. A. Pople, M. Head-Gordon, K. Raghavachari, and G. W. Trucks. Size-consistent Brueckner theory limited to double substitutions. *Chem. Phys. Lett.*, 164:185, 1989.

[96] C. Møller and M. S. Plesset. Note on an Approximation Treatment for Many-Electron Systems. *Phys. Rev.*, 46(7):618–622, October 1934.

[97] N. C. Handy. Density functional theory: an alternative to quantum chemistry? In R. Broer, P. J. C. Aerts, and P. S. Bagus, editors, *New Challenges in Computational Quantum Chemistry*, pages 59–70. Rijksuniversiteit Groningen, Groningen, 1994.

[98] P. Hohenberg and W. Kohn. Inhomogeneous electron gas. *Phys. Rev.*, 136(3B):B864–B871, November 1964.

[99] W. Kohn and L. J. Sham. Self-consistent Equations Including Exchange and Correlation Effects. *Phys. Rev. A*, 140(4):1133–1138, 1965.

[100] John Norman Murrell, S. Carter, Stavros C. Farantos, P. Huxley, and A. J. C. Varandas. *Molecular Potential Energy Functions.* Wiley–Interscience, Chichester, 1984.

[101] K. S. Sorbie and J. N. Murrell. *Mol. Phys.*, 29:1387–1407, 1975.

[102] B. T. Sutcliffe. The Eckart Hamiltonian for molecules – a critical exposition. In R. G. Wooley, editor, *Quantum Dynamics of Molecules: the new experimental challenge to theorists*, volume 57 of *NATO ASI series: Series B, Physics*, pages 1–37, New York, 1980. NATO, Plenum Press. Published in cooperation with NATO Scientific Affairs Division.

[103] P. Jensen. Calculation of Molecular Rotation-Vibration Energies Directly from the Potential Energy Function. In S. Wilson and G. H. F. Diercksen, editors, *Methods in Computational Molecular Physics*, volume 293 of *NATO ASI series: Series B, Physics*, page 423, Dordrecht, The Netherlands, July 1992. NATO, Kluwer Academic Publishers. Proceedings of a NATO ASI held in Bad Windsheim, Germany, July 22-August 2, 1991.

[104] Martin L. Sage. Large-Amplitude Vibrations in Triatomic Molecules: A New Approach. *J. Phys. Chem.*, 98(13):3317–3321, 1994.

Mirjana Mladenović. Rovibrational Hamiltonians for general polyatomic molecules in spherical polar parametrization. I. Orthogonal representations. *J. Chem. Phys.*, 112(3):1070–1081, January 2000.

Mirjana Mladenović. Rovibrational Hamiltonians for general polyatomic molecules in spherical polar parametrization. II. Nonorthogonal descriptions of internal molecular geometry. *J. Chem. Phys.*, 112(3):1082–1095, January 2000.

[105] Robert G. Littlejohn and Matthias Reinsch. Gauge fields in the separation of rotations and internal motions in the n-body problem. *Rev. Mod. Phys.*, 69(1):213–276, January 1997.

[106] E. P. Wigner. *Group Theory and Its Application to the Quantum Mechanics of Atomic Spectra*, volume 5 of *Pure and Applied Physics.* Academic Press, New York, 1959. English trans. J.J. Griffin.

[107] Michael R. Wall and Daniel Neuhauser. Extraction, through filter-diagonalization, of general quantum eigenvalues or classical normal mode frequencies from a small number of residues or a short-time segment of a signal. I. Theory and application to a quantum-dynamics model. *J. Chem. Phys.*, 102(20):8011–8022, May 1995.

[108] Shi-Wei Huang and Tucker Carrington, Jr. A comparison of iterative methods for calculating energy levels. In Mark M. Law, Ian A. Atkinson, and Jeremy M. Hutson, editors, *Rovibrational Bound States in Polyatomic Molecules*. Collaborative Computational Project on Heavy Particle Dynamics, Daresbury, Warrington, WA4 4AD, United Kingdom, 1999.

[109] Z. Bačić and J. C. Light. Theoretical Methods For Rovibrational States Of Floppy Molecules. *Annu. Rev. Phys. Chem.*, 40:469–498, 1989.

[110] G. D. Carney, L. L. Sprandel, and C. W. Kern. *Adv. Chem. Phys.*, 37:305, 1978.

[111] F. Culot, F. Laruelle, and J. Liévin. A vibrational CASSCF study of stretch-bend interactions and their influence on infrared intensities in the water molecule. *Theor. Chim. Acta*, 92:211–26, 1995.

[112] R. Schinke. *Photodissociation Dynamics*. Cambridge University Press, Cambridge, 1993.

[113] Abigail J. Dobbyn, Michael Stumpf, Hans-Martin Keller, and Reinhard Schinke. Theoretical study of the unimolecular dissociation HO_2 $\rightarrow$H+O_2. II. Calculation of resonant states, dissociation rates, and O_2 product state distributions. *J. Chem. Phys.*, 104(21):8357–8381, June 1996.

[114] Hans-Martin Keller, Heiner Floethmann, Abigail J. Dobbyn, Reinhard Schinke, Hans-Joachim Werner, Cornelia Bauer, and Pavel Rosmus. The unimolecular dissociation of HCO. II. Comparison of calculated resonance energies and widths with high-resolution spectroscopic data. *J. Chem. Phys.*, 105(12):4983–5004, September 1996.

[115] Hans-Martin Keller, Michael Stumpf, Thomas Schröder, Christoph Stöck, Friedrich Temps, Reinhard Schinke, Hans-Joachim Werner, Cornelia Bauer, and Pavel Rosmus. Unimolecular dissociation dynamics of highly vibrationally exited DCO ($\widetilde{X}^2A'$). II. Calculation of resonance energies and widths and comparison with high-resolution spectroscopic data. *J. Chem. Phys.*, 106(13):5359–5378, April 1997.

[116] Hyo Weon Jang and John C. Light. Artificial boundary inhomogeneity method for quantum scattering solutions in an $\mathcal{L}$ basis. *J. Chem. Phys.*, 102(8):3262–3268, February 1995.

[117] Gregory S. Whittier and John C. Light. Calculation of resonances of HCO by the artificial boundary inhomogeneity method. *J. Chem. Phys.*, 107(6):1816–1823, August 1997.

[118] Bill Poirier and Tucker Carrington, Jr. A preconditioned inexact spectral transform method for calculating resonance energies and widths, as applied to HCO. *J. Chem. Phys.*, 116(4):1215–1227, January 2002.

[119] Michelle Silva, Rienk Jongma, Robert W. Field, and Alec M. Wodtke. THE DYNAMICS OF 'STRETCHED MOLECULES': Experimental Studies of Highly Vibrationally Excited Molecules With Stimulated Emission Pumping. *Annu. Rev. Phys. Chem.*, 52:811–852, 2001.

[120] William H. Press, Saul A. Teukolsky, William T. Vetterling, and Brian P. Flannery. *Numerical Recipes in C: The Art of Scientific Computing*. Cambridge University Press, Cambridge, second edition, 1992.

[121] E. Anderson, Z. Bai, C. Bischof, S. Blackford, J. Demmel, J. Dongarra, J. Du Croz, A. Greenbaum, S. Hammarling, A. McKenney, and D. Sorensen. *LAPACK Users' Guide*. Society for Industrial and Applied Mathematics, Philadelphia, PA, third edition, 1999.

[122] S. Cohen and A. Hindmarsh. CVODE, a Stiff/Nonstiff ODE Solver in C. *Computers in Physics*, 10(2):138–143, March 1996.

[123] Matteo Frigo and Steven G. Johnson. The Fastest Fourier Transform in the West. Technical Report MIT-LCS-TR-728, Massachusetts Institute of Technology, September 1997. URL address: `www.fftw.org`.

[124] S. C. Farantos. POMULT: a program for computing periodic orbits in Hamiltonian systems based on multiple shooting algorithms. *Comput. Phys. Commun.*, 108(2&3):240–258, February 1998. URL address: `www.cpc.cs.qub.ac.uk/cpc/adhg`.

[125] David Levine. *PGAPack Parallel Genetic Algorithm Library V1.0*. Mathematics and Computer Science, Argonne National Laboratory, 9700 South Cass Avenue, Argonne, IL 60439, January 1996. URL address: `www.mcs.anl.gov/pgapack.html`.

[126] Bruce R. Johnson and William P. Reinhardt. Adiabatic separations of stretching and bending vibrations: Application to H_2O. *J. Chem. Phys.*, 85(8):4538–4556, October 1986.

[127] G. J. Atchity and K. Ruedenberg. Perimetric scale–shape coordinates for triatomic molecules. *Theor. Chem. Acc.*, 96:205–211, 1997.

[128] J. R. Cash and A. H. Karp. A variable order Runge-Kutta method for initial value problems with rapidly varying right-hand sides. *ACM Transactions on Mathematical Software*, 16(3):201–222, September 1990.

[129] Laurent O. Jay. Structure Preservation for Constrained Dynamics with Super Partitioned Additive Runge–Kutta Methods. *SIAM J. Sci. Comput.*, 20(2):416–446, March 1999.

[130] B. Cano and J. M. Sanz-Serna. Error Growth in the Numerical Integration of Periodic Orbits, with Application to Hamiltonian and Reversible Systems. *SIAM J. Numer. Anal.*, 34(4):1391–1417, August 1997.

[131] Liqing Zhang. Two-sided approximation to periodic solutions of ordinary differential equations. *Numer. Math.*, 66(3):399–409, 1993.

[132] M. N. Vrahatis and T. C. Bountis. An efficient method for computing periodic orbits of conservative dynamical systems. In John Seimenis and N. Copernicus, editors, *Hamiltonian Mechanics: Integrability and Chaotic Behaviour*, volume 331 of *NATO ASI series: Series B, Physics*, pages 261–274, New York, January 1995. NATO, Plenum Press. Published in cooperation with NATO Scientific Affairs Division.

M. N. Vrahatis, A. E. Perdiou, V. S. Kalantonis, E. A. Perdios, K. Papadakis, R. Prosmiti, and S. C. Farantos. Application of the characteristic bisection method for locating and computing periodic orbits in molecular systems. *Comput. Phys. Commun.*, 138(1):53–68, 2001.

[133] K. Lust, D. Roose, A. Spence, and A. R. Champneys. An Adaptive Newton–Picard Algorithm with Subspace Iteration for Computing Periodic Solutions. *SIAM J. Sci. Comput.*, 19(4):1188–1209, July 1998.

[134] J. H. Holland. *Adaptation in Natural and Artificial Systems: An Introductory Analysis with Applications to Biology, Control, and Artificial Intelligence*. The MIT Press, Cambridge Mass., USA, reprint edition, 1992. Originally published by University of Michigan Press, Ann Arbor in 1975.

[135] David E. Goldberg. *Genetic Algorithms in Search, Optimization, and Machine Learning*. Addison–Wesley, Reading, MA, 1989.

[136] Xavier Hüe. Genetic Algorithms for Optimization. Background and Applications. Technology Watch Report, Edinburgh Parallel Computing Centre, The University of Edinburgh, February 1997. Available from `www.epcc.ed.ac.uk/epcc-tec/documents`.

[137] S. Stamatiadis, R. Prosmiti, and S. C. Farantos. AUTO_DERIV: Tool for automatic differentiation of a FORTRAN code. *Comput. Phys. Commun.*, 127(2&3):343–355, May 2000. URL address: `www.cpc.cs.qub.ac.uk/cpc/summaries/adls`.

[138] MATHEMATICA v. 4.2. Wolfram Research, Inc. URL address: `www.wolfram.com`.

[139] Maple v. 8. Waterloo Maple, Inc. URL address: `www.maplesoft.com`.

[140] Matlab v. 6.5. The Mathworks, Inc. URL address: `www.matlab.com`.

[141] INTERNATIONAL ORGANIZATION FOR STANDARDIZATION. *ISO/IEC 1539-1:1991*, 1991. Information technology — Programming languages — Fortran.

[142] Michael Metcalf and John Reid. *FORTRAN 90/95 explained*. Oxford University Press, Great Clarendon Street, Oxford OX2 6DP, UK, second edition, 1996.

[143] C. Beck, R. Schinke, and J. Koput. Vibrational spectroscopy of phosphaethyne (HCP). I. Potential energy surface, variational calculations, and comparison with experimental data. *J. Chem. Phys.*, 112(19):8446–8457, May 2000.

[144] Wim Klopper, Martin Quack, and Martin A. Suhm. HF dimer: Empirically refined analytical potential energy and dipole hypersurfaces from ab initio calculations. *J. Chem. Phys.*, 108(24):10096–10115, June 1998.

[145] INTERNATIONAL ORGANIZATION FOR STANDARDIZATION. *ISO/IEC 1539-1:1997*, 1997. Information technology — Programming languages — Fortran.

[146] B. E. Turner, T. Tsuji, J. Bally, and J. Cernicharo. Phosphorus in the dense interstellar medium. *Astrophys. J.*, 365:569–585, December 1990.

[147] J. K. Tyler. Microwave Spectrum of Methinophosphide, HCP. *J. Chem. Phys.*, 40:1170–1171, 1964.

[148] J. W. C. Johns, J. M. R. Stone, and G. Winnewisser. *J. Mol. Spectrosc.*, 38:437–440, 1971.

[149] A. Cabaña, Y. Doucet, J.-M. Garneau, C. Pépin, and P. Puget. The vibration-rotation spectrum of methinophosphide: the overtone bands $2v_1$ and $2v_3$, the summation bands $v_1 + v_2$ and $v_2 + v_3$, and the difference band $v_1 - v_2$. *J. Mol. Spectrosc.*, 96:342–350, 1982.

[150] Kevin K. Lehmann, Stephen C. Ross, and Lawrence L. Lohr. Experimental and ab initio determination of the bending potential of HCP. *J. Chem. Phys.*, 82(10):4460–4469, May 1985.

[151] Yit-Tsong Chen, David M. Watt, Robert W. Field, and Kevin K. Lehmann. Observation of highly vibrationally excited $\widetilde{X}\ ^1\Sigma^+$ HCP by stimulated emission pumping spectroscopy. *J. Chem. Phys.*, 93(3):2149–2151, August 1990.

[152] Martin A. Mason and Kevin K. Lehmann. Reinvestigation of the HCP electronic spectrum: Experimental determination of D_0 for the $\widetilde{X}$ state and observation of hyperfine quantum beats in the $\widetilde{B}$ state. *J. Chem. Phys.*, 98(7):5184–5190, April 1993.

[153] P. Dréan, J. Demaison, L. Poteau, and J.-M. Denis. Rotational Spectrum and Structure of HCP. *J. Mol. Spectrosc.*, 176(1):139–145, March 1996.

[154] Haruki Ishikawa, Yit-Tsong Chen, Yasuhiro Ohshima, Jianghong Wang, and Robert W. Field. Stimulated emission pumping spectroscopy of HCP near the isomerization barrier: $E_{VIB} \leq 25315$ cm^{-1}. *J. Chem. Phys.*, 105(17):7383–7401, November 1996.

[155] Michael Jung, Brenda P. Winnewisser, and Manfred Winnewisser. High resolution FT-IR spectra of the ν_1, ν_2, and ν_3 bands of $H^{12}CP$ and of the ν_1 and ν_2 bands of $H^{13}CP$. *J. Mol. Struct.*, 413–414:31–48, September 1997.

[156] Haruki Ishikawa, Chioko Nagao, Naohiko Mikami, and Robert W. Field. Observation of the "isomerization states" of HCP by stimulated emission pumping spectroscopy: Comparison between theory and experiment. *J. Chem. Phys.*, 106(7):2980–2983, February 1997.

[157] Haruki Ishikawa, Chioko Nagao, Naohiko Mikami, and Robert W. Field. Spectroscopic investigation of the generation of "isomerization" states: Eigenvector analysis of the bend-CP stretch polyad. *J. Chem. Phys.*, 109(2):492–503, July 1998.

[158] Haruki Ishikawa, Chioko Nagao, and Naohiko Mikami. Observation of the Highly Excited Vibrational Levels of HCP: Application of IR-UV-SEP Triple Resonance Spectroscopy. *Chem. Lett.*, 9:941–942, September 1999.

[159] Luca Bizzocchi, Sven Thorwirth, Holger S. P. Müller, Frank Lewen, and Gisbert Winnewisser. Submillimeter-Wave Spectroscopy of Phosphaalkynes: HCCCP, NCCP, HCP, and DCP. *J. Mol. Spectrosc.*, 205(1):110–116, January 2001.

[160] S. P. Karna, P. J. Bruna, and F. Grein. *Can. J. Phys.*, 68:499–507, 1990.

[161] A. B. Sannigrahi and F. Grein. Configuration interaction study of the potential energy surface of the three lowest singlet A' and A'' states of HCP. *Chem. Phys. Lett.*, 214(6):609–614, September 1993.

[162] Yit-Tsong Chen and Delano P. Chong. Comparison of theoretical vibrational and rotational energies of the HCP molecule with experimental values. *J. Chem. Phys.*, 99(11):8870–8876, 1993.

[163] Cristina Puzzarini, Riccardo Tarroni, Paolo Palmieri, Jean Demaison, and Maria Luisa Senent. Rovibrational energy levels and equilibrium geometry of HCP. *J. Chem. Phys.*, 105(8):3132–3141, August 1996.

[164] Christian Beck, Hans-Martin Keller, S. Yu. Grebenshchikov, Reinhard Schinke, Stavros C. Farantos, Koichi Yamashita, and Keiji Morokuma. Highly excited vibrational states of HCP and their analysis in terms of periodic orbits: The genesis of saddle–node states and their spectroscopic signature. *J. Chem. Phys.*, 107(23):9818–9834, December 1997.

[165] Jacek Koput and Stuart Carter. The potential energy surface and vibrational-rotational energy levels of HCP. *Spectrochim. Acta A: Molecular and Biomolecular Spectroscopy*, 53(8):1091–1100, July 1997.

[166] Shinkoh Nanbu, Stephen K. Gray, Tomoko Kinoshita, and Mutsumi Aoyagi. Theoretical study of the potential energy surfaces and bound states of HCP. *J. Chem. Phys.*, 112(13):5866–5876, April 2000.

[167] Matthew P. Jacobson and Mark S. Child. Spectroscopic signatures of bond-breaking internal rotation. I. Saddle point induced polyad breakdown. *J. Chem. Phys.*, 114(1):250–261, January 2001.

Matthew P. Jacobson and Mark S. Child. Spectroscopic signatures of bond-breaking internal rotation. II. Rotation-vibration level structure and quantum monodromy in HCP. *J. Chem. Phys.*, 114(1):262–275, January 2001.

[168] H. Ishikawa, R. W. Field, S. C. Farantos, M. Joyeux, J. Koput, C. Beck, and R. Schinke. HCP↔CPH Isomerization: Caught in the Act. *Annu. Rev. Phys. Chem.*, 50:443–484, 1999.

[169] J. Bredenbeck, C. Beck, R. Schinke, J. Koput, S. Stamatiadis, S. C. Farantos, and M. Joyeux. The vibrational spectrum of deuterated phosphaethyne: A quantum mechanical, classical, and semiclassical analysis. *J. Chem. Phys.*, 112(20):8855–8865, May 2000.

[170] T. E. Gier. HCP, A Unique Phosphorus Compound. *J. Am. Chem. Soc.*, 83:1769–1770, 1961.

[171] Stavros C. Farantos, Hans-Martin Keller, Reinhard Schinke, Koichi Yamashita, and Keiji Morokuma. Normal mode and isomerization bending states in HCP: Periodic orbit assignment and spectroscopic signature. *J. Chem. Phys.*, 104(24):10055–10058, June 1996.

[172] J. Lavigne, C. Pépin, and A. Cabaña. The Vibration–Rotation Spectrum of DCP. *J. Mol. Spectrosc.*, 99:203–208, 1983.

[173] J. Lavigne, C. Pépin, and A. Cabaña. The Vibration–Rotation Spectrum of $D^{12}CP$ in the Region of the v_2 Band: The Spectroscopic Constants for the States 00^00, 01^10, 02^00 and the Bond Lengths of the Molecule. *J. Mol. Spectrosc.*, 104:49–58, 1984.

[174] C. Pépin and A. Cabaña. The $v_1 + v_2$ Vibration–Rotation Band of $D^{12}CP$ and Evidence for Fermi Resonance in the 100, 002 Diad. *J. Mol. Spectrosc.*, 119:101–106, 1986.

[175] Michael Jung. *Hochauflösende Fourier-Transform-Infrarot-Spektroskopie der dreiatomigen Moleküle HCP, DCP und HBS.* PhD thesis, Physikalisch-Chemisches Institut, Justus-Liebig-Universität Giessen, 2000.

[176] John Svitak, Zhiming Li, John Rose, and Michael E. Kellman. Spectral patterns and dynamical bifurcation analysis of highly excited vibrational spectra. *J. Chem. Phys.*, 102(11):4340–4354, March 1995.

John Svitak, Zhiming Li, John Rose, and Michael E. Kellman. Erratum: Spectral patterns and dynamical bifurcation analysis of highly excited vibrational spectra [J. Chem. Phys. 102, 4340 (1995)]. *J. Chem. Phys.*, 103(9):3870, September 1995.

[177] Marc Joyeux, Dominique Sugny, Vivian Tyng, Michael E. Kellman, Haruki Ishikawa, Robert W. Field, Christian Beck, and Reinhard Schinke. Semiclassical study of the isomerization states of HCP. *J. Chem. Phys.*, 112(9):4162–4172, March 2000.

[178] T. Baer and W. L. Hase. *Unimolecular Reaction Dynamics: Theory and Experiments*, volume 31 of *International Series of Monographs on Chemistry*. Oxford University Press, Oxford, 1996.

[179] A. Fontijin. *Pure Appl. Chem.*, 39:287, 1974.

D. J. Hucknall. *Chemistry of Hydrocarbon Combustion*. Chapman and Hall, London, 1985.

[180] B. J. Finlayson-Pitts and J. N. Pitts, Jr. *Atmospheric Chemistry: Fundamentals and Experimental Techniques*. John Wiley & Sons, New York, 1986.

R. Atkinson, D. L. Baulch, R. A. Cox, R. F. Hampson, J. A. Kerr, M. J. Rossi, and J. Troe. Evaluated kinetic and photochemical data for atmospheric chemistry: Supplement VII, Organic species – IUPAC subcommittee on gas kinetic data evaluation for atmospheric chemistry. *J. Phys. Chem. Ref. Data*, 28(2):191–393, 1999.

B. Hanoune, S. Dusanter, L. ElMaimouni, P. Devolder, and B. Lemoine. Rate constant determinations by laser photolysis/diode laser infrared absorption: examples of $HCO+O_2 \rightarrow HO_2+CO$ and $CH_2OH+O_2 \rightarrow HCH(O)+HO_2$ reactions at 294 K. *Chem. Phys. Lett.*, 343(5–6):527–534, August 2001.

[181] S. Chu and A. Balgarno. *Proc. R. Soc. London, Ser. A*, 342:194, 1975.

[182] George William Adamson. *The spectroscopy of the formyl radical*. PhD thesis, Dept. of Chemistry, MIT, Cambridge, MA, 1994.

[183] D. W. Neyer and P. L. Houston. The HCO Potential Energy Surface; Probes using Molecular Scattering and Photodissociation. In K. Liu and A. Wagner, editors, *The Chemical Dynamics and Kinetics of Small Radicals*, volume 6 of *Advanced Series in Physical Chemistry*, pages 469–503. World Scientific Publ. Co., Singapore, 1995.

[184] J. D. Robinson, R. J. Foltynowicz, K. Prentice, P. Bell, and E. R. Grant. Laser-assisted $(1+1')$-photon ionization-detected absorption spectrum of the $3p\,\pi\,{}^2\Pi$ state of HCO and DCO. *J. Chem. Phys.*, 116(19):8384–8395, May 2002.

[185] Joseph D. Tobiason, James R. Dunlop, and Eric A. Rohlfing. Dispersed fluorescence spectroscopy of jet-cooled DCO. *Chem. Phys. Lett.*, 235(3-4):268–276, March 1995.

[186] C. Stöck, Xiaonong Li, H.-M. Keller, R. Schinke, and F. Temps. Unimolecular dissociation dynamics of highly vibrationally excited DCO ($\widetilde{X}\ {}^2A'$). I. Investigation of dissociative resonance states by stimulated emission pumping spectroscopy. *J. Chem. Phys.*, 106(13):5333–5358, 1997.

[187] Joel M. Bowman, Joseph S. Bittman, and Lawrence B. Harding. Ab initio calculations of electronic and vibrational energies of HCO and HOC. *J. Chem. Phys.*, 85(2):911–921, July 1986.

[188] Hubert Romanowski, Ki-Tung Lee, Joel M. Bowman, and Lawrence B. Harding. Coupled channel calculation of resonances in H+CO. *J. Chem. Phys.*, 84(9):4888–4893, May 1986.

[189] Hans-Joachim Werner, Cornelia Bauer, Pavel Rosmus, Hans-Martin Keller, Michael Stumpf, and Reinhard Schinke. The unimolecular dissociation of HCO: I. Oscillations of pure CO stretching resonance widths. *J. Chem. Phys.*, 102(9):3593–3611, 1995.

[190] S. Stamatiadis, S. C. Farantos, Hans-Martin Keller, and Reinhard Schinke. Saddle–node states in the spectra of HCO and DCO: a periodic orbit classification of vibrational levels. *Chem. Phys. Lett.*, 344(5–6):565–572, August 2001.

[191] Kermit K. Murray, Thomas M. Miller, Doreen G. Leopold, and W. C. Lineberger. Laser photoelectron spectroscopy of the formyl anion. *J. Chem. Phys.*, 84(5):2520–2525, March 1986.

[192] Joel M. Bowman and Bela Gazdy. A simple method to adjust potential energy surfaces: Application to HCO. *J. Chem. Phys.*, 94(1):816, January 1991.

[193] Andrew D. Sappey and David R. Crosley. Laser-induced fluorescence in the $\widetilde{B} - \widetilde{X}$ system of the HCO radical. *J. Chem. Phys.*, 93(11):7601–7608, 1990.

[194] Desheng Wang and Joel M. Bowman. Complex L^2 calculations of bound states and resonances of HCO and DCO. *Chem. Phys. Lett.*, 235(3-4):277–285, March 1995.

[195] Desheng Wang and Joel M. Bowman. L^2 calculations of resonances and final rotational distributions for HCO→H+CO. *J. Chem. Phys.*, 100(2):1021–1027, January 1994.

[196] D. E. Milligan and M. E. Jacox. *J. Chem. Phys.*, 41:3032, 1964.

[197] R. N. Dixon. *Trans. Faraday Soc.*, 564:3141, 1969.

[198] G. W. Adamson, X. Zhao, and R. W. Field. The HCO $\tilde{B}^2A' \leftrightarrow \tilde{X}^2A'$ System: Fluorescence Excitation and Stimulated Emission Pumping Spectra. *J. Mol. Spectrosc.*, 160(1):11–38, July 1993.

[199] David W. Neyer, Xin Luo, Itamar Burak, and Paul L. Houston. Photodissociation dynamics of state-selected resonances of HCO $\widetilde{X}\ ^2A'$ prepared by stimulated emission pumping. *J. Chem. Phys.*, 102(4):1645–1657, January 1995.

[200] Joseph D. Tobiason, James R. Dunlop, and Eric A. Rohlfing. The unimolecular dissociation of HCO: A spectroscopic study of resonance energies and widths. *J. Chem. Phys.*, 103(4):1448–1469, 1995.

[201] Seon-Woog Cho, William L. Hase, and Kandadai N. Swamy. A model analytic potential energy function for formyl radical decomposition. *J. Phys. Chem. A*, 94:7371–7377, 1990.

[202] J. N. Murrell and J. A. Rodriguez. Predicted Rate Constants for the Exothermic Reactions of Ground State Oxygen Atoms and CH Radicals. *J. Mol. Struct.*, 139(3–4):267, September 1986.

[203] M. E. Jacox. NIST Vibrational and Electronic Energy Levels Database. Technical Report v. 3.0, NIST, Washington,DC, 1993.

[204] R. P. Wayne. *Chemistry of Atmospheres*. Oxford University Press, New York, second edition, 1991.

[205] J. B. Burkholder. Ultraviolet absorption spectrum of HOCl. *J. Geophys. Res.*, 98:2963–2974, 1993.

[206] M. J. Prather. More Rapid Polar Ozone Depletion through the Reaction of HOCl with HCl on Polar Stratospheric Clouds. *Nature*, 355(6360):534–537, February 1992.

P. J. Crutzen, R. Müller, Ch. Brühl, and Th. Peter. On the potential importance of the gas phase reaction CH_3O_2+ClO→ClOO+CH_3O and the heterogeneous reaction HOCl+HCl→H_2O+Cl_2 in özone holeċhemistry. *Geophys. Res. Lett.*, 19:1113–1116, 1992.

[207] A. Callegari, J. Rebstein, J. S. Muenter, R. Jost, and T. R. Rizzo. The spectroscopy and intramolecular vibrational energy redistribution dynamics of HOCl in the $v_{OH} = 6$ region, probed by infrared-visible double resonance overtone excitation. *J. Chem. Phys.*, 111(1):123–133, July 1999.

Gregory Dutton, Rhett James Barnes, and Amitabha Sinha. State selected unimolecular dissociation of HOCl near threshold: The $6v_{OH}$ vibrational state. *J. Chem. Phys.*, 111(11):4976–4992, September 1999.

A. Callegari, J. Rebstein, R. Jost, and T. R. Rizzo. State-to-state unimolecular reaction dynamics of HOCl near the dissociation threshold: The role of vibrations, rotations, and IVR probed by time- and eigenstate-resolved spectroscopy. *J. Chem. Phys.*, 111(16):7359–7368, October 1999.

Andrea Callegari, Roman Schmied, Patrice Theulé, Julia Rebstein, and Thomas R. Rizzo. Eigenstate-resolved unimolecular dissociation dynamics of HOCl at $v_{OH} = 7$ and 8. *Phys. Chem. Chem. Phys.*, 3(12):2245–2252, 2001.

[208] Bernd Abel, Hilmar H. Hamann, Alexander A. Kachanov, and Jürgen Troe. Intracavity laser absorption spectroscopy of HOCl overtones. I. The $3v_1 + 2v_2$ band and numbers of vibrational states. *J. Chem. Phys.*, 104(9):3189–3197, March 1996.

B. Abel, A. Charvát, S. F. Deppe, and H. H. Hamann. State resolved intramolecular dynamics in highly excited HOCl. *Ber. Bunsenges. Phys. Chem.*, 101:329, 1997.

[209] R. J. Barnes, G. Dutton, and A. Sinha. Unimolecular dissociation of hocl near threshold - quantum state and time-resolved studies. *J. Phys. Chem.*, 101(45):L8374–L8377, November 1997.

Rhett James Barnes and Amitabha Sinha. State selected unimolecular dissociation of HOCl. *J. Chem. Phys.*, 107(9):3730–3733, September 1997.

M. R. Wedlock, R. Jost, and T. R. Rizzo. Direct measurement of eigenstate-resolved unimolecular dissociation rates of HOCl. *J. Chem. Phys.*, 107(23):10344–10347, December 1997.

[210] J. Weiß, J. Hauschildt, S. Yu. Grebenshchikov, R. Düren, R. Schinke, J. Koput, S. Stamatiadis, and S. C. Farantos. Saddle–node bifurcations in the spectrum of HOCl. *J. Chem. Phys.*, 112(1):77–93, January 2000.

[211] R. M. Escribano, G. Di Lonardo, and L. Fusina. Empirical anharmonic force field and equilibrium structure of hypochlorous acid, HOCl. *Chem. Phys. Lett.*, 259(5–6):614–618, September 1996.

[212] L. Halonen and T. K. Ha. Ab initio calculation and anharmonic force field of hypochlorous acid, HOCl. *J. Chem. Phys.*, 88(6):3775–3779, 1988.

[213] Kirk A. Peterson. Accurate ab initio near-equilibrium potential energy and dipole moment functions of HOCl and HOBr. *Spectrochim. Acta A: Molecular and Biomolecular Spectroscopy*, 53(8):1051–1064, July 1997.

[214] Jacek Koput and Kirk A. Peterson. The ab initio potential energy surface and spectroscopic constants of HOCl. *Chem. Phys. Lett.*, 283(3–4):139, February 1998.

[215] Sergei Skokov, Kirk A. Peterson, and Joel M. Bowman. An accurate ab initio HOCl potential energy surface, vibrational and rotational calculations, and comparison with experiment. *J. Chem. Phys.*, 109(7):2662–2671, August 1998.

[216] R. Schinke. Trajectory study of the reaction $O(^1D_2)$+HCl→OH+Cl on a fitted ab initio surface. *J. Chem. Phys.*, 80(11):5510–5517, June 1984.

[217] A. Laganá, G. Ochoa de Aspuru, and E. Garcia. The largest angle generalization of the rotating bond order potential: Three different atom reactions. *J. Chem. Phys.*, 108(10):3886–3896, March 1998.

[218] B. R. Johnson anr N. W. Winter. Classical trajectory study of the effect of vibrational energy on the reaction of molecular hydrogen with atomic oxygen. *J. Chem. Phys.*, 66(9):4116–4120, May 1977.

[219] Vladimir A. Mandelshtam and Howard S. Taylor. Spectral projection approach to the quantum scattering calculations. *J. Chem. Phys.*, 102(19):7390–7399, May 1995.

[220] J. S. Wells, R. L. Sams, and W. J. Lafferty. *J. Mol. Spectrosc.*, 77:349, 1979.

W. J. Lafferty and W. B. Olson. The high resolution infrared spectra of the v_2 and v_3 bands of HOCl. *J. Mol. Spectrosc.*, 120:359–373, 1986.

[221] M. E. Kellman. Algebraic Methods in Spectroscopy. *Annu. Rev. Phys. Chem.*, 46:395–421, 1995.

[222] C. C. Martens and G. S. Ezra. Classical and semiclassical mechanics of strongly resonant systems: A Fourier transform approach. *J. Chem. Phys.*, 86(1):279–307, January 1987.

Ευχαριστίες

Στο τέλος της μακράς προσπάθειας της συγγραφής της διατριβής μου θέλω να ευχαριστήσω, καταρχήν την οικογένειά μου για την υποστήριξή τους καθώς και τον επιβλέποντα Καθηγητή Σ. Φαράντο για τη συνεργασία και για τις δυνατότητες που μου παρείχε ώστε να επεκτείνω τις γνώσεις μου σε θέματα πέραν του άμεσου ερευνητικού μου τομέα. Δεν ξεχνώ ότι χωρίς τις παροτρύνσεις του δε θα είχε αρχίσει ποτέ η συγγραφή του παρόντος έργου. Θέλω επίσης να ευχαριστήσω τον Dr. R. Schinke και την ερευνητική του ομάδα για την πολύ αποδοτική συνεργασία καθώς και για τη φιλοξενία τους στο Max-Planck-Institut für Strömungsforschung. Σημαντική είναι ακόμη η οικονομική υποστήριξη που μου παρείχαν τα Τμήματα Φυσικής και Χημείας του Πανεπιστημίου Κρήτης και το Ινστιτούτο Ηλεκτρονικής Δομής και Laser του Ιδρύματος Τεχνολογίας και Έρευνας.

Θέλω να ευχαριστήσω επίσης τους Θοδωρή και Βούλα Πιερράτου, Γιώργο και Μαρούσα Κουνδουράκη, Λάμπρο και Νατάσα Νικολόπουλου, Αντώνη Κουμπενάκη και την οικογένειά του, και Τσαμπίκο και Μάνια Κόττου, για την οικογενειακή ατμόσφαιρα που μου προσέφεραν το διάστημα παραμονής μου στο Ηράκλειο και στο Göttingen, τους Νίκο Σιμάτο, Μιχάλη Καπνιστό και Μαρία Λασηθιωτάκη που συμπλήρωναν το στενό κύκλο των φίλων μου καθώς και όλους τους υπόλοιπους συναδέλφους μεταπτυχιακούς που με διάφορους τρόπους συνέβαλαν στην διεξαγωγή του έως τώρα ερευνητικού μου έργου.